

10-10-2016

# Evaluation of Redundancy of Twin Steel Box-Girder Bridges

Huy V. Pham  
hpham005@fiu.edu

**DOI:** 10.25148/etd.FIDC001242

Follow this and additional works at: <https://digitalcommons.fiu.edu/etd>

 Part of the [Civil Engineering Commons](#)

---

## Recommended Citation

Pham, Huy V., "Evaluation of Redundancy of Twin Steel Box-Girder Bridges" (2016). *FIU Electronic Theses and Dissertations*. 2720.  
<https://digitalcommons.fiu.edu/etd/2720>

This work is brought to you for free and open access by the University Graduate School at FIU Digital Commons. It has been accepted for inclusion in FIU Electronic Theses and Dissertations by an authorized administrator of FIU Digital Commons. For more information, please contact [dcc@fiu.edu](mailto:dcc@fiu.edu).

FLORIDA INTERNATIONAL UNIVERSITY

Miami, Florida

EVALUATION OF REDUNDANCY OF TWIN STEEL BOX-GIRDER BRIDGES

A dissertation submitted in partial fulfillment of

the requirements for the degree of

DOCTOR OF PHILOSOPHY

in

CIVIL ENGINEERING

by

Huy Van Pham

2016

To: Interim Dean Ranu Jung  
College of Engineering and Computing

This dissertation, written by Huy Van Pham, and entitled Evaluation of Redundancy of Twin Steel Box-Girder Bridges, having been approved in respect to style and intellectual content, is referred to you for judgment.

We have read this dissertation and recommend that it be approved.

---

Ali Mostafavi

---

Seung Jae Lee

---

Arindam Gan Chowdhury

---

Ton-lo Wang

---

Atorod Azizinamini, Major Professor

Date of Defense: October 10, 2016

The dissertation of Huy Van Pham is approved.

---

Interim Dean Ranu Jung  
College of Engineering and Computing

---

Andrés G. Gil  
Vice President for Research and Economic Development  
and Dean of the University Graduate School

Florida International University, 2016

© Copyright 2016 by Huy Van Pham

All rights reserved.

## DEDICATION

This dissertation is dedicated to my parents for their unconditional love and supports, to all of my family members and friends for their encouragements and to my advisor, Dr. Azizinamini, for his guidance throughout the course of the research.

## ACKNOWLEDGMENTS

I would like to dedicate my deepest gratitude to my advisor, Dr. Atorod Azizinamini, for all of his guidance and support along the way. His great vision and experience has taught me many invaluable lessons throughout these years at Florida International University.

I would like to express special thanks my dissertation committee members, Dr. Ton-Lo Wang, Dr. Arindam Gan Chowdhury, Dr. Seung Jae Lee, and Dr. Ali Mostafavi for significant suggestions throughout the project and comments on my dissertation.

I would like to thank Dr. Aaron Yakel and Dr. Jawad Gull for their significant helps and suggestions in both experimental and numerical works. I also would like to thank my fellow graduate students, Alireza Mohammadi and Ramin Taghinezad for their valuable comments throughout the project.

I would like to thank Florida Department of Transportation (FDOT) for sponsoring this research. I would like to thank FDOT Research Center and its staffs for their collaborations throughout the project.

Finally, I dedicate the greatest gratitude to my parents and family members for their unconditional supports, love, and encouragement. I'm grateful to you for being with me at every step I have made. Nothing would be meaningful without you.

## ABSTRACT OF THE DISSERTATION

### EVALUATION OF REDUNDANCY OF TWIN STEEL BOX-GIRDER BRIDGES

by

Huy Van Pham

Florida International University, 2016

Miami, Florida

Professor Atorod Azizinamini, Major Professor

Based on the definition given in the AASHTO LRFD Bridge Design Specifications, twin steel box-girder bridges are classified as bridges with fracture critical members (FCMs), in which a failure of a tension member is expected to lead to a collapse of the bridge. However, a number of such bridges with either a partial or full-depth crack in one girder have been reported and are still providing service without collapsing. The main objective of this research project is to understand the behavior of twin steel box-girder bridges and to develop methods for evaluating their redundancy level in the event of the fracture of one tension member.

The research project included an experimental investigation on a small-scale steel twin box-girder bridge, field testing of a full-scale twin box-girder, analysis of existing research and design data, and an extensive amount of numerical analyses carried out on calibrated 3-D nonlinear finite element models.

The results from this study provide in-depth understanding of twin steel box-girder bridge behavior before and after a fracture in the tension member occurs. In addition to the experimentally verified finite element method, the report also proposes simplified methods for evaluating the load-carrying capacity of twin steel box-girder bridges under

concentrated loads and provides a list of important factors that could control the reserve capacity of the damaged bridge.

The main conclusion of this research is that the redundancy exists in twin steel box-girder bridges in an event that a fracture of a tension member(s) takes place. This research project also provides a comprehensive roadmap for assessing the redundancy of twin steel box-girder bridges in which the elements of the roadmap are identified, and solutions for several of the steps are provided. The development of solutions for remaining steps of the roadmap is proposed for a future research.



## TABLE OF CONTENTS

|           |   |    |
|-----------|---|----|
| Chapter 1 | Introduction.....   | 1  |
| 1.1       | Problem Statement .....   | 1  |
| 1.2       | Background .....  | 2  |
| 1.3       | Current Approaches.....   | 10 |
| 1.3.1     | Direct Analysis Approach with Redundancy Criteria -NCHRP Report 406.....                          | 10 |
| 1.3.2     | Simplified Analytical Modeling Methods for Redundancy Assessment of Twin Box-Girder Bridges ..... | 13 |
| 1.3.3     | Limitations and Shortcomings .....  | 16 |
| 1.4       | Research Objectives .....   | 18 |
| 1.5       | Dissertation Organization.....  | 18 |
| Chapter 2 | Research Methodology .....  | 20 |
| 2.1       | Main Characteristics of Comprehensive Methodology for Assessment .....                            | 22 |
| Chapter 3 | Laboratory Testing on Small-Scale Specimen.....   | 28 |
| 3.1       | Specimen Design.....  | 28 |
| 3.1.1     | Analysis of Composite Section .....   | 32 |
| 3.2       | Specimen Construction .....   | 35 |
| 3.3       | Instrumentation Plan .....  | 37 |
| 3.4       | Test Setup.....   | 42 |
| 3.5       | Testing Plan.....   | 46 |
| 3.5.1     | Elastic Tests .....   | 46 |
| 3.5.2     | Cyclic Test .....   | 49 |
| 3.5.3     | Ultimate Load Tests .....   | 50 |
| Chapter 4 | Laboratory Testing Results .....  | 53 |
| 4.1       | Elastic Tests.....  | 53 |
| 4.1.1     | On Undamaged Specimen.....  | 53 |
| 4.1.2     | On Damaged Specimen with Bottom Flange Fractured in One Girder .....                              | 55 |
| 4.1.3     | On Damaged Specimen with Bottom Flange and Webs Fractured in One Girder .....                     | 57 |
| 4.1.4     | Summary of Elastic Tests .....  | 60 |
| 4.2       | Cyclic Test.....  | 64 |
| 4.3       | Ultimate Test A .....   | 74 |
| 4.3.1     | Global Behavior .....   | 75 |
| 4.3.2     | Local Behavior.....   | 82 |
| 4.3.3     | Load-Transferring Mechanism .....   | 88 |
| 4.4       | Reconstruction of Bridge Specimen.....  | 90 |
| 4.5       | Ultimate Test B .....   | 93 |
| 4.5.1     | Global Behavior .....   | 93 |
| 4.5.2     | Local Behavior.....   | 97 |

|   |   |     |
|---|---|-----|
| 4.6   | Ultimate Test C .....   | 103 |
| 4.6.1   | Global Behavior .....   | 104 |
| 4.6.2   | Local Behavior .....  | 107 |
| 4.7   | Ultimate Test D .....   | 112 |
| 4.7.1   | Global Behavior .....   | 113 |
| 4.7.2   | Local Behavior .....  | 118 |
| 4.8   | Damage Repair .....   | 123 |
| 4.9   | Ultimate Test E .....   | 124 |
| 4.9.1   | Global Behavior .....   | 126 |
| 4.9.2   | Local Behavior .....  | 132 |
| Chapter 5 Finite Element Modeling — Procedures and Verification .....         |   | 136 |
| 5.1   | FEM of Bridge Specimen .....  | 136 |
| 5.2   | Fracture Damage and Connection Modeling .....                         | 137 |
| 5.3   | Steel Behavior Modeling .....   | 139 |
| 5.4   | Concrete Material Properties .....                                    | 141 |
| 5.5   | Concrete and Reinforcement Behavior Modeling .....                    | 144 |
| 5.6   | Bearing Pad and Contact Surface Modeling .....                        | 148 |
| Chapter 6 Validating FE Models with Experimental Data .....                   |   | 156 |
| 6.1   | Undamaged Bridge Specimen .....                                       | 156 |
| 6.1.1   | Test 1 - No Rail, No Continuity, Symmetric Loading (NNS) .....        | 156 |
| 6.1.2   | Test 2 - No Rail, No Continuity, Unsymmetrical Loading (NNU) .....    | 159 |
| 6.1.3   | Test 3 - No Rail, with Continuity, Unsymmetrical Loading (NYU) .....  | 161 |
| 6.2   | Bridge Specimen with Bottom Flange Fractured in One Girder .....      | 164 |
| 6.2.1   | Test 9 - with Rail, No Continuity, Unsymmetrical Loading (YNU) .....  | 164 |
| 6.2.2   | Test 10 - No Rail, No Continuity, Symmetric Loading (NNS) .....       | 166 |
| 6.3   | Bridge Specimen with Full-Web Fractured in One Girder .....           | 169 |
| 6.3.1   | Test 16 - with Rail, No Continuity, Unsymmetrical Loading (YNU) ..... | 169 |
| 6.3.2   | Test 17 - No Rail, No Continuity, Symmetric Loading (NNS) .....       | 171 |
| 6.4   | Verification of FEMs with Ultimate Test A .....                       | 173 |
| 6.5   | Verification of FEMs with Ultimate Test B .....                       | 180 |
| 6.6   | Summary .....   | 185 |
| Chapter 7 Field Testing of Ft. Lauderdale Twin Box-Girder Bridge 860600 ..... |   | 187 |
| 7.1   | Objective .....   | 190 |
| 7.2   | Bridge Configuration .....  | 190 |
| 7.3   | Instrumentation .....   | 194 |
| 7.3.1   | Potentiometers (Displacement Sensors) .....                           | 195 |
| 7.3.2   | Strain Gauges .....   | 200 |
| 7.4   | Loading .....   | 203 |
| 7.5   | Finite Element Modeling .....   | 207 |
| 7.6   | Qualitative Review of Test Data .....                                 | 209 |
| 7.7   | Comparison of Field Test Data and FEA Results .....                   | 213 |

|            |   |     |
|------------|---|-----|
| Chapter 8  | Redundancy Analysis of Ft. Lauderdale Twin Box-Girder Bridge 860600.....  | 228 |
| 8.1        | Bridge Girder Flexural Capacity .....   | 228 |
| 8.1.1      | Effective Width of Concrete Deck.....   | 229 |
| 8.1.2      | Section Compactness .....   | 230 |
| 8.1.3      | Nominal Moment Capacity.....  | 231 |
| 8.2        | Linear Elastic Analysis of the Bridge .....   | 235 |
| 8.3        | Nonlinear Finite Element Analysis .....   | 239 |
| 8.4        | Redundancy Analysis.....  | 242 |
| 8.4.1      | Member Failure ( $LF_1$ ).....  | 242 |
| 8.4.2      | Ultimate Limit State ( $LF_u$ ).....  | 243 |
| 8.4.3      | Damage Condition Limit State ( $LF_d$ ).....  | 244 |
| 8.4.4      | Functionality Limit State ( $LF_f$ ).....   | 245 |
| 8.5        | Summary .....   | 246 |
| Chapter 9  | Simplified Methods of Predicting Remaining Capacity of Damaged Twin Steel Box-Girder Bridges under Concentrated Loads.....      | 247 |
| 9.1        | One-Way Shear Provision for Bridge Slabs.....   | 248 |
| 9.2        | Two-Way (Punching) Shear Provision for Bridge Slabs .....   | 250 |
| 9.3        | Literature Review on Compressive Membrane Action.....   | 251 |
| 9.4        | Literature Review on Direct Load Transfer .....   | 265 |
| 9.5        | Methods for Predicting Punching Shear Capacity of Damaged Twin Steel Box-Girder under Single Concentrated Load.....             | 269 |
| 9.5.1      | Proposed New Shear Span Factor for Two-Way Slabs Subjected to Concentrated Load .....   | 269 |
| 9.5.2      | Proposed Method for Predicting Punching Shear Resistance of Bridge Slabs under CMA and Direct Load Transfer Effects.....        | 279 |
| 9.6        | Methods for Predicting Shear Capacity of Damaged Twin Steel Box-Girder under Four Concentrated Loads .....                      | 281 |
| 9.7        | Comparisons between Predictions and Experimental Results for Damaged Twin Steel Box-Girder under Single Concentrated Load ..... | 284 |
| 9.7.1      | Under Single Concentrated Load – Tests A, C, and D .....  | 285 |
| 9.7.2      | Under Four Concentrated Loads – Test E.....   | 287 |
| 9.8        | Investigation of Punching Shear Resistance of Slabs across the Bridge in Transverse Direction .....                             | 291 |
| 9.9        | Summary .....   | 297 |
| Chapter 10 | Proposed Notional Approach for Evaluating Redundancy of Twin Steel Box-Girder Bridges.....                                      | 299 |
| 10.1       | Key Components of the Notional Approach .....   | 299 |
| 10.2       | Suggestions for Developing Redundancy Criteria .....  | 303 |
| Chapter 11 | Parameters Affecting Load-Carrying Capacity of Bridge .....   | 307 |
| 11.1       | Cross-frames.....   | 307 |
| 11.2       | Railing .....   | 309 |

|            |  |     |
|------------|--|-----|
| 11.3       | Structural Indeterminacy and Cantilever End .....                                  | 310 |
| 11.4       | Bridge Span Length .....   | 311 |
| 11.5       | Summary.....   | 312 |
| Chapter 12 | Summary and Future Considerations.....   | 314 |
| 12.1       | Research Summary .....   | 314 |
| 12.2       | Field Tests of In-Service Bridge.....  | 317 |
| 12.3       | Laboratory Tests on Small-Scale Specimen.....                                      | 318 |
| 12.3.1     | Conclusions from Elastic Tests Conducted on Laboratory Test<br>Specimen.....       | 319 |
| 12.3.2     | Conclusions from Cyclic Tests Conducted on Laboratory Test<br>Specimen.....        | 320 |
| 12.3.3     | Conclusions from Ultimate Load Tests Conducted on Laboratory Test<br>Specimen..... | 321 |
| 12.4       | Summary of Proposed Approaches .....   | 325 |
| 12.5       | Suggestions for Future Study .....   | 326 |
| References | .....  | 327 |
| VITA       | .....  | 332 |

## LIST OF TABLES

| TABLE   | PAGE |
|---|------|
| Table 3-1 Plan for Elastic and Cyclic Tests.....                                    | 48   |
| Table 3-2 Plan for Ultimate Load Tests.....   | 52   |
| Table 4-1 Summary of Elastic Tests on Undamaged Specimen.....                       | 54   |
| Table 4-2 Summary of Elastic Tests on Bottom Flange Fractured Specimen.....         | 56   |
| Table 4-3 Summary of Elastic Tests on Full-Web Fractured Specimen.....              | 58   |
| Table 4-4 Summary of all Elastic Tests.....   | 64   |
| Table 5-1 Concrete Cylinder Strengths for First Specimen.....                       | 141  |
| Table 5-2 Concrete Cylinder Strengths for Reconstructed Specimen.....               | 142  |
| Table 5-3 Concrete Tensile Strengths for Reconstructed Specimen.....                | 143  |
| Table 5-4 Input Parameters for Properties of Concrete Materials.....                | 147  |
| Table 5-5 Summary of KEYOPTs Defaults in ANSYS.....                                 | 153  |
| Table 5-6 Summary of Default and Input Real Constants.....                          | 154  |
| Table 6-1 Comparison of Displacement between FEA Results and all Elastic Tests. ... | 186  |
| Table 7-1 Thickness of Top and Bottom Flanges of the Bridge Girders.....            | 192  |
| Table 7-2 General Structure and Testing Specifications.....                         | 194  |
| Table 7-3 Test Truck-1 Specifications.....  | 204  |
| Table 7-4 Test Truck-2 Specifications.....  | 204  |
| Table 7-5 Loading Path Definitions.....   | 206  |
| Table 7-6 Loading Scenario Definitions.....   | 207  |
| Table 8-1 Live Load Capacity of the Bridge as a Multiplier of HS-20 Trucks.....     | 241  |
| Table 8-2 Summary of Redundancy Analysis Results on the Ft. Lauderdale Bridge ....  | 246  |

|  |     |
|--|-----|
| Table 9-1 Influence of $a_v/d$ on Shear Resistance of Bridge Slab Portion over Intact Girder .....                           | 275 |
| Table 9-2 Influence of $a_v/d$ on Shear Resistance of Bridge Slab Portion over Damaged Girder .....                          | 278 |
| Table 9-3 Comparison between Test Results and Predicting Methods. ....   | 287 |
| Table 9-4 Comparison of between Punching Shear Test Results (Kathol et al., 1995) and the Proposed Method's Predictions..... | 287 |
| Table 9-5 Comparison of between Test E and Predictions Using Beam Shear Approach.....  | 290 |
| Table 9-6 Comparison of between Test E and Predictions Using Punching Shear Approach.....                                    | 291 |
| Table 9-7 Comparison of Punching Shear Resistance of Slabs at Locations L1, L2, L3 and L4 and the predicted values.....      | 296 |
| Table 10-1 Validation of the Notional Approach. ....   | 301 |
| Table 11-1 Effects of Span Length on the Bridge Performance. ....  | 312 |

## LIST OF FIGURES

| FIGURE  | PAGE |
|---|------|
| Figure 1-1 FSEL twin box-girder bridge (Source: FHWA Report No FHWA/TX-10/9-5498-1).....                  | 7    |
| Figure 1-2 FSEL first bridge fracture test (Source: FHWA Report No FHWA/TX-10/9-5498-1).....              | 8    |
| Figure 1-3 Bottom flange cut after the explosion (Source: FHWA Report No FHWA/TX-10/9-5498-1). ....       | 8    |
| Figure 1-4 FSEL second bridge fracture test (Source: FHWA Report No FHWA/TX-10/9-5498-1). ....            | 9    |
| Figure 1-5 FSEL third bridge fracture test (Source: FHWA Report No FHWA/TX-10/9-5498-1).....              | 9    |
| Figure 1-6 Yield line model proposed by Barnard et al. (2010).....  | 15   |
| Figure 2-1 Probability density functions of load and resistance of damaged and undamaged bridges. ....    | 26   |
| Figure 3-1 Dimension of one steel box girder. ....  | 29   |
| Figure 3-2 Center-to-center flange distance (Adopted from AASHTO LRFD Bridge Design Specifications). .... | 30   |
| Figure 3-3 Cross-section of the tested specimen. ....   | 31   |
| Figure 3-4 Internal bracing locations in each box girder.....   | 32   |
| Figure 3-5 The top plan view of the testing specimen.....   | 32   |
| Figure 3-6 Location of plastic neutral axis. ....   | 35   |
| Figure 3-7 Welding details.....   | 36   |
| Figure 3-8 Complete specimen ready for casting. ....  | 37   |
| Figure 3-9 Casting the concrete deck.....   | 37   |
| Figure 3-10 Locations of strain gauges and potentiometers along the length of the specimen. ....          | 38   |

|  |    |
|--|----|
| Figure 3-11 Strain gauges in the Section 2. ....   | 39 |
| Figure 3-12 Strain gauges in the Section 3. ....   | 39 |
| Figure 3-13 Strain gauges in the Section 4. ....   | 40 |
| Figure 3-14 Strain gauges in the Section 5. ....   | 40 |
| Figure 3-15 Strain gauges in the Section 6. ....   | 41 |
| Figure 3-16 Strain gauges in the Section 8. ....   | 41 |
| Figure 3-17 Potentiometers in Section 5. ....  | 42 |
| Figure 3-18 Potentiometers in Section 2. ....  | 42 |
| Figure 3-19 Longitudinal view of test specimen. ....   | 43 |
| Figure 3-20 Setup for continuity effect. ....  | 44 |
| Figure 3-21 Schematic drawing of loading system. ....  | 45 |
| Figure 3-22 Specimen with complete loading setup. ....   | 45 |
| Figure 3-23 Typical three-ramp loading history for the elastic tests. ....                           | 48 |
| Figure 4-1 Saw cutting of bottom flange in east girder. ....   | 55 |
| Figure 4-2 East girder with bottom flange and web fractured in one girder. ....                      | 58 |
| Figure 4-3 Results of elastic tests on undamaged specimen. ....                                      | 62 |
| Figure 4-4 Results of elastic tests on specimen with bottom flange fractured in east<br>girder. .... | 62 |
| Figure 4-5 Results of elastic tests on specimen with full-depth fracture in east girder. ...         | 63 |
| Figure 4-6 Schematic description of the cyclic loading test. ....                                    | 65 |
| Figure 4-7 Cracks on the deck surface during cyclic test. ....                                       | 66 |
| Figure 4-8 Crack in the damaged girder: (a) before and (b) after the cyclic test. ....               | 67 |
| Figure 4-9 Crack growth in the damaged girder. ....  | 68 |
| Figure 4-10 Crack opening measuring gauge on the exterior face. ....                                 | 69 |
| Figure 4-11 Crack base opening vs. number of loading cycles. ....                                    | 70 |



|   |    |
|---|----|
| Figure 4-12 Mid-span displacement vs. number of loading cycles in the fractured girder. ....        | 71 |
| Figure 4-13 Displacement range (max – min) vs. number of loading cycles. ....                       | 71 |
| Figure 4-14 Stiffness of each girder during the cyclic test. ....                                   | 72 |
| Figure 4-15 (a) Strain locations and (b) Strain profile in each cross-frame brace.....              | 73 |
| Figure 4-16 Maximum shear transfer in one cross-frame.....  | 74 |
| Figure 4-17 Schematic description of Test A. ....   | 75 |
| Figure 4-18 Load vs. deflection curve of the specimen during ultimate load Test A.....              | 76 |
| Figure 4-19 Punching in the top of the concrete surface looking to South.....                       | 77 |
| Figure 4-20 Punching in the bottom of the deck.....   | 78 |
| Figure 4-21 Damage at North end (left) and South end (right). ....                                  | 79 |
| Figure 4-22 Location of potentiometers at supports. ....  | 80 |
| Figure 4-23 Displacement of the both girders near the south support. ....                           | 80 |
| Figure 4-24 Displacement of the both girders near the north support. ....                           | 81 |
| Figure 4-25 Uplift at (a) north support and (b) south support. ....                                 | 81 |
| Figure 4-26 Strain gauges at the mid-span section. ....   | 83 |
| Figure 4-27 Longitudinal strain at the top and bottom flanges of the intact girder at mid-span..... | 84 |
| Figure 4-28 Longitudinal strain at the bottom flange of the intact girder. ....                     | 84 |
| Figure 4-29 Comparison of longitudinal strains in the intact and damaged girders at Section 5.....  | 85 |
| Figure 4-30 Strains of the transverse rebar at mid-span. ....                                       | 86 |
| Figure 4-31 Longitudinal strain of rebars in longitudinal direction at mid-span.....                | 87 |
| Figure 4-32 Transverse strain at the top and bottom of deck at mid-span.....                        | 88 |
| Figure 4-33 Shear transferred through one cross-frame in Test A. ....                               | 90 |

|   |     |
|---|-----|
| Figure 4-34 Damage in (a) the inner top flange, (b) the outer top flange of the damaged girder. ....        | 91  |
| Figure 4-35 Alignment of two fractured segments. ....   | 92  |
| Figure 4-36 The reconstructed specimen before (left) and after casting (right). ....                        | 92  |
| Figure 4-37 Schematic description of Test B. ....   | 93  |
| Figure 4-38 Test B: Load vs. displacement curves at (a) mid-span, (b) Section 5 and (c) cantilever end..... | 95  |
| Figure 4-39 Displacements at (a) north support and (b) south support. ....                                  | 96  |
| Figure 4-40 Shear transferred through a cross-frame in Test B.....  | 97  |
| Figure 4-41 Average longitudinal strains at top flanges of the intact girder. ....                          | 100 |
| Figure 4-42 Longitudinal strains at the bottom flange of the intact girder. ....                            | 100 |
| Figure 4-43 Comparison of longitudinal strains in the intact and damaged girders at Section 5.....          | 101 |
| Figure 4-44 Longitudinal strain in rebars at mid-span.....  | 101 |
| Figure 4-45 Transverse strain in rebars at mid-span.....  | 102 |
| Figure 4-46 Schematic deflection shape of the deck. ....  | 102 |
| Figure 4-47 Transverse strain of the deck near mid-span. ....   | 103 |
| Figure 4-48 Schematic description of Test C. ....   | 104 |
| Figure 4-49 Punching damage in test C.....  | 105 |
| Figure 4-50 Shear transferred through a cross-frame in test C.....  | 105 |
| Figure 4-51 Test C: Load vs. displacement curves at (a) mid-span, (b) Section 5 and (c) cantilever end..... | 106 |
| Figure 4-52 Displacements at (a) north support and (b) south support. ....                                  | 107 |
| Figure 4-53 Average longitudinal strains at top flanges of the intact girder. ....                          | 110 |
| Figure 4-54 Longitudinal strains at the bottom flange of the intact girder. ....                            | 110 |

|   |     |
|---|-----|
| Figure 4-55 Comparison of longitudinal strains in the intact and damaged girders at Section 5.....          | 111 |
| Figure 4-56 Longitudinal strain in rebars at mid-span.....  | 111 |
| Figure 4-57 Transverse strain in rebars at mid-span.....  | 112 |
| Figure 4-58 Transverse strain on the deck near mid-span. ....   | 112 |
| Figure 4-59 Schematic description of Test D. ....   | 113 |
| Figure 4-60 Test D: Load vs. displacement curves at (a) mid-span, (b) Section 5 and (c) cantilever end..... | 115 |
| Figure 4-61 Punching damage in Test D. ....   | 116 |
| Figure 4-62 Displacements at (a) north support and (b) south support. ....                                  | 117 |
| Figure 4-63 Shear transferred through a cross-frame in Test D. ....   | 118 |
| Figure 4-64 Average longitudinal strains at top flanges of the intact girder. ....                          | 120 |
| Figure 4-65 Longitudinal strains in bottom flange of the intact girder at Sections 2, 3, 4, and 5.....      | 120 |
| Figure 4-66 Comparison of longitudinal strains in the intact and damaged girders at Section 5.....          | 121 |
| Figure 4-67 Longitudinal strain in rebars at mid-span.....  | 121 |
| Figure 4-68 Transverse strain in rebars at mid-span.....  | 122 |
| Figure 4-69 Transverse strain on the deck near mid-span. ....   | 122 |
| Figure 4-70 Repair of punching shear damage from Tests C and D. ....  | 124 |
| Figure 4-71 (a) Test setup for Test E and (b) schematic locations of loading foot prints. ....              | 125 |
| Figure 4-72 Damage in Test E. ....  | 128 |
| Figure 4-73 Test E: Load vs displacement curves at (a) mid-span, (b) Section 5 and (c) cantilever end.....  | 129 |
| Figure 4-74 Shear damage at ends in Test E.....   | 130 |
| Figure 4-75 Displacements at (a) north support and (b) south support. ....                                  | 131 |

|  |     |
|--|-----|
| Figure 4-76 Shear transferred through a cross-frame in Test E.....   | 132 |
| Figure 4-77 Average longitudinal strains at top flanges of the intact girder. ....   | 133 |
| Figure 4-78 Longitudinal strains at the bottom flange of the intact girder. ....   | 134 |
| Figure 4-79 Comparison of longitudinal strains in the intact and damaged girders at<br>Section 5.....                        | 134 |
| Figure 4-80 Longitudinal strain of rebars at mid-span. ....  | 135 |
| Figure 4-81 Transverse strain on the deck near mid-span. ....  | 135 |
| Figure 5-1 Finite element bridge model.....  | 137 |
| Figure 5-2 Process to simulate a fracture condition.....   | 138 |
| Figure 5-3 Finite element model with full-web fracture condition.....  | 139 |
| Figure 5-4 Stress-strain behavior of steel girder and rebars. ....   | 140 |
| Figure 5-5 Modeling of stress-strain curve of concrete in compression.....   | 144 |
| Figure 5-6 SOLID65 concrete element in ANSYS.....  | 145 |
| Figure 5-7 Smeared reinforcement bars.....   | 145 |
| Figure 5-8 Failure surfaces of concrete under (a) biaxial and (b) triaxial loading states<br>(Willam and Warnke, 1975). .... | 148 |
| Figure 5-9 Typical stress-strain curve for steel-reinforced bearings (AASHTO-<br>C14.7.6.3.3-1). ....                        | 149 |
| Figure 5-10 Contact surface between the bearing pad and bottom flange of girder.....   | 150 |
| Figure 5-11 Mid-span displacement before and after modeling the bearing pads.....  | 155 |
| Figure 6-1 Schematic description of Test 1. ....   | 157 |
| Figure 6-2 Comparison of vertical displacement at the bottom flange of each girder in<br>Test 1.....                         | 157 |
| Figure 6-3 Comparison of longitudinal strain at the bottom flange of each girder in<br>Test 1.....                           | 158 |
| Figure 6-4 Comparison of longitudinal strain at the top flange of each girder in<br>Test 1.....                              | 158 |

|   |     |
|---|-----|
| Figure 6-5 Schematic description of Test 2.....   | 159 |
| Figure 6-6 Comparison of vertical displacement at the bottom flange of each girder in Test 2.....   | 160 |
| Figure 6-7 Comparison of longitudinal strain at the bottom flange of each girder in Test 2.....     | 160 |
| Figure 6-8 Comparison of longitudinal strain at the top flange of each girder in Test 2.....        | 161 |
| Figure 6-9 Schematic description of Test 3.....   | 162 |
| Figure 6-10 Comparison of vertical displacement at the bottom flange of each girder in Test 3.....  | 162 |
| Figure 6-11 Comparison of longitudinal strain at the bottom flange of each girder in Test 3.....    | 163 |
| Figure 6-12 Comparison of longitudinal strain at the top flange of each girder in Test 3.....       | 163 |
| Figure 6-13 Schematic description of Test 9.....  | 164 |
| Figure 6-14 Comparison of vertical displacement at the bottom flange of each girder in Test 9.....  | 165 |
| Figure 6-15 Comparison of longitudinal strain at the bottom flange of each girder in Test 9.....    | 165 |
| Figure 6-16 Comparison of longitudinal strain at the top flange of each girder in Test 9.....       | 166 |
| Figure 6-17 Schematic description of Test 10.....   | 167 |
| Figure 6-18 Comparison of vertical displacement at the bottom flange of each girder in Test 10..... | 167 |
| Figure 6-19 Comparison of longitudinal strain at the bottom flange of each girder in Test 10.....   | 168 |
| Figure 6-20 Comparison of longitudinal strain at the top flange of each girder in Test 10.....      | 168 |
| Figure 6-21 Schematic description of Test 16.....   | 169 |

|   |     |
|---|-----|
| Figure 6-22 Comparison of vertical displacement at the bottom flange of each girder in Test 16.....   | 170 |
| Figure 6-23 Comparison of longitudinal strain at the bottom flange of undamaged girder in Test 16.....  | 170 |
| Figure 6-24 Schematic description of Test 17.....   | 171 |
| Figure 6-25 Comparison of vertical displacement at the bottom flange of each girder in Test 17.....   | 172 |
| Figure 6-26 Comparison of longitudinal strain at the bottom flange of undamaged girder in Test 17.....  | 172 |
| Figure 6-27 Comparison of load vs. vertical deflection curves using displacement-control analysis.....  | 174 |
| Figure 6-28 Comparison of load vs. vertical deflection curve using load-control analysis.....   | 174 |
| Figure 6-29 Vertical displacements at the bottom flange of each girder and at center of the deck at mid-span.....                               | 175 |
| Figure 6-30 Reactions vs. EG vertical displacement.....   | 176 |
| Figure 6-31 Prediction of uplift in finite element analysis.....  | 176 |
| Figure 6-32 Comparison of longitudinal strains at the top flange of WG at mid-span. .   | 177 |
| Figure 6-33 Comparison of longitudinal strain at bottom flange at mid-span.....   | 177 |
| Figure 6-34 Comparison of transverse strain on the top of deck.....   | 178 |
| Figure 6-35 Location of concrete crushing in FEA and in experiment.....   | 179 |
| Figure 6-36 Shear cracking in south (left) and north (right) supports.....  | 179 |
| Figure 6-37 Stress contour at mid-span in the steel girders.....  | 180 |
| Figure 6-38 Load vs average vertical displacements at (a) mid-span, (b) Section 5, and (c) cantilever end.....                                  | 182 |
| Figure 6-39 Transverse strain on the deck at mid-span.....  | 183 |
| Figure 6-40 Comparison of longitudinal strains at the bottom flange of the intact girder at (a) mid-span, (b) Section 3, and (c) Section 5..... | 184 |

|  |     |
|--|-----|
| Figure 7-1 First two spans of the ramp bridge - underneath view. ....                  | 189 |
| Figure 7-2 First span of the ramp bridge 860600 - elevation view from west.....        | 189 |
| Figure 7-3 Elevation view of the bridge. ....  | 190 |
| Figure 7-4 Cross-section of the Ft. Lauderdale bridge 860600. ....                     | 191 |
| Figure 7-5 Internal bracing of superstructure girders. ....                            | 193 |
| Figure 7-6 Locations of potentiometers in the first two spans.....                     | 195 |
| Figure 7-7 Arrangement of potentiometers at Location 1 in the first span.....          | 196 |
| Figure 7-8 Gauge and channel ID of first span displacement sensors. ....               | 196 |
| Figure 7-9 Displacement sensor beneath bottom flange of box-girder (typical). ....     | 197 |
| Figure 7-10 Displacement sensor on SIP form below concrete deck. ....                  | 198 |
| Figure 7-11 Arrangement of the potentiometers at Location 2 in the second span. ....   | 199 |
| Figure 7-12 Gauge and channel ID of displacement sensors at Location 2.....            | 199 |
| Figure 7-13 Locations of strain gauges in the first span. ....                         | 200 |
| Figure 7-14 Strain transducers on box-girders (typical). ....                          | 201 |
| Figure 7-15 Gauge and channel ID's of strain gauges at Section 1.....                  | 202 |
| Figure 7-16 Gauge and channel ID's of strain gauges at Section 2.....                  | 202 |
| Figure 7-17 Gauge and channel ID's of strain gauges at Section 3.....                  | 203 |
| Figure 7-18 Test Truck-1 axle spacing. ....  | 205 |
| Figure 7-19 Test Truck-2 axle spacing. ....  | 205 |
| Figure 7-20 Test truck path locations. ....  | 206 |
| Figure 7-21 Finite element model of the first span of Ft. Lauderdale bridge 860600.... | 208 |
| Figure 7-22 Reproducibility of strain response histories (typical). ....               | 210 |
| Figure 7-23 Reproducibility of displacement response histories (typical). ....         | 210 |
| Figure 7-24 Example of variable thermal drift observed during testing.....             | 211 |

|   |     |
|---|-----|
| Figure 7-25 Comparison of raw and thermally corrected strain data. ....   | 212 |
| Figure 7-26 Strain history comparison – crawl speed vs. roadway speed at Section 2..  | 213 |
| Figure 7-27 Vertical deflection of west edge of WG: 59 ft from north abutment,<br>Truck-1 on path-3. ....                         | 214 |
| Figure 7-28 Vertical deflection of west edge of WG: 225.5 ft from north abutment,<br>Truck-1 on path-3. ....                      | 214 |
| Figure 7-29 Vertical deflection of west edge of EG: 59 ft from north abutment,<br>Truck-1 on path-3 and Truck-2 on path-1.....    | 215 |
| Figure 7-30 Vertical deflection of west edge of WG: 225.5 ft from north abutment,<br>Truck-1 on path-3 and Truck-2 on path-1..... | 215 |
| Figure 7-31 Vertical deflection of west edge of EG: 59 ft from north abutment,<br>Truck-1 followed by Truck-2 on path-1. ....     | 216 |
| Figure 7-32 Vertical deflection of east edge of EG: 225.5 ft from north abutment,<br>Truck-1 followed by Truck-2 on path-1. ....  | 216 |
| Figure 7-33 Longitudinal stress at 6 ft from north abutment in the west edge of<br>bottom flange of WG: Truck-1 on Path-3.....    | 217 |
| Figure 7-34 Longitudinal stress at 6 ft from North Abutment in the west edge of<br>bottom flange of EG: Truck-1 on path-3. ....   | 218 |
| Figure 7-35 Longitudinal stress at 58 ft from north abutment in the west edge of<br>bottom flange of WG: Truck-1 on path-3. ....  | 218 |
| Figure 7-36 Longitudinal stress at 58 ft from north abutment in the east edge of<br>bottom flange of WG: Truck-1 on path-3. ....  | 219 |
| Figure 7-37 Longitudinal stress at 138 ft from north abutment in the west edge of<br>bottom flange of WG: Truck-1 on path-3. .... | 219 |
| Figure 7-38 Longitudinal stress at 138 ft from north abutment in the east edge of<br>bottom flange of WG: Truck-1 on path-3. .... | 220 |
| Figure 7-39 Longitudinal stress at 6 ft from north abutment in the west edge of<br>bottom flange of WG: loading scenario-5. ....  | 220 |
| Figure 7-40 Longitudinal stress at 6 ft from north abutment in the west edge of<br>bottom flange of EG: loading scenario-5.....   | 221 |



|  |     |
|--|-----|
| Figure 7-41 Longitudinal stress at 58 ft from north abutment in the west edge of bottom flange of WG: loading scenario-5. ....                     | 221 |
| Figure 7-42 Longitudinal stress at 58 ft from north abutment in the east edge of bottom flange of WG: loading scenario-5. ....                     | 222 |
| Figure 7-43 Longitudinal stress at 138 ft from north abutment in the west edge of bottom flange of WG: loading scenario-5. ....                    | 222 |
| Figure 7-44 Longitudinal stress at 138 ft from north abutment in the east edge of bottom flange of WG: loading scenario-5. ....                    | 223 |
| Figure 7-45 Longitudinal stress at 6 ft from north abutment in the west edge of bottom flange of EG - Truck-1 followed by Truck-2 on path-1. ....  | 224 |
| Figure 7-46 Longitudinal stress at 6 ft from north abutment in the east edge of bottom flange of EG: Truck-1 followed by Truck-2 on path-1. ....   | 224 |
| Figure 7-47 Longitudinal stress at 58 ft from north abutment in the west edge of bottom flange of EG: Truck-1 followed by Truck-2 on path-1. ....  | 225 |
| Figure 7-48 Longitudinal stress at 58 ft from north abutment in the east edge of bottom flange of EG: Truck-1 followed by Truck-2 on path-1. ....  | 225 |
| Figure 7-49 Longitudinal stress at 138 ft from north abutment in the west edge of bottom flange of WG: Truck-1 followed by Truck-2 on path-1. .... | 226 |
| Figure 7-50 Longitudinal stress at 138 ft from north abutment in the east edge of bottom flange of EG: Truck-1 followed by Truck-2 on path-1. .... | 226 |
| Figure 8-1 Box-girder composite section, Ft Lauderdale bridge. ....  | 228 |
| Figure 8-2 Rebar layout in concrete slab. ....   | 232 |
| Figure 8-3 Worst case scenario for HS-20 loading of the bridge. ....   | 236 |
| Figure 8-4 Worst case scenario of loading for two trucks with unit weight. ....  | 237 |
| Figure 8-5 Web reactions due to application of two trucks with unit weight. ....   | 237 |
| Figure 8-6 Position of the HS-20 truck for maximum moment in girders. ....   | 238 |
| Figure 8-7 Von Mises stresses in single-span bridge under maximum moment, undamaged condition. ....  | 240 |

|   |     |
|---|-----|
| Figure 8-8 Von Mises stresses in single-span bridge under maximum moment, full-web cracked condition. ....  | 240 |
| Figure 8-9 Load vs. vertical deflection of single- and three-span bridges with different conditions. ....   | 241 |
| Figure 9-1 Determination of effective width (a) assuming 45° horizontal spreading from the center of the load in Dutch practice, (b) assuming 45° horizontal spreading from the far corner of the load in French practice (Adopted from Lantsoght, 2015)..... | 249 |
| Figure 9-2 The method to determine effective width (a) per load print and (b) per axle.....   | 249 |
| Figure 9-3 Comparison between results from Tests C and D and predictions from design provisions.....  | 251 |
| Figure 9-4 Compressive membrane action in laterally restrained reinforced concrete slabs (adopted from Kirkpatrick et al. 1984). ....   | 252 |
| Figure 9-5 Typical load vs. deflection for restrained reinforced concrete slab (adopted from Rankin et al. 1991). ....  | 253 |
| Figure 9-6 (a) Idealized geometry of deformation of half span of laterally rigidly-restrained strip and (b) idealized stress-strain relationship of concrete. ....  | 255 |
| Figure 9-7 (a) Idealized geometry of deformation of half span of laterally rigidly-restrained strip and (b) variation of arching moment ratio with mid-span deflection. ...   | 256 |
| Figure 9-8 Curves of arching moment coefficient (k). ....   | 257 |
| Figure 9-9 Analogy of three-hinged arch.....  | 259 |
| Figure 9-10 Restraint model proposed by Taylor (2000). ....   | 261 |
| Figure 9-11 Effective width for slabs subjected CMA. ....   | 261 |
| Figure 9-12 Formation of direct compression strut in beam.....  | 266 |
| Figure 9-13 Subdivision of perimeter and slab properties to be used for parts of perimeter: (a) for $2d_1 > a_v > 1.5d_1$ ; (b) for $a_v < 1.5d_1$ (Adopted from Lantsoght (2013) based on Regan (1982)). ....  | 268 |
| Figure 9-14: Schematic drawings of strut formation in (a) one-way and (b) two-way slabs.....  | 270 |

|   |     |
|---|-----|
| Figure 9-15 Approaches of investigating the direct load transfer effects for bridge slabs subjected to concentrated load over (a) the intact girder and (b) the damaged girder. ....  | 272 |
| Figure 9-16 Shear span factor for slab portion over the intact girder. ....   | 276 |
| Figure 9-17 Shear span factor for slab portion over the damaged girder. ....  | 279 |
| Figure 9-18 Determination of effective width using French horizontal load spreading. ....   | 282 |
| Figure 9-19 Load distribution (a) under 4-point loading and (b) single concentrated loading configuration. ....   | 283 |
| Figure 9-20 Deflection of the specimen under 4-point loading configuration. ....  | 284 |
| Figure 9-21 Effective width determined (a) assuming 45° horizontal spreading from the center of the load, (b) assuming 45° horizontal spreading from the far corner of the load. .... | 288 |
| Figure 9-22 Shear stress in the slab along the main span of the bridge specimen. ....   | 289 |
| Figure 9-23 Locations across the bridge investigated for the punching shear capacity. ....  | 292 |
| Figure 9-24 Comparison of the bridge specimen's load-carrying capacities with concentrated loads applied at different locations. ....   | 293 |
| Figure 9-25 Stress distributions under concentrated load at (a) L1, (b) L2, (c) L3 and (d) L4. ....   | 295 |
| Figure 10-1 Summary of notional approach. ....  | 302 |
| Figure 10-2 Lognormal PDFs for Required Strength (median = 800, COV = 0.1) and resistance of Damaged Bridge (median = 840, COV = 0.1) ....  | 305 |
| Figure 10-3 Cumulative Density Function of Damaged Bridges. ....  | 305 |
| Figure 11-1 Effects of cross-frames. ....   | 308 |
| Figure 11-2 Effects of railing system. ....   | 310 |
| Figure 11-3 Effects of continuity. ....   | 311 |

## Chapter 1 Introduction

### 1.1 Problem Statement

Sudden collapse of bridges such as the Silver Bridge (West Virginia DOT, 2016) and the I-35W Mississippi River Bridge (National Transportation Safety Board, 2008) show that fracture of a single member can cause the collapse of an entire bridge. In bridge engineering parlance, these members are known as fracture critical members (FCMs), although the precise definition may vary. In 2010 the American Association of State Highways and Transportation Officials (AASHTO) defined an FCM as a “component in tension whose failure is expected to result in the collapse of the bridge or the inability of the bridge to perform its function.” Although design and construction of bridges with FCMs is not currently prohibited, these bridges must be designed and fabricated to special requirements, and since 1988 the National Bridge Inspection Standards have required a hands-on, full inspection, typically every two years. These requirements burden bridge owners and transportation agencies with huge initial and annual expenses.

Currently, all two-girder bridges, regardless of their configurations, are classified as bridges with fracture critical elements. However, a number of two-girder bridges with cracks in one girder, even full-depth, have been reported and were still in service without collapse. One example is the Lafayette Bridge, part of US-52 Hwy over the Mississippi River near Savanna, IL. The Lafayette Bridge is composed of two side-by-side units, each containing two plate girders. Cross-frames exist between the girders within each unit; however, the units themselves are unconnected. In 1975, after eight years of service, the Lafayette Bridge experienced a full-depth fracture of one of the main girders, and the

bridge deck sagged 7 in., but the structure did not collapse (Fisher et al., 1977). In 1977, the I-79 Neville Island Bridge in Pittsburgh, PA, was found to have a full-depth fracture of one of its two girders and remained in service and displayed only a slight deflection, until a boater noticed the fracture (Schwendeman and Hedgren, 1978). These examples suggest that the stability of the bridge is not always linked strictly to the performance of fracture critical members, and a redundancy load path might exist in bridges with FCMs even though it is not acknowledged based on the current definition of fracture critical structures.

There has been increased interest in the fracture critical classification of twin box-girder bridges due to several recent cases of bridges with FCMs performing well and supporting highway live loads after a fracture of one of the main-supporting girders. One of the first research studies on the redundancy evaluation of twin steel box-girder bridges was performed by HNTB Corporation and Milwaukee Transportation Partners (2005). In addition, full-scale testing of a simple span twin box-girder superstructure at the University of Texas, Austin, has shown that under uniform loading, twin box-girder superstructures have significant levels of redundancy and can remain stable after a complete fracture of the bottom flange and webs of one of the girders (Barnard et al., 2010). If twin steel box-girder bridges are proved to be redundant structures, the requirements of hands-on inspection every two years might not be necessary and significant savings will be realized.

## **1.2 Background**

National Cooperative Highway Research Program (NCHRP) Report 406 (Ghosn and Moses, 1998) is one of the first of several research projects on fracture critical bridges that have been conducted by bridge researchers for different sponsoring agencies in recent

years. In that report, an attempt was made to quantify the redundancy of different bridge structures. To that end, four load factors and three reserve ratios based on the load factors are defined. Limiting values for each reserve ratio are intended to ensure redundancy. The results of other studies are also available for researchers in this field, among them Ghosn et al. (2010), Connor et al. (2005), Frangopol et al. (1991 and 2007) and Pham et al. (2014).

In June 2012, the Federal Highway Administration (FHWA) issued a memo intended to clarify the agency's policy regarding the design, fabrication, and inspection of fracture critical bridges. In addition, two major research projects on redundancy of twin box-girder bridges were conducted by HNTB/MTP for the Wisconsin Department of Transportation (DOT) and by the University of Texas-Austin for the Texas DOT. Additional information on these three resources is provided below.

### **FHWA Memo**

In June 2012, FHWA issued a memorandum on clarification of requirements for fracture critical members. The memo stated:

“The purpose of this memo is to provide clarification of the FHWA policy for the classification of Fracture Critical Members. For design and fabrication, only Load Path Redundancy may be considered. For in-service inspection protocol, Structural Redundancy demonstrated by refined analysis is now formally recognized and may also be considered. Internal member redundancy is currently not recognized in the classification of Fracture Critical Members for either design and fabrication or in-service inspection. Finally, this memo introduces a new member classification, a System Redundant Member (SRM),

which is a non-load-path-redundant member that gains its redundancy by system behavior.”

The memo clarifies the FHWA policy on specification of proper material and testing for design and fabrication and also proper in-service inspection protocol. It also mentions that the analysis requirements of AASHTO LRFD section 6.6.2 is supported, which requires bridge owner and bridge engineer agreement on the level of complexity of the bridge analysis.

### **HNTB/MTP Research Project (2005)**

In 2005, Milwaukee Transportation Partners (MTP), in collaboration with HNTB Corp., published a report on “Redundancy of Box Girder Steel Bridges” based on a study on the Marquette Interchange HPS twin box-girder bridges. The intent of that project was to either demonstrate that the selected twin box-girder bridges are redundant in their as-designed condition or to make recommendations to render them redundant.

Marquette Interchange includes eight directional ramps to be constructed using a twin box-girder system. It was decided that these bridges be designed and fabricated in accordance to fracture critical requirements and the major target was to eliminate the two-year inspection requirement. Therefore, two of the ramp bridges were modeled using elaborate nonlinear finite element models, while the other six bridges of the interchange were modeled using simplified grillage models. In these grillage models, all main girders, slab strips, and diaphragms were modeled using beam elements in a 2-D planar grid. The 2-D models were calibrated against the results of the two 3-D models to make them more reliable. The considered damage for each bridge was a total steel section fracture of one of

the two box girders at 0.4 times of the end span. A stepwise pushover analysis was used to monitor the responses of all of the bridge elements through the incremental loading process.

The results of both 2-D and 3-D analyses show that these bridges were able to carry the live loads greater than the minimum required loads. In addition, the dynamic effects due to sudden failure of one of the box girders on global stability of the bridge were evaluated, which was beyond the requirements of NCHRP Report 406. A simplified approach was selected to attack this problem. Although, the analyses showed that this dynamic effect controls the failure, the two girder bridges proved to have enough capacity to accommodate such sudden failures.

This project demonstrated that twin box-girder bridges in their as-designed condition have sufficient reserved capacity to be classified as non-fracture critical and no additional requirement should be added to the current design methods. The redundancy of this type of bridge comes from the alternate load path embedded in these structures, such as continuity of girders, concrete deck 3-D action, and participation of cross-frames and diaphragms to carry the loads of damaged girder.

#### **Texas DOT Research Project 9-5498 (2006-2010)**

Texas DOT and Federal Highway Administration (FHWA) co-sponsored a full-scale experimental study at the Ferguson Structural Engineering Laboratory (FSEL) in the University of Texas-Austin. In this research project, Karl Frank et al. conducted a valuable full-scale experiment and presented analytical and finite element solutions to evaluate the load carrying capacity of a composite twin steel box-girder bridge. The outcome of the



research was analytical and numerical solutions to find the “redundant capacity” of twin box-girder bridges. Major experimental and computational resources for this FSEL project were continued for four years (2006-2010). Different aspects of this project included analytical structural analysis presented through hand calculations, numerical structural analyses conducted through finite element modeling, laboratory experiments to evaluate the capacity of specific bridge elements, and a full-scale test on a reconstructed twin box-girder bridge.

In the analytical part of this study, the capacity of the bridge was estimated using the yield line method. In this method, a failure pattern (Yield Line) is assumed for the bridge and then by equating the internal work done by the internal forces and the external work done by the external forces, the maximum capacity of the structure is found. This method was successfully applied to the tested bridge and a lower bound solution was resulted for the load capacity of the bridge.

The laboratory tests focused on the pullout capacity of the shear connectors of the bridge girders, which connect the girders to the concrete deck. One of the conclusions of the Texas research is that the shear connectors play a key role in the redundancy of damaged two steel box-girder bridges. As a result, tests were conducted to comprehend the behavior of shear studs in static and dynamic states.

The full-scale bridge test of this research project revealed the intrinsic redundant behavior of twin box-girder bridges, despite the fact that the test was conducted in the worst-case scenario from the point of view of redundancy. The tested bridge was a simple-span bridge and therefore it had no redundancy due to continuity of its superstructure. All external diaphragms of this bridge were removed. The railings of the bridge were

constructed with expansion joints that limit the contribution of the railing to the load-carrying capacity of the bridge. The bridge had a horizontal curvature and the fractured girder was the outside girder that has the maximum internal forces. Therefore, it is observed that the situation of a real-life bridge cannot be worse than this bridge from redundancy standpoint. Figure 1-1 shows a picture of this test bridge before conducting the tests.



**Figure 1-1 FSEL twin box-girder bridge (Source: FHWA Report No FHWA/TX-10/9-5498-1).**

Three different tests were conducted on this bridge. In the first test, the bottom flange of the exterior girder was suddenly failed using an explosive to simulate a sudden fracture while an equivalent HS-20 load was positioned above the fractured girder and in the worst possible location. Figure 1-2 illustrates the bridge during the explosion and Figure 1-3 shows the bottom flange cut after the explosion. The response of the bridge during and after this test was satisfactory and its maximum deflection was less than 1 in.

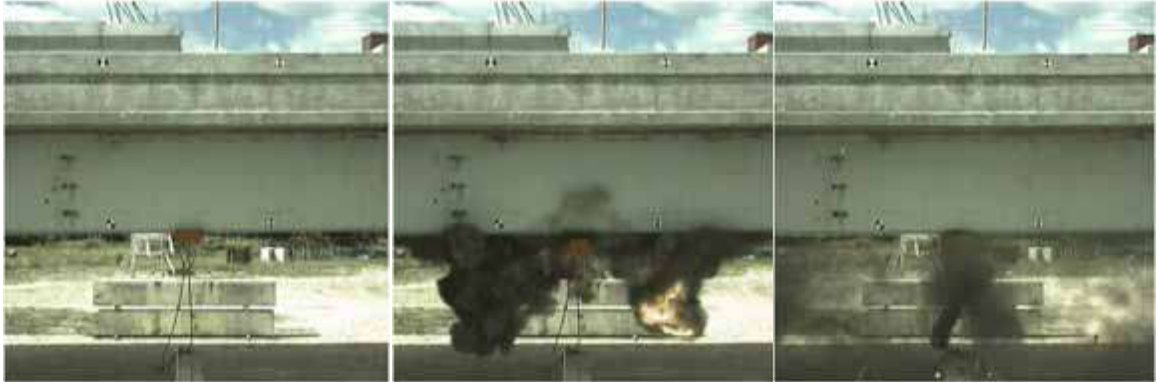


**Figure 1-2 FSEL first bridge fracture test (Source: FHWA Report No FHWA/TX-10/9-5498-1).**



**Figure 1-3 Bottom flange cut after the explosion (Source: FHWA Report No FHWA/TX-10/9-5498-1).**

In the second test, the bridge and equivalent HS-20 truck loading were supported by means of a scissor jack while about 83% of the webs of the cracked girder were manually cut. The scissor jack was then removed suddenly using an explosive charge attached on the jack. This simulated the sudden nature of the crack. Figure 1-4 shows the supporting scissor jack before, during, and after the explosion. Again, the bridge safely sustained the load with a maximum deflection of 7 in.



**Figure 1-4 FSEL second bridge fracture test (Source: FHWA Report No FHWA/TX-10/9-5498-1).**

The third test was a static test to measure the load capacity of the damaged bridge. In this test, the load on the bridge was increased incrementally until the bridge was not able to carry more loads. In this test, the bridge carried 363 kips of load which, considering the extent of the damage, was a remarkable capacity. Figure 1-5 shows the incremental loading of the bridge and also the bridge in its collapsed mode.



**Figure 1-5 FSEL third bridge fracture test (Source: FHWA Report No FHWA/TX-10/9-5498-1).**

The capacity of the tested bridge is also evaluated by means of a numerical simulation. In this approach, a sophisticated finite element model of the bridge is developed using Abaqus/Standard finite element program. In the simulation, the nonlinear material

properties of steel and concrete, contact properties of railing joint, and the stud connection failure were taken into account. The results of the numerical simulation showed a good agreement with the collected data. In addition, the finite element models were able to capture the observed failures during the second and third tests.

Based on the performed experiment and computer simulations, major failures in this type of bridges include:

- Pull-out failure of shear studs (which is tension failure of the concrete surrounding the studs) resulting in haunch separation, and
- Crushing of railing concrete in compression.

A number of theses and reports were published by Barnard (2006), Hovell (2007), Neuman (2009), and others based on the results of this experimental work, each of them investigating different aspects of the tested bridge's behavior.

These studies provide valuable information about the redundancy of twin box-girder bridges; however, they do not completely explain the behavior and failure modes of these bridges under different loading conditions.

### **1.3 Current Approaches**

Following are brief description of two available methods for assessing the redundancy of two steel box-girder bridges, together with their limitations.

#### **1.3.1 Direct Analysis Approach with Redundancy Criteria - NCHRP Report 406**

NCHRP Report 406 was one of the first studies undertaken to study the redundancy of bridges at system level and develop a step-by-step-procedure, called direct analysis

approach, to evaluate the redundancy of highway bridges (Ghosn and Moses, 1998). This procedure introduces four critical limit states that need to be checked and the minimum load levels (or load factors) that bridges can carry before these limit states are reached. These limit states and their corresponding load factors are described as follows:

- **Member failure limit state** is a check of individual member safety using elastic analysis or the capacity of the structure to resist its first member failure.

$$LF_1 = \frac{R - D}{L} \leftarrow \text{Linear Elastic Analysis} \quad \text{EQ 1.1}$$

Where:

$R$  = Resistance

$D$  = Dead load effects

$L$  = Live load effects

- **Ultimate limit state** is defined as the ultimate capacity of the undamaged bridge system or the load required for the formation of a collapse mechanism in the bridge system divided by the weight of two HS-20 trucks. In mathematical format, this definition yields in:

$$LF_u = \frac{\text{Ultimate Load Capacity of Undamaged Bridge from Nonlinear FEA}}{2 \times 72 \text{ kips}} \quad \text{EQ 1.2}$$

Where:

$72 \text{ kips}$  = Weight of one HS-20 Trucks

- **Damaged condition limit state** is defined as the ultimate capacity of the bridge system after removal or cracking of one load-carrying component from the structure model.

$$LF_d = \frac{\textit{Ultimate Load Capacity of Damaged Bridge}}{2 \times 72 \textit{ kips}} \quad \text{EQ 1.3}$$

- **Functionality limit state** is defined as the capacity of the structure to resist a live load displacement in a main longitudinal member equal to the span length/100. The functionality limit state load factor is obtained from dividing this capacity by the weight of two HS-20 trucks.

$$LF_f = \frac{\textit{Load Capacity corresponding to } \frac{L}{100} \textit{ deflection}}{2 \times 72 \textit{ kips}} \quad \text{EQ 1.4}$$

In this study, redundancy of a bridge is defined as the capability of the bridge structure to continue to carry loads after the failure of one main member, hereby ratios of  $LF_u$ ,  $LF_f$ ,  $LF_d$  to  $LF_1$  are measures of the redundancy level of bridges in the ultimate, functional and damaged limit states, respectively. These ratios are also called as system reserve factors. A bridge will be considered as redundant if all system reserve factors satisfy the following criteria:

$$\textit{For ultimate limit state: } R_u = \frac{LF_u}{LF_1} \geq 1.30$$

$$\textit{For damaged conditioned limit state: } R_d = \frac{LF_d}{LF_1} \geq 0.5$$

$$\textit{For functional limit state: } R_f = \frac{LF_f}{LF_1} \geq 1.10$$

These three minimum redundancy criteria, 1.30, 0.5, and 1.10, came from target reliability indices, which were collected from reliability analysis of a large number of common-type four-girder bridges. It was assumed that four-girder bridges are always redundant while two-girder bridges are non-redundant. The target reliability indices for ultimate limit state, functional limit state and damaged limit states were found to be 4.35, 3.75 and 0.8 respectively.

In addition to the direct analysis procedures as described above, the research also developed tables of system reserve factors for typical bridge configurations so that practice bridge engineers and owners can use without performing any nonlinear finite element analysis (FEA).

In order to evaluate the redundancy of a bridge using this approach, it is necessary to carry out nonlinear finite element analysis of the bridge systems.

### **1.3.2 Simplified Analytical Modeling Methods for Redundancy Assessment of Twin Box-Girder Bridges**

The simplified analytical methods are developed to evaluate the redundancy of twin steel box-girder bridges (Barnard et al. 2010). These simplified methods were developed based on the results of experimental tests on full-scale twin steel box-girder bridge carried out in Texas DOT Research Project 9-5498 which was summarized previously.

First, Barnard et al. (2010) proposed initial strength checks such that if the bridge under investigation satisfied these checks, it could be considered a redundant structure. The main philosophy of these checks was to ensure that 1) the intact girder can support the weight of the bridge and of a HS-20 truck, 2) the deck has sufficient strength to transmit the load carried by the fractured girder to the intact girder, and 3) the shear studs have sufficient tension capacity. These initial checks were considered as a first-level screening. Barnard et al. also demonstrated that if the first two conditions were satisfied, the twin steel box-girder bridge can still sustain the load without collapsing. Under this scenario, a yield line analysis can be employed to evaluate “the ability of the deck to transmit load to the intact girder without the shear studs connecting the deck to the fractured girder.” The simplified procedure, developed by Barnard et al. (2010), requires carrying out a refined analysis



(nonlinear finite element analysis), if the capacity predicted from the yield line analysis proves to be inadequate. In all the redundancy assessment approaches suggested by the Texas investigation, an arbitrary load equal to two times the weight of an HS-20 truck is utilized.

In the yield line analysis approach, once the yield line pattern is chosen, the analysis is performed using a virtual work principle. The principle of virtual work requires that the external virtual work done by the external forces be equal to the internal virtual work done by the internal forces of each element. The yield line pattern, chosen for the bridge tested in Texas, is illustrated in Figure 1-6. In this yield line analysis approach, three parameters are required to define the yield line pattern. These parameters are angle  $\phi$ , length  $a$ , and angle  $\theta$ . The angle  $\theta$  can be calculated based on the curvature of the bridge and it is zero for a straight bridge. The angle  $\phi$ , is suggested to be constant at 55 degrees according to the results of a parametric study. The length  $a$ , is determined by finding the value that produces minimum truck load. It is important to note that length  $a$ , and magnitude of truck load are mutually dependent; therefore, one needs to be fixed to find the other. The minimum truck load is the last one that gave a physically admissible solution for the length  $a$ .

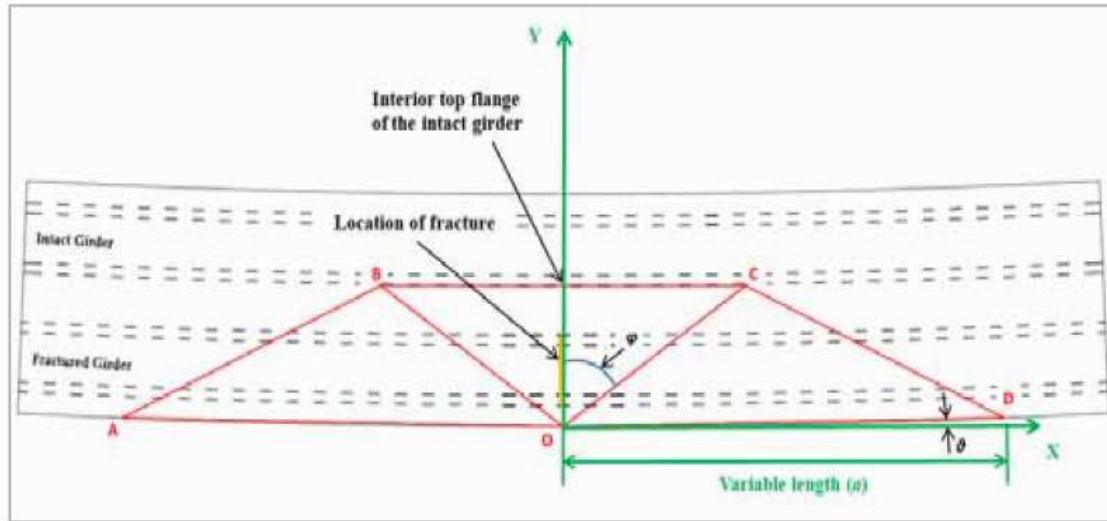


**Figure 1-6 Yield line model proposed by Barnard et al. (2010).**

The internal work of each line with length  $l$  can be calculated as:

$$dIW = m_b * l * \theta_{rotation}$$

where  $m_b$  is bending moment of each deck strip along each yield line and  $\theta_{rotation}$  is angle of rotation of each plate. Then the external work is calculated by summing each point load multiplied by the virtual deflection of each location. Finally, by setting internal work equal to external work and solving the equation, either length  $a$ , or the magnitude of truck load will be determined depending upon which variable is fixed at the beginning. If the magnitude of truck load is fixed, then both the internal work and external work can be expressed as a function of length  $a$ , and vice versa.

The detailed information on how to calculate  $m_b$ ,  $l$ ,  $\theta_{rotation}$  and external work can be found in the report “Modeling the Response of Fracture Critical Steel Box-Girder Bridges” (Barnard et al., 2010).

### 1.3.3 Limitations and Shortcomings

#### **Direct Analysis Approach (NCHRP Report 406)**

Although the framework developed in NCHRP Report 406 is comprehensive and has been used in several research projects such as HNTB/MTP project on Marquette Interchange HPS twin box-girder bridges, it contains limitations and drawbacks that need to improve as following:

1. Although this study provides a tabulated system of factors for several common types of bridge configurations, it doesn't include any steel box-girder bridges. It means nonlinear finite element analysis for every single steel box-girder bridge is required for each redundancy assessment. Performing nonlinear FEAs and repeating the procedure for all steel box-girder bridges in the fracture critical list can be very costly and time-consuming.
2. The redundancy criteria proposed in this research were determined based on calibration of reliability indices of a large number of multi-girder common-type bridges. This might be not fully applicable to bridges with fracture critical members, particularly twin steel box-girder bridges that are investigated in this research.
3. Since the deck was modeled as several parallel beams, it might not capture well the true nonlinear behavior of concrete. In addition, the failure of slab due to crushing of the concrete under transverse bending or shear failure was not considered during the finite element analysis.

4. Private discussion with the principal investigator of NCHRP 406 indicates that assessing the redundancy of two steel box-girder bridges after damage was not the objective of this particular investigation. Therefore, the application of recommendations made by NCHRP 406 to assess the redundancy of damaged two steel box-girder bridges is questionable.

#### **Simplified Methods Proposed by Barnard et al. (Texas DOT Research Project 9-5498)**

It is important to note that the methods of predicting the capacity of twin steel box-girder bridges, proposed in Texas DOT Research Project 9-5498, focused on a single loading condition of a fully distributed load. The loading configurations used in the research could have created different responses than what could happen in a more realistic loading state. Furthermore, the yield line analysis that was proposed in case the shear studs didn't have sufficient strength included several limitations, including:

1. The failure mode observed in the test was based on uniform loading. Therefore, the statement that the same failure mode would be obtained under an HS-20 truck load is questionable and needs justification and verification.
2. This method requires an assumed failure mode/pattern; however, under different loading configurations, a different failure mode/pattern can be obtained. This would imply that the suggested method can't be generalized.
3. This analysis might not be applicable to abrupt failure modes like shear and punching shear of the deck.
4. As an upper bound method, this yield line analysis will predict a collapse load that may be greater than the true collapse load.
5. Arbitrary use of load factor of 2 against HS-20 trucks needs justification.

## **1.4 Research Objectives**

The main objective of this research is to assess the redundancy of two steel box-girder bridges and ultimately lead to the development of practical tools to assess their redundancy and remove them from fracture critical list, where feasible.

## **1.5 Dissertation Organization**

This dissertation involved conducting a significant amount of analytical, numerical and experimental work. This dissertation study was funded by FDOT and the majority of this dissertation is included in the final report submitted to FDOT for the research project BDV29-977-17. The outline of the dissertation is presented below.

Chapter 1 presents the introduction and an overview of available information.

Chapter 2 provides an overall philosophy for assessing the redundancy of two steel box-girder bridges. This chapter provides the roadmap that ultimately could lead to development of tools that will assist departments of transportation and bridge owners assessing the redundancy of the two steel box-girder bridges and removing them from the fracture critical list, where feasible. The development of complete tools needed is beyond the scope of this project. Therefore, this chapter provides a list of technical challenges that were addressed within this project together with a list of remaining technical questions that will be the subject of a proposed pooled fund project under development. This chapter also provides justification for different activities undertaken within this project.

Chapter 3 provides design, details and instrumentation plans for the small-scale laboratory test specimen constructed and tested in the FDOT structural laboratory.

Chapter 4 presents the results obtained from the tests on small-scale test specimen.

Chapter 5 presents the finite element modeling techniques used for development of nonlinear model.

Chapter 6 presents the calibration process for nonlinear finite element model utilizing results of small-scale test specimen tested in the structural laboratory.

Chapter 7 presents the results of field tests conducted on a multi-span two steel box-girder bridge in service.

Chapter 8 provides application of recommended procedures by NCHRP 406 to assess redundancy of two steel box-girder bridges after damage.

Chapter 9 provides summary of parametric studies conducted using calibrated nonlinear finite element model developed and described in Chapter 6.

Chapter 10 provides a simple method of predicting the punching shear of bridge deck slabs and taking into consideration both compressive membrane action direct load transfer effects.

Chapter 11 provides a summary and conclusions.

## Chapter 2 Research Methodology

There is ample evidence indicating that two steel box-girder bridges are redundant, even if tension flanges of one steel box-girder are completely fractured, including the behavior of bridges that have continued to carry traffic load after damage and with little noticeable change to their global behavior, as well as the full-scale tests on test specimens loaded to failure. However, as is the case with any engineering process, it is still necessary to develop a sound and scientific approach to prove that two steel box-girder bridges are redundant and safe after damage. The need for the development of this comprehensive assessment procedure is grounded in the creation of the fracture critical concept within the bridge community in the United States. It is interesting to note that the need to prove that two steel box-girder bridges are redundant after damage, is not as a result of collapse of these bridge types after damage.

The guidelines provided by AASHTO *LRFD Bridge Design Specifications* and FHWA and summarized in Chapter 1, allow the assessment of the safety and redundancy of two steel box-girder bridges using detailed numerical work.

Commentary section 6.6.2 of the AASHTO *LRFD Bridge Design Specifications* provides general guidelines that can be used to evaluate the performance of bridges with fracture critical members and states: "... The criteria for a refined analysis used to demonstrate that part of a structure is not fracture-critical have not yet been codified. Therefore, the loading cases to be studied, location of potential cracks, degree to which the dynamic effects associated with a fracture are in the analysis, and fineness of the models and choice of element type should all be agreed upon by the owner and the engineer. The

ability of a particular software product to adequately capture the complexity of the problem should also be considered and the choice of software should be mutually agreed upon by the owner and the engineer. Relief from the full factored loads associated with the strength I load combination of Table 3.4.1-1 should be considered, as should the number of loaded design lanes versus the number of striped traffic lanes”.

AASHTO *LRFD Bridge Design Specifications* and FHWA requirements for assessing the redundancy of damaged two steel box-girder bridges are feasible through detailed nonlinear three dimensional finite element analyses, using calibrated model. However, even with such an approach there is still one important missing piece of information to complete the process: the load level that the damaged bridge must sustain with respect to strength and deflection and other applicable serviceability criteria. The research study conducted in Texas arbitrarily uses two times HS-20 truck load and doesn't address the loading combination that must be used during analysis.

It is also important to note that the work sponsored by the National Steel Bridge Alliance and carried out at Purdue University is limited to the development of the nonlinear finite element model of damaged bridges, which has been accomplished in a number of studies and does not address any other technical issues involved. The main advantage of the Purdue work is the development of the mesh generation procedure for specific software. The proposed pooled fund project will take advantage of this valuable addition to the body of knowledge, as described later in this chapter.



## 2.1 Main Characteristics of Comprehensive Methodology for Assessment

The requirements stated above necessitate that the methodology to assess the redundancy of two steel box-girder bridges after damage should have the following characteristics:

1. Methodology must develop the load level that the damaged bridge must resist using a rational process.
2. The suggested approach for assessment of redundancy of the damaged bridge is in the form of conducting detailed nonlinear finite element analyses.

Based on the results of this current research study, discussions with various sectors of the steel bridge industry, and practical considerations, the following paths are suggested to assess the redundancy of two steel box-girder bridges.

### **Modified Simple Texas Approach**

The first step in the suggested methodology is the use of simple hand calculation in the form of a modified simple approach suggested by Texas DOT Research Project 9-5498. Additional work needs to be carried out to further develop the suggested simple evaluation approach by Texas DOT, and this could be achieved by reducing the level of conservatism inherent in the Texas suggested approach, using the results of this research project. In its present form the results from the Texas simplified approach are highly conservative as compared to the test results. For instance, the full-scale bridge tested in Texas demonstrated 363 kips of load capacity, while the current version of simplified Texas method prediction is 107 kips.

Once developed, the modified Texas simple approach could be used as the first step in the process of evaluating the redundancy of damaged two steel box-girder bridges without any need for conducting detailed finite element analysis. The entire process could be carried out using hand calculations and will involve considering each bridge, one at a time. Still-missing information in this process are the strength criteria such as the minimum load level that the damaged bridge should resist and other applicable serviceability criteria, such as deflection of the bridge after damage and before retrofitting the bridge. The suggested approach to develop such criteria is explained in the next section in the proposed notional approach.

In the event that a modified Texas simple approach does not result in removing the two steel box-girder bridges from the fracture critical list, the notional approach, which is described in the next section, could then be used.

### **Proposed Notional Approach to Assess the Redundancy of Damaged Two Steel Box-Girder Bridges**

Conducting detailed nonlinear finite element analysis remains the only viable approach for assessing the redundancy of damaged two steel box-girder bridges. However, as mentioned previously, the level of effort involved in addressing the redundancy of all two steel box-girder bridges within inventory of a given state requires significant amounts of financial, labor and computer resources. The notional approach to reduce the level of effort involved, consists of grouping the two steel box-girder bridges within a state inventory into several groups and developing a notional simple-span two steel box-girder bridge that would represent each group and carries out the detailed nonlinear finite element analysis on the notional bridge. This approach reduces the level of efforts involved at two

different levels. First, conducting a detailed nonlinear analysis on a simple-span bridge is much easier than conducting similar analysis on a multi-span bridge. Second, only one analysis will need to be carried out for each group. In this approach, proving the redundancy of a notional bridge will be equivalent to proving that all bridges within the group of simple- and multi-span two steel box-girder bridges in the group, under consideration, are redundant.

The notional approach demands comprehension of the following issues:

1. Development of a calibrated nonlinear finite element model that accurately depicts the modes of failure under types of loading specified by *AASHTO LRFD Bridge Design Specifications*. It should be noted that this current research project demonstrates that punching shear is a possible failure mode in damaged two steel box-girder bridges, and that the capacity of the damaged bridge is influenced by presence of damage in fractured girder. The Texas research study was not able to identify this mode of failure because of the type of loading used in their research.
2. Development of criteria to group two steel box-girder bridges within the inventory of a given state DOT and developing notional simple-span two steel box-girder bridge representing the group.
3. Establishment of the load level that damaged two steel box-girder bridges must resist as, well as establishment of other serviceability limit states that must be checked to ensure public safety.
4. Development of a Guide for application of the notional approach for assessing redundancy of damaged two steel box-girder bridges with examples and other documentations, such as video tapes that would assist state DOTs.

Following is a brief discussion of information that has been developed as a result of this current study. Chapters 3 through 7 of this report provide documentation of efforts that were undertaken to develop a test-verified calibrated three dimensional finite element model that could be used to assess the redundancy of the damaged two steel box-girder bridges. Chapter 8 provides a summary of assessment of the redundancy of a full-scale bridge using the direct analysis approach, proposed in NCHRP Report 406. Chapter 9 provides a summary of the efforts and start of the process for establishing the notional simple-span two steel box-girder bridges and grouping criteria.

Following is brief discussion of procedures that could be used to develop the load level that damaged two steel box-girder bridges must sustain before retrofit or complete replacement. The development of load level that two damaged two steel box-girder bridges must resist will demand carrying out reliability-based analysis with a safety level agreed upon by bridge owners. This effort could consist of the following steps.

1. Establish a probability density function (PDF) for load-carrying capacity of the damaged bridges, considering realistic modes of failure. This step will demand a large number of simulations. For the purpose of research, there will be a need to develop an approximate method for estimating the remaining capacity of damaged bridges. This current research study demonstrates that punching shear is most likely mode of failure, which in turn could significantly simplify the efforts involved in this step.
2. Establish the required load level. As damage to a bridge increases, the PDF for resistance, as shown in Figure 2-1, shifts to the left and the overlapping area between PDFs of load and resistance increases. The increase in overlapping area

increases the probability of failure and lowers the safety level. This is true if PDF of load remains unchanged.

The determination of the load level that damaged two steel box-girder bridges must resist could be established by first establishing the level of safety (beta index) for damaged bridges that is agreeable by owners. This safety level could be established by consensus or through analysis of bridges that are agreed to be redundant (Ghosn and Moses, 1998). Once the safety level is established, the PDF of load could be shifted to the left or right until the overlapping area under the two PDFs results in a desired safety level. This process will establish the position of PDF for load, which in turn will establish the load level that damaged two steel box-girder bridges must resist.

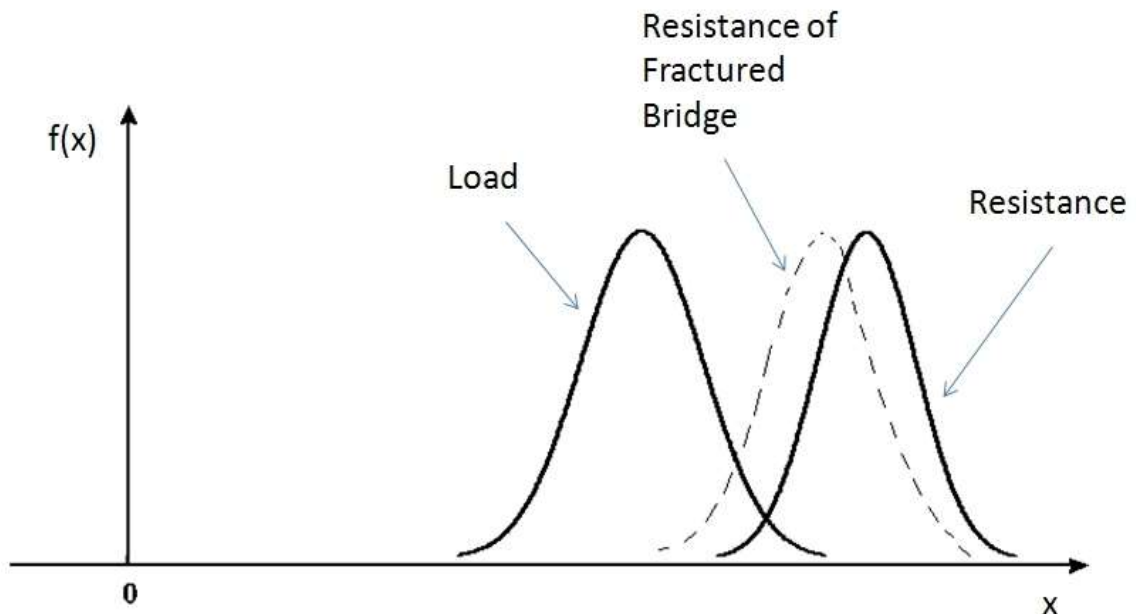


**Figure 2-1 Probability density functions of load and resistance of damaged and undamaged bridges.**

Another important practical consideration is the ability of a damaged bridge to carry the traffic until the damage is detected and repaired without jeopardizing public safety.

This consideration could demand checking the deflection of the damaged bridge and ensuring the serviceability of the bridge during the time period that damage will go on without detection. This aspect of the problem could be checked approximately while conducting analysis on the notional bridge.

## Chapter 3 Laboratory Testing on Small-Scale Specimen

In order to investigate the behavior of twin steel box-girder bridges in nonlinear range and modes of failure, and to calibrate nonlinear 3-D finite element model, laboratory testing of a small-scale twin steel box-girder bridge specimen was incorporated into this project. Detailed information on design and construction of the small-scale specimen, the instrumentation and testing plan is discussed in the following sections.

### 3.1 Specimen Design

This small-scale bridge was designed based on AASHTO *LRFD Bridge Design Specifications* (2010). Even though the specimen was a small-scale version, it was designed to replicate the proportions of a typical cross-section of a twin steel box-girder bridge. The span to depth ratio of the specimen is proportioned to satisfy the traditional deflection criteria of the AASHTO *LRFD Bridge Design Specifications*. The test specimen was proportioned to flange and web slenderness ratios based on AASHTO criteria. The slenderness of the webs and bottom flange was limited so that longitudinal stiffeners were required only at the bottom flange near the interior support. The final cross-section details of the box-girder were designed as follows and are also illustrated in Figure 3-1.

$$D = 20.6875 \text{ in. (depth of web)}$$

$$t_w = \frac{3}{8} \text{ in. (thickness of web)}$$

$$b_{tf} = 6 \text{ in. (width of top flange)}$$

$$t_{tf} = \frac{1}{2} \text{ in. (thickness of top flange)}$$

$$b_{bf} = 18 \text{ in. (width of bottom flange)}$$

$$t_{bf} = \frac{1}{2} \text{ in. (thickness of bottom flange)}$$

$$d = D + t_{bf} + t_{tf} = 21.6875 \text{ in. (depth of girder)}$$

$$D_t = d + \text{slab thickness} = 21.6875 + 5$$

$$= 26.6875 \text{ in. (total depth of the cross section)}$$

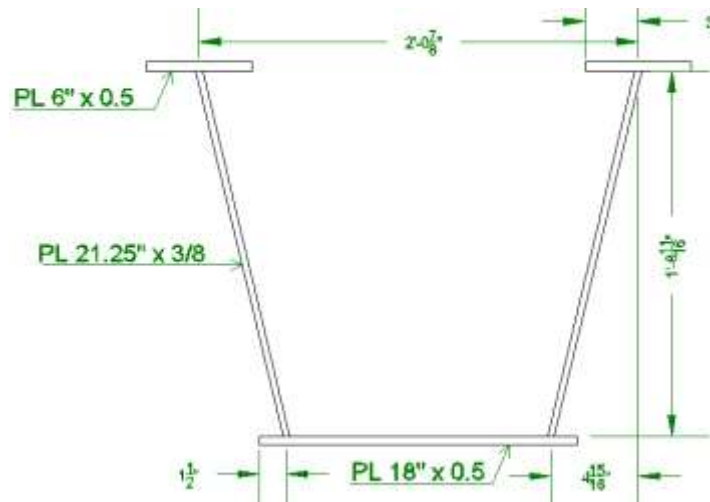


**Figure 3-1 Dimension of one steel box girder.**

Although AASHTO 6.11.6.2.2 requires all curved steel box girders to be designed as non-compact sections, straight steel box girders can be designed as a compact section. The depth to thickness ratio of the web was designed to be 56 and less than the limit of 150 for webs without longitudinal stiffeners. The width of bottom flange was 18 in., which is less maximum of one fifth of the span length. The web was designed to be entirely in tension, meaning  $D_{cp} = 0$  (see plastic moment calculation for verification). All of the compactness checks below verify that the section is compact.

Cross-section proportion limit checks:

$$\frac{D}{t_w} = 56 < 150 \text{ (OK)}$$



$$\frac{b_{tf}}{2 * t_{tf}} = 6 < 12 \text{ (OK)}$$

$$b_{tf} = 6 \geq \frac{D}{6} \text{ (OK)}$$

$$a = 29.688 \text{ in.}$$

$$w = 24.875 \text{ in.}$$

$$0.8 * w \leq a \leq 1.2 * w \text{ (OK) see Figure 3-2.}$$

$$\text{Slope of web} = \frac{1}{4.2} \leq \frac{1}{4} \text{ (OK)}$$

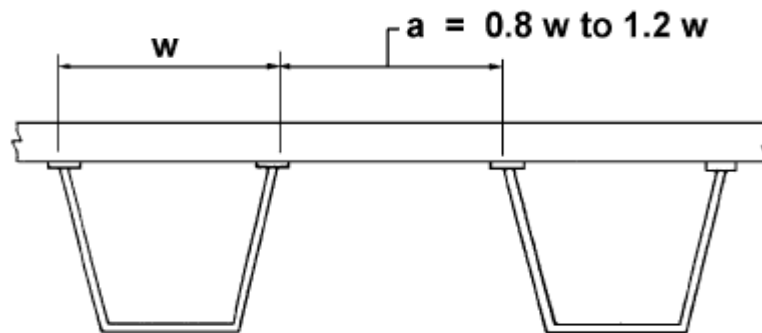


**Figure 3-2 Center-to-center flange distance (Adopted from AASHTO LRFD Bridge Design Specifications).**

The width of the specimen was 109 in. and the distance between two box-girders, from center to center, was 54.5 in. Since the deck thickness couldn't be scaled directly as the box-girder, the deck thickness was chosen to allow enough space for four mats of conventional reinforcement bars. For these reasons, the specimen deck was set at 5-in. depth. The deck was reinforced by #4 bars at every 6 in. in longitudinal direction for both top and bottom reinforcement mat. The transverse bars were also #4 and installed every 6 in. as well. The railing system was a removable system including several railing segments, and each segment has a dimension of 5 in. x 8 in. x 10 ft. The rail was sized to increase elastic stiffness of the entire structure by 10%, which is comparable to the rail contribution for a

full size structure. Each rail segment was reinforced by four longitudinal bars with stir-ups spaced at every 10 in. The rail was connected to the deck by bolt connections (1.5" diameter B7 rods) at the ends of each railing segment. The final detail of the specimen cross-section is illustrated in Figure 3-3.

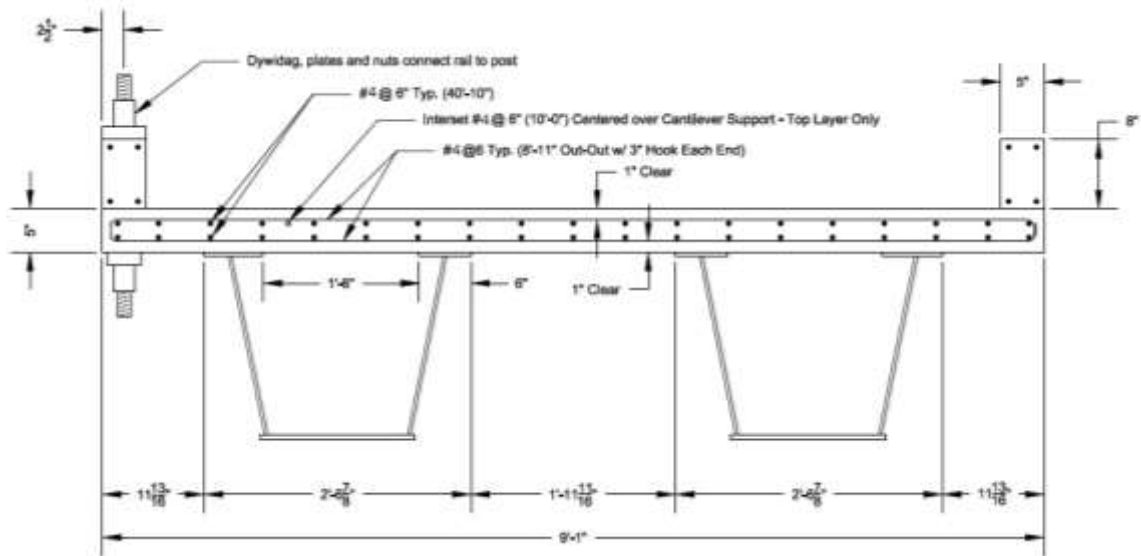


**Figure 3-3 Cross-section of the tested specimen.**

Each box-girder was designed to have two internal diaphragms at the supports and two internal cross-frames at every one-third length of the main span and one internal cross-frame 2 ft away from the cantilever end. The internal cross-frames are denoted as X-bracing in Figure 3-4.

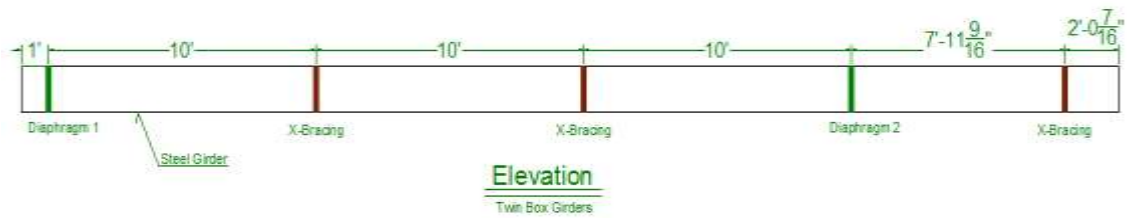


**Figure 3-4 Internal bracing locations in each box girder.**

At every location where the internal diaphragms and internal cross-frames are present, one external cross-frame was installed connecting two box-girders. Five sets of top lateral bracings were constructed and welded to the top flanges in each box-girder. All locations of cross-frame, diaphragm and top lateral bracing are plotted schematically in Figure 3-5. All the internal and external cross-frames are connected to the box girders by bolt connections through stiffener plates.

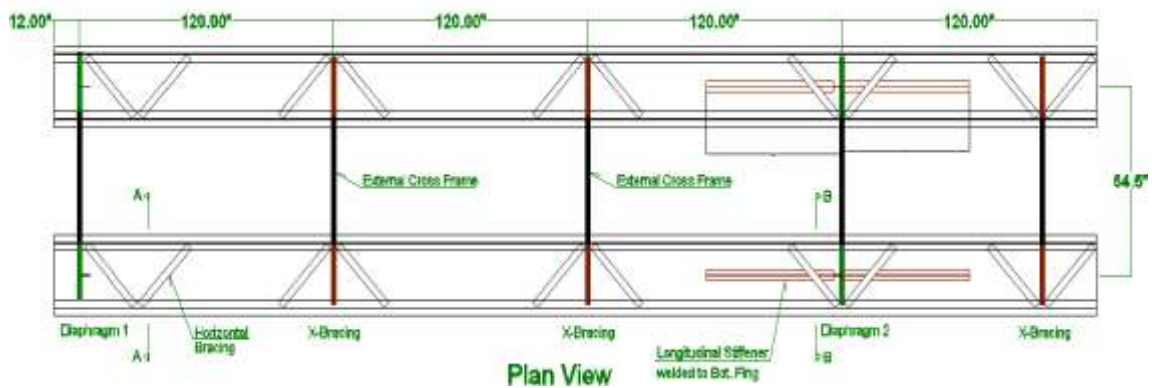


**Figure 3-5 The top plan view of the testing specimen.**

### 3.1.1 Analysis of Composite Section

For material properties, all steel plates are grade 50 steel and were assumed to have yield strength of 50 ksi (1 ksi = 1,000 lbf per square inch), and compressive strength of concrete was assumed to be 4.5 ksi for design purposes. The reinforcements are grade 60

steel and were assumed to have yield strength of 60 ksi. (The actual concrete properties that were determined at the time the deck was poured and when tests were performed are reported in Chapter 5.) The effective width of the concrete deck for the composite section of each girder was found to be 54.5 in., which is one-half of the width of the entire deck. Assuming the concrete deck and rebar to be in compression and steel girder in tension, the force in each element is calculated as follows:

$$C_c = 0.85 \times f_c' \times b_{eff} \times \beta_1 \times t_s = 1,042 \text{ kips}$$

$$C_{rebar\_top} = A_{rebar\_top} \times F_{y_{rebar}} = 1.78 \text{ in}^2 \times 60 \text{ ksi} = 107 \text{ kips}$$

$$C_{rebar\_bot} = A_{rebar\_bot} \times F_{y_{rebar}} = 1.78 \text{ in}^2 \times 60 \text{ ksi} = 107 \text{ kips}$$

$$T_{girder} = A_{girder} \times F_y = 30.937 \text{ in}^2 \times 50 \text{ ksi} = 1,547 \text{ kips}$$

Since  $T_{girder} > C_c + C_{rebar\_top} + C_{rebar\_bot}$ , the plastic neutral axis (PNA) is in the steel girder. Now, assuming the PNA is in the top flanges, the location of PNA measured from the top fiber of the top flanges can be determined as following:

$$PNA = \frac{1}{2} \times \left( \frac{T_{girder} - C_c - C_{rebar\_top} - C_{rebar\_bot}}{2 \times F_y \times b_{tf} \times t_{tf}} \right) = 0.243 \text{ in.}$$

The nominal plastic moment capacity can be calculated by taking moments of the forces from the steel girder, rebar and deck about PNA. Since PNA is in the top flanges, this suggests that a portion of top flange above the PNA is in compression and the portion below the PNA is in tension. Location of neutral axis of bottom flange, webs and top flanges, reinforcements, and deck measured from the location of PNA are as follows:

$$y_c = PNA + \frac{t_s}{2} = 2.743 \text{ in.}$$

$$y_{rebar\_top} = 4.0 \text{ in.}$$

$$y_{rebar\_bot} = 1.5 \text{ in.}$$

$$y_{tf\_c} = 0.122 \text{ in.}$$

$$y_{tf\_t} = 0.129 \text{ in.}$$

$$y_w = 10.6 \text{ in.}$$

$$y_{bf} = 21.2 \text{ in.}$$

$$M_c = C_c \times y_c = 2858 \text{ kips} - \text{in}$$

$$M_{rebar\_top} = C_{rebar\_top} \times y_{rebar\_top} = 428 \text{ kips} - \text{in}$$

$$M_{rebar\_bot} = C_{rebar\_bot} \times y_{rebar\_bot} = 160 \text{ kips} - \text{in}$$

$$M_{tf\_c} = C_{tf\_c} \times y_{tf\_c} = PNA \times b_{tf} \times 2 \times F_y \times y_{tf\_c} = 18 \text{ kips} - \text{in}$$

$$M_{tf\_t} = C_{tf\_t} \times y_{tf\_t} = (t_{tf} - PNA) \times b_{tf} \times 2 \times F_y \times y_{tf\_t} = 20 \text{ kips} - \text{in}$$

$$M_w = C_w \times y_w = A_w \times F_y \times y_w = 2 \times 7.97 \text{ in}^2 \times 50 \text{ ksi} \times 10.6 \text{ in} = 8,448 \text{ kips} - \text{in}$$

$$M_{bf} = C_{bf} \times y_{bf} = A_{bf} \times F_y \times y_{bf} = 9 \text{ in}^2 \times 50 \text{ ksi} \times 21.2 \text{ in} = 9,540 \text{ kips} - \text{in}$$

$$M_p = M_c + M_{rebar\_top} + M_{rebar\_bot} + M_{tf\_c} + M_{tf\_t} + M_w + M_{bf} = 21,472 \text{ kips} - \text{in} = 1,789 \text{ kips} - \text{ft}$$

In addition, the yielding moment calculation yields  $M_y$  equal 1364 kips-ft. The nominal capacity of the section is calculated as following:

$$M_n = M_p \times \left(1.07 - 0.7 \times \frac{D_p}{D_t}\right) = 1789 \times \left(1.07 - 0.7 \times \frac{t_s + PNA}{26.6875}\right) = 1,668 \text{ kips} - \text{ft}$$

$$M_n \leq 1.3 * M_y = 1,773 \text{ kips} - \text{ft} \text{ (OK)}$$

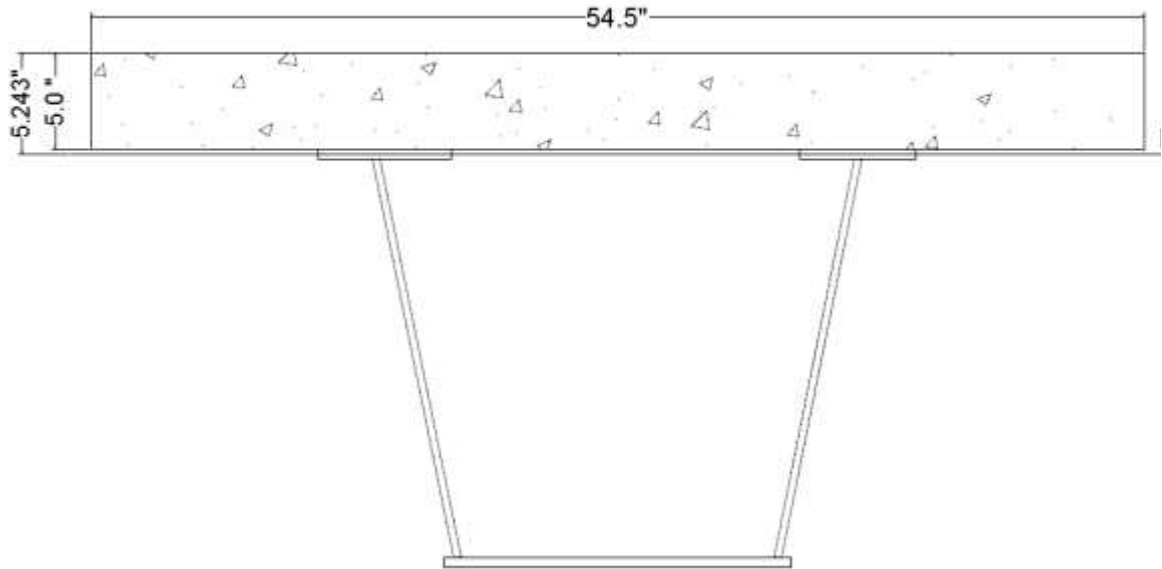


**Figure 3-6 Location of plastic neutral axis.**

### **3.2 Specimen Construction**

After completing the design phase, the shop drawings for steel girders, stiffeners, diaphragms and cross-frames were prepared. All steel components were fabricated at Tampa Steel Erecting Company. The steel material used for fabrication is ASTM A709 Grade 50. Bolts are A325 Type 1 material with 0.625 in. in diameter. The diameter for holes is slightly larger than that of the bolts with 0.6875-in. diameter. All steel was blast-cleaned to near-white condition and the steel surfaces were coated with self-curing inorganic zinc primer. The welding was performed in accordance with the bridge welding code D1.5 Specifications. All of the fillet welds were terminated within either  $0.5 \pm 0.25$  in. or  $0.25 \pm 0.125$  in. from the edge of a plate, depending on the length of welded leg, as illustrated in Figure 3-7.

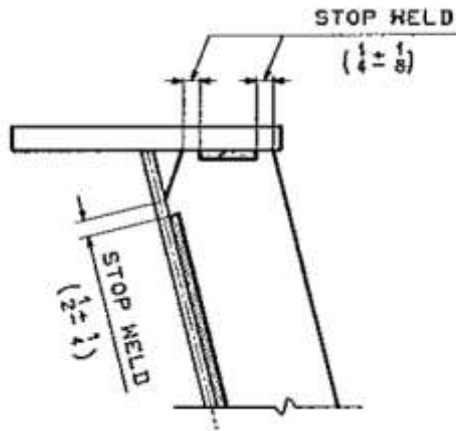


**Figure 3-7 Welding details.**

After the fabrication was completed, two steel girders and five external cross-frames were assembled at the shop to check for any fit-up issue. Then, they were disassembled and shipped to FDOT Structures Laboratory to complete the remaining construction works. At FDOT Structures Laboratory, the girder and cross-frames were reassembled and then the formworks and the reinforcements were installed as shown in Figure 3-8. The instrumentations were also installed. Details on the instrumentation plan are discussed in the next section.

The bridge deck was casted using class II concrete mix with 28-day strength of 4,500 psi, 3 in. slump and 0.75 in. maximum aggregate size. This is also the type of concrete that is used by FDOT in other construction projects. The casting process is shown in Figure 3-9. After the concrete got hardened, the entire specimen was relocated to a final position and ready for testing as illustrated in Figure 3-22.



**Figure 3-8 Complete specimen ready for casting.**



**Figure 3-9 Casting the concrete deck.**

### **3.3 Instrumentation Plan**

In order to obtain useful data with the most economical setup, the strain gauges and potentiometers were installed differently for each section. Strains were monitored in the



steel girders, the cross-frames, and the deck in order to capture responses of each component as well as load-transferring mechanisms.

Sections where potentiometers and strain gauges were installed are illustrated in Figure 3-10. In the original plan, strains were monitored at eight sections, labeled by Section 1 to 8 in green. However, a decision was made to remove gauges at Sections 1 and 7 due to the limitation of the channels in the data acquisition system and the sections were not renumbered. The details of instrumentation for each section are illustrated schematically from Figure 3-11 to Figure 3-18. Section 2, located at mid-span of the main span is the most critical section and was therefore treated very carefully. In Section 5, strains in cross-frames were also monitored. This setting of strain gauges allows the data to be collected in almost all of the important sections.

The deflections were monitored at five locations, labeled in red as “North,” “Location 2,” “Location 5,” “South,” and “End.” At each of these sections, there were four potentiometers attached to the top flanges of both box-girders. The typical potentiometer locations are shown in Figure 3-17. However, in Section 2 at mid-span, an additional potentiometer was installed to measure the deflection at the center of the deck as illustrated in Figure 3-18.

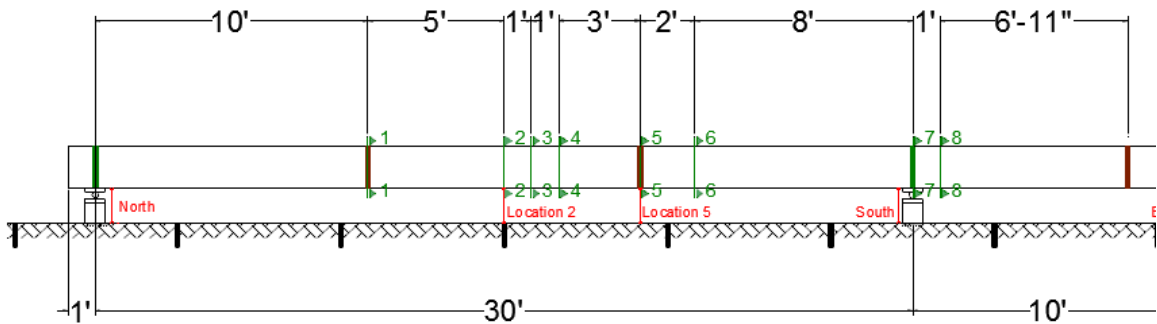


**Figure 3-10 Locations of strain gauges and potentiometers along the length of the specimen.**

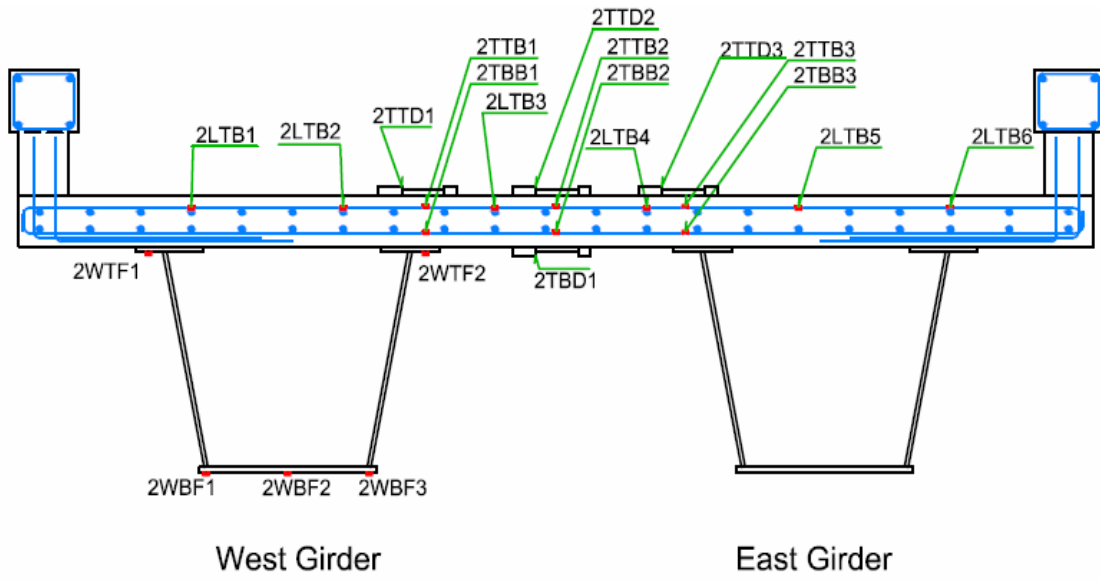


Figure 3-11 Strain gauges in the Section 2.

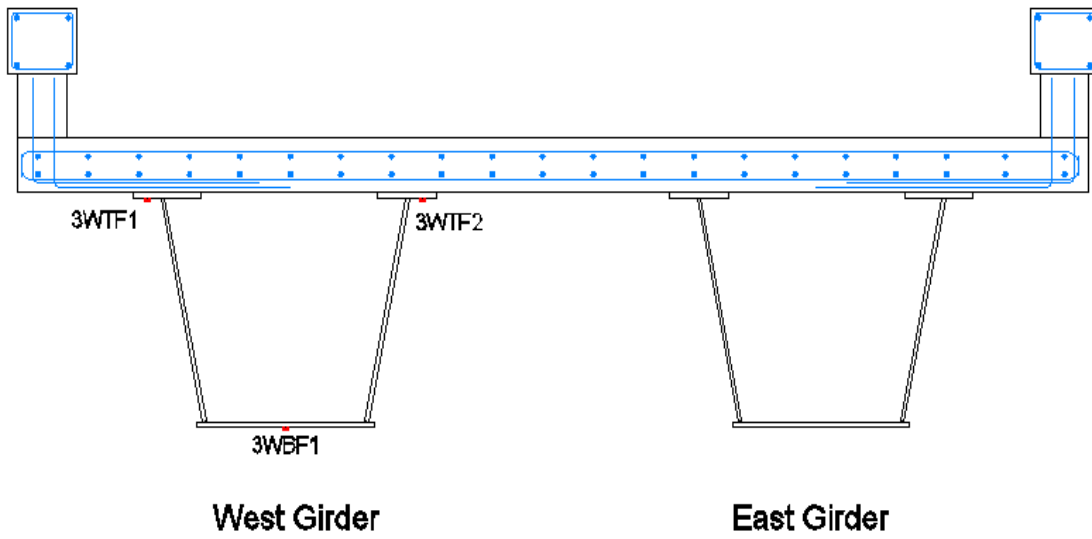


Figure 3-12 Strain gauges in the Section 3.

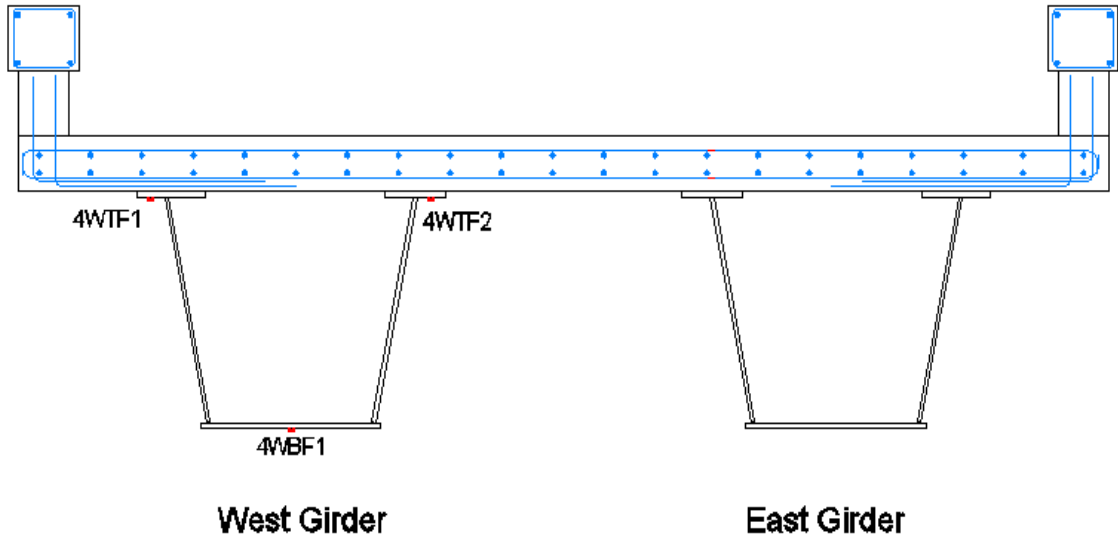


Figure 3-13 Strain gauges in the Section 4.

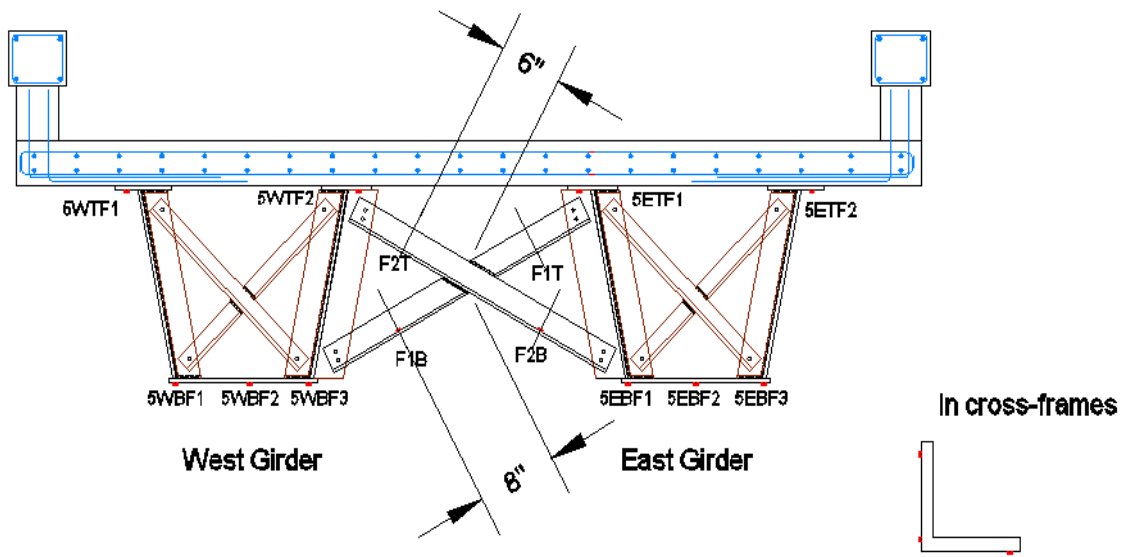


Figure 3-14 Strain gauges in the Section 5.

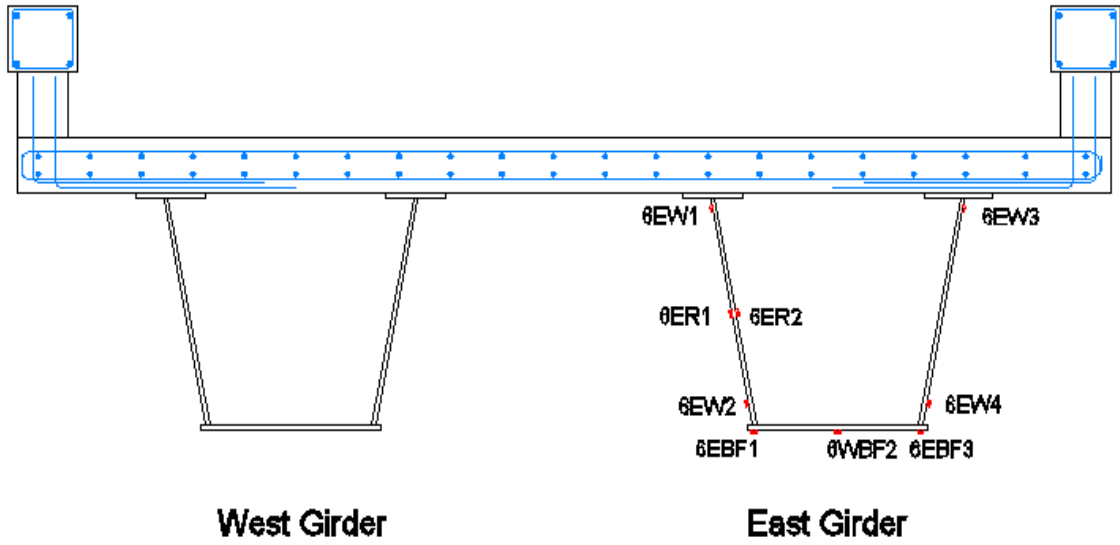


Figure 3-15 Strain gauges in the Section 6.

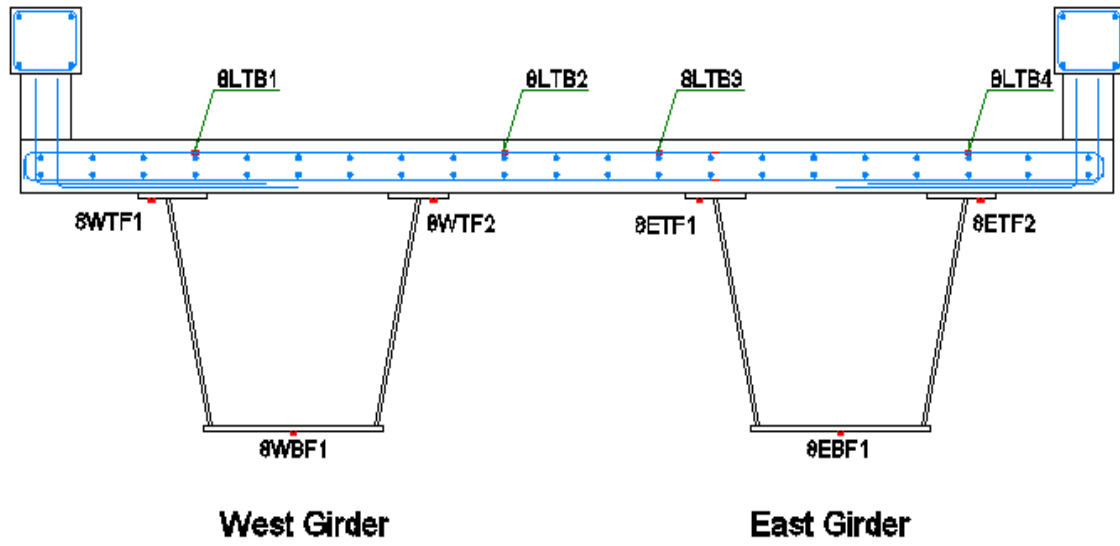


Figure 3-16 Strain gauges in the Section 8.

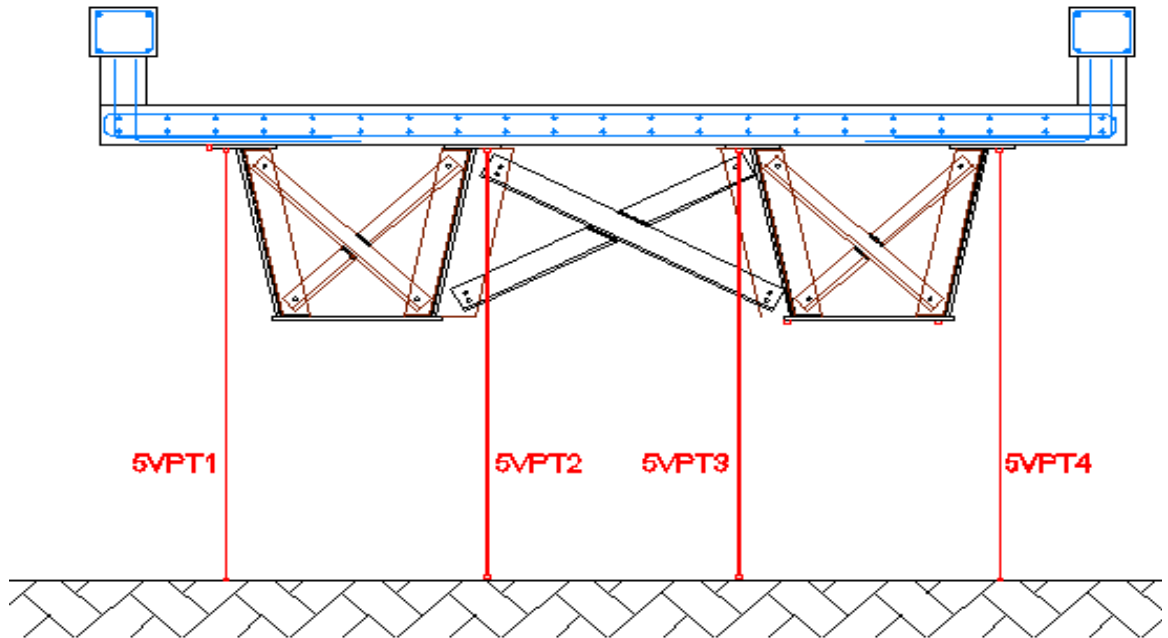


Figure 3-17 Potentiometers in Section 5.

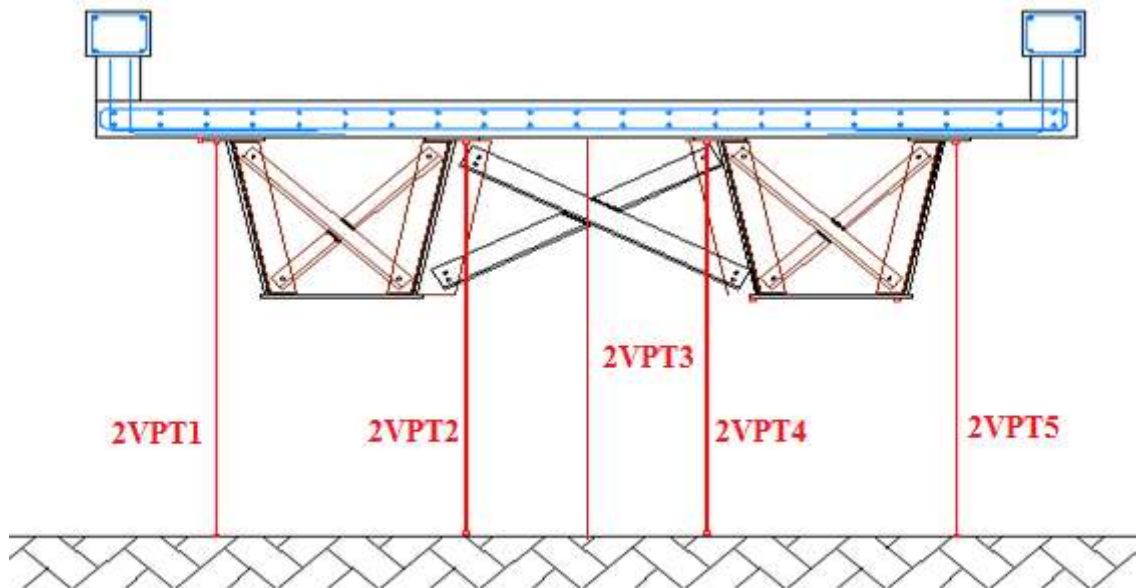
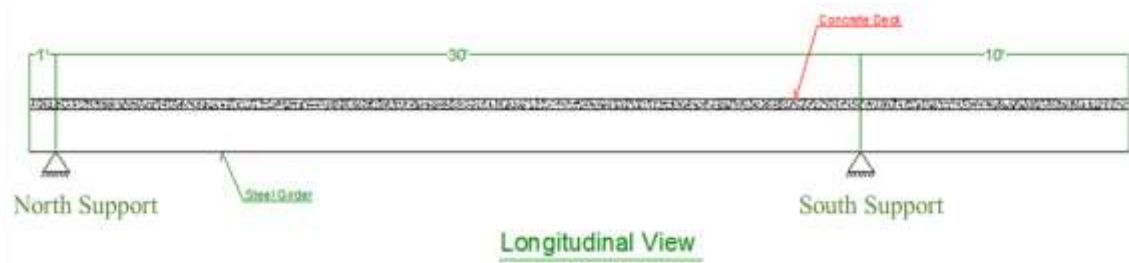


Figure 3-18 Potentiometers in Section 2.

### 3.4 Test Setup

Since this research was intended to investigate and gather information on the behavior of the twin steel box-girder bridges under both simple span and continuous span

conditions, a unique specimen configuration was devised so that both cases can be studied. The total length of the specimen is 41 ft comprising a 31-ft main span and a 10-ft second span as shown in Figure 3-19. The support, which is closer to the second span, is labeled as the south support. The one further away from the second span is labeled as the north support. The second span was configured so that it may act as a free cantilever in the non-loaded or non-anchored state. But when it is restrained to move vertically at its free end, the bridge will become a continuous structure with two spans. The restraining system at the cantilever end is composed of a transverse stiff I-beam anchored to the strong floor through two steel rods as shown in Figure 3-20. Two load cells were placed between the deck and the I-beam. As the load cells are in contact with the I-beam, the anchoring forces that will prevent the cantilever end from moving upwards are recorded. The I-beam can be raised out of the way to remove the restraint.



**Figure 3-19 Longitudinal view of test specimen.**



**Figure 3-20 Setup for continuity effect.**

Loading system used for this experiment included a FDOT loading frame of 130-in. width, two actuators, a loading beam (stiff I-beam) and steel reinforced elastomeric bearing pads as shown in Figure 3-21. One actuator has an 800-kip capacity and the other one has a 450-kip capacity. With this loading setup either one-point loading or two-point loading scenarios can be carried out. Figure 3-22 shows the complete specimen that was ready to be tested.

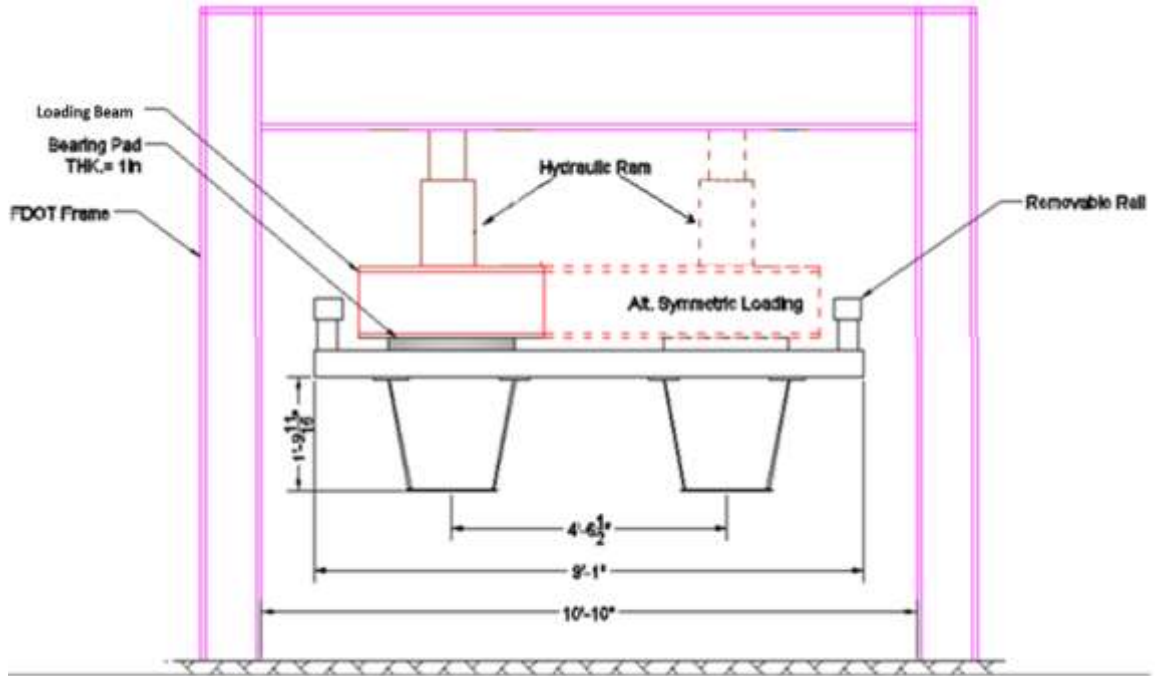


Figure 3-21 Schematic drawing of loading system.



Figure 3-22 Specimen with complete loading setup.



## 3.5 Testing Plan

In order to comprehend the behavior of two steel box-girder bridges in both linear and nonlinear range and to examine the modes of failures, a number of tests including elastic tests, cyclic fatigue test, and ultimate load tests were carried out on the laboratory small-scale specimens. The testing plan for each test is discussed in the following sections.

### 3.5.1 Elastic Tests

The goals of the elastic tests were to investigate the effects of rail, continuity, and loading configuration on elastic behaviors of laboratory specimen before and after damage was simulated in one girder, and to establish a baseline for the finite element model calibration.

The specimen was tested in a total of 18 elastic tests, under three different damage conditions. The first set of tests was carried out on the undamaged specimen. The second set of tests was carried out after the bottom flange in one of the girders was fractured. The last set of tests was carried out with bottom flange and webs completely fractured in one of the girders. Each set consisted of six tests with different combinations of rail, continuity, and loading configuration. The testing plan for all elastic tests is summarized in Table 3-1. In this table, the letter “Y” stands for “Yes” and the letter “N” stands for “No”. The letter “S” stands for symmetrical loading configuration indicating the loads are applied to both girders, while the letter “U” stands for unsymmetrical loading configuration. It should be noted that throughout the elastic tests, the west girder (WG) remained intact. The east girder (EG) was the only girder that was cut to simulate fracture and also the one to which the load was applied in unsymmetrical loading scenarios.

In all of the elastic tests, the load was applied to the specimen through 2"x9"x36" loading pad(s), with three slow dynamic loading ramps. Figure 3-23 shows one example of one loading history of one elastic test. Based on the finite element analysis and hand calculation results, the applied loads were selected to be 50 kips for unsymmetrical loading or 100 kips for symmetrical loading with 50 kips over each girder, in order to ensure the responses of the specimen to be in a linear range under both undamaged and damaged conditions.

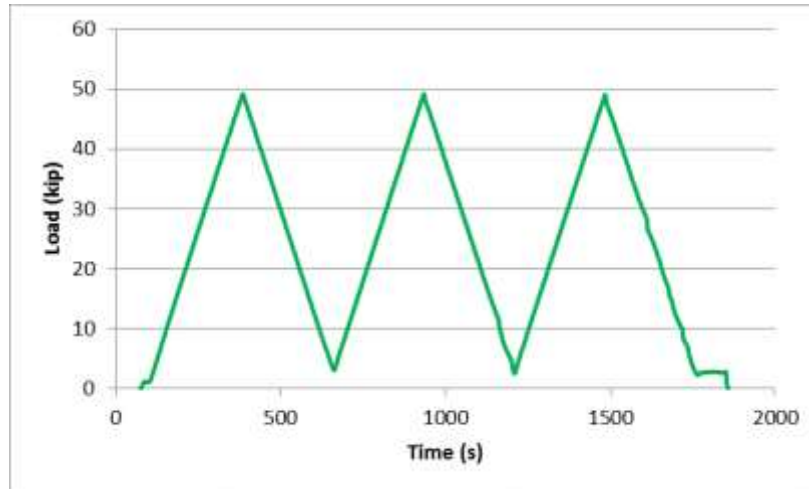


Figure 3-23 Typical three-ramp loading history for the elastic tests.

Table 3-1 Plan for Elastic and Cyclic Tests

| Test  | Name   | Number of Loaded Girder | Rail | Continuity | Loading Type | Max Load (kips)                   |
|---|--------|-------------------------|------|------------|--------------|-----------------------------------|
| <b>Undamaged Condition</b>                        |        |                         |      |            |              |                                   |
| 1   | Static | 2                       | N    | N          | S            | 50 each                           |
| 2   |        | 1                       | N    | N          | U            | 50                                |
| 3   |        | 1                       | N    | Y          | U            | 50                                |
| 4   |        | 2                       | Y    | N          | S            | 50 each                           |
| 5   |        | 1                       | Y    | Y          | U            | 50                                |
| 6   |        | 1                       | Y    | N          | U            | 50                                |
| <b>Bottom Flange Fractured Condition</b>          |        |                         |      |            |              |                                   |
| 7   | Static | 2                       | Y    | N          | S            | 50 each                           |
| 8   |        | 1                       | Y    | Y          | U            | 50                                |
| 9   |        | 1                       | Y    | N          | U            | 50                                |
| 10  |        | 2                       | N    | N          | S            | 50 each                           |
| 11  |        | 1                       | N    | N          | U            | 50                                |
| 12  |        | 1                       | N    | Y          | U            | 50                                |
| 13  | Cyclic | 1                       | Y    | N          | U            | 60 kips and almost million cycles |
| <b>Webs and Bottom Flange Fractured Condition</b> |        |                         |      |            |              |                                   |
| 14  | Static | 2                       | Y    | N          | S            | 50 each                           |
| 15  |        | 1                       | Y    | Y          | U            | 50                                |
| 16  |        | 1                       | Y    | N          | U            | 50                                |
| 17  |        | 2                       | N    | N          | S            | 50 each                           |
| 18  |        | 1                       | N    | N          | U            | 50                                |
| 19  |        | 1                       | N    | Y          | U            | 50                                |

Notation: Y is Yes; N is No; S is Symmetric; U is unsymmetrical.

### 3.5.2 Cyclic Test

As indicated in Table 3-1, the cyclic test was carried out under the damage condition in which EG had its entire bottom flange fractured. The purpose of this cyclic test was to see what would happen to the bridge under the traffic load assuming a fracture/damage occurred in the bottom flange without being noticed. The cyclic load magnitude was determined based on the *AASHTO LRFD Bridge Design Specifications* (2010). First, the fatigue category for the bridge specimen was selected based on its structural characteristics such as cross-frame and stiffener design details. The cyclic load is then defined as the load required such that the maximum stress produced on the specimen would be equal to the threshold stress of the selected fatigue category according to the *AASHTO LRFD Bridge Design Specifications*. The determination of the cyclic load required several iterative finite element analyses of the bridge.

It should be noted that this procedure assumes the structure is designed for infinite life and is most efficient when it just meets this requirement (threshold stress). Therefore, if a fracture would occur without being noticed, the same (design) load causing the threshold stress would continue to be applied. This same load was then applied to the damaged bridge at the traffic rate equivalent to infinite life for a period of two years.

This laboratory specimen satisfies the requirements for type C fatigue category. The threshold stress for type C category is 10 ksi. The load on the undamaged structure required to cause a maximum stress of 10 ksi is 60 kips, which was determined from finite element analysis. The average daily traffic truck passing the bridge equivalent to infinite life is 1286 trucks per day (AASHTO, 2010). For every two years, the total trucks that would pass the bridge will be 938667 trucks or cycles. The truck load is applied to the

specimen at a rate of 1 Hz, so the total estimated time to perform the cyclic test was 10.9 days.

### **3.5.3 Ultimate Load Tests**

A total of five ultimate load tests were carried out. In these ultimate load tests, the laboratory specimens were loaded to failure with one girder completely fractured at mid-span. The purposes of the ultimate load tests were to investigate the inelastic behavior, maximum load-carrying capacities and modes of failure of a twin steel box-girder bridge when the bottom flange and the webs were completely fractured in one girder. All of the ultimate load tests are summarized in Table 3-2.

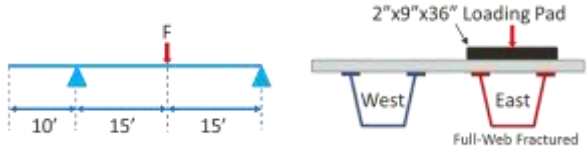
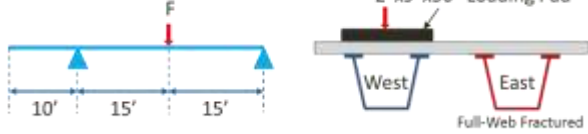


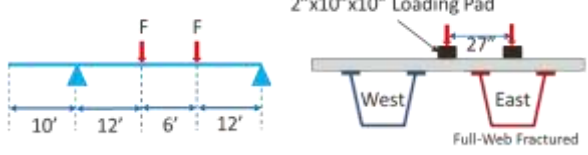
In Tests A and D, the specimen was loaded incrementally to failure over the fracture location at mid-span. These test setups were to generate the worst-case loading scenarios. The results from these tests will provide the remaining capacities of the system and explain how the bridge system remains stable after a full-depth fracture of one of the girders. In test A, the load was applied through a 9 in. x 36 in. elastomeric pad covering the entire width of the damaged girder, while in Test D, the load was applied through a 10 in. square elastomeric pad placed at the center of the damaged girder. The difference, between Test A and D, will explain how much the capacity of the damaged structure will be affected by the distance between the loading point and top flanges.

In Test B and C, the specimen was loaded incrementally at mid-span over the intact girder. Similar to Test A, the load was applied through 9 in. x 36 in. elastomeric pad covering the entire width of the intact girder in Test B. In Test C, the specimen was loaded through 10 in. x 10 in. loading pad placed at the center of the intact girder. The results from

Test B and C, in combination with the results of Test A and D, can be used to evaluate how much the intact girder and damaged girder, as components, contribute to the total load-carrying capacity of the whole system.

Test E was set up with four-point loading to simulate truck footprints. Each truck footprint was simulated by a 10-in. square elastomeric pad. The main purpose of this test was to see how much load the damaged bridge system can carry and, more importantly, to investigate how the specimen will fail ultimately and to investigate how the failure modes vary as it changes from a single point load to a truck load configuration.

**Table 3-2 Plan for Ultimate Load Tests**

| Ultimate Test | Loading Configuration  | Type of Load  |
|---------------|--|---|
| A             |    | Load was applied incrementally until failure occurred.  |
| B             |    | Load was applied until the plateau in load-deflection curve was observed. Test was discontinued before the failure. |
| C             |    | Load was applied until the failure occurred by punching through the slab  |
| D             |   | Load was applied until the failure occurred by punching through the slab  |
| E             |  | Load was applied until failure occurred.  |

## Chapter 4 Laboratory Testing Results

### 4.1 Elastic Tests

Results of 18 elastic tests are split into three sections corresponding to the three damage levels of the specimen. Experimental results for the undamaged specimen, and the damaged specimen with bottom flange fractured and full-web fractured in one girder are presented respectively in Section 4.1.1, Section 4.1.2 and Section 4.1.3. The results provided in this section will focus on only the steel box-girder responses. It is important to note that the maximum displacements, reported here, are the average of top flange vertical displacements of each girder at mid-span while the maximum strains are the average of longitudinal strains measured in the bottom flange of each girder at mid-span. The shear forces in the cross-frame reported in the following sections are measured at the cross-frame, located at Section 5, 5 ft away from the mid-span. Again, note that WG was the intact girder and EG was the only girder to be damaged.

#### 4.1.1 On Undamaged Specimen

Six tests were carried out to examine linear elastic responses of the undamaged bridge specimen with different combinations of rail, continuity and loading configuration. Results for each elastic test are summarized in **Table 4-1**.



**Table 4-1 Summary of Elastic Tests on Undamaged Specimen**

| Test | Characteristics | Max Disp. in WG (in) | Max Disp. in EG (in) | Max Strain in WG (in/in*10 <sup>6</sup> ) | Max Strain in EG (in/in*10 <sup>6</sup> ) | Shear Force in Cross-Frame (kip) |
|------|-----------------|----------------------|----------------------|---|---|----------------------------------|
| 1    | NNS             | 0.317                | 0.324                | 460                                       | 464                                       | 0.5                              |
| 2    | NNU             | 0.110                | 0.203                | 168                                       | 286                                       | 1.6                              |
| 3    | NYU             | 0.094                | 0.179                | 140                                       | 257                                       | 1.6                              |
| 4    | YNS             | 0.285                | 0.303                | 418                                       | 410                                       | 0.3                              |
| 5    | YYU             | 0.086                | 0.174                | 137                                       | 238                                       | 1.6                              |
| 6    | YNU             | 0.100                | 0.194                | 162                                       | 263                                       | 1.5                              |

As expected, for symmetrical loading scenarios as in Tests 1 and 4, both girders experienced almost identical behaviors as indicated by the maximum displacement and strain in two girders. These symmetrical loading tests can be treated as tests of only one half of specimen. The results from Test 1 indicated that 50 kips of load would produce approximately 460  $\mu\epsilon$  ( $1 \mu\epsilon = \text{in/in} \cdot 10^6$ ) longitudinal strain in the bottom flange of one girder. The maximum longitudinal strain in WG in Test 2 was 168  $\mu\epsilon$  and this suggests that the WG resisted 36.5% of the total applied load. For unsymmetrical loading tests, the maximum displacement of EG was 72.8% higher than that of WG, on average.

Between Tests 2 and 3, the presence of continuity decreased the maximum displacement and strain in EG approximately by 11.8% and 10.1%, respectively. The railing system decreased the maximum displacement by 4.4% and the maximum strain by 8.0% for EG as shown in Tests 2 and 6.

Altogether, the effects of railing systems and continuity reduced the maximum displacement and strain in EG by 14.3% and 16.8%, respectively as illustrated in Tests 2 and 5. These numbers were 1% and 21.8% for WG.

Under symmetrical loading configuration, the role of cross-frames was insignificant. However, under unsymmetrical loading configuration, the effect of cross-frames became clearer as the forces in the cross-frame increased triple from 0.4 kips to 1.6

kips, on average. The total shear forces transferred through two cross-frames were approximately 3.2 kips which was equivalent to 6% of the applied load (assuming two cross-frames at Sections 1 and 5 transferred the same amount of forces).

#### 4.1.2 On Damaged Specimen with Bottom Flange Fractured in One Girder

In this series of tests, the bottom flange in the EG was fractured at mid-span as illustrated in Figure 4-1. Due to that fracture in bottom flange, the maximum longitudinal strain in EG was now measured from its webs, while maximum longitudinal strain in WG was still measured from its bottom flange. The same six tests that had been carried out for the undamaged bridge were repeated. Again, the effects of each parameter, including rail, continuity, and loading configuration, were investigated based on the responses of the steel box-girders.



Figure 4-1 Saw cutting of bottom flange in east girder.

The overall maximum responses in the steel box-girders are summarized in **Table 4-2**.

**Table 4-2 Summary of Elastic Tests on Bottom Flange Fractured Specimen**

| Test | Characteristics | Max Disp. in WG (in) | Max Disp. in EG (in) | Max Strain in WG (in/in*10 <sup>6</sup> ) | Max Strain in EG (in/in*10 <sup>6</sup> ) | Shear Force in Cross-Frame (kip) |
|------|-----------------|----------------------|----------------------|---|---|----------------------------------|
| 7    | YNS             | 0.293                | 0.337                | 459                                       | 851                                       | 0.3                              |
| 8    | YYU             | 0.089                | 0.180                | 146                                       | 506                                       | 1.7                              |
| 9    | YNU             | 0.107                | 0.206                | 176                                       | 578                                       | 1.7                              |
| 10   | NNS             | 0.308                | 0.337                | 449                                       | 1260                                      | 0.2                              |
| 11   | NNU             | 0.114                | 0.218                | 180                                       | 610                                       | 1.7                              |
| 12   | NYU             | 0.094                | 0.188                | 148                                       | 539                                       | 1.7                              |

As illustrated in Test 7 and Test 10 with symmetrical loading, EG experienced clearly higher displacements than WG. For instance, for the test NNS, the difference in the displacement between WG and EG increased from 2.2% for the undamaged specimen to 9.4% for this bottom flange fractured damage condition. It was because stiffness of EG decreased after its bottom flange was fractured.

Between Tests 11 and 12, the presence of continuity decreased the maximum displacement and strain in EG by approximately 13.8% and 11.6%, respectively. Tests 9 and 11 indicated that the railing system decreased the displacement by 5.5% and strain by 5.2% in EG. Comparing the results from Tests 8 and 11, the effects of railing systems and continuity together reduced the displacement and strain in EG by 17.4% and 17%, respectively. Compared with the undamaged specimen, the effects of railing system and continuity were comparable with respect to reduction in the maximum displacement and strain in EG (17.4% and 17% for the bottom flange fractured specimen vs 14.3% and 16.8% for the undamaged specimen).

Similarly, the data in the WG and cross-frames were found comparable to those before the bottom flange fracture occurred. The maximum displacement in EG increased 6.5% on average as the bottom flange was fractured. Only strains in EG increased

significantly. It was because of high local stress intensity at the junction of the web and bottom flange that was produced when bottom flange fractured. Considering the worst-loading scenario which is NNU, the effect of fracture of bottom flange in EG increased the maximum strain in WG by 7%. This suggested the load transferred to WG now increased from 36.5% to 39.1%.

Overall, the elastic responses of bottom flange fractured and undamaged specimen were comparable.

#### **4.1.3 On Damaged Specimen with Bottom Flange and Webs Fractured in One Girder**

In this testing series, the damage intensity was extended by fracturing the entire webs of EG in addition to the existing fracture in the bottom flange as illustrated in Figure 4-2. It is also important to note that since the web was now fully fractured, the longitudinal strain data in EG at mid-span were lost and not reported here.



**Figure 4-2 East girder with bottom flange and web fractured in one girder.**

The maximum responses in the steel box-girders under the full-web fracture condition are presented in **Table 4-3**.

**Table 4-3 Summary of Elastic Tests on Full-Web Fractured Specimen**

| Test | Characteristics | Max Disp. in WG (in) | Max Disp. in EG (in) | Max Strain in WG (in/in*10 <sup>6</sup> ) | Max Strain in EG (in/in*10 <sup>6</sup> ) | Shear Force in Cross-Frame (kip) |
|------|-----------------|----------------------|----------------------|---|---|----------------------------------|
| 14   | YNS             | 0.449                | 0.675                | 867                                       | N/A                                       | 3.6                              |
| 15   | YYU             | 0.197                | 0.446                | 390                                       | N/A                                       | 5.3                              |
| 16   | YNU             | 0.268                | 0.542                | 479                                       | N/A                                       | 5.1                              |
| 17   | NNS             | 0.511                | 0.757                | 891                                       | N/A                                       | 4.0                              |
| 18   | NNU             | 0.297                | 0.593                | 503                                       | N/A                                       | 4.8                              |
| 19   | NYU             | 0.212                | 0.472                | 398                                       | N/A                                       | 5.5                              |

The results from tests with symmetrical loading indicated that the maximum displacements in EG were now significantly higher than that of WG. For instance, in Test 17 (NNS), EG experienced 48.1% higher displacement than WG did while it was only 2.2% and 9.4% for the undamaged state and the bottom flange fractured damage state,

respectively. Also, the displacements in both girders increased dramatically compared to previous damage states. The maximum displacement in WG, averaged from six elastic tests, increased 88% and 91% for the undamaged state and bottom flange fractured damage state, respectively. For EG, these numbers were 152% and 140%.

Between Tests 18 and 19, the presence of continuity decreased the maximum displacement by 20.4% for EG and 28.6% for WG. Tests 18 and 16 indicated that presence of the railing system reduced the maximum displacement by 8.6% for EG and 9.7% for WG. The effects of continuity and rail together reduced the maximum displacement by 24.8% for EG and 33.7% for WG. The effects of continuity and rail increased more significantly than that of two previous damage states. This suggests that as the damage intensity increases, the continuity and rail effects will increase.

The maximum longitudinal strain in WG increased significantly, compared to two previous cases. The maximum longitudinal strain in WG was 891  $\mu\epsilon$  for Test 17 (NNS) and 503  $\mu\epsilon$  for Test 18 (NNU). For the undamaged specimen, these numbers were 460  $\mu\epsilon$  and 168  $\mu\epsilon$  for Test 1 (NNS) and Test 2 (NNU), respectively. This comparison suggested that the majority of the applied load was transferred to the intact girder by assuming the 50 kips of load would produce an amount of 460  $\mu\epsilon$  in the bottom flange of one girder. In other words, the contribution of the damaged girder, after its entire webs and flange were fractured, was negligible. This conclusion was later verified by means of finite element analysis in which the stress in the damaged girder was found to be negligible.

The forces in cross-frames also increased as compared to previous damage cases. The cross-frame forces increased from 1.21 kips on average on bottom flange fractured tests to 4.72 kips on average when the whole web and bottom flange were fractured.

Assuming two cross-frames in the main span carried the same amount of forces, the total load carried by the cross-frames would be 9.44 kips (4.72 kips x 2). It was equivalent to 19% of the applied load.

Overall, the specimen with complete fracture in the bottom flange and webs in EG, had its stiffness reduced significantly as the EG almost lost all of its flexural stiffness. As a result, the maximum displacement and strain increased significantly in the intact girder, WG. However, the beneficial effects of both continuity and rail system and cross-frames increased clearly.

#### **4.1.4 Summary of Elastic Tests**

Overall, all elastic tests were performed successfully. The test data showed that the bridge had completely linear-elastic responses in all three damage conditions as shown from Figure 4-3 to Figure 4-5. Several important observations for all elastic tests are summarized as follows:

- The rail and continuity helped to increase the load-carrying capacity of the specimen. As the damage intensity increases, their beneficial effects also increase. For instance, the rail and continuity effects together reduced the displacement of the damaged girder by 14.3%, 17.4% and 24.8%, for the undamaged, bottom flange fractured and full-web fractured damage states, respectively.
- In addition to the deck, cross-frames were found to play an important role in transferring the load from the damaged girder to intact girder. Similar to the effects of the rail and continuity, the more damage the bridge experienced, the more important the cross-frames were. The estimated contribution of cross-frames were

5%, 5% and 19% for the undamaged, bottom flange fractured and full-web-fractured damage states, respectively. However, it should be mentioned that the relatively large contribution of cross-frames found in these experiments could be related to the scale of the test specimen used.

- In general, the elastic responses of the specimen, under the undamaged and bottom flange fractured damage states, were comparable. For instance, the maximum displacement of EG increased by an average of 6.5% when the bottom flange was fractured.
- With the bottom flange and webs completely fractured, the flexural stiffness of the damaged girder was negligible. Under the same loading configuration, more load was transferred to the intact girder, or the strain in the intact girder increased as the damage intensity increases. For instance, the average maximum strain in all six elastic tests in the intact girder increased 5% when the bottom flange of EG was fractured and 138% when the entire webs of EG were fractured. This indicates that as the damage takes place, the load resisted by the damaged girder is transferred to the intact girder.



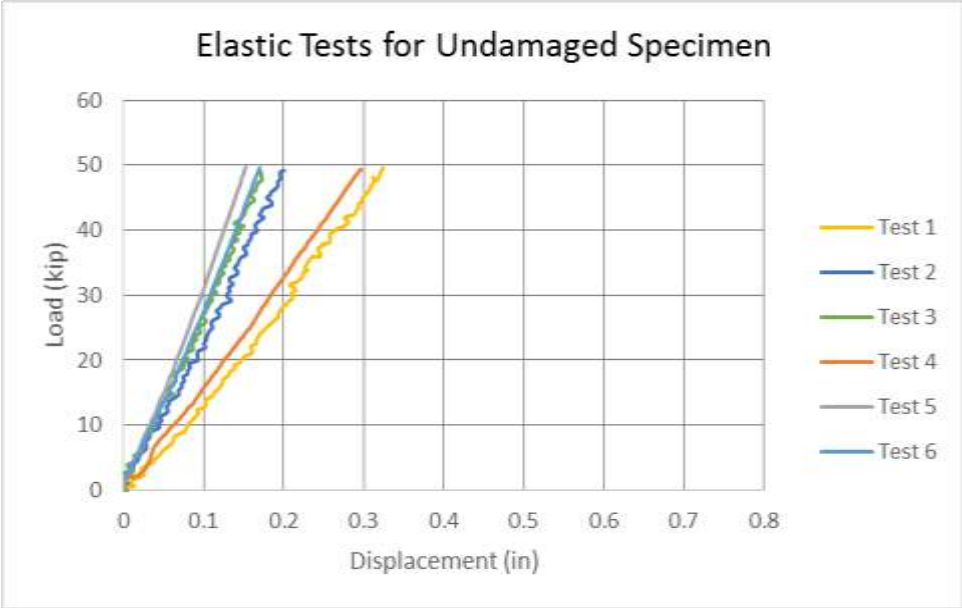


Figure 4-3 Results of elastic tests on undamaged specimen.

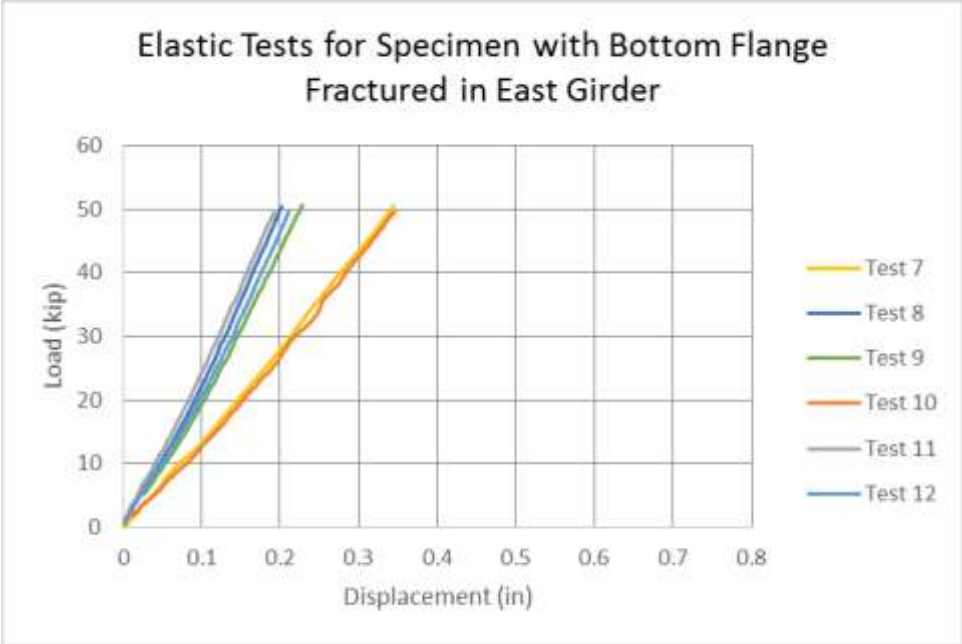


Figure 4-4 Results of elastic tests on specimen with bottom flange fractured in east girder.

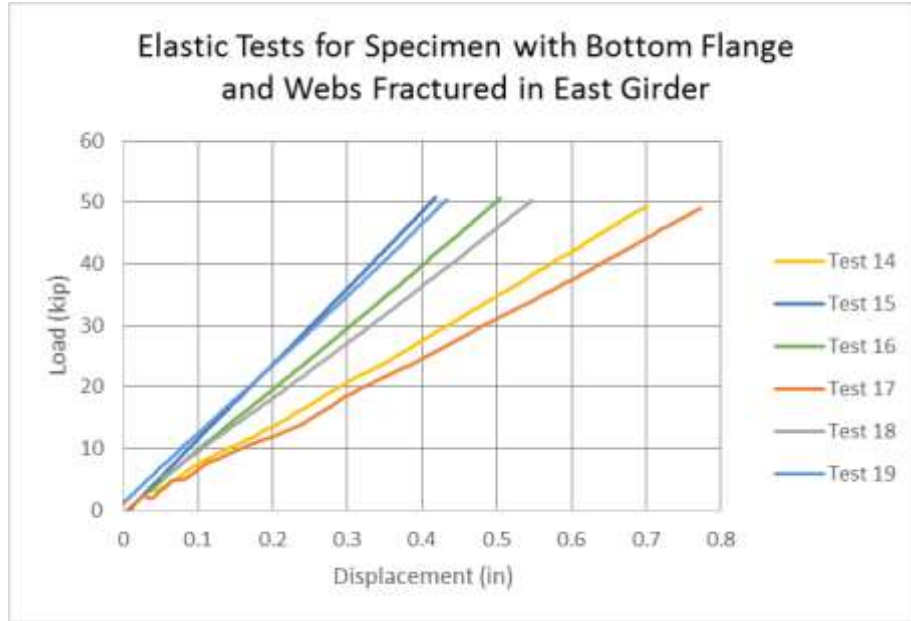


Figure 4-5 Results of elastic tests on specimen with full-depth fracture in east girder.

Results of all elastic tests are summarized in **Table 4-4**.

**Table 4-4 Summary of all Elastic Tests**

| Test  | Characteristics      | Max Disp. in WG (in) | Max Disp. in EG (in) | Max Strain in WG (in/in*10 <sup>6</sup> ) | Max Strain in EG (in/in*10 <sup>6</sup> ) | Force in Cross- Frame (kip) |
|---|----------------------|----------------------|----------------------|---|---|-----------------------------|
| <b>Undamaged (Tests 1-6)</b>  |                      |                      |                      |   |   |                             |
| 1   | NNS                  | 0.317                | 0.324                | 460                                       | 464                                       | 0.5                         |
| 2   | NNU                  | 0.110                | 0.203                | 168                                       | 286                                       | 1.6                         |
| 3   | NYU                  | 0.091                | 0.179                | 140                                       | 257                                       | 1.6                         |
| 4   | YNS                  | 0.285                | 0.303                | 418                                       | 410                                       | 0.3                         |
| 5   | YYU                  | 0.109                | 0.174                | 137                                       | 238                                       | 1.6                         |
| 6   | YNU                  | 0.124                | 0.194                | 162                                       | 263                                       | 1.5                         |
| <b>Fractured bottom flange (Tests 7-13)</b>                         |                      |                      |                      |   |   |                             |
| 7   | YNS                  | 0.293                | 0.337                | 459                                       | 851                                       | 0.3                         |
| 8   | YYU                  | 0.089                | 0.180                | 146                                       | 506                                       | 1.7                         |
| 9   | YNU                  | 0.107                | 0.206                | 176                                       | 578                                       | 1.7                         |
| 10  | NNS                  | 0.308                | 0.337                | 449                                       | 1260                                      | 0.2                         |
| 11  | NNU                  | 0.114                | 0.218                | 180                                       | 610                                       | 1.7                         |
| 12  | NYU                  | 0.094                | 0.188                | 148                                       | 539                                       | 1.7                         |
| 13  | Cyclic Loading (YNU) | ---- <sup>1</sup>    | ---- <sup>1</sup>    | ---- <sup>1</sup>                         | ---- <sup>1</sup>                         | ---- <sup>1</sup>           |
| <b>Fractured web in addition to the bottom flange (Tests 14-19)</b> |                      |                      |                      |   |   |                             |
| 14  | YNS                  | 0.449                | 0.675                | 867                                       | N/A                                       | 3.6                         |
| 15  | YYU                  | 0.197                | 0.446                | 390                                       | N/A                                       | 5.3                         |
| 16  | YNU                  | 0.268                | 0.542                | 479                                       | N/A                                       | 5.1                         |
| 17  | NNS                  | 0.511                | 0.757                | 891                                       | N/A                                       | 4.0                         |
| 18  | NNU                  | 0.297                | 0.593                | 503                                       | N/A                                       | 4.8                         |
| 19  | NYU                  | 0.212                | 0.472                | 398                                       | N/A                                       | 5.5                         |

<sup>1</sup> See Section 4.2

## 4.2 Cyclic Test

It is important to note that the bridge specimen was tested under cyclic load when the bottom flange in the east girder was fractured. The specimen was tested with rail, no continuity and under unsymmetrical loading, as illustrated in Figure 4-6. The magnitude of cyclic load was 60 kips as explained in Section 2.4.1. The loading rate was 1 Hz. (one second for each loading cycle) and the estimated number of loading cycle was 938,667. However, after 213,101 cycles, the test was stopped. It was because the initial bottom flange fracture started propagating through the entire webs and reached top flanges as shown in Figure 4-8. Some minor cracks were observed on the deck surface at the center

of the bridge as illustrated in Figure 4-7. One reason for stopping the test was to prevent the crack from growing and damaging the deck, which then might collapse the bridge, while the ultimate goal of this project was to determine the maximum load-carrying capacity of the bridge under static loading. The results from the ultimate load test were necessary to calibrate the nonlinear finite element model. The duration of this cyclic test at the time of stop was equivalent to 5.5 months of daily traffic. This suggests a complete cyclic loading test might be needed in the future research to determine if the bridge will collapse under the fatigue test.

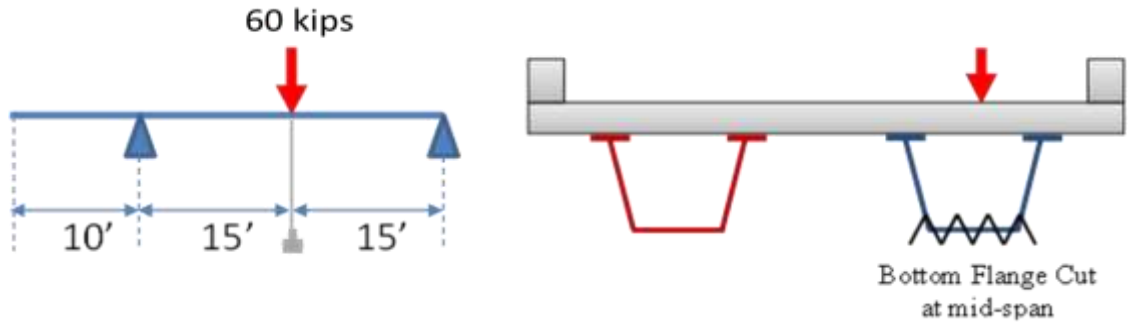


**Figure 4-6 Schematic description of the cyclic loading test.**



**Figure 4-7 Cracks on the deck surface during cyclic test.**

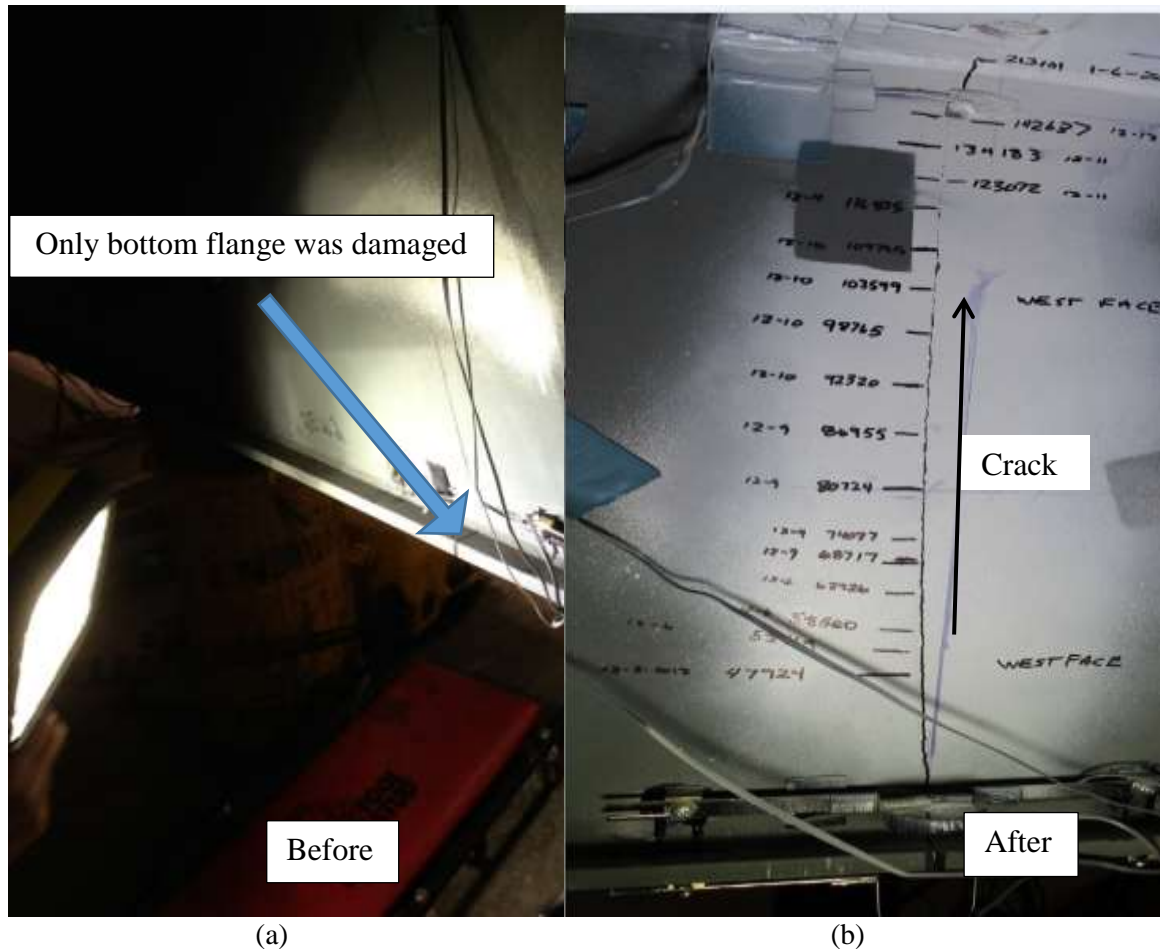


**Figure 4-8 Crack in the damaged girder: (a) before and (b) after the cyclic test.**

One of the responses observed visibly was the crack propagation from the bottom flange to the web of the damaged girder. Figure 4-9 shows growth of the crack length in the damaged girder during the cyclic test. The crack length data between the 1<sup>st</sup> and 50,000<sup>th</sup> cycle was missing because the crack propagation began overnight and was not observed until the next morning. The crack length was linearly proportional to the number of cycles until around the 160,000 cycles when the crack began to reach the top flanges, at which point the rate of growth slowed. The crack grew nearly evenly in both sides of the web of east girder until loading cycles of 80,000<sup>th</sup>. After that, the crack grew with a slower rate in the inside web than the outside web due to contributions of the cross-frames and the intact

girder to the inside web of the damaged girder. This was consistent with experimental data from elastic tests and FEA results, which showed the outside face of the damaged girder always had higher displacement and stress than the inside face.

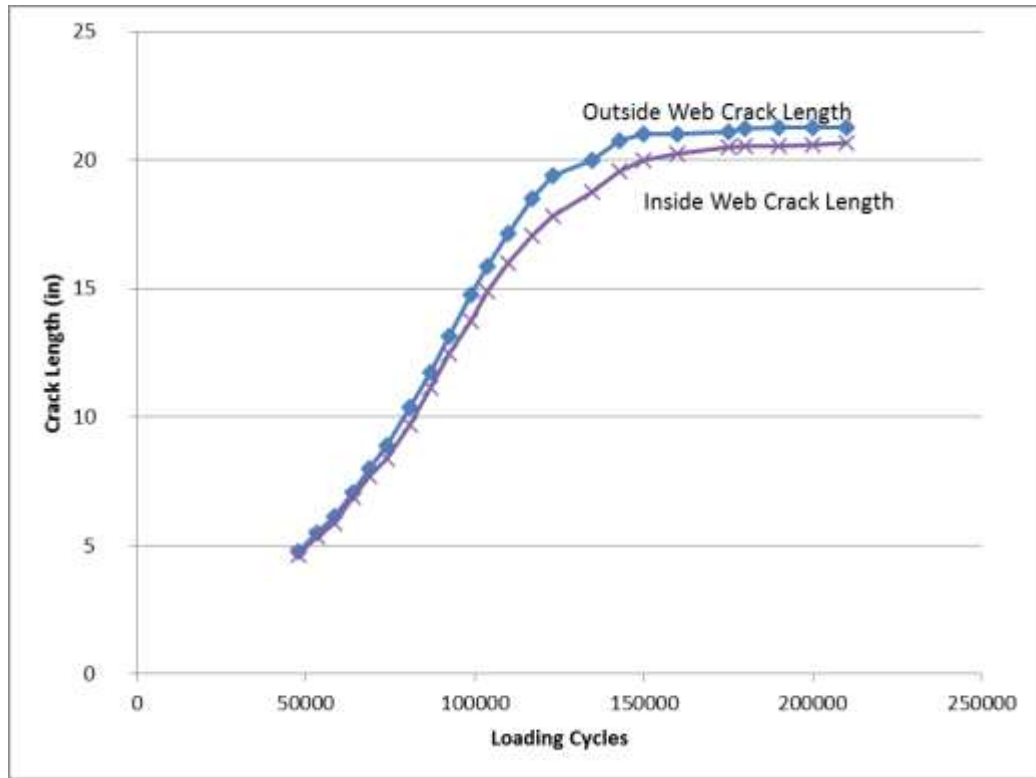


**Figure 4-9 Crack growth in the damaged girder.**

As the cracks grew into the webs, the stiffness of the specimen changed. For this reason, all of the monitored data including the crack opening at the base, displacement, displacement range, and shear force show similar patterns to that of the growth of crack length when they are plotted versus the number of cycles.

The setup to measure the crack base opening, or the separation between two halves of the fractured girder in longitudinal direction, is illustrated in Figure 4-10. The crack base opening was measured at both the inside and outside faces of the bottom flange of the fractured girder and is illustrated in Figure 4-11. During the first 25,000 cycles, the

difference between maximum and minimum crack opening was nearly constant and suggests the bottom flange fracture had not yet begun to propagate into web. Between 50,000 and 10,000 cycles, the crack opening increased rapidly. At the last cycle, the maximum crack opening was around 0.19 in. for the outside web and 0.175 in. for the inside one.

At the same time, the stiffness of the bridge measured at the fractured location was found to have decreased approximately 54% from 260 kips/in to 120 kips/in.

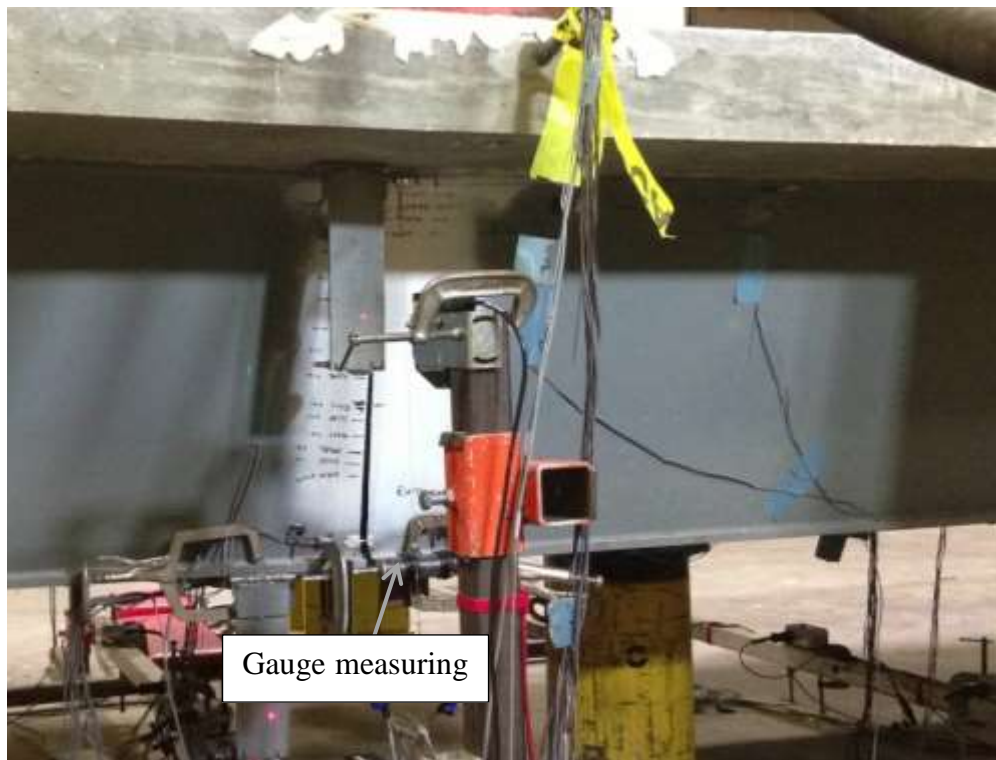


**Figure 4-10 Crack opening measuring gauge on the exterior face.**



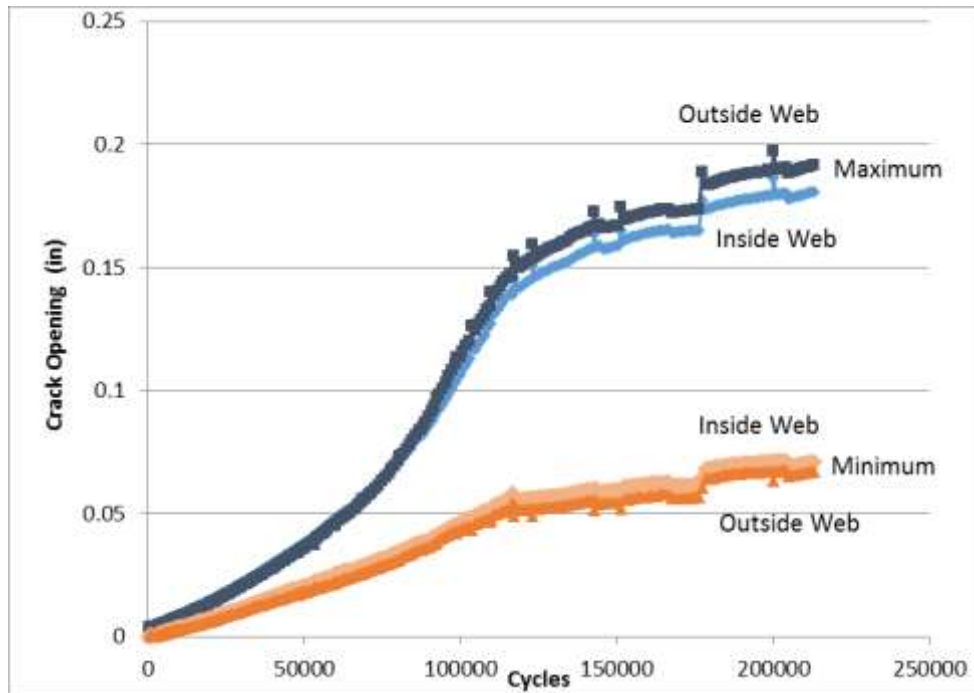


**Figure 4-11 Crack base opening vs. number of loading cycles.**

The maximum displacement and minimum displacement of the girders were collected for each loading cycle. Figure 4-12 shows how the maximum and minimum displacement of the fractured girder changed over time. The maximum displacement increased from 0.25 in. to 0.7 in. while the minimum displacement also increased from 0.03 in. to 0.24 in. during the test. Figure 4-13 plots the displacement range for both girders (which is equal to maximum displacement minus minimum displacement in each girder) that shows the vertical deflection of each girder in a cycle. Both plots show similar behavior and trends to that of the crack length growth plot.

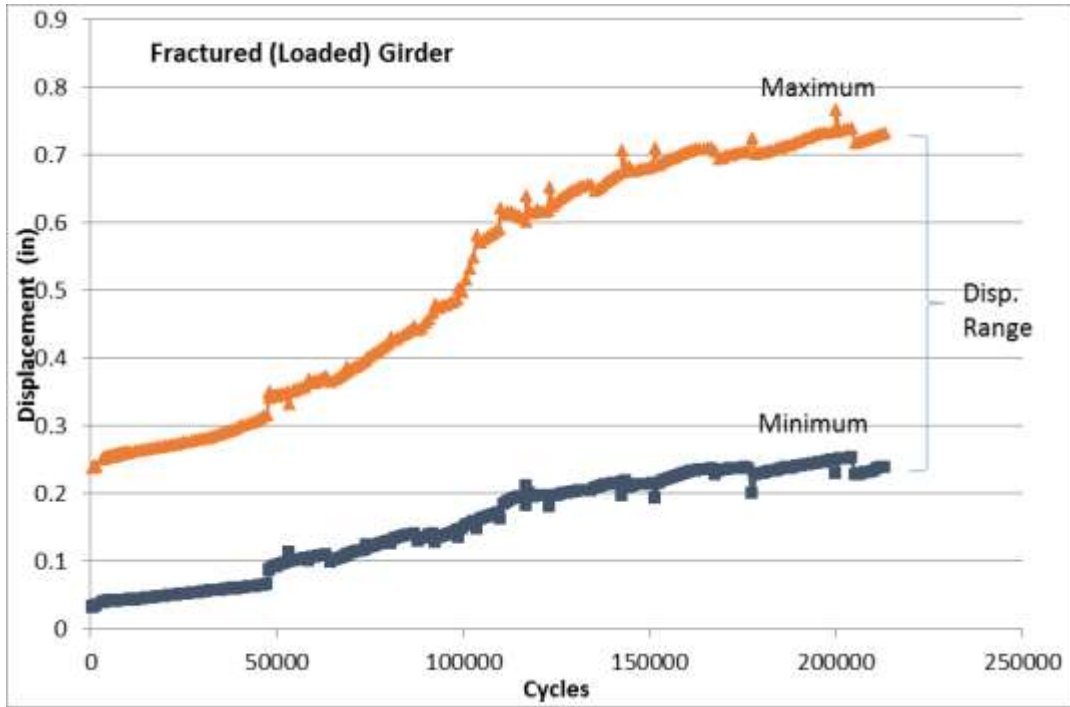


Figure 4-12 Mid-span displacement vs. number of loading cycles in the fractured girder.

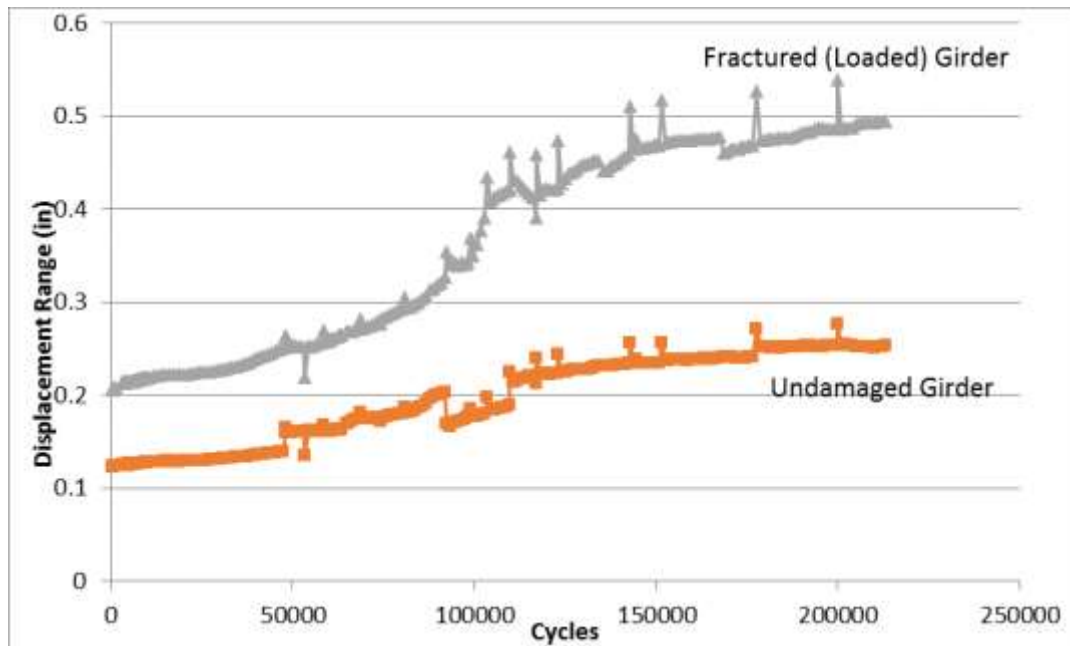
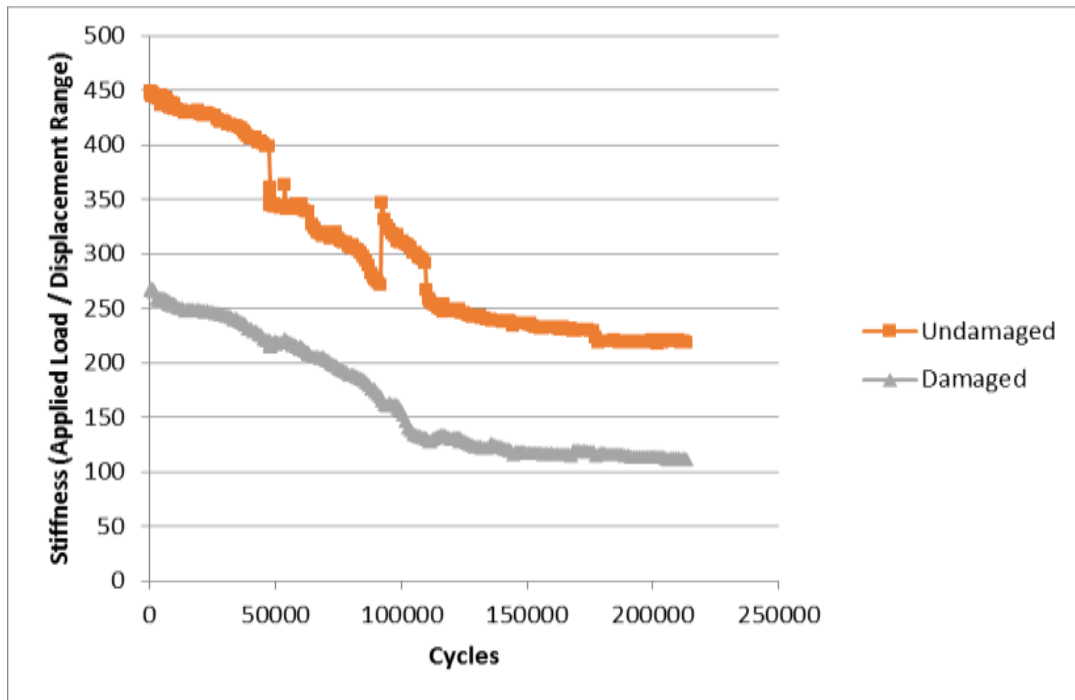


Figure 4-13 Displacement range (max – min) vs. number of loading cycles.

The stiffness of each girder over time is plotted in Figure 4-14. The stiffness of each girder is calculated by dividing the applied load by the displacement range in each cycle. Since the applied load for each cycle was constant at 60 kips, the stiffness curve was shown inversely proportional to displacement range curve. The damaged girder had a stiffness of 260 kips/in at the beginning of the cyclic test when bottom flange fractured. The stiffness reduced 60%, to 105 kips/in, at the end of the test when the web was completely fractured. Similarly, the stiffness reduction, for the undamaged girder, was around 235 kips/in, which was equivalent to 52% of its initial stiffness.



**Figure 4-14 Stiffness of each girder during the cyclic test.**

The locations of strain gauges in each cross-frame brace are denoted as  $e1$ ,  $e2$ , and  $e3$  as shown in Figure 4-15a. The strain profile was assumed linear in each brace leg as illustrated in Figure 4-15b. The average axial strain in the angle cross-section can be calculated using the following equation:

$$e_{avg} = \frac{e_1}{4} + \frac{e_2}{2} + \frac{e_3}{4}$$

With that average axial strain, the axial force in a cross-frame brace can be calculated by multiplying the average axial strain by the cross-section area of the brace and steel Young's modulus. Then, the shear transfer force, or the vertical component of the axial force, can be calculated based on the cross-frame geometry.

Figure 4-16 shows the maximum shear transfer in one cross-frame with respect to the number of loading cycles. The maximum shear transfer in the cross-frame was found to have increased from 2.5 kips at the beginning to almost 6.5 kips when the web was completely fractured.

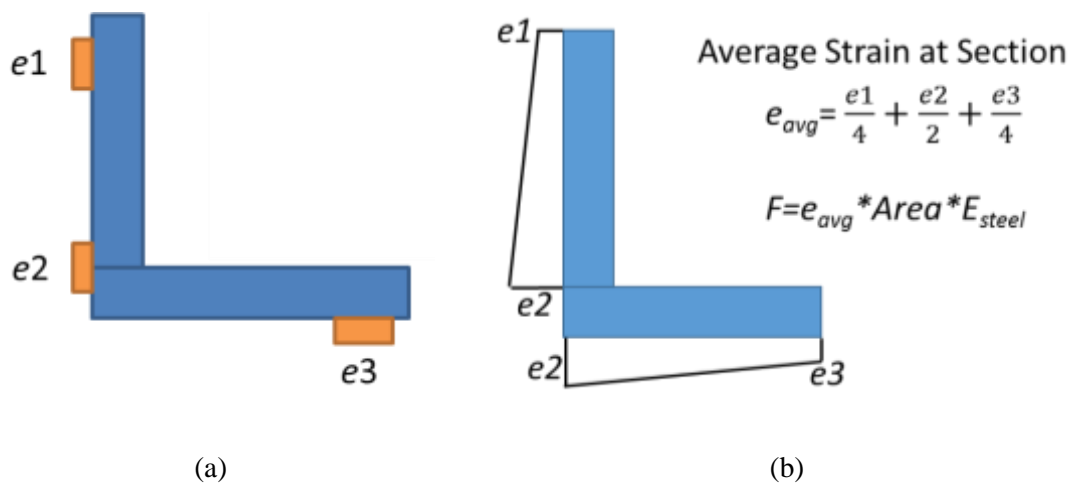


**Figure 4-15 (a) Strain locations and (b) Strain profile in each cross-frame brace.**

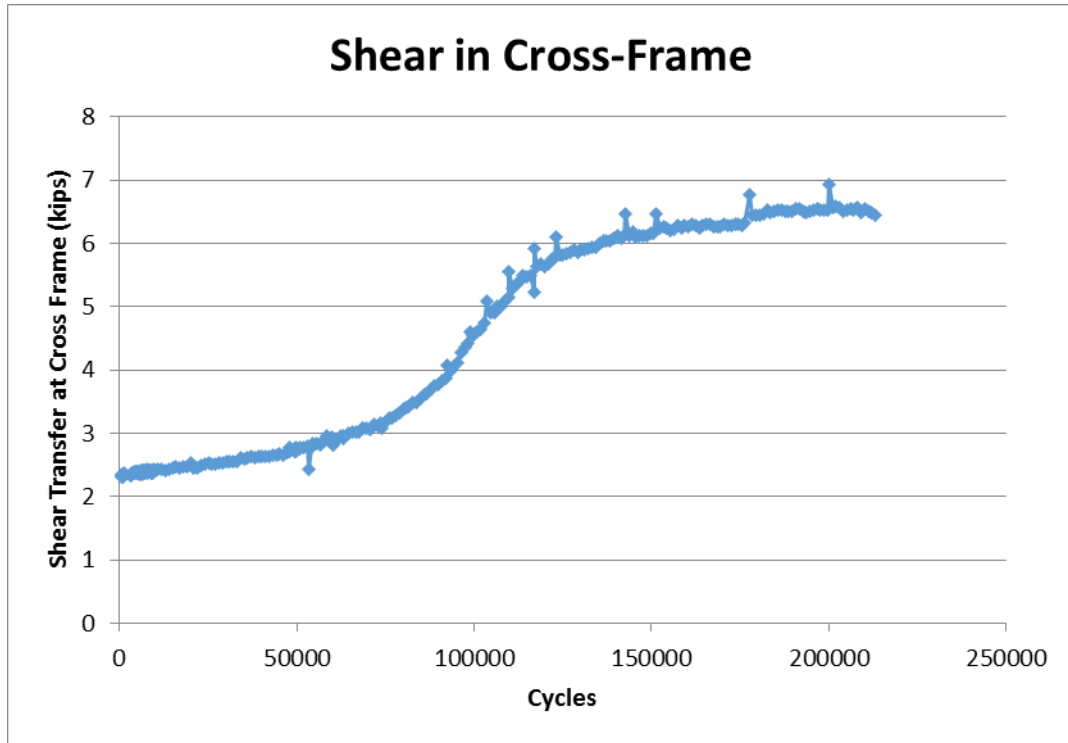


**Figure 4-16 Maximum shear transfer in one cross-frame.**

In general, as the crack length grew into the webs, the stiffness of the specimen decreased. It led to an increase in the crack opening at the base, the girder displacements, the displacement range as well as the cross-frame transfer force. It is important to note that all of these behaviors, when plotted versus the number of loading cycles, showed a similar pattern to that of the growth of crack length.

### 4.3 Ultimate Test A

In the ultimate load test A, the bridge specimen was tested under a full-web fracture damage condition, without rail system and continuity. The load was applied through a displacement-controlled hydraulic ram, over the damaged girder through a 2 in. x 9 in. x 36 in. loading pad placed at the mid-span location as illustrated in Figure 4-17.

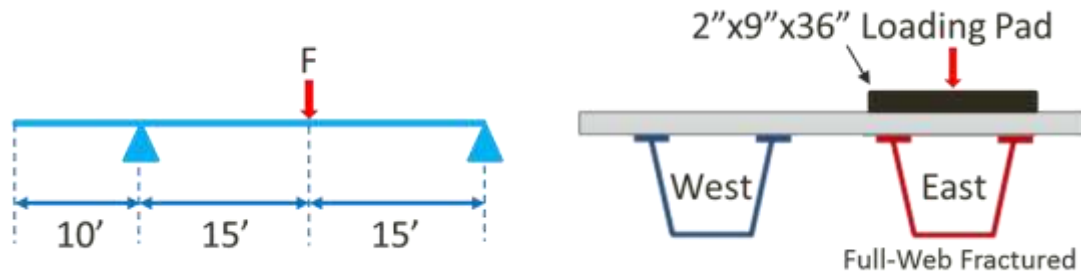


**Figure 4-17 Schematic description of Test A.**

### 4.3.1 Global Behavior

The overall responses during Test A are illustrated in Figure 4-18. Up to 60 kips of loading the bridge specimen showed a linearly elastic response with an initial stiffness of approximately 90 kips/in. As the load increased from 80 kips to 140 kips, some cracks in the deck were noticed and at the same time, the stiffness of the specimen was decreasing visibly. Twisting of the girders was observed as well. At the load of 140 kips, the capacity of the bridge slightly decreased by 1 kip because one bolt in the bottom connection of the cross-frame near mid-span was sheared. The intact girder started showing uplift at the cantilever support. The specimen reached its maximum capacity at 156 kips with 2.5 in. of displacement.

After reaching the maximum capacity of 156 kips, the concrete deck was crushed by the loading pad and the load dropped to 133 kips. The test continued and the specimen was still able to sustain some additional load with many ups and downs until it failed at 5.5 in. of displacement. These ups and downs in this loading period corresponded to several damages observed, including: 1) the visible cracking and crushing in concrete propagating toward the ends of specimen, 2) the bottom of the concrete deck between the two girders near mid-span spalling off, 3) the uplifting at the support and 4) the tear up of the deck at

both ends of intact girder. As seen in Figure 4-18, during this loading period, the load fluctuated and reached a local maximum load of 144 kips at 4-in. displacement. It, then, slowly dropped down to 123 kips at 5.5-in. displacement before the test was halted. This sequence of failure suggests that the bridge was trying to transfer the load to the intact girder through an alternative load path after the primary load path had failed. This load-transfer mechanism is discussed further in the following section.

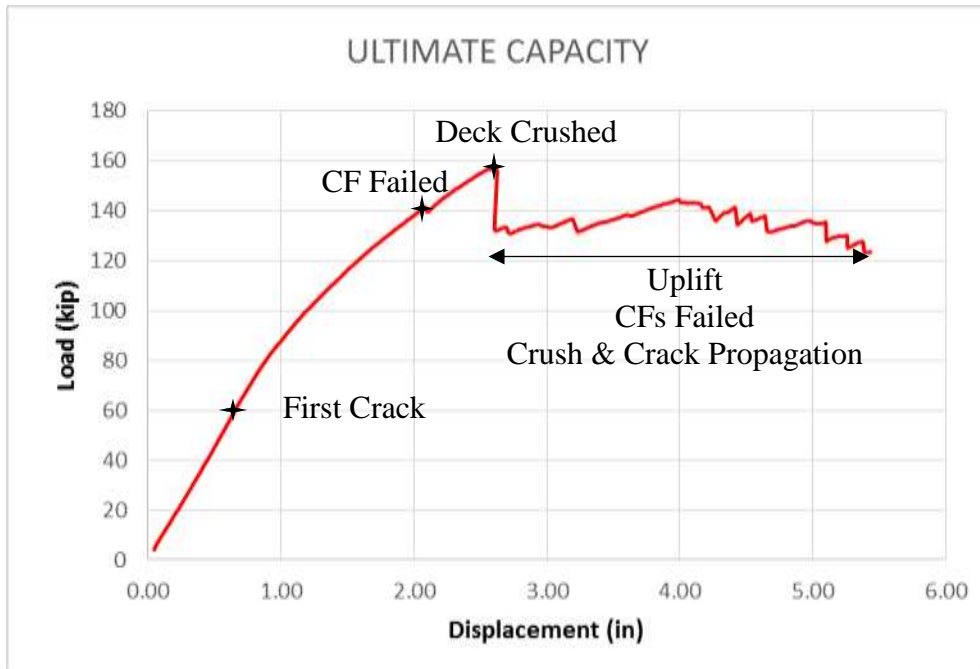


**Figure 4-18 Load vs. deflection curve of the specimen during ultimate load Test A.**

A 1 ft by 1 ft grid was marked on the concrete surface to map the damage area more accurately as illustrated in Figure 4-19. In general, the major damage was observed in the deck over an area of 5 ft long by 3 ft wide at where the load was applied. Cracking started along the inside top flange of the damaged girder, then it propagated toward the intact girder. The cracking pattern was approximated by the black lines in Figure 4-19. This cracking pattern indicates that the deck failed predominantly in one-way shear failure mode. The deck damage showed that the damage propagated toward the north support more

than the south support. It could be due to the presence of the cantilever portion in the south end. This cantilever made the south portion of the specimen measured from the loading point was stiffer than the north portion of the specimen. Eventually, the deck was punched by the loading pad along the inside top flange of the damaged girder when the specimen reached its maximum capacity. The spalling of concrete in the bottom of the deck is illustrated in Figure 4-20.



**Figure 4-19 Punching in the top of the concrete surface looking to South.**





**Figure 4-20 Punching in the bottom of the deck.**

The concrete deck was also damaged at both ends of the specimen. The mechanism for the observed failure can be explained by considering the hypothetical situation in which the deck is cut longitudinally between the girders leaving two separate and independent structures. The east structure is then damaged and the load point is displaced downward the same magnitude as produced in the actual test. Obviously, the magnitude of load causing this displacement will be much less than what observed in test. Due to the low flexural capacity at the damage location, the displaced shape will essentially be a mechanism with hinge rotation about the load point and linear segments to the supports. It is important to note how the ends of the girder will now project above the supports and that the undamaged girder has no load applied and is therefore straight and level. Finally, keeping the load point of the damaged girder at the fixed level of displacement, consider the forces required to re-join the two separate structures and fuse the deck back together. At the ends of the girder, the (hypothetical) damaged girder will be above the undamaged one and need to be pulled downward, which then imparts an equal and opposite upward force on the undamaged girder. The effects of this transverse shear can be clearly seen in

Figure 4-21 where the deck above the undamaged girder appears to have been pulled upwards and seemingly ripped off at the ends.

This same hypothetical situation can be used to examine the failure mechanism near the load point. In this region, the (hypothetical) damaged girder will be below the undamaged. Since the displacement level is being held by the loading beam, the undamaged girder will be pulled downward when the two separate structures are hypothetically re-joined. The effect of the resulting shear force can be seen in Figure 4-20.

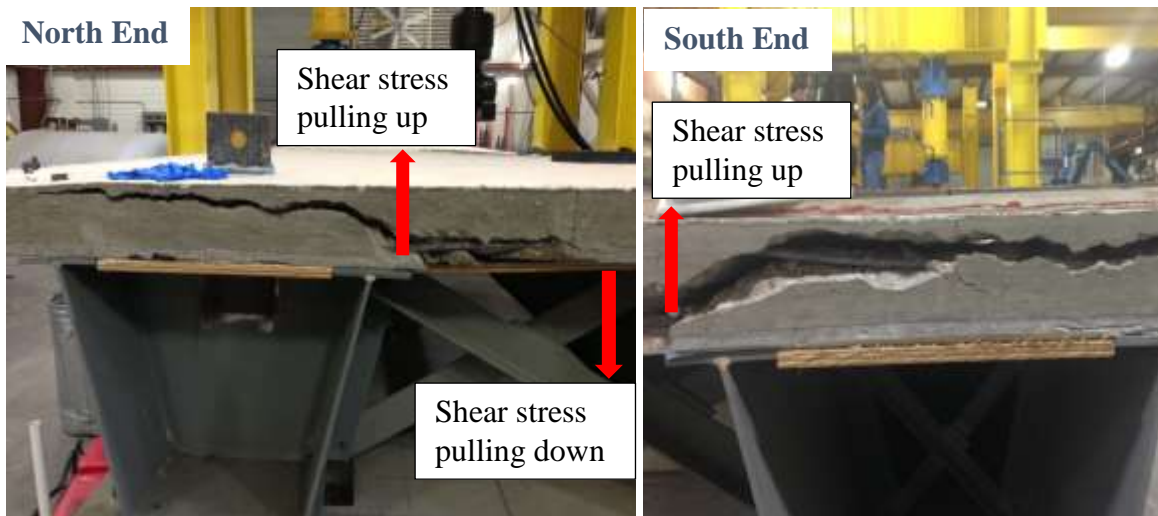


**Figure 4-21 Damage at North end (left) and South end (right).**

Another important behavior observed was the uplift at supports of the intact girder. Displacements near the supports were monitored at location 1 (14 in. from the bearing line of the South support) and location 2 (17 in. from the north end of steel box girders) as depicted in Figure 4-22. Figure 4-23 and Figure 4-24 plot the vertical displacements at these two locations. These plots show that the intact girder (or the West Girder) began to uplift at the south support shortly at 100 kips before the specimen reached its maximum capacity of 156 kips while the north support was uplifted just right after the maximum

capacity was reached. The final uplifts were measured as 0.48 in. near the south support and 0.11 in. near the north support.



Figure 4-22 Location of potentiometers at supports.

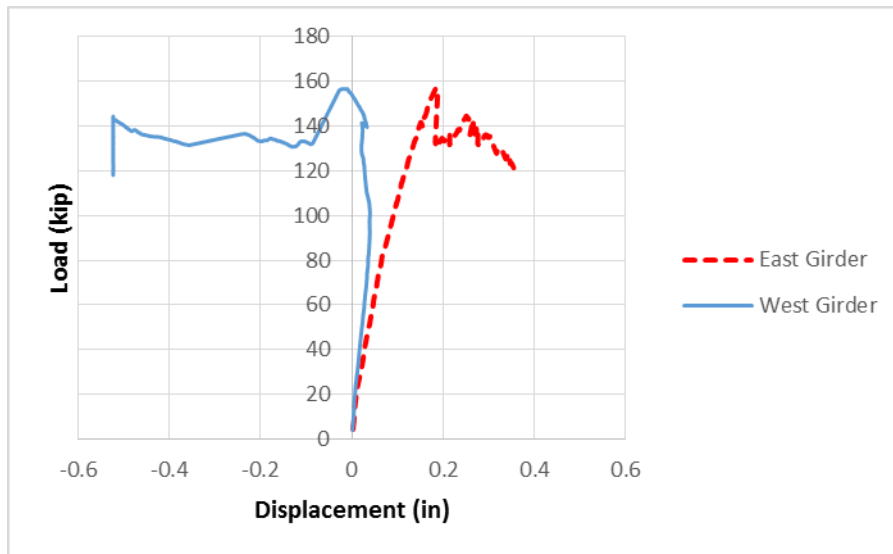
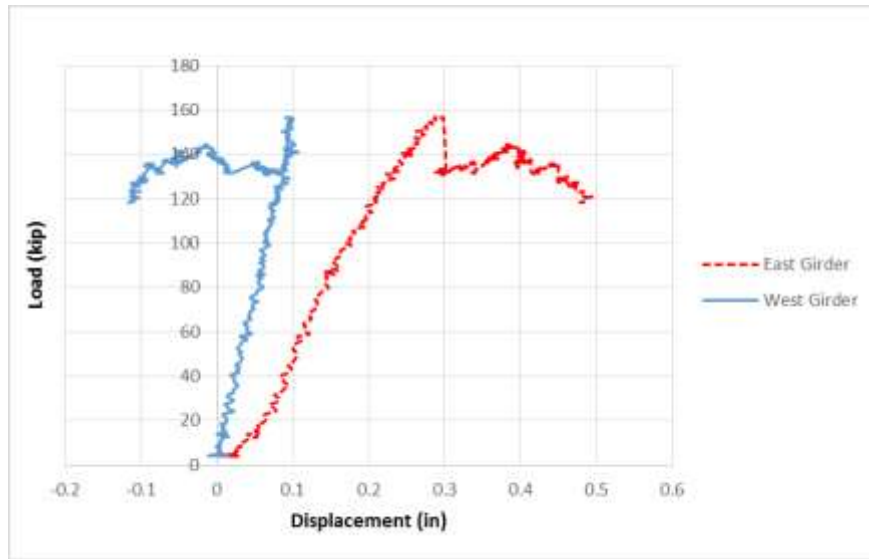


Figure 4-23 Displacement of the both girders near the south support.



**Figure 4-24 Displacement of the both girders near the north support.**



(a) North support

(b) South support

**Figure 4-25 Uplift at (a) north support and (b) south support.**

### 4.3.2 Local Behavior

It is important to note that responses of the reinforcements and the deck were only monitored at the mid-span section. All of the strain gauges at the mid-span section are provided again in Figure 4-26. Some of these strain gauges were damaged after the maximum load capacity was reached; therefore, their data will be omitted. Following are assumptions regarding the direction of the strain gauges and material properties of steel plates.

- Sign Convention:

Positive longitudinal strain: the member is in tension.

Negative longitudinal strain: the member is in compression.

Positive transverse strain: the member is in tension.

Negative transverse strain: the member is in compression.

\* Note that the directions of measured strains that are mentioned in this report are with respect to the global coordinate system.

- Material Properties:

Yield stress for the reinforcement bars: 60 ksi.

Yield strain for the reinforcement bars:  $60 \text{ ksi} / 29,000 \text{ ksi} * 10^6 = 2,070 \text{ } \mu\epsilon$ .

Yield stress for the steel: 50 ksi.

Yield strain for the steel:  $50 \text{ ksi} / 29,000 \text{ ksi} * 10^6 = 172 \text{ } \mu\epsilon$ .

It is noted that gauges 2TTD1, 2TTD2 and 2TTD3 were shifted away from the mid-span by 1 ft toward the south support to avoid contact with loading pads.

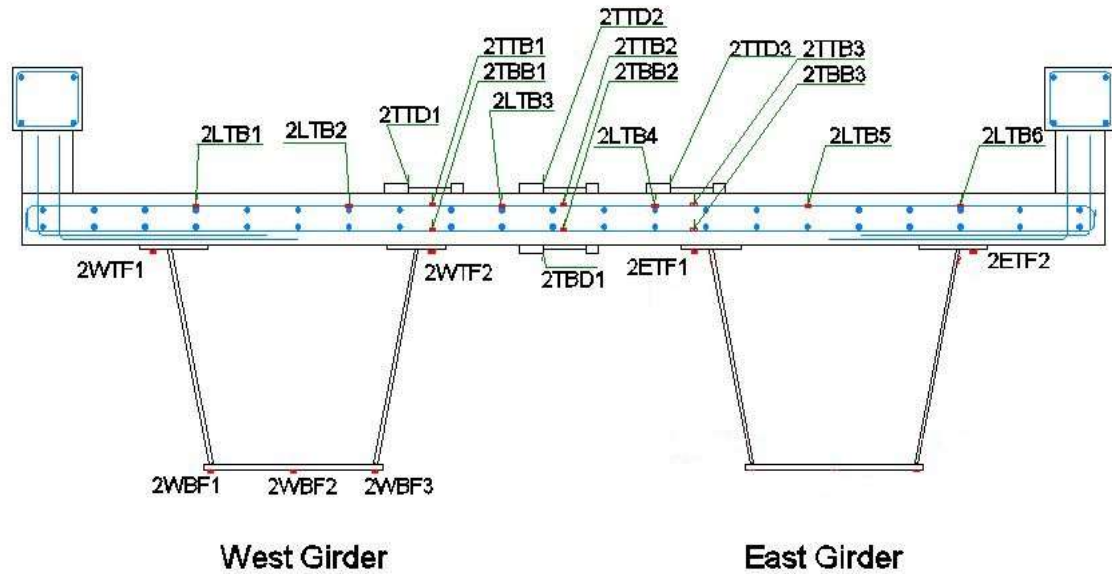


**Figure 4-26 Strain gauges at the mid-span section.**

Figure 4-27 shows longitudinal strains in the intact girders at the mid-span. The intact girder (WG) had the top flanges in compression and the bottom flange in tension. That all of the longitudinal strains were linear and the maximum strain was approximately  $1300 \mu\epsilon$  indicated that the intact girder was still in the elastic range. The longitudinal strains in the bottom flange of the intact girder within 5 ft distance from the mid-span is plotted in Figure 4-28. The similarity in the bottom flange longitudinal strains indicated that the load was distributed uniformly within 5 ft distance from the mid-span. The comparison of the intact girder and damaged girder at Section 5 (5 ft away from the mid-span), as illustrated in Figure 4-29, showed that the damaged girder had its top flange in tension and its bottom flange in compression while the intact girder had its top flange in compression and its bottom flange in tension. This indicated that intact girder had concave-up deflection while the damaged girder had concave-down deflection.

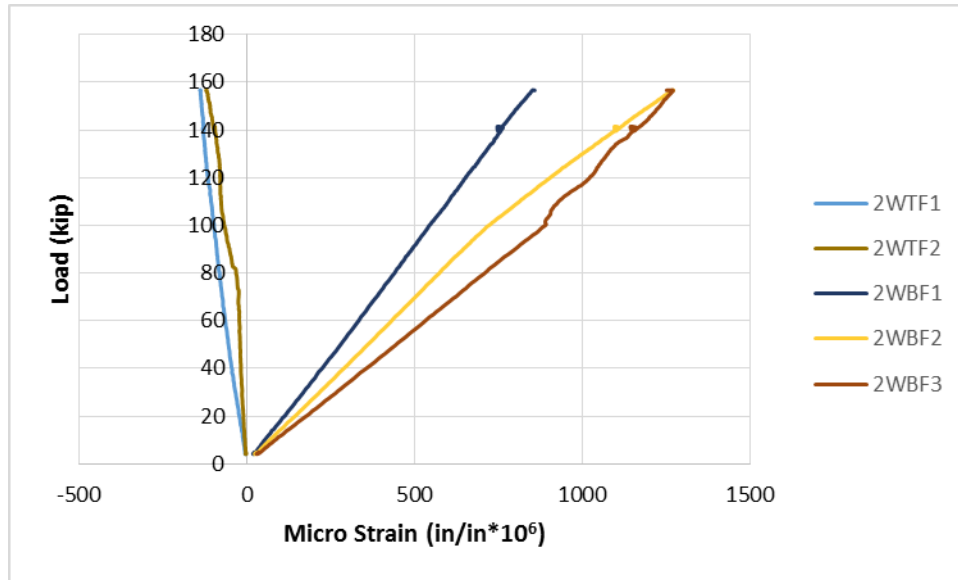


Figure 4-27 Longitudinal strain at the top and bottom flanges of the intact girder at mid-span.

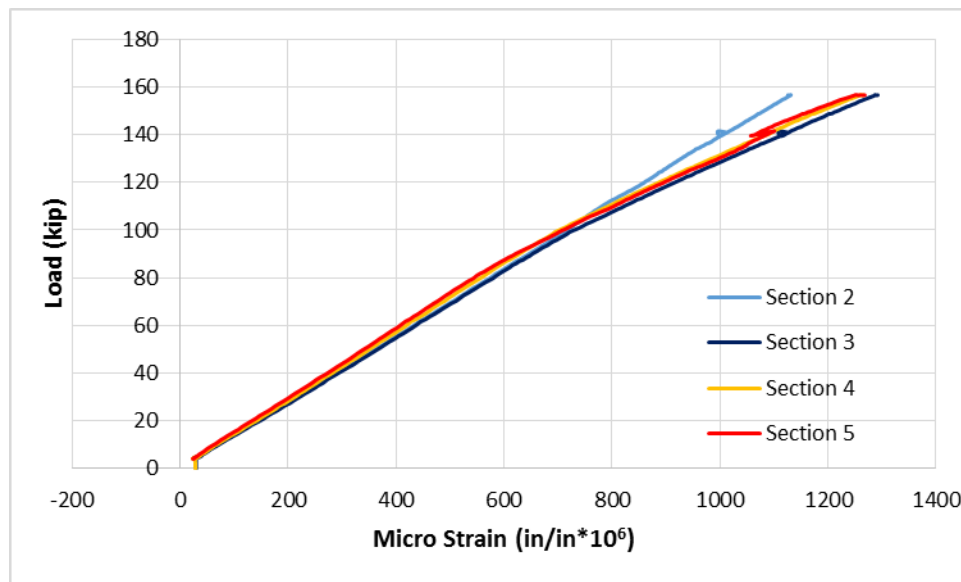
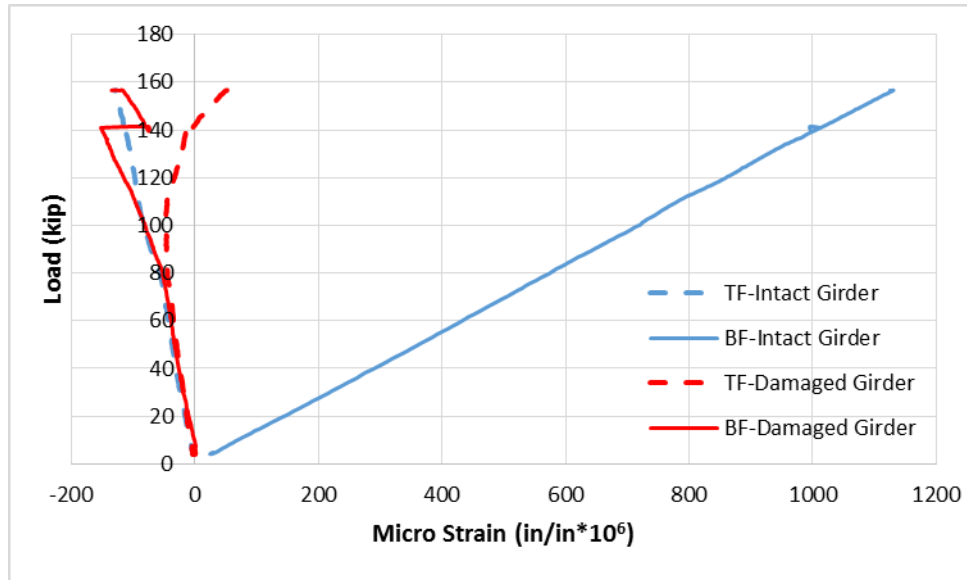


Figure 4-28 Longitudinal strain at the bottom flange of the intact girder.



**Figure 4-29 Comparison of longitudinal strains in the intact and damaged girders at Section 5.**

Responses in transverse rebars at mid-span were measured from six strain gauges 2TTB1, 2TBB1, 2TTB2, 2TBB2, 2TTB3 and 2TBB3 (see Figure 4-26 for their locations.) All of the strains in the transverse rebars were positive or in tension except at gauge 2TBB3, located near the damaged girder as illustrated in Figure 4-30. However, gauge 2TTB2, which was located at the center of the cross-section, had its strain fluctuating around zero. This suggests that the gauge 2TTB2 was an inflection point in the deflected shape of the cross-section. The plot also suggests that the strains at gauges 2TTB1 and 2TTB3 were much higher than that of other gauges. Gauge 2TTB1 had a strain of  $2600 \mu\epsilon$  suggesting the transverse re-bar yielded at this location, which is the inside top flange of the intact girder.



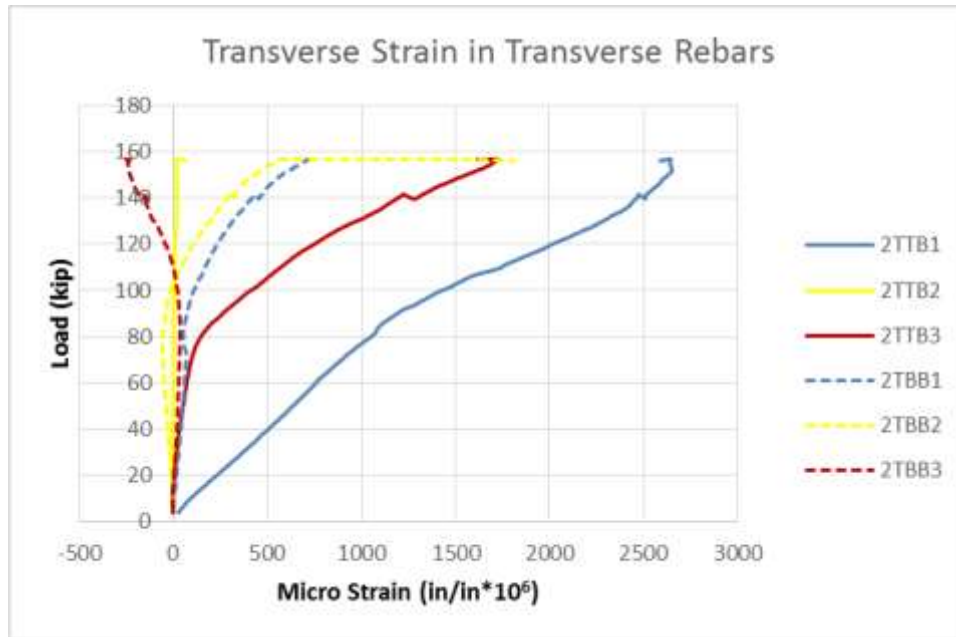


**Figure 4-30 Strains of the transverse rebar at mid-span.**

Responses in longitudinal top rebars from six strain gauges 2LTB1, 2LTB2, 2LTB3, 2LTB4, 2LTB5, 2LTB6 (see Figure 4-26 for their locations) are plotted in Figure 4-31. The strain gauge 2LTB3 data was exactly zero throughout the test suggesting this gauge was either broken or lost its connection. Two gauges, 2LTB1 and 2LTB2, located over the top of the intact girder, and gauge 2LTB4, located between two girders, had negative transverse strain while the other two 2LTB5 and 2LTB6 located over the top of the damaged girder had positive strains. This suggests the deck changed its deflected shape from concave up to concave down at a location somewhere between gauges 2LTB4 and 2LTB5.

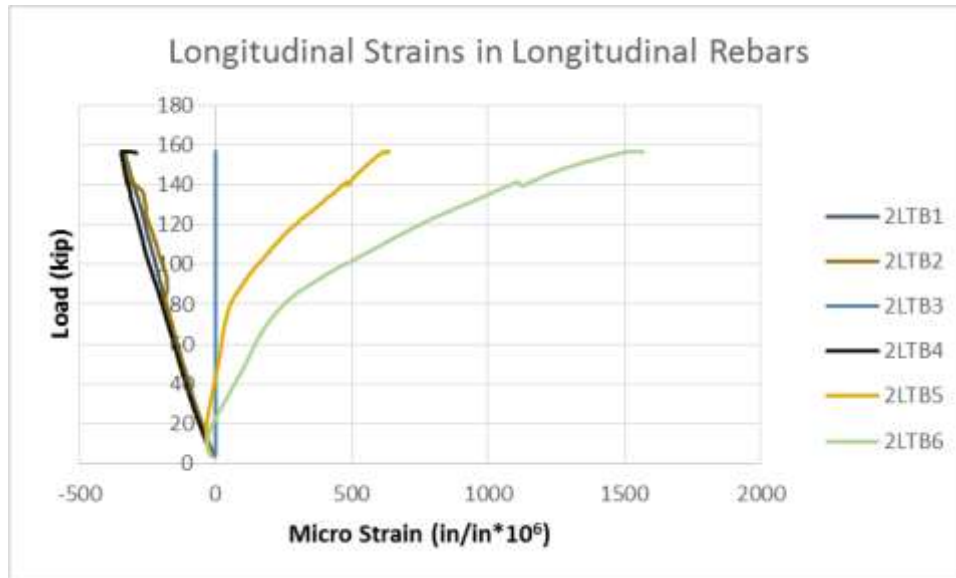


**Figure 4-31 Longitudinal strain of rebars in longitudinal direction at mid-span.**

Figure 4-32 showed the deck experienced positive transverse strains at location of 2TTD1, 2TTD2, and 2TBD1; and negative strain at location 2TTD3. This suggests that the top of deck was in compression at location 2TTD3, right on the top of the inside top flange of the damaged girder, while the other gauges showed the deck was in tension, which further suggests the inflection point of the deflected curve of the deck cross-section was somewhere close to the top flange of the damaged girder. This observation was consistent with data obtained from transverse and longitudinal reinforcement bars.

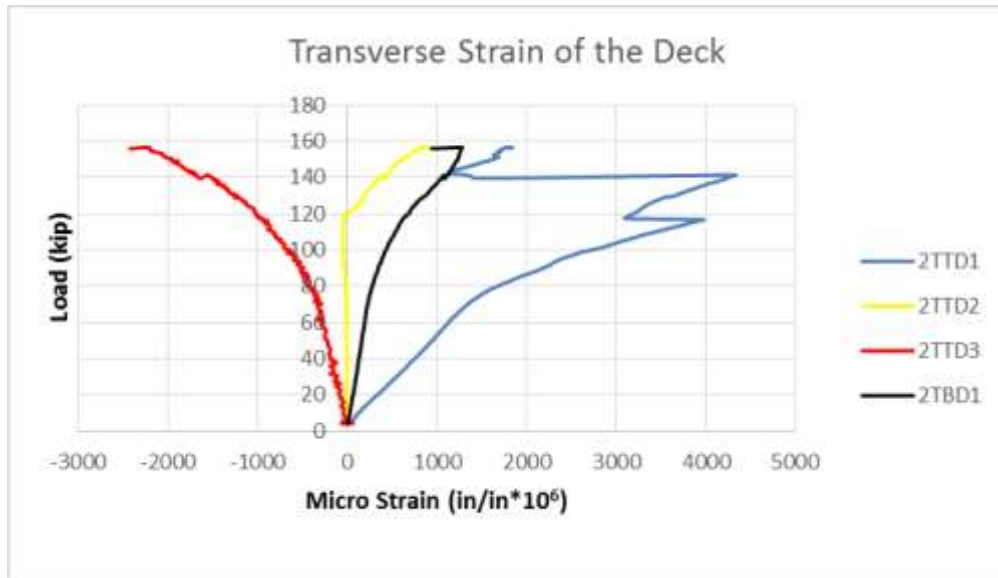


Figure 4-32 Transverse strain at the top and bottom of deck at mid-span.

### 4.3.3 Load-Transferring Mechanism

Based on the collected data, a major portion of the applied load was transferred directly, in transverse direction, to the intact girder mainly through the deck before the maximum capacity of the specimen was reached. After that, the concrete deck was punched by the loading pad, and the applied load was redistributed through a secondary load path. In this second load path, the cross-frames were found to be involved more actively than they had before. As illustrated in Figure 4-33b, the shear transfer capacity of one cross-frame increased and also at a faster rate. This explains why most cross-frame connections failed during this loading period, after the deck was punched by the loading pad. At the end of the test, every single external cross-frame was found to have at least one bolt connection broken. The locations of all broken cross-frame connections are illustrated in Figure 4-33a.

Since the deck and external cross-frames were found to be two major components that transferred the load from damaged girder to undamaged girder, it is interesting to quantify how much load was transferred through these components. It is important to note that there were only two external cross-frames in the main span of the specimen. Each of them is located 5 ft away from the mid-span. Figure 4-33b shows the amount of shear force transferred (vertical direction) in one external cross-frame. The shear transferred through this cross-frame only plotted until the maximum capacity of the specimen was obtained. The first shear drop was approximately 3 kips at 2.1-in. displacement with 140 kips of applied load, and it was due to the failure of bottom connection of the tension brace. It should be noted that even though the capacity of the cross-frame dropped 3 kips, the capacity of the specimen decreased only 1 kip as seen in Figure 4-18. The difference could be due to the fact that the calculated shear drop of 3 kips was based on the assumption that the strain profile was linear along each brace as shown in Figure 4-15b. It should be noted that after one connection failed, this cross-frame should have lost its load-resisting capability completely. However, the welded connection between two L-angle braces as shown by the red dot in Figure 4-33a enabled this tension brace to continue carrying more forces until another failure in the bottom connection of the compression brace. Therefore, after the failure of the first connection in the tension brace, the data in cross-frames were no more unreliable.

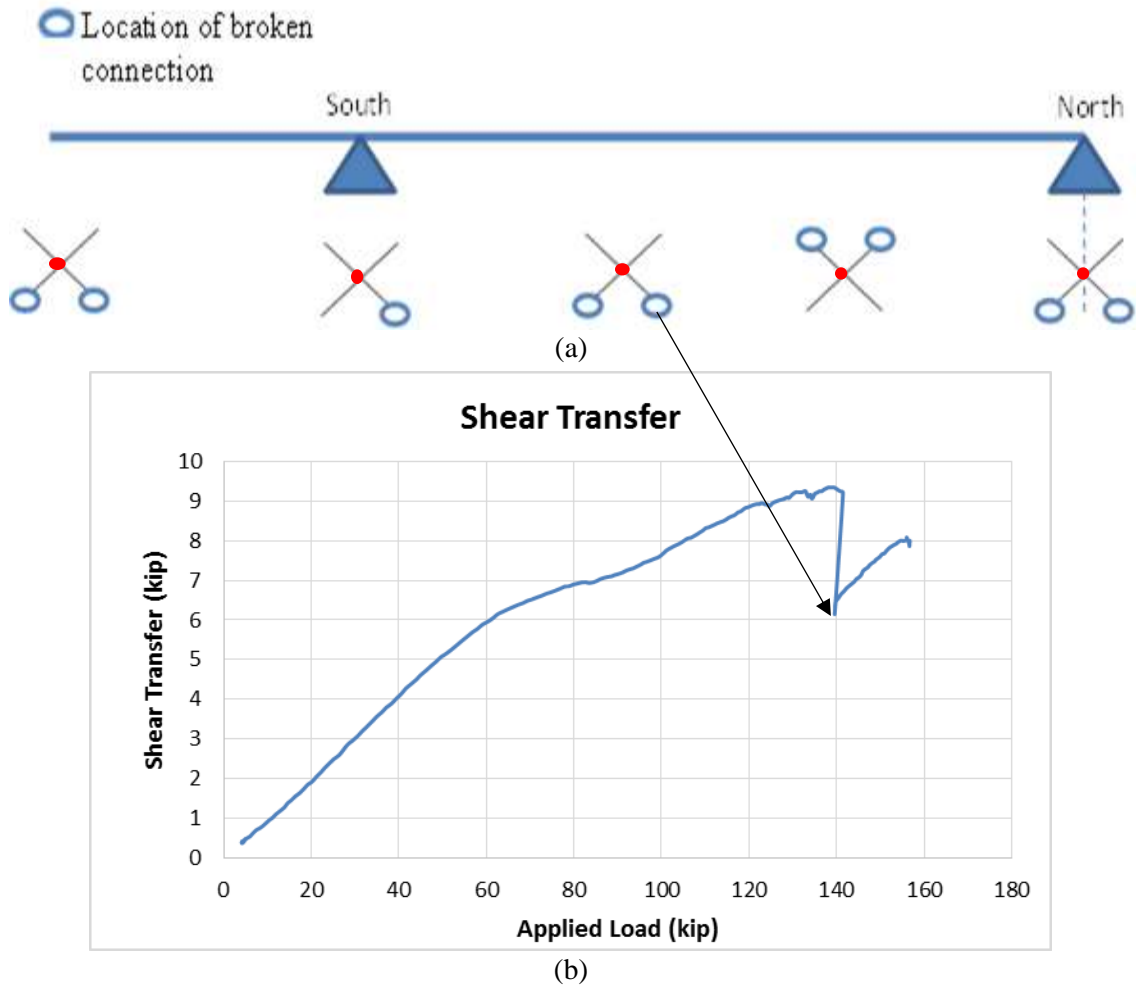


Figure 4-33 Shear transferred through one cross-frame in Test A.

#### 4.4 Reconstruction of Bridge Specimen

As illustrated in Test A, recorded strains in the steel box girders indicated that these girders were still in a good condition. Therefore, these girders were retained so that a new specimen can be reconstructed by casting a new deck for additional ultimate load tests. For that reason, only the deck was demolished and reinforcements were removed. After detaching the steel box girders from the deck, a thorough inspection showed only the top flanges of fractured girder at fracture location experienced severe damage which had been

already expected, and this damage almost cut the damaged girder into halves as illustrated in Figure 4-34.



**Figure 4-34 Damage in (a) the inner top flange, (b) the outer top flange of the damaged girder.**

Eventually, it was decided that this damaged girder should be cut into two halves to make the reconstruction of the specimen easier. The results of FEAs showed that the effect of having the damaged girder cut completely into two separate pieces is negligible. However, misalignment of two fractured segments, as shown in Figure 4-35a, brought up some difficulties during the reconstruction process. In order to fix it, the bolts connecting the external cross-frames were loosened, and then the slop in the bolt holes were used to shift the girder segments into better alignment. Then the cross-frame bolts were tightened up again. Finally, scab plates were used to bring these two segments closer as much as possible. Figure 4-35b illustrates the damaged girder with the welded scab plates. Please note that once the deck was cast, these scab plates were removed. After aligning the fractured segments, the new specimen was reconstructed as it had been previously. Figure 4-36 shows the complete specimen after the reconstruction.



(a) Before aligned



(b) After aligned

**Figure 4-35 Alignment of two fractured segments.**



**Figure 4-36 The reconstructed specimen before (left) and after casting (right).**

## 4.5 Ultimate Test B

In this test, the specimen was tested with the same loaded area as it was in Test A, except the loading was now moved over the intact girder as illustrated in Figure 4-37. In this test, the specimen was loaded until the plateau in load-deflection curve was observed without any failure. The purpose of this test to examine the behavior and verify the capacity and behavior of the intact girder.

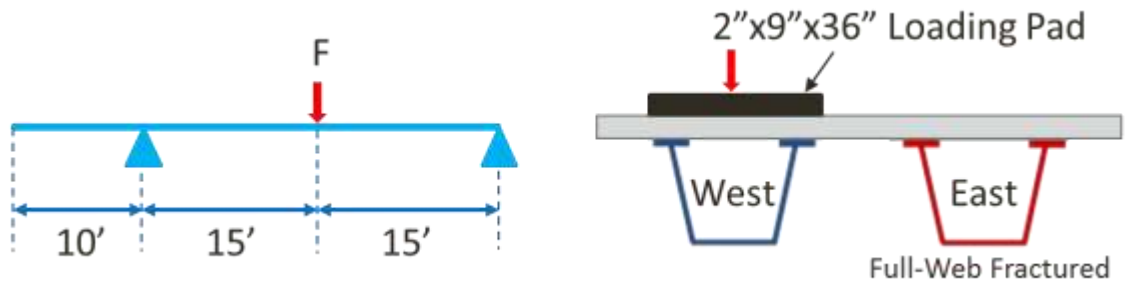


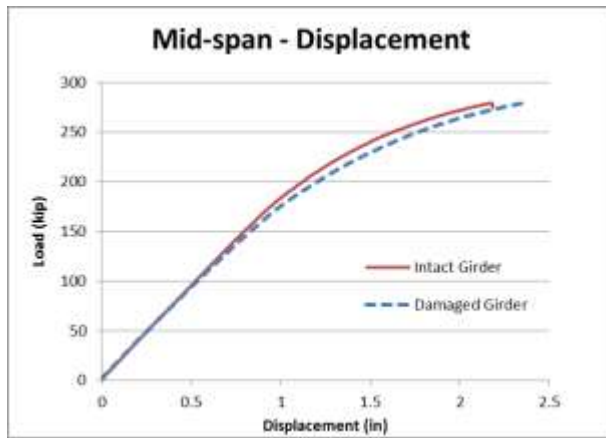
Figure 4-37 Schematic description of Test B.

### 4.5.1 Global Behavior

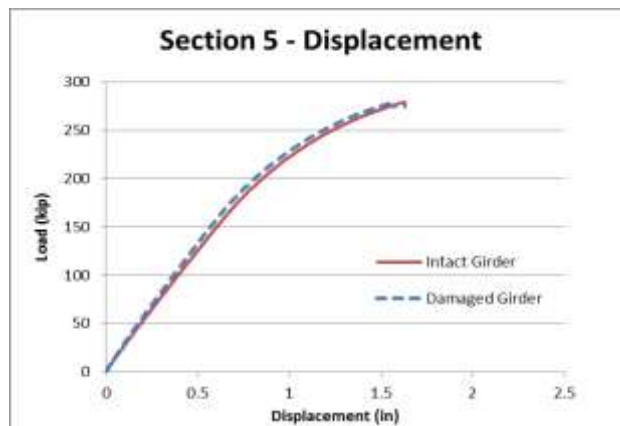
The specimen was loaded up to approximately 270 kips in which the nonlinear plateau of load-deflection curve was observed. This load-deflection curve, which is illustrated in Figure 4-38a, shows the specimen responded linearly up to 150 kips of load with 0.82 in. of displacement before the system stiffness started decreasing. The initial stiffness of the specimen was approximately 200 kips/in. There was no significantly visible damage observed during this test. However, the deck showed some minor cracks around loading pads. The longitudinal strains measured at mid-span indicated that the intact girder has yielded and permanent deformation was observed after unloading.



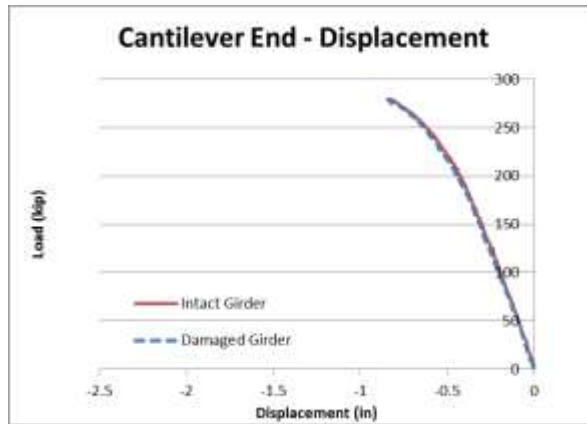
Figure 4-38 shows that the specimen displaced uniformly across its cross-section as well as along the length of the specimen. The average displacements were 2.25 in. at mid-span, 1.63 in. at Section 5, and 1.71 in. at cantilever end. Both girders experienced downward displacements at near supports as illustrated in Figure 4-39 and this was consistent with the observation which no up-lift occurred during the test. Shear force in one cross-frame is plotted in Figure 4-40. This indicates the shear transferred from the undamaged girder to the damaged girder was less than 1 kip. That negligible shear force in cross-frame, plus the nearly identical displacement across the cross-section indicates that the contribution of damaged girder the load-resisting capacity of the specimen under this loading configuration wasn't significant. This suggests that the capacity, obtained in this test, should be similar to the plastic capacity of the composite section of the undamaged bridge. As shown in Section 3.1.1, the plastic moment capacity of cross-section is found to be 1789 kips-ft. This indicates the maximum capacity of the section under a concentrated load at mid-span is 239 kips using the formula,  $P=M_n \times 4/L$ . A similar prediction was achieved by FEA of single undamaged girder bridge with 245 kips of load. This hand calculation and finite element predictions were in good agreement with the capacity of the specimen obtained from this test which was 270 kips. The small difference could be attributed to the fact that the compressive strength of concrete was assumed to be 4.5 ksi for design purposes while the actual value was found to be 7.2 ksi. Another reason was because the load was assumed to be concentrated at one single point in the hand calculation while it was not in the actual test.



(a)

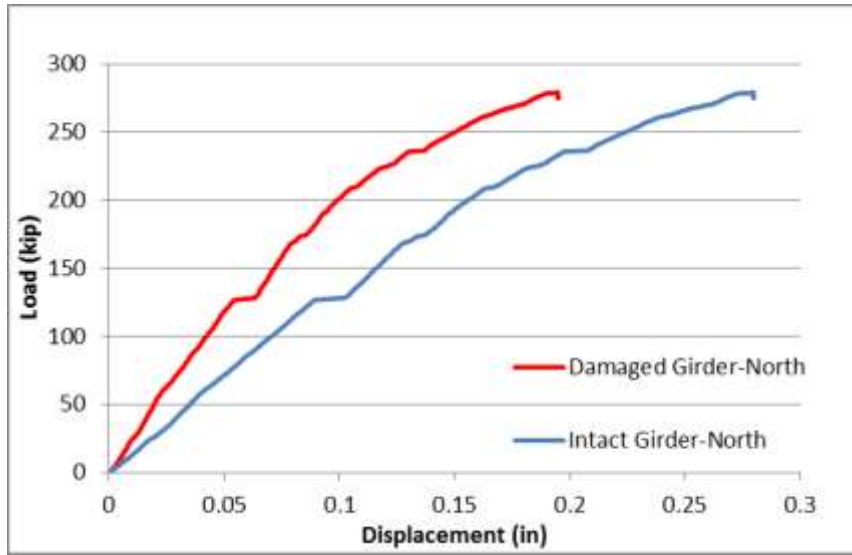


(b)

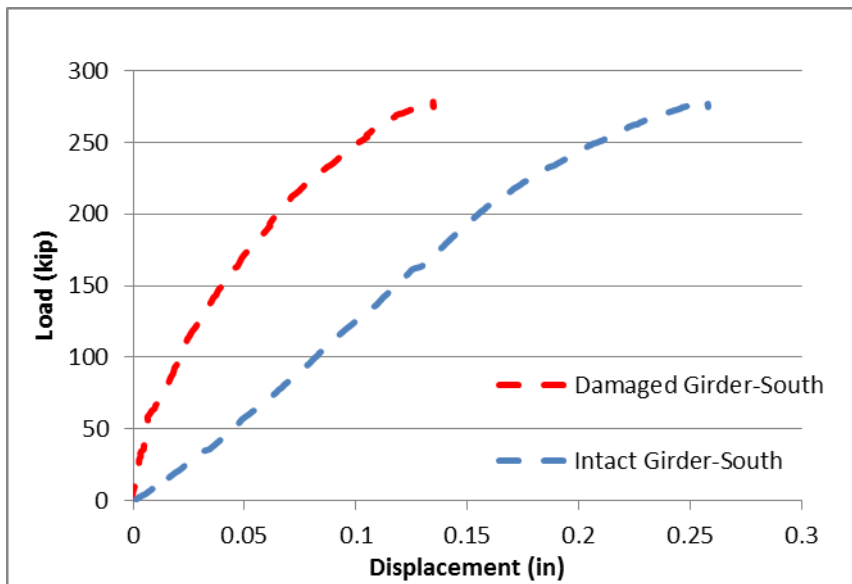


(c)

Figure 4-38 Test B: Load vs. displacement curves at (a) mid-span, (b) Section 5 and (c) cantilever end.



(a)



(b)

Figure 4-39 Displacements at (a) north support and (b) south support.

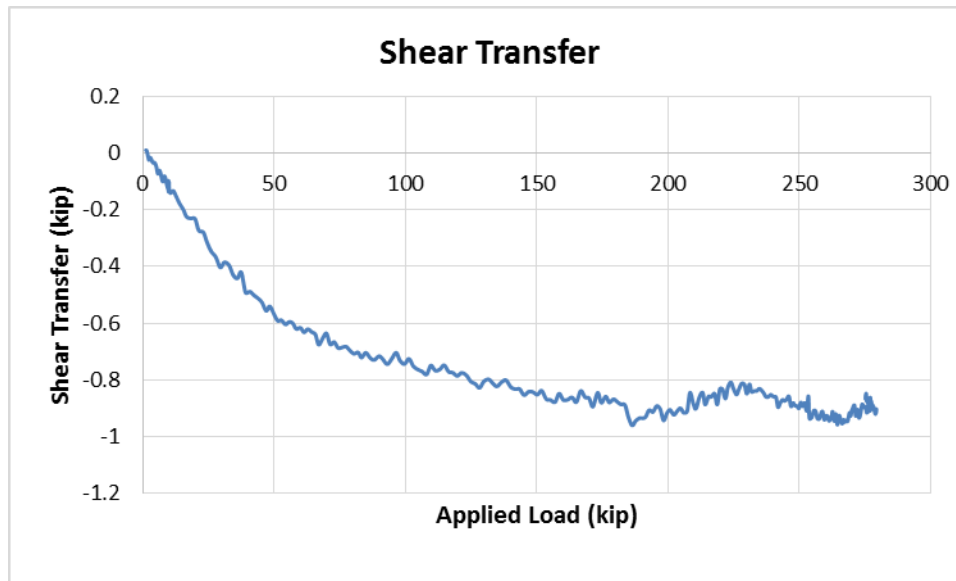


Figure 4-40 Shear transferred through a cross-frame in Test B.

#### 4.5.2 Local Behavior

The summary of longitudinal strains at the bottom flange and top flanges of the undamaged girder (WG) along the length of the bridge are summarized in Figure 4-41 and Figure 4-42. The bottom flange strain was computed by taking average of strains at gauges 2WBF1, 2WBF2 and 2WBF3 while the average strain in top flanges was computed by taking an average of the strains measured at gauges 2WTF1 and 2WTF2. As expected, the bottom flange strain was highest at Section 2 with  $7700 \mu\epsilon$  and lowest at Section 5 with  $1880 \mu\epsilon$ . The strain in top flanges was small at mid-span, indicating the location of the plastic neutral axis was somewhere in the top flanges. This location is in a good agreement with hand calculation of the plastic neutral axis as computed earlier in Section 3.1.1.

A comparison of longitudinal strains of both girders at Section 5 is plotted in Figure 4-43. Top flanges experienced  $-112 \mu\epsilon$  and  $-57 \mu\epsilon$  on average in the intact girder and

damaged girder, respectively. The average strain at the bottom flange of the intact girder was 1880  $\mu\epsilon$ , and it was 135  $\mu\epsilon$  for the damaged girder. This suggests that some of the applied load was transferred to the damaged girder, but not that significant. Because the cross-frame force was found to be less 1 kip of load as shown previously in Figure 4-40, if some load was transferred to the damaged girder, it was mainly transferred through the deck.

The longitudinal strains measured at the top reinforcements at mid-span are shown in Figure 4-44. These gauges are located approximately 1.5 in. below the top of the deck. Gauges 2LTB1, 2LTB2, 2LTB3, and 2LTB4 are negative while gauges 2LTB5 and 2LTB6 are positive. This indicates the deck would change its deflection from concave up to concave down somewhere between gauge 2LTB4 and 2LTB5, close to the inside top flange of the damaged girder.

Figure 4-45 shows responses of top and bottom transverse reinforcements at mid-span. Gauges 2TTB1 and 2TBB1, located over the interior top flange of undamaged girder, had strains of 252  $\mu\epsilon$  and 1590  $\mu\epsilon$ , respectively. Gauges 2TTB2 and 2TBB2, located at center of the deck, between two girders, had maximum strain at 24  $\mu\epsilon$  and 40  $\mu\epsilon$ , respectively. Lastly, gauges 2TTB3 and 2TBB3 are located over the interior top flange of damaged girder showed strain values of 16  $\mu\epsilon$  and -142  $\mu\epsilon$ . The strain data in the bottom transverse reinforcement changing from 1590  $\mu\epsilon$  to 40  $\mu\epsilon$  to -142  $\mu\epsilon$  indicates that the deck had changed its transverse deflection shape from concave up to concave down. This was consistent with the conclusion obtained from the strain data of the longitudinal reinforcements. A schematic drawing showing how the specimen deflected at mid-span is illustrated in Figure 4-46.

Cracking of the deck was recorded with three crack gauges at the top of the deck and one at the bottom face. Figure 4-47 shows that the gauge 2TTD1 experienced significantly higher strain than the others, which indicates that the cracking is largest at this location. Only gauge 2TBD1 at center bottom of the deck experienced negative value which mean the deck is in compression.

Overall, the data suggest that the specimen in this test would be likely to fail in a flexural mode. The load-carrying capacity found in this test was in a good agreement with the maximum capacity of the intact girder that was computed by hand calculation and FEA. Again the results also indicate that the contribution of the damaged girder to global behavior of the system was negligible. Lastly, if the deck was assumed to crack at  $\epsilon = 160 \mu\epsilon$  ( $f_R = 600$  psi with  $E=3,800$  ksi), strain data from longitudinal and transverse reinforcements indicated that the deck might have been cracked at several locations at mid-span. These minor cracks in the deck were also observed after the test.

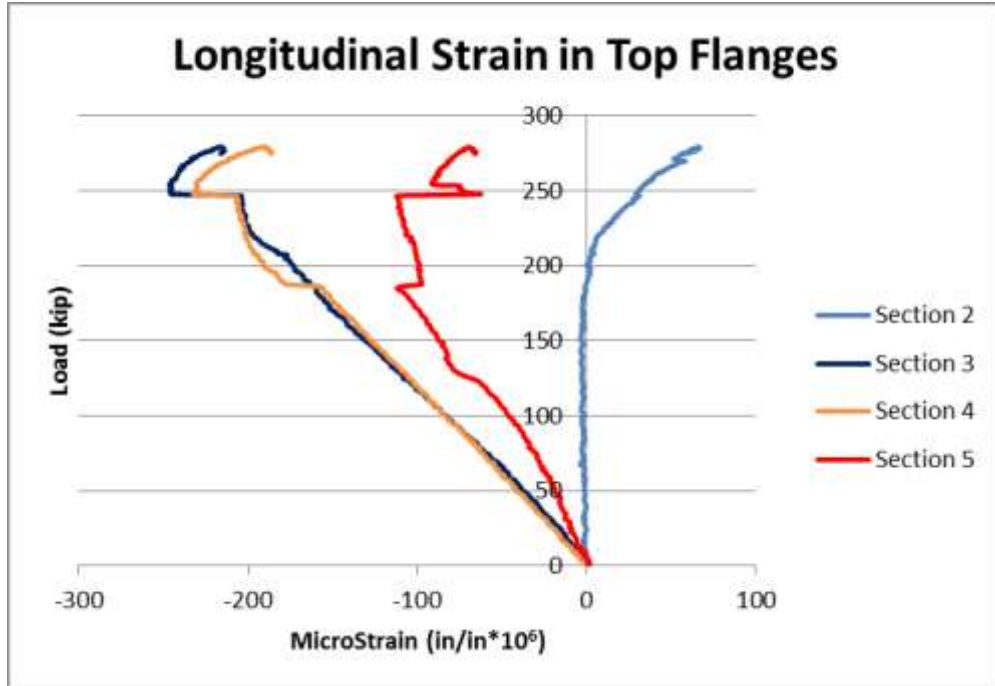


Figure 4-41 Average longitudinal strains at top flanges of the intact girder.

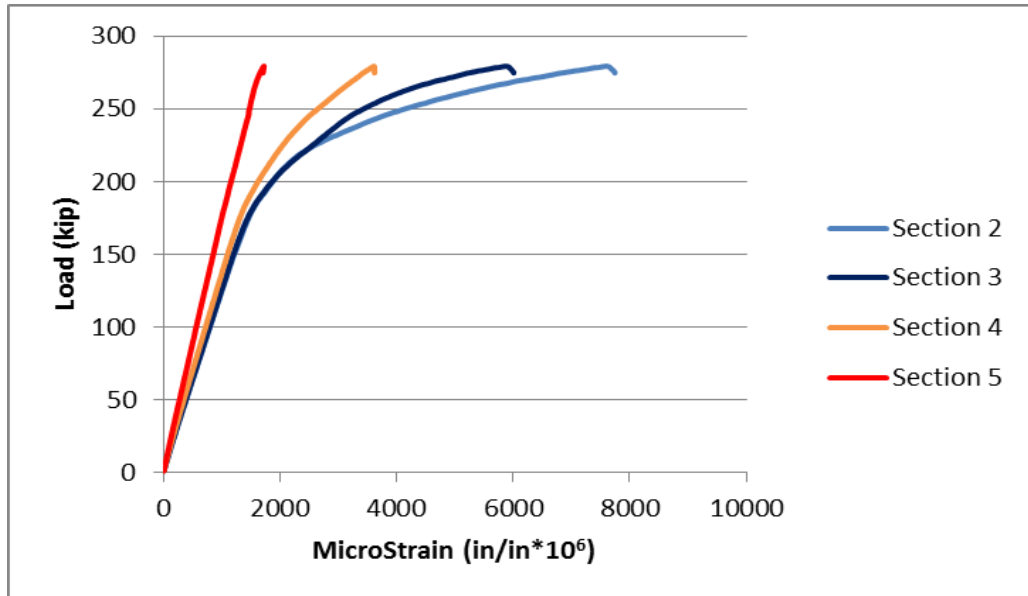


Figure 4-42 Longitudinal strains at the bottom flange of the intact girder.

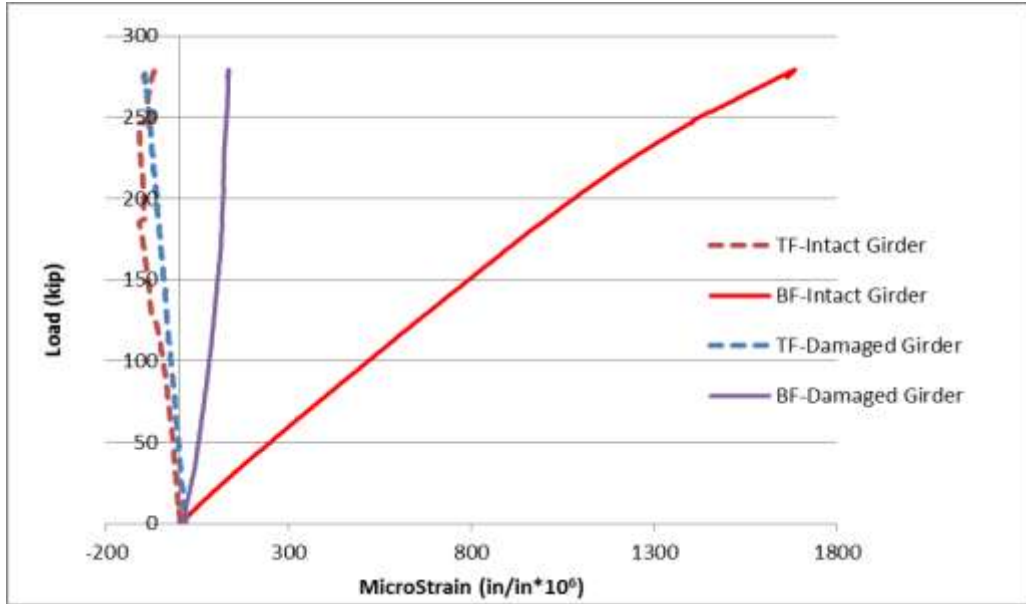


Figure 4-43 Comparison of longitudinal strains in the intact and damaged girders at Section 5.

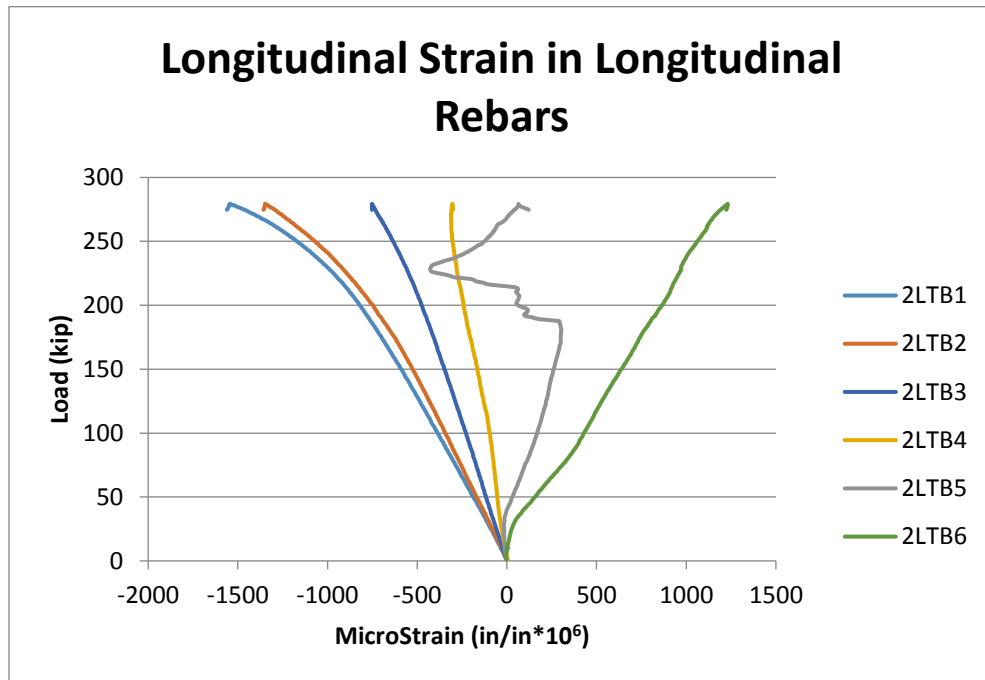


Figure 4-44 Longitudinal strain in rebars at mid-span.



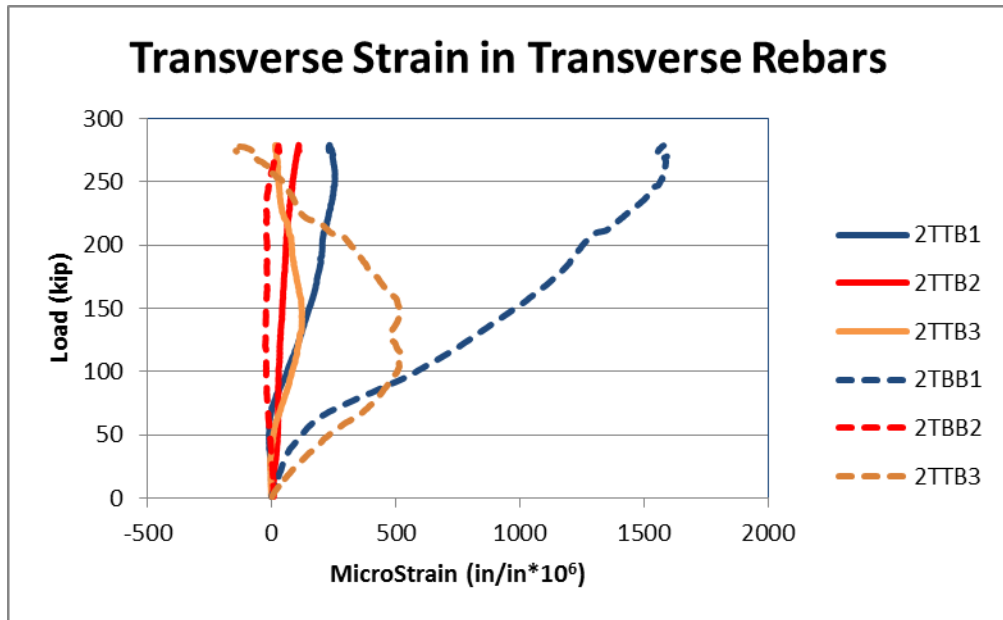


Figure 4-45 Transverse strain in rebars at mid-span.

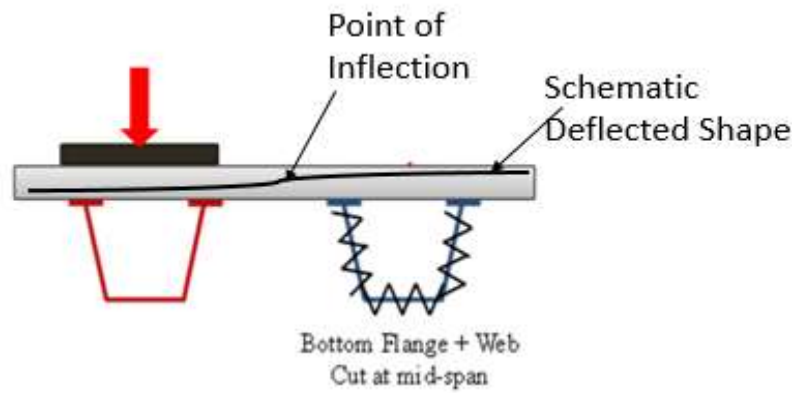


Figure 4-46 Schematic deflection shape of the deck.

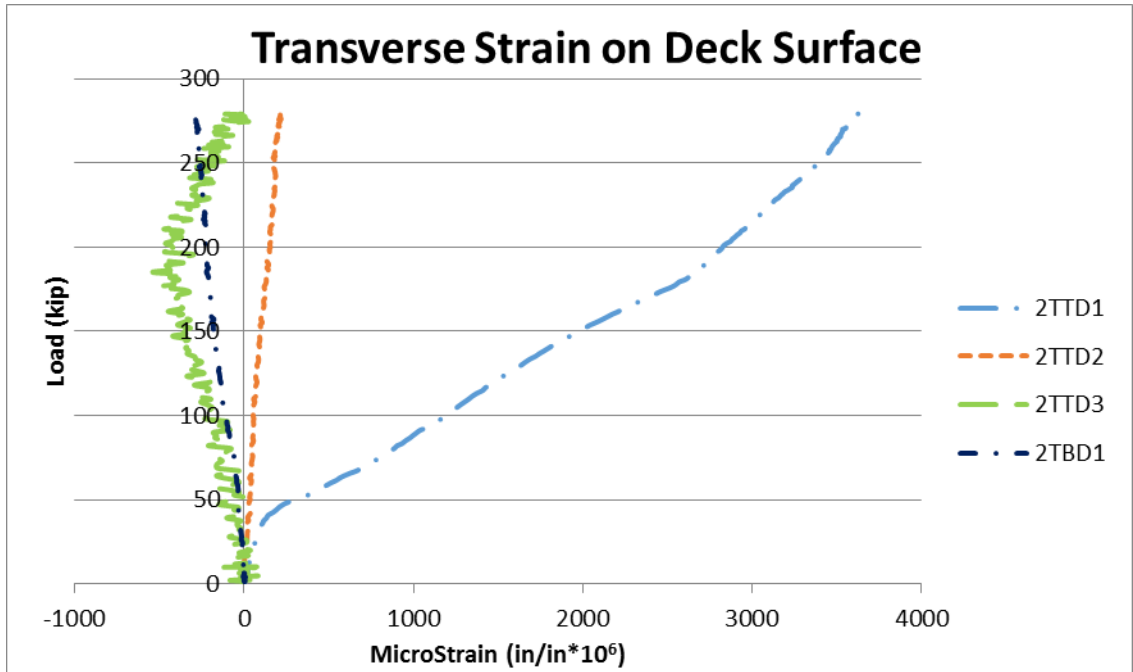


Figure 4-47 Transverse strain of the deck near mid-span.

#### 4.6 Ultimate Test C

In ultimate Test C, the load was applied through a 10-in.-square loading pad, over the intact girder at mid-span location. The purpose of this test was to see the effect of concentrated loading configuration on the failure mode of the bridge. The schematic illustration of the test is shown in Figure 4-48. For this test, the load was applied until the specimen failed completely. It is important to note that because this test was continued after Test B without any repair, the results presented, herein, will include any permanent deformation inherited from the previous test.

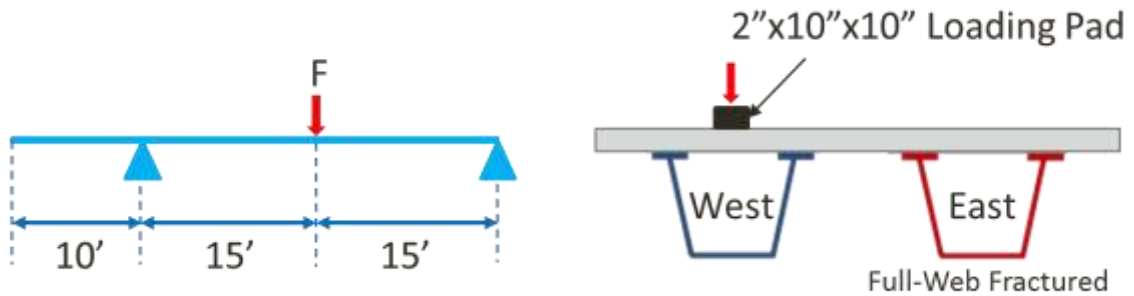


Figure 4-48 Schematic description of Test C.

#### 4.6.1 Global Behavior

In this test, the specimen carried up to 180 kips of load before the deck was suddenly punched through by the loading pad. Load versus displacement curves of the damaged girder along its length are plotted in Figure 4-51. The specimen showed approximately 0.7 in. of permanent deformations at mid-span. The stiffness of the specimen was approximately 196 kips/in. It was similar to the data observed in Test B which was showing a stiffness of 200 kips/in. Similar to Test B, both damaged and undamaged girders experienced similar displacements along the length. The average displacements at mid span, Section 5 and cantilever end were approximately 1 in., 0.78 in. and 0.75 in., respectively. During the test, the specimen responded nearly linearly then failed abruptly without any warning. The deck was punched through by the loading pad as illustrated in Figure 4-49. Unlike ultimate Test A, no girder uplift was observed during the test and it is also illustrated in Figure 4-52 where both girders experienced downward displacements at the supports. The shear transferred through one of the external cross-frames is plotted in Figure 4-50. The shear force in the monitored cross-frame under this

loading configuration was very small, with less than 2 kips before the deck was punched through.



Figure 4-49 Punching damage in test C.

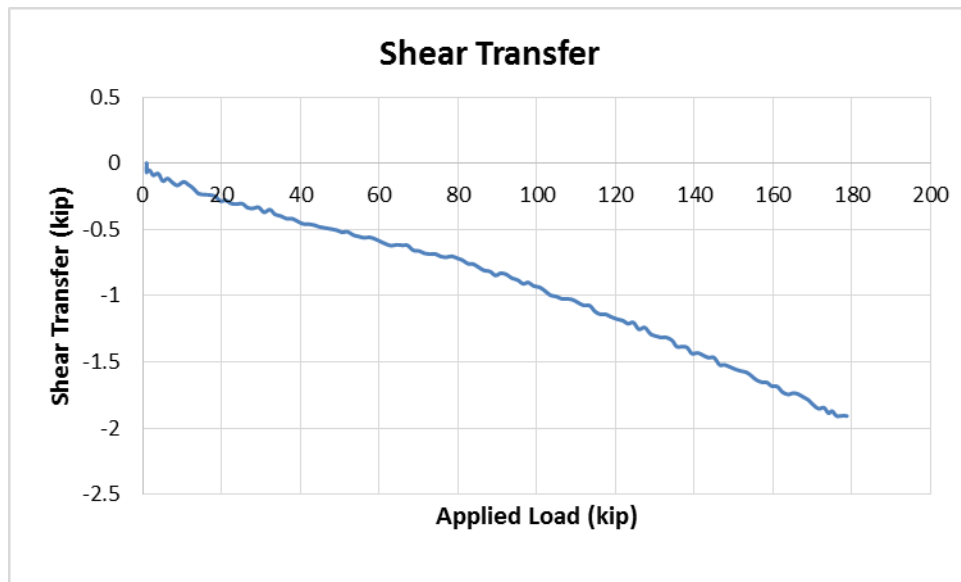
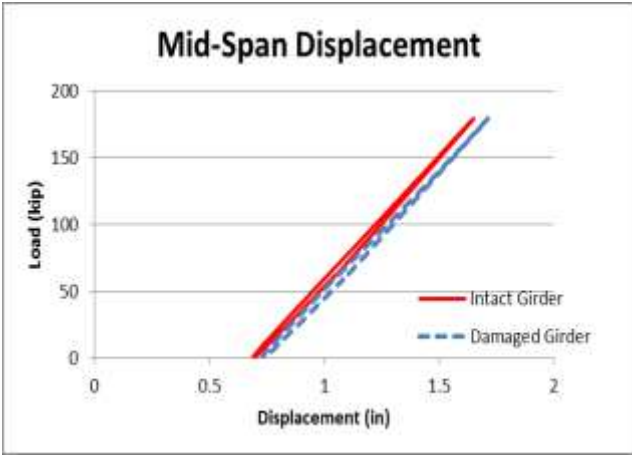
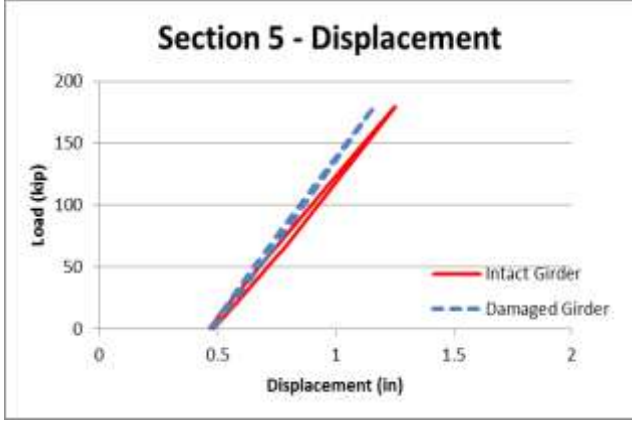


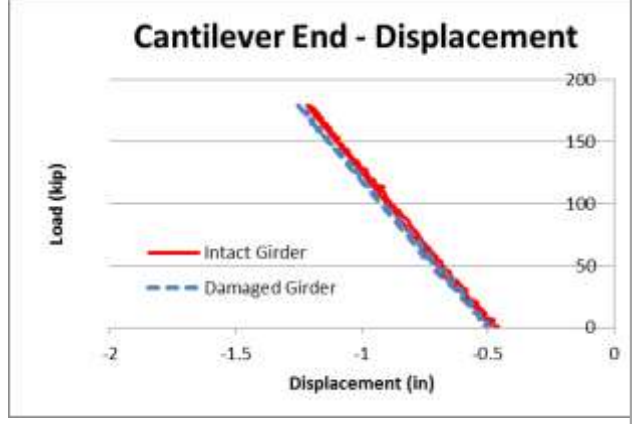
Figure 4-50 Shear transferred through a cross-frame in test C.



(a)

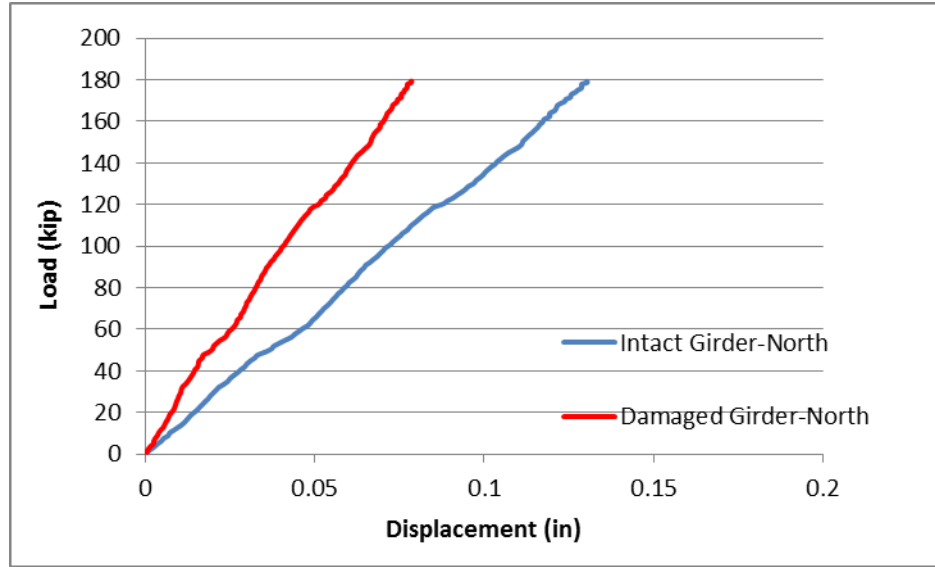


(b)

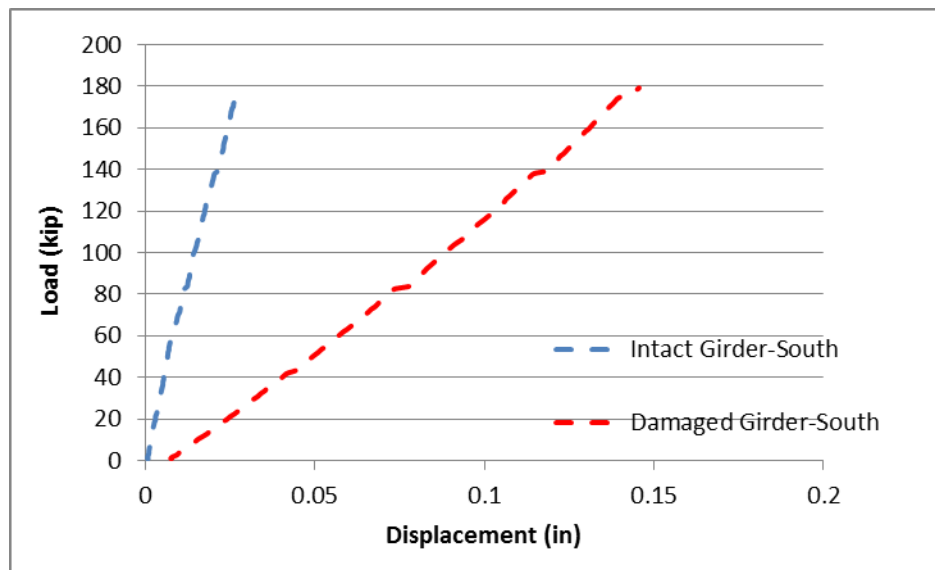


(c)

Figure 4-51 Test C: Load vs. displacement curves at (a) mid-span, (b) Section 5 and (c) cantilever end.



(a)



(b)

Figure 4-52 Displacements at (a) north support and (b) south support.

#### 4.6.2 Local Behavior

It is important to note that all strains, plotted in this test and following tests, will be offset by its initial value so that the data will begin from zero. This means that any permanent deformation inherited from previous test will not be discussed here. This will

allow a better comparison between experimental data and finite element analysis results, at a later time.

The comparison of strains in bottom flange and top flanges of the intact girder along the length is illustrated in Figure 4-53 and Figure 4-54, respectively. That the intact girder experienced maximum strain of 1740  $\mu\epsilon$  indicated the bottom flange of intact girder just yielded. The strains in the top flanges were small and negative (compression), indicating that the neutral axis should be somewhere at the top flange. Figure 4-54 suggests that the only location that experienced a tension yielding was the bottom flange of the intact girder at the mid-span. This suggests that the moment produced in this test at mid-span should be close to the yielding capacity of the intact girder. The moment produced, in the intact girder by 180 kips of load, can be approximated by the using formula  $M_n = P \times L/4$ , assuming the participation of the damaged girder was negligible. This formula yields an estimated moment of 1350 kips-ft while the yield moment capacity computed by design calculation is 1366 kips-ft.

At Section 5, the bottom flanges were in tension while the top flanges were in compression for both girders. The intact girder had longitudinal strain in the bottom flange significantly higher than that of the damaged girder, as illustrated in Figure 4-55. These data are consistent with earlier findings which stated the contribution of the damaged girder to the system's capacity was very minimal.

Figure 4-56 plots strains in longitudinal rebars at mid-span. The maximum positive strain occurred at gauge 2LTB6 with 560  $\mu\epsilon$  while the maximum negative one was -840  $\mu\epsilon$ . All the longitudinal rebar gauges were in compression, except gauges 2LTB5 and 2LTB6. These observations were similar to what was observed in Test B.

Figure 4-57 plots strain recorded at both top and bottom transverse rebars. Changing in the strain from positive at gauge 2TBB1 to negative at gauge 2TBB2 suggested that the moment, in longitudinal direction, had changed from positive to negative. This indicates that the deck changes its transverse deflection shape from concave up to concave down. Therefore, the location of inflection point at mid-span should be located somewhere between 2TBB1 and 2TBB2. Comparing with the data obtained from Test B, this suggests that the point of inflection at mid-span section was shifted more toward to the intact girder when the loading area was decreased.

Figure 4-58 illustrates transverse strain on the deck surface. The location, closest to the loading point, has experienced the largest crack, as expected. The strains at locations 2TTD2 and 2TTD3 are very small. The fact that gauge 2TBD1 attached to the bottom of the deck surface showed a negative value suggests the deck was in compression at this location.

Overall, the recorded data were very similar to those obtained in Test B up to 180 kips of load. The data indicated that the load was mainly resisted by the intact girder. No girder uplift was observed, and cross-frame forces were negligible. However, this test had punching shear as a failure mode while Test B was likely to fail in flexural mode. The reason that this test failed much faster could be attributed to the smaller size of the loading area. In this test, the specimen was loaded in a more concentrated manner than it was in Test B.



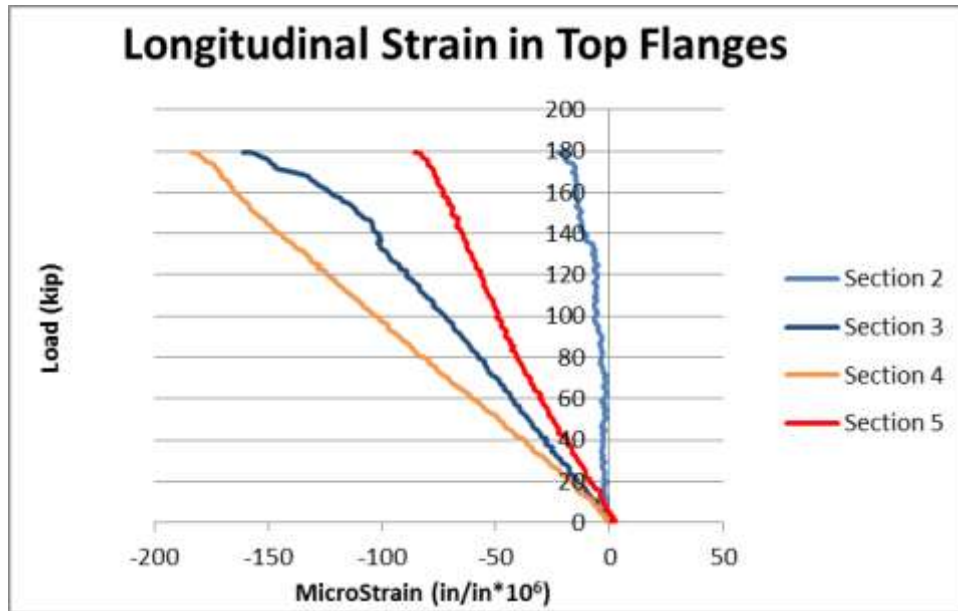


Figure 4-53 Average longitudinal strains at top flanges of the intact girder.

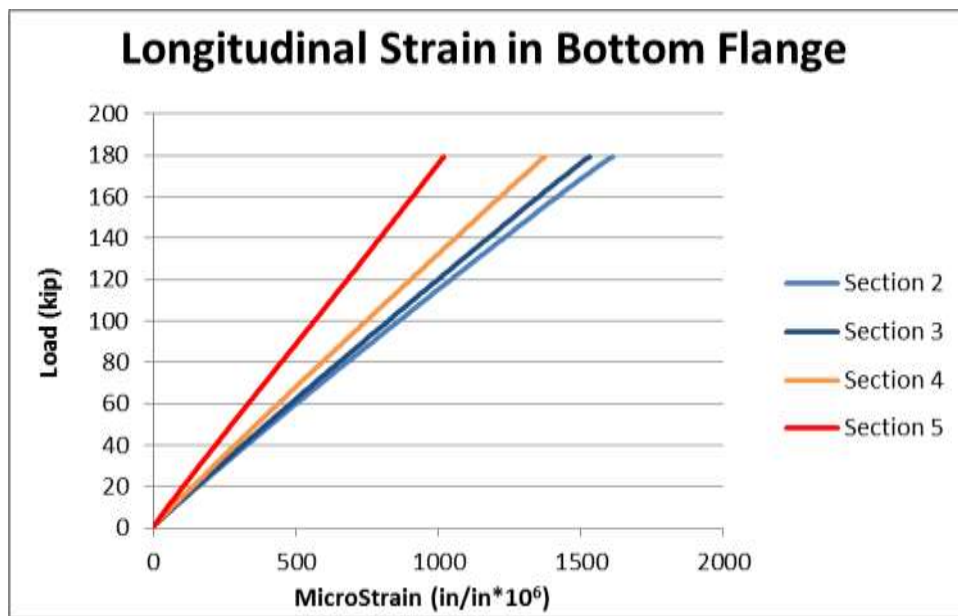


Figure 4-54 Longitudinal strains at the bottom flange of the intact girder.

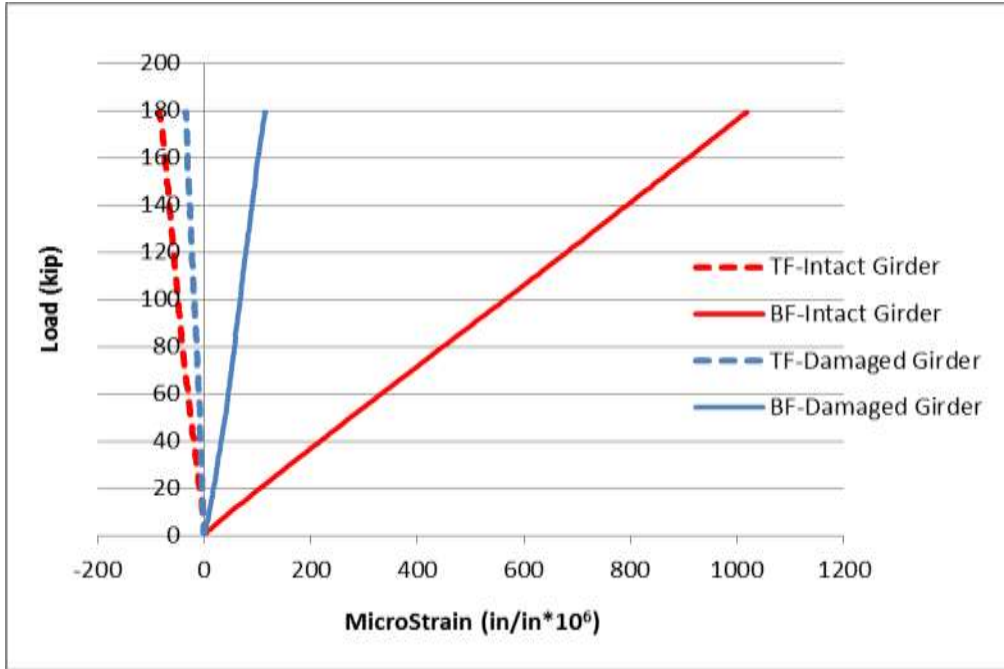


Figure 4-55 Comparison of longitudinal strains in the intact and damaged girders at Section 5.

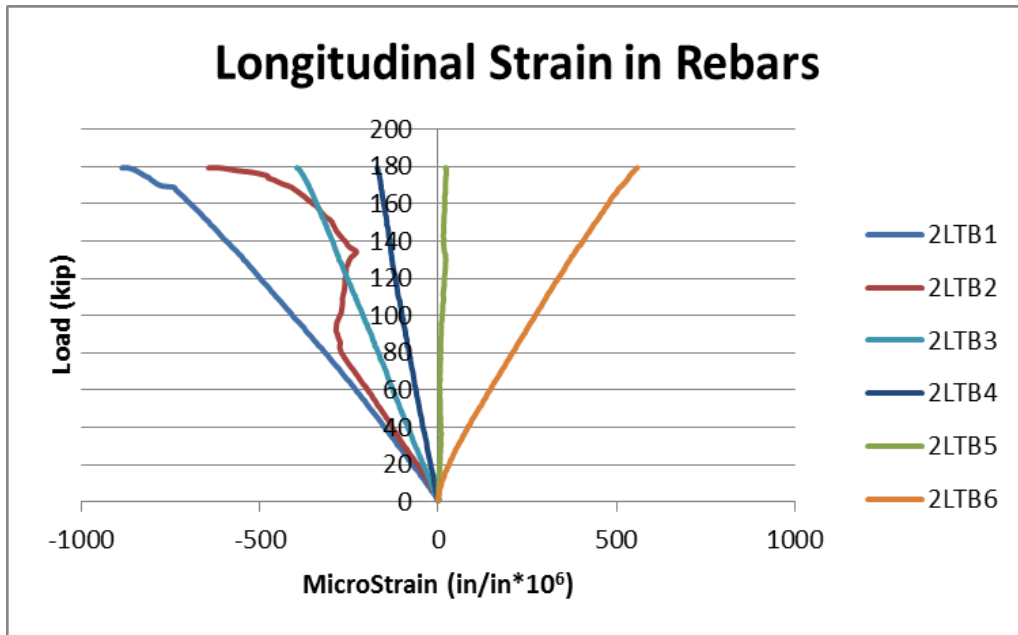


Figure 4-56 Longitudinal strain in rebars at mid-span.

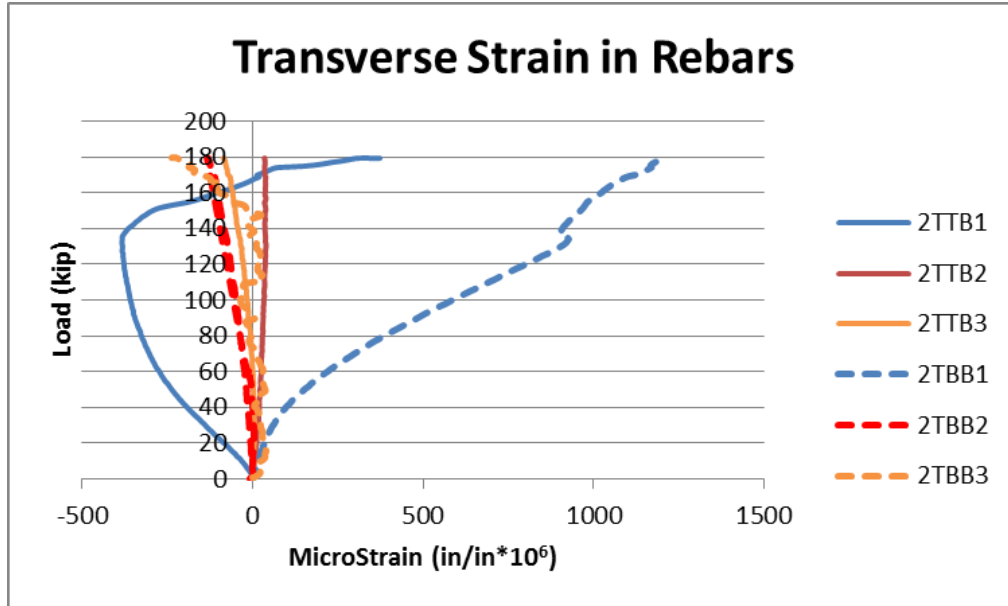


Figure 4-57 Transverse strain in rebars at mid-span.

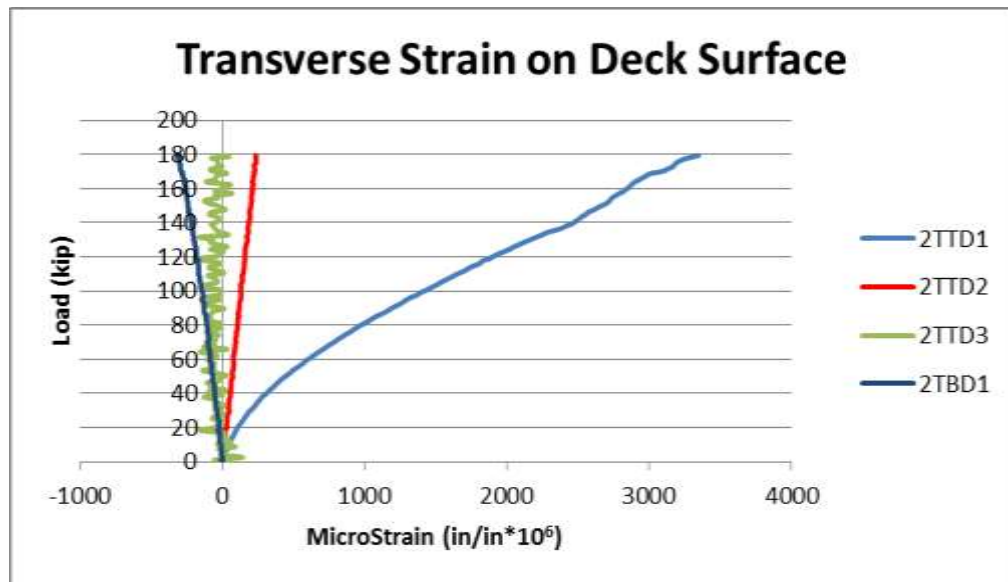
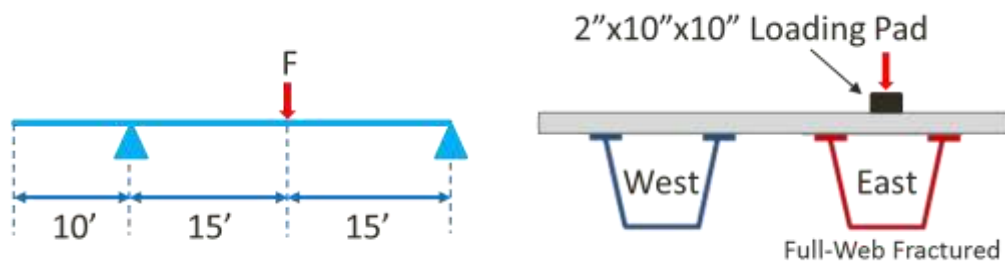


Figure 4-58 Transverse strain on the deck near mid-span.

#### 4.7 Ultimate Test D

In this ultimate Test D, the load was applied through a 10-in.-square loading pad which was the same as in Test C, but over center of damaged girder at mid-span location.

The results of this test, in addition to that of previous ultimate tests, will provide a comprehensive comparison that could explain the effects of damaged girder and loading configurations on the behaviors of the specimen. The schematic drawing of loading configuration in Test D is shown in Figure 4-59. The specimen was loaded until failure. Since this test was continued on the same specimen without any repair, the results presented in this section will include any permanent deformation inherited from both Tests B and C.



**Figure 4-59 Schematic description of Test D.**

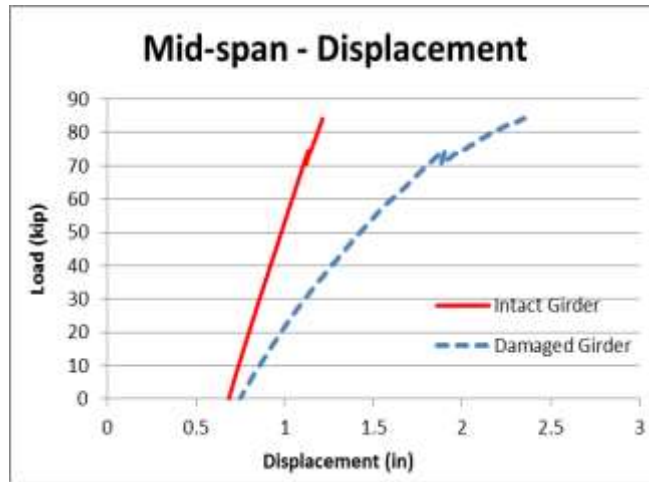
#### 4.7.1 Global Behavior

In this test, the specimen carried up to 83 kips of load before the deck was punched through by the loading pad. The applied load versus the displacement curves of the damaged girder along its length are plotted in Figure 4-60. The specimen showed linearly elastic response up to 60 kips. Approximately 0.7 in. of permanent deformations at mid-span was observed as a results of previous tests. The initial stiffness of bridge under this loading condition was 87 kips/in and was similar to the initial stiffness obtained in Test A. However, comparing with Test B and C, the initial stiffness of the specimen was reduced an average of 55%. There was a 2-kip drop in capacity after reaching 72 kips of load due to cracks in the concrete deck. After that the specimen continued to carry up to 83 kips

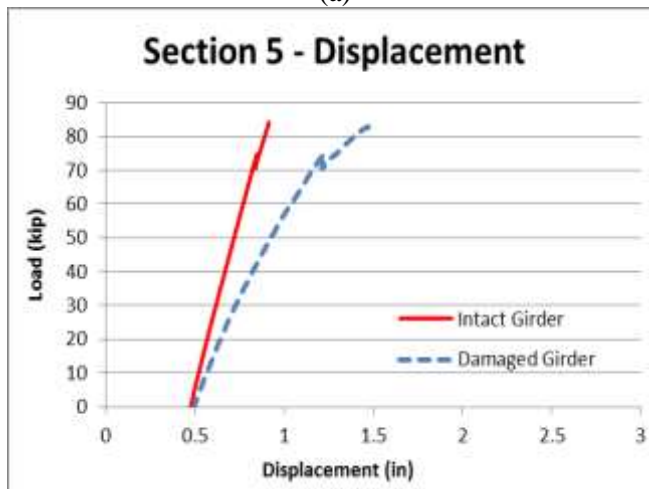
before it failed abruptly by punching shear. Figure 4-61 illustrates that the punching damage was confined exactly to the area of the loading pad and it was similar to the failure mode obtained in Test C.

In contrast to Test B and C but similar to Test A, Figure 4-60b shows that the damaged girder experienced a significantly higher displacement than the intact girder. The displacement data at different sections suggests that the further away from mid-span, the smaller displacement difference two girders experienced as illustrated in Figure 4-60b and c. At the supports and the cantilever end, both girders experienced very similar displacements. Figure 4-62 shows that both girders displaced downward during the entire test. This suggests that no uplift occurred at the supports.

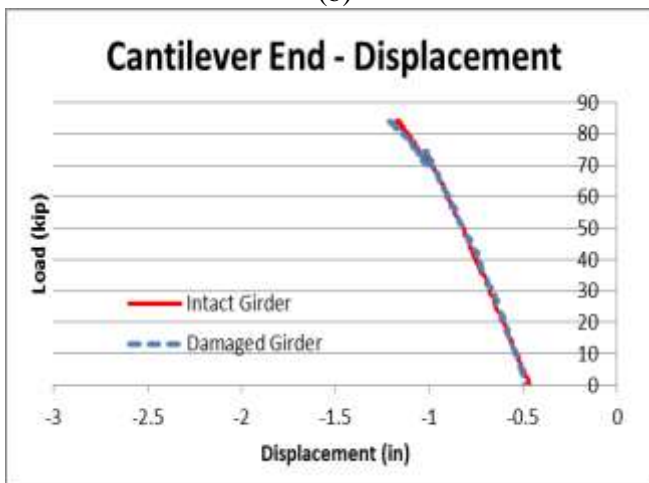
The shear transferred through one external cross-frame was less than 2 kips and is illustrated in Figure 4-63. Assuming the shear force in the other cross-frame was the same, the total shear force carried by all of the external cross-frames, in the main span, would be less than 4 kips. This indicates that applied load was mainly resisted and transferred to the intact girder through the deck.



(a)



(b)

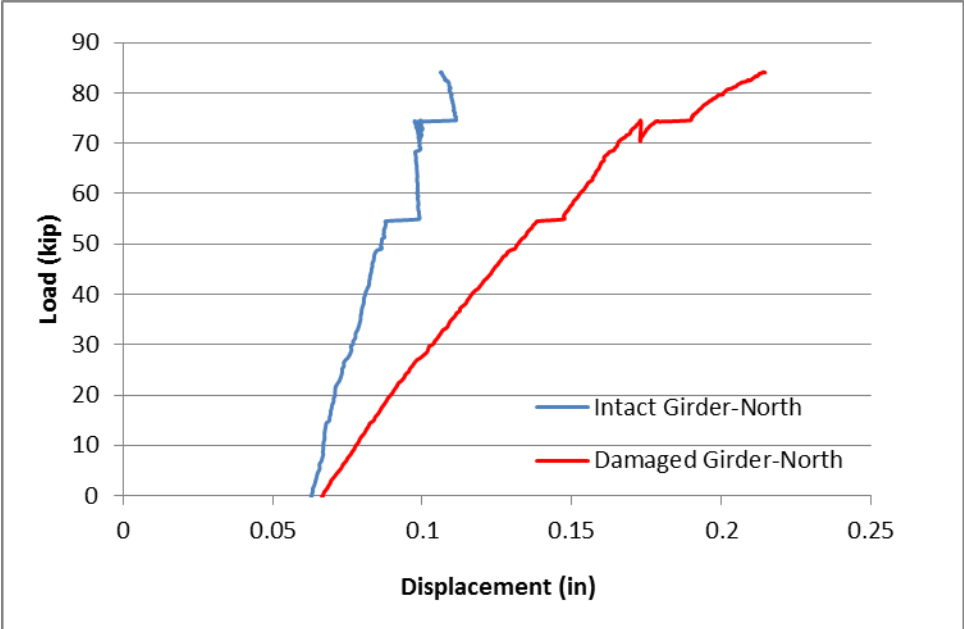


(c)

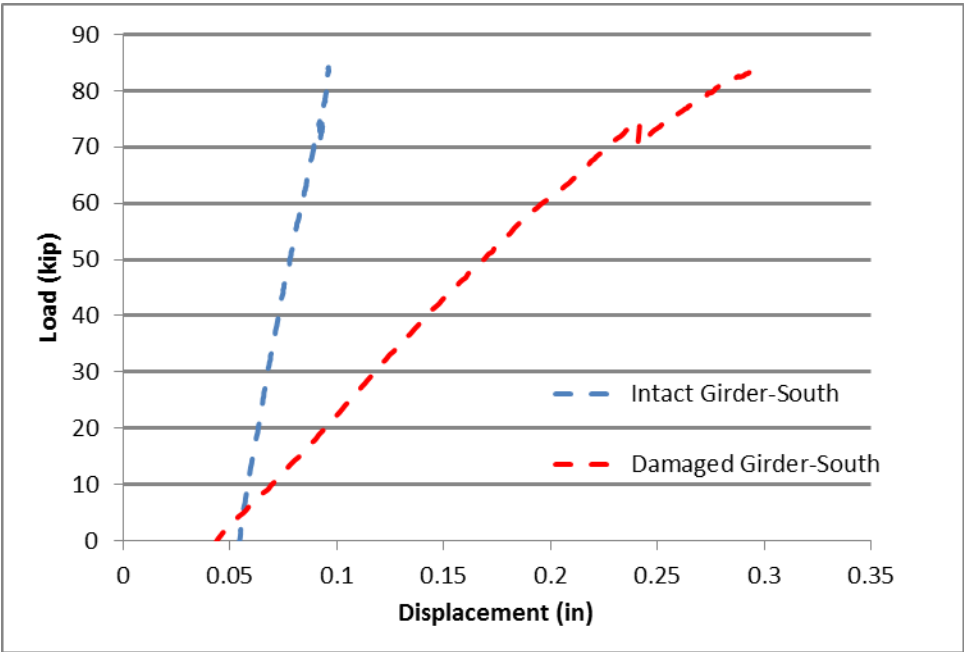
Figure 4-60 Test D: Load vs. displacement curves at (a) mid-span, (b) Section 5 and (c) cantilever end.



**Figure 4-61 Punching damage in Test D.**



(a)



(b)

Figure 4-62 Displacements at (a) north support and (b) south support.



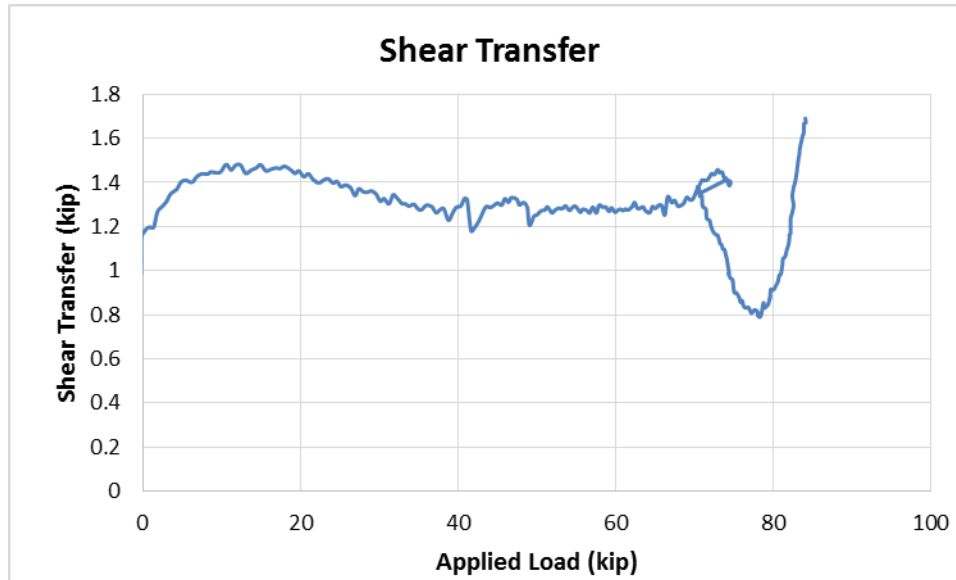


Figure 4-63 Shear transferred through a cross-frame in Test D.

#### 4.7.2 Local Behavior

Due to the fact that the deck failed much earlier in this test than it did in other tests, the maximum strain, obtained was also smaller in a similar proportion. The average longitudinal strain in the top flanges of the intact girder is shown in Figure 4-64. The data for the bottom flange of the intact girder along the length of the bridge are illustrated in Figure 4-65. The longitudinal strains, in the bottom flange, were comparable from Section 2 to Section 5. This suggests the load that was transferred to the intact girder was distributed quite uniformly between these sections (Note that Section 2 is mid-span section and Section 5 is 5 ft away from mid-span).

Similar to Test A, the strains, obtained at Section 5, indicated that the damaged girder had the bottom flange in compression and the top flange in tension. A comparison between the intact and damaged girders is illustrated in Figure 4-66. For the intact girder, average strain was  $-25 \mu\epsilon$  and  $760 \mu\epsilon$  for the top flange and the bottom flange, respectively.

For the damaged girder, it was  $70 \mu\epsilon$  and  $-280 \mu\epsilon$  for the top flange and the bottom flange, respectively.

Among six gauges installed to measure strain in the top longitudinal reinforcements, two gauges were damaged which were 2LTB1 and 2LTB2. Only gauges 2LTB5 and 2LTB6 were in tension while others were in compression. This indicates the deck would change its deflection from concave up to concave down somewhere between gauge 2LTB4 and 2LTB5. The maximum strain was  $1300 \mu\epsilon$  obtained at gauge 2LTB6 over the outside top flange of the damaged girder. This indicates the top layer of longitudinal rebar have not yielded yet. Strains in top and bottom transverse rebars are plotted in Figure 4-68, indicating some of the transverse rebars yielded.

Figure 4-69 shows the transverse strains recorded on the deck surface. Gauges 2TBD1 and 2TTD3 experienced negative strains while gauges 2TTD1 and 2TTD2 had positive strains which mean the deck were in tension at these locations. Since gauges 2TTD2 and 2TTD3 are next to each other and had opposite sign of change in strain, this suggests that the point of inflection was somewhere between these two gauges. Combining this finding and the findings based on the longitudinal rebars, the point of inflection was approximately near the inside top flange of the damaged girder.

In general, the specimen showed similar behavior to what observed, in Test A, up to 83 kips of load. However, two different failure modes were observed. In this test, the load area was reduced and the specimen failed predominantly in punching shear (or two-way shear failure) without any warning while the failure was likely a combination of both one-way and two-way shear failure in Test A. The applied load was found to be transferred mainly through the deck. The fact that the deck was punched through faster in this test (83

kips) than it was in Test C (180 kips) could be attributed to the effect of the girders on supporting the deck, especially where the load was applied.

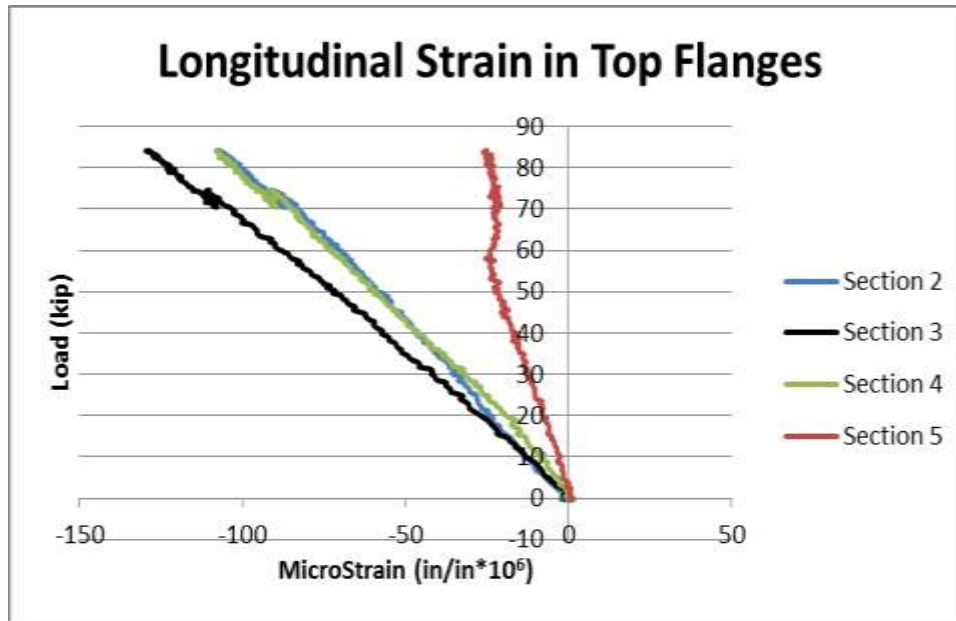


Figure 4-64 Average longitudinal strains at top flanges of the intact girder.

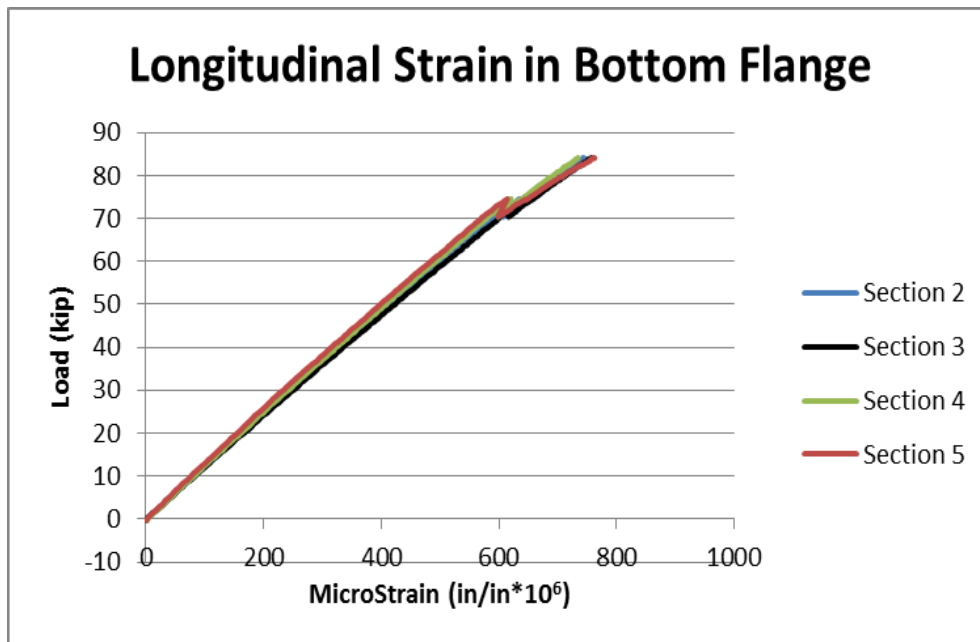


Figure 4-65 Longitudinal strains in bottom flange of the intact girder at Sections 2, 3, 4, and 5.

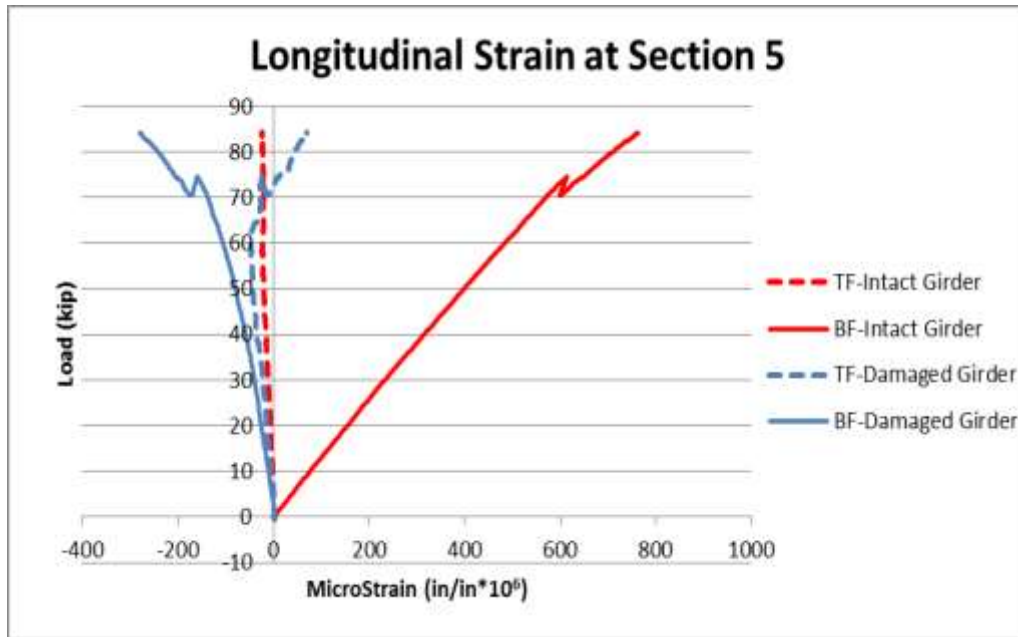


Figure 4-66 Comparison of longitudinal strains in the intact and damaged girders at Section 5.

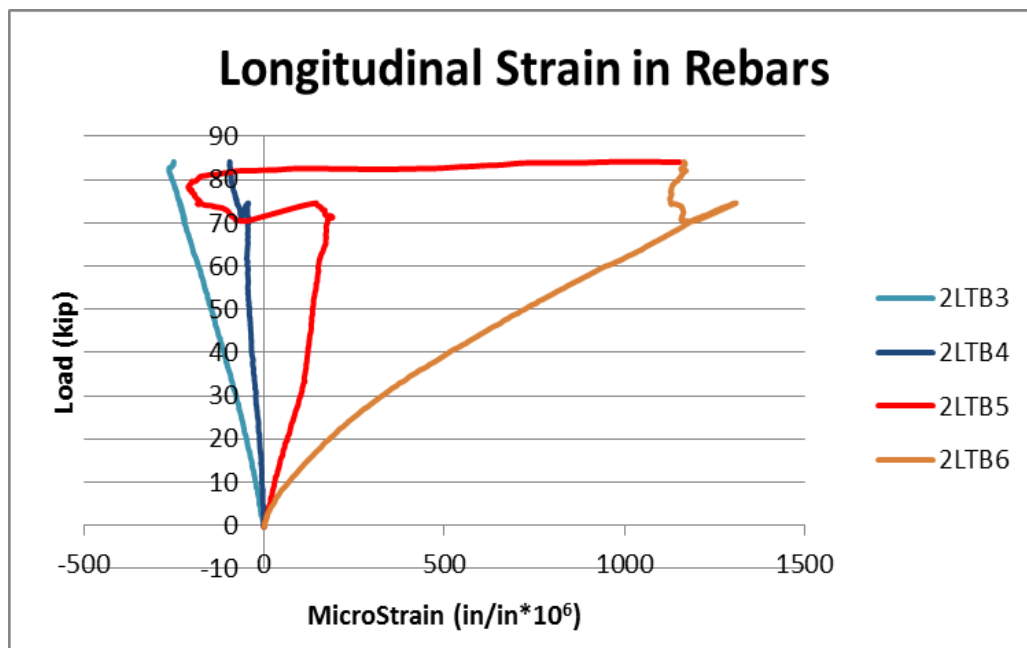


Figure 4-67 Longitudinal strain in rebars at mid-span.

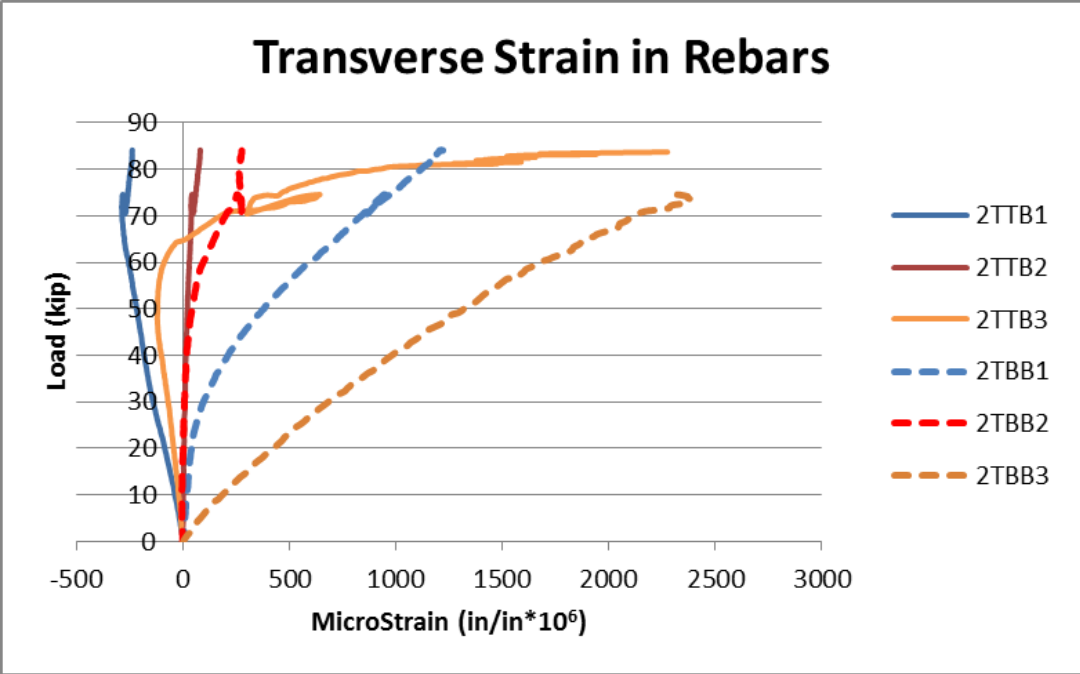


Figure 4-68 Transverse strain in rebars at mid-span.

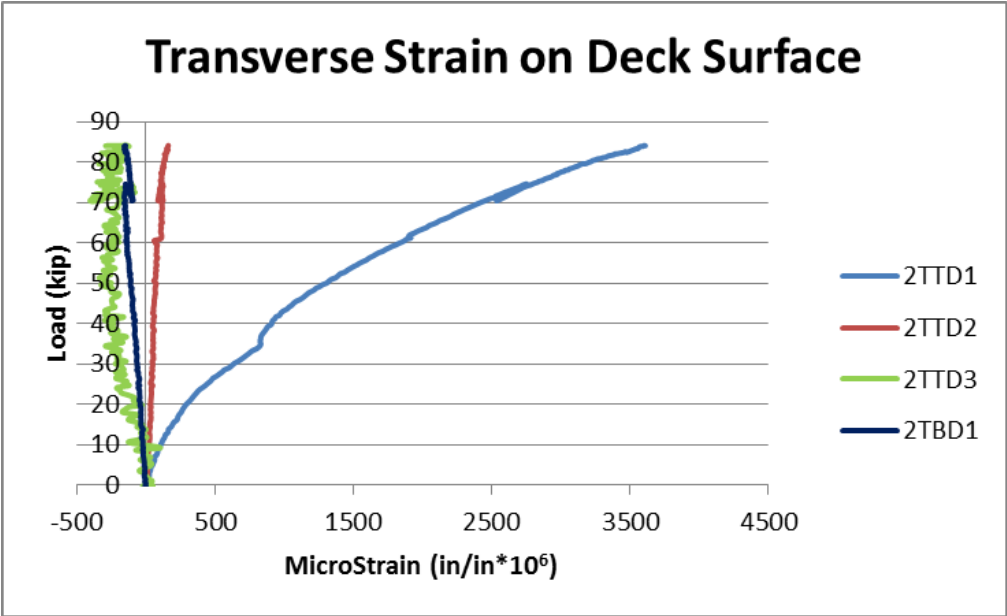


Figure 4-69 Transverse strain on the deck near mid-span.

#### 4.8 Damage Repair

After completing Tests C and D, a decision was made to repair damage due to punching in the deck before carrying out one last ultimate test in which the specimen was loaded under a truck footprint. In order to repair these damages, first of all, spalling concrete fragments were removed around punched square holes. Then tapcons were drilled into the concrete to act as shear studs. After that, an attempt was made to get a saturated surface dry (SSD) condition in the holes. The main material used for the repair was MasterEmaco T302, a two-component polymer-modified cement-based repair mortar with an integral corrosion inhibitor. The expected compressive strength for this composition is 6,000 psi. Once the mortar mix was thoroughly mixed, the moistened concrete fragments were added in, since no pea gravel was available on hand at that time. Then, the mortar mix was poured into the holes and then vibrated in order to get the best possible penetration. Once the repair patch was troweled, moist cure bags were placed over the repair areas. Some pictures taken during the repair are shown in Figure 4-70.



**Figure 4-70 Repair of punching shear damage from Tests C and D.**

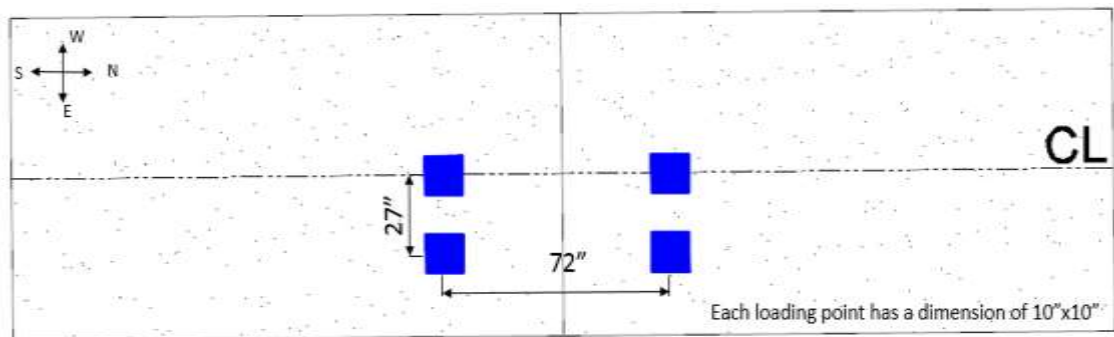
#### **4.9 Ultimate Test E**

In this test, the load was applied through four loading pads in order to simulate the truck footprints. The loading pads were the same as in previous tests with a dimension of 10 in. x 10 in. The distance between north wheels and south wheels was 72 in., while the distance between west wheels and east wheels was 27 in. from center to center. The west wheels were placed at the center of cross-section while the east wheels were at the center of damaged girder. The schematic description of Test E loading set up is shown in Figure

4-71. The purpose of this test was to investigate whether the same failure mode of punching shear will be obtained, under truck-load configuration.



(a)



(b)

Figure 4-71 (a) Test setup for Test E and (b) schematic locations of loading foot prints.



#### 4.9.1 Global Behavior

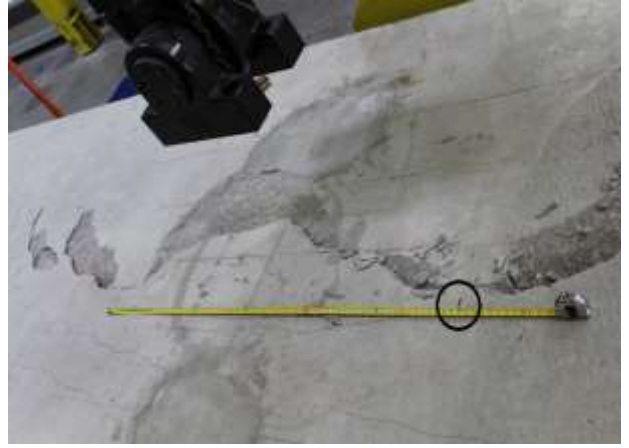
In this test, the specimen carried up to 235 kips of load before it failed abruptly as shown in Figure 4-73a. It should be noted that this is the total load distributed to all four loading points and the deflection is measured from the mid-span location, not under the loading points. The initial stiffness of bridge under this loading condition was approximately 103 kips/in which was similar to its initial stiffness under Tests A and D where the load was applied toward to the damaged girder. The intact girder responded almost linearly in the entire test. The damaged girder responded linearly up to 150 kips when the first cracks were noticed especially along the west loading points. As the load continued to increase, the initial cracks formed around the south-west loading point and north-west loading point propagated toward each other in the longitudinal direction as well as toward the intact girder in the transverse direction as shown in Figure 4-72a-c. As the load increased, these longitudinal cracks finally met each other and penetrated further into the deck creating a heavy crushing line on the deck at its centerline where the west wheels were placed. Figure 4-72d also shows there was a significant damage occurred along the inside top flange of the intact girder. It was due to the fact that the applied load was distributed to the intact girder and created a significant amount of shear force at the section along the inside top flange of the intact girder. Figure 4-74 illustrated that the concrete deck at the ends was also cracked and almost ripped off, similar to what was observed in Test A. The reasons this happened was explained previously in Test A. By assuming the participation of the damaged girder in resisting the applied load is negligible, this test will resemble to the case where the slab is linearly supported by the undamaged box girder and subjected to multiple concentrated loads over the overhang region of the slab. Overall, the

crack and damage pattern suggested that the specimen failed predominantly in one-way shear failure.

The displacements at Section 5 and at cantilever end are plotted in Figure 4-73b-c. The displacements measured at the cantilever end were about the same for both girders up to 150 kips of load. This suggests that the shear cracks, illustrated in Figure 4-74, might begin at this point of time causing the differential displacement between two girders. The displacements monitored near the supports increased during the entire test as illustrated in Figure 4-75. This indicates no uplift occurred in this test. Shear force captured in the cross-frame at Section 5 was only 7 kips as shown in Figure 4-76. This indicates that the contribution of cross-frame under this loading configuration was also small and the applied load was transferred to the intact girder mainly through the deck. The reason that the specimen experienced a different failure mode in this test than in previous tests and the load was transferred to the intact girder mainly through deck is attributed to the loading configuration that was used in the test. In this test, the specimen was loaded with four points, instead of one, and the loads were placed much closer to the intact girder so that it facilitated transferring the load to the intact girder in both longitudinal and transverse directions.



(a)



(b)

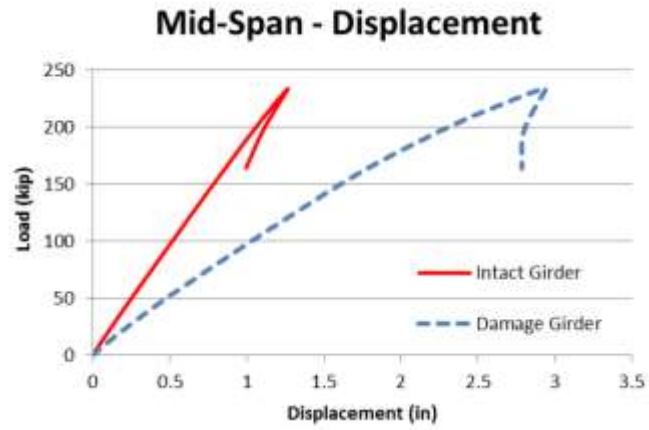


(c)

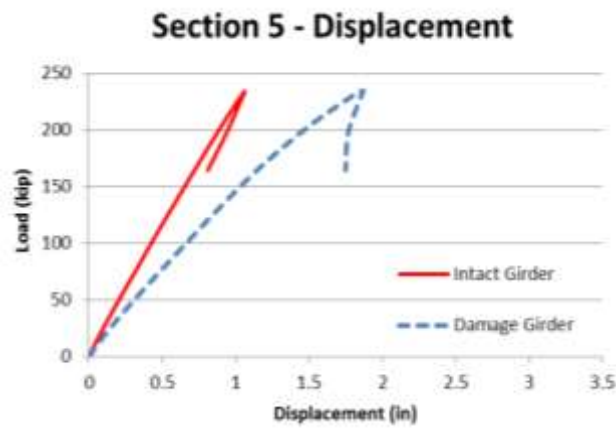


(d)

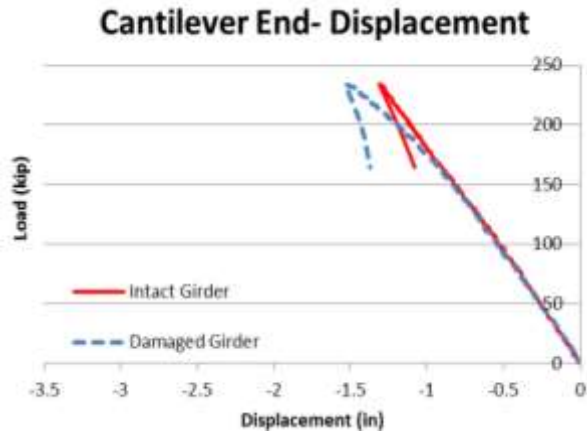
**Figure 4-72 Damage in Test E.**



(a)



(b)



(c)

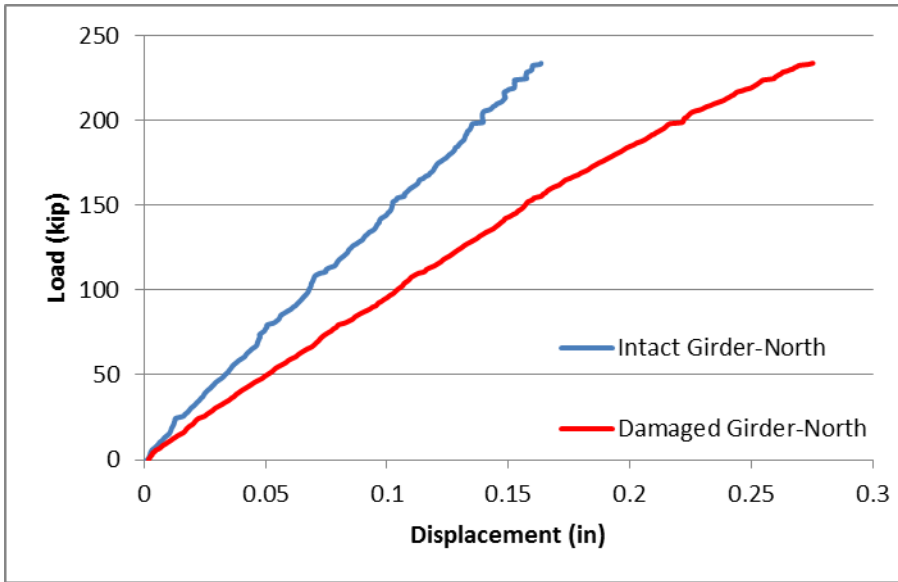
Figure 4-73 Test E: Load vs displacement curves at (a) mid-span, (b) Section 5 and (c) cantilever end.



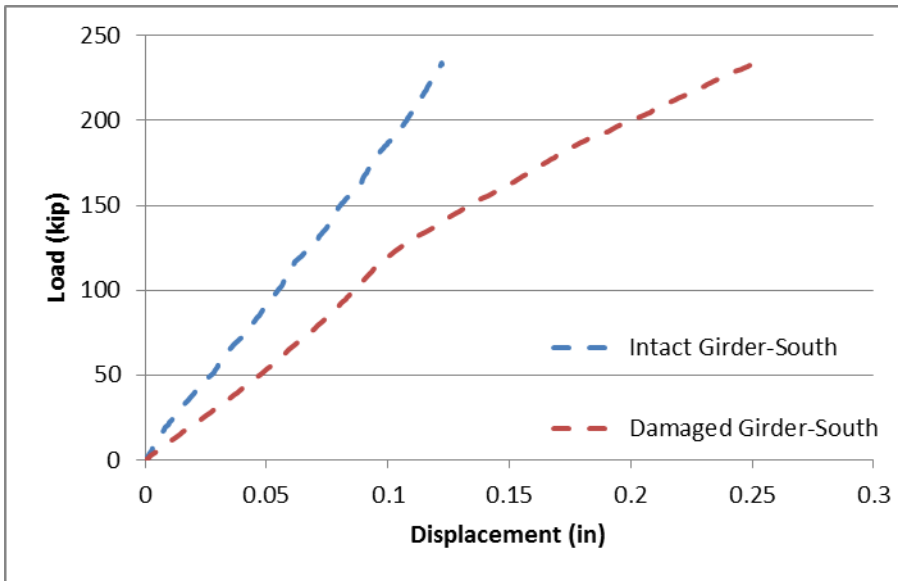
(a)

(b)

**Figure 4-74 Shear damage at ends in Test E.**



(a)



(b)

Figure 4-75 Displacements at (a) north support and (b) south support.

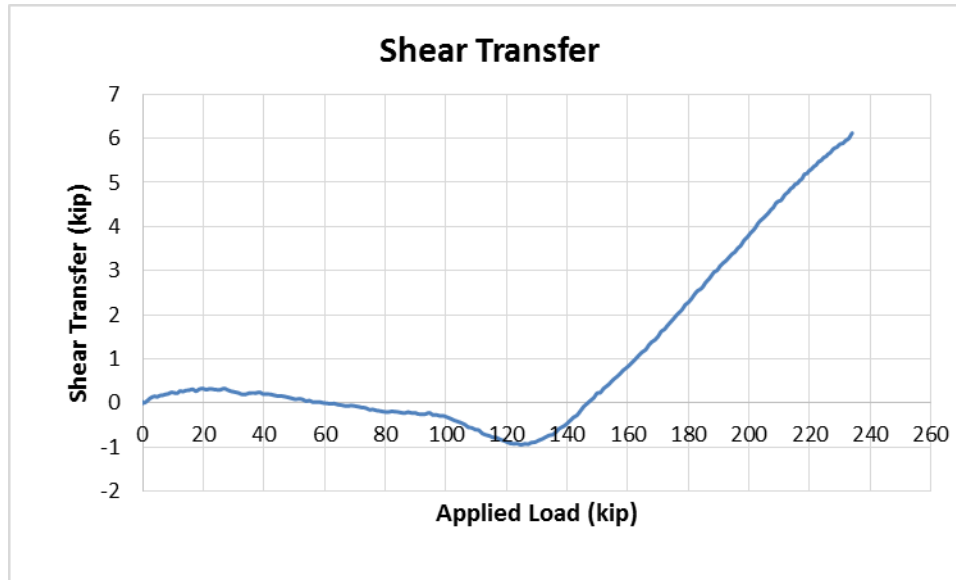


Figure 4-76 Shear transferred through a cross-frame in Test E.

#### 4.9.2 Local Behavior

The top flange longitudinal strains of the intact girder are plotted in Figure 4-77. These were average strains of both top flanges. The average longitudinal strains in the top flanges were  $-240 \mu\epsilon$ ,  $-270 \mu\epsilon$ ,  $-250 \mu\epsilon$  and  $-107 \mu\epsilon$  respectively for Sections 2, 3, 4, 5. Longitudinal strains, obtained in the bottom flange were also averaged and are illustrated in Figure 4-78. They were  $1717 \mu\epsilon$ ,  $1740 \mu\epsilon$ ,  $1683 \mu\epsilon$  and  $1846 \mu\epsilon$  for Sections 2, 3, 4, and 5, respectively. These longitudinal strains in the top flanges and bottom flange at Sections 2, 3, 4 and 5 indicated the load was distributed more uniformly than it was in other tests with single concentrated load. These strains also indicate the bottom flange just yielded at these sections. At Section 5, the bottom flange experienced slightly larger strain than other sections. It could be due to the fact that, the loading pads were positioned closer to that section. The data from the intact girder and damaged girder is compared in Figure 4-79.

The bottom flange of the damaged girder was in compression while it was in tension for the intact girder.

The longitudinal strains in the rebars are shown in Figure 4-80. Three gauges were damaged as results of previous tests. All gauges in the transverse rebars were damaged; therefore, not reported here. The crack gauges on the top and bottom of the deck also had similar trends as they was observed in Tests A and D. Gauge 2TTD1 had significantly high tensile strain, indicating the major crack occurred over the inside top flange of the intact girder. Gauges 2TTD2 and 2TBD1 were very small. This indicates the point of inflection was at center of the bridge cross-section. While the center of gravity of the load was right at the center of the damaged girder in Test A and D, in this test with truck-load configuration, the center of gravity of the load was shifted closer to the intact girder. This was the reason why the point of inflection was also shifted toward to the intact girder.

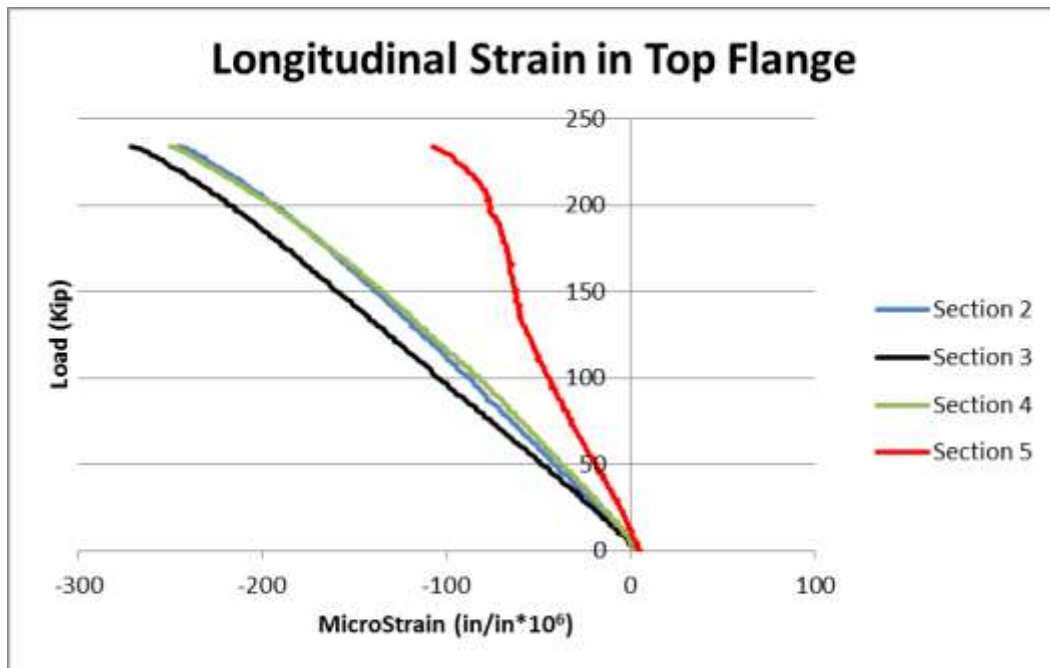


Figure 4-77 Average longitudinal strains at top flanges of the intact girder.



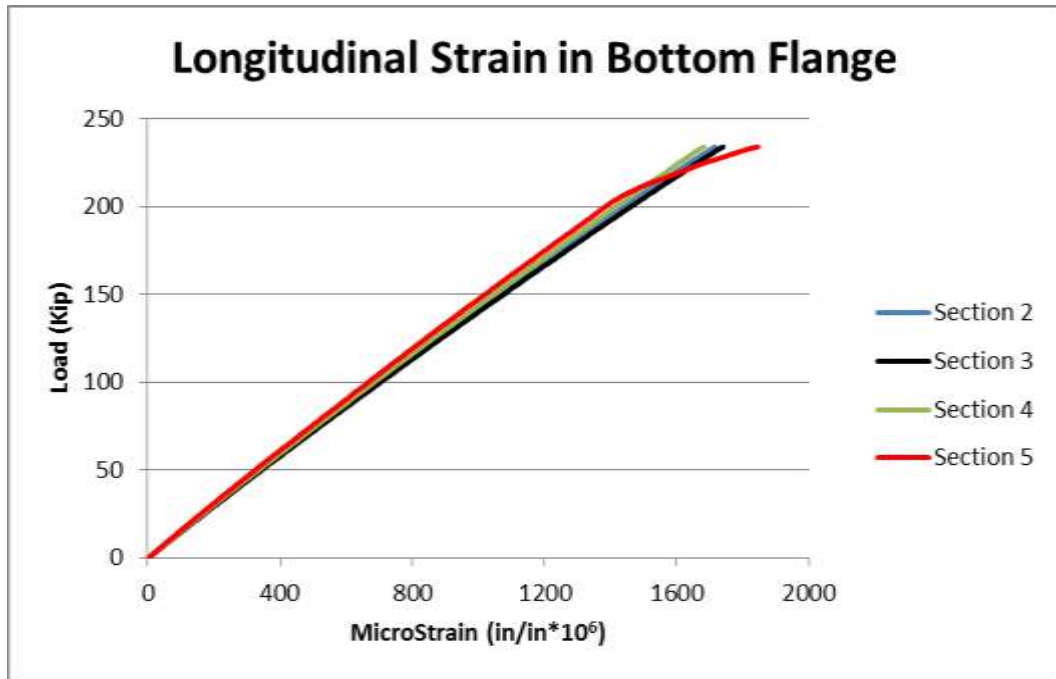


Figure 4-78 Longitudinal strains at the bottom flange of the intact girder.

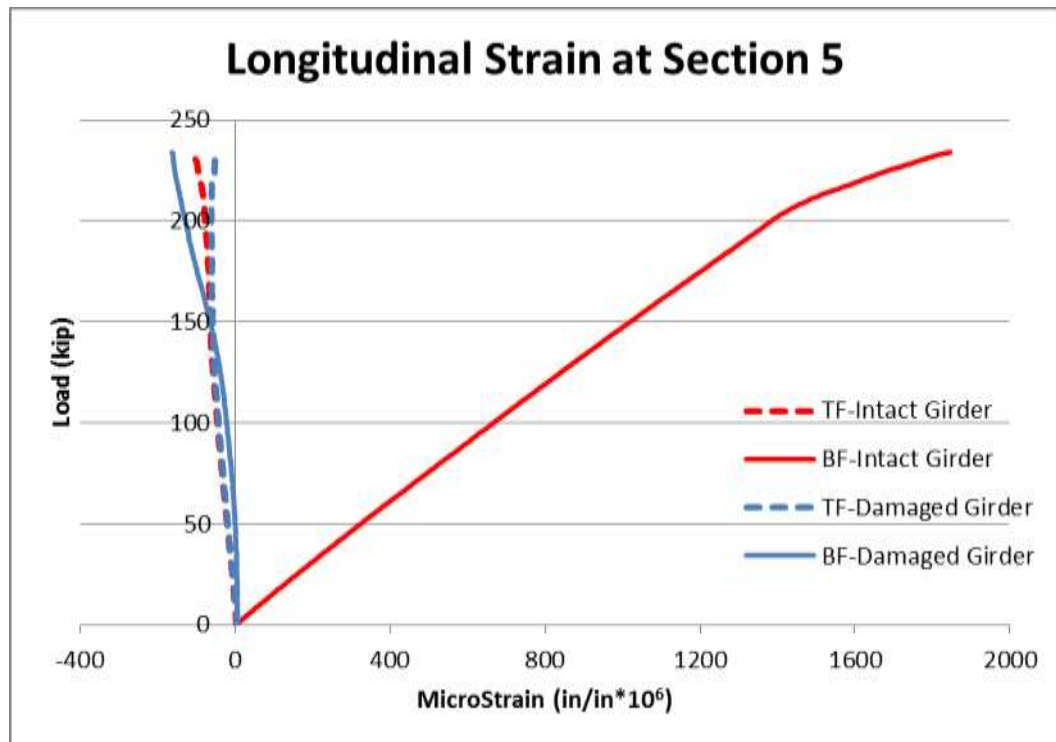


Figure 4-79 Comparison of longitudinal strains in the intact and damaged girders at Section 5.

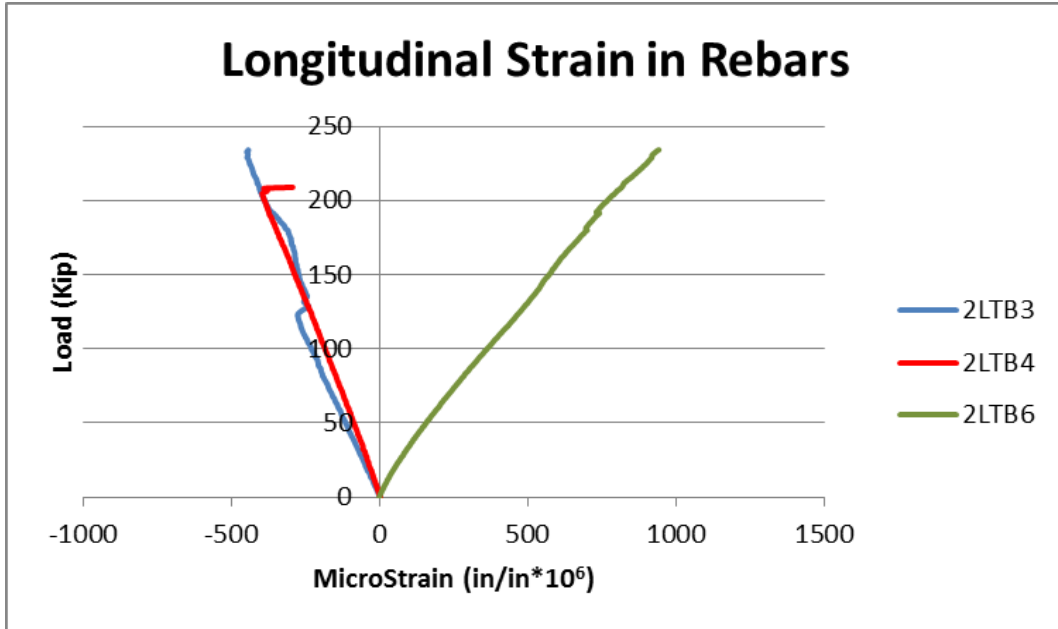


Figure 4-80 Longitudinal strain of rebars at mid-span.

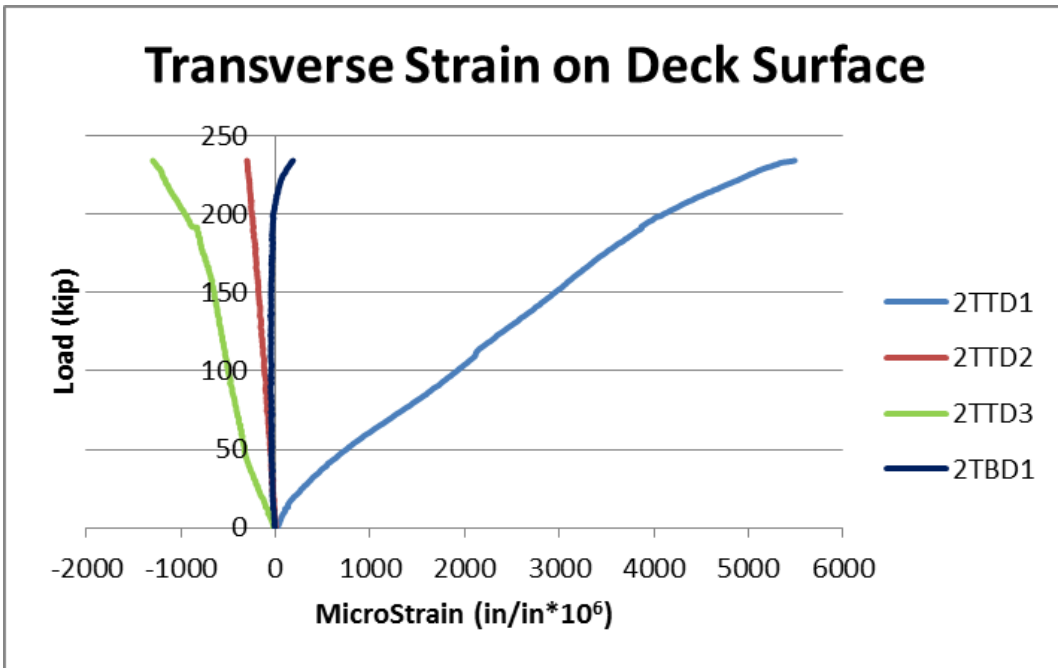


Figure 4-81 Transverse strain on the deck near mid-span.

## Chapter 5 Finite Element Modeling — Procedures and Verification

ANSYS, a finite element modeling software package, was utilized in this research to predict and capture the behavior of the bridge specimen that couldn't be captured in the laboratory testing. Material nonlinearities were taken into account when modeling both steel and concrete behavior. The steel materials were assumed to have multi-linear isotropic hardening responses. The concrete was also modeled as a multi-linear isotropic hardening material but with cracking and crushing capabilities enabled. The cracking and crushing characteristics of concrete are usually neglected or simplified in other research because they generally increase the analysis time significantly and cause convergence issues. The contact areas between the steel girder or the deck and pads were also taken into consideration in modeling. The contacts between girder bottom flange and supporting bearing pads were modeled to capture any uplift incident while the contact between loading pads and concrete deck was also modeled to simulate any slippage occurrence. The details of the numerical model are described in the following sections.

### 5.1 FEM of Bridge Specimen

The steel box-girder bridge was modeled to represent the test specimen as realistically as possible. The steel plate girder was modeled using 4-node shell element, SHELL181 with six degrees of freedom at each node. This shell element is well suited for linear, larger rotation and large strain nonlinear application and will therefore reduce non-convergence issue. For the same reasons, the stiffeners and the interior diaphragms were also modeled by SHELL181 elements. However, the interior and exterior cross-frames and lateral bracings were modeled by using 2-node beam elements, BEAM188 with six degrees

of freedom at each node. BEAM188 element is based on Timoshenko beam theory with shear deformation effects included. This element is suitable for analyzing slender structures such as cross-frames and bracings. The concrete deck and rail were modeled using 8-node solid elements, SOLID65 with three translational degrees of freedom at each node. This element is typically used for three-dimensional modeling of solids with or without reinforcing bars. Specially, this particular element has additional cracking and crushing capabilities making it a perfect element for concrete modeling. Figure 5-1 illustrates the complete model of the bridge in ANSYS.

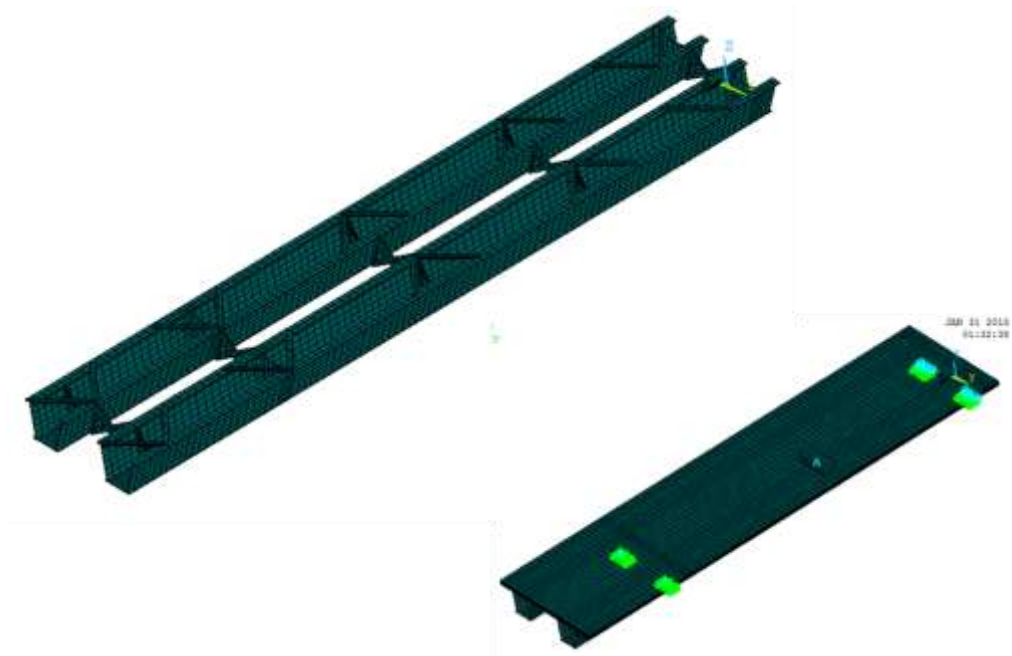


**Figure 5-1 Finite element bridge model.**

## **5.2 Fracture Damage and Connection Modeling**

Basically, there are two approaches to simulate fracture/crack condition in the girder. The first and the simplest approach is removing or deleting the selected elements at fractured location. The second approach is separating the coincident nodes in the bottom

flange and webs, at fracture location before merging all other coincident nodes. Although both approaches provided similar results in general, the later one was eventually chosen because it was the best representation of how the fracture was induced in the experiment.

The process to simulate the fractured condition is described as illustrated in Figure 5-2a-d. Note that two nodes plotted next to each other are coincident nodes with the same location. First, node at fractured location is selected as shown by red dot in Figure 5-2a. The selected node is then separated from its companion node by shifting to the right a small distance as illustrated in Figure 5-2b. Once separated, all other coincident nodes are merged together as shown in Figure 5-2c. In the last step, the separated node is brought back to the original location as shown in Figure 5-2d. The final simulation of full-web fracture condition is illustrated in Figure 5-3. It should be noted that two fractured segments still are connected together by sharing the same nodes at the top flanges.

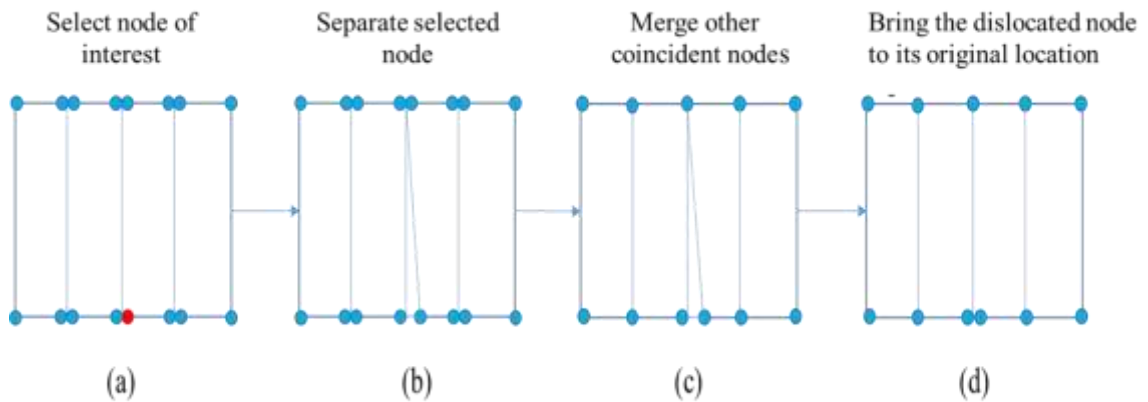


**Figure 5-2 Process to simulate a fracture condition.**

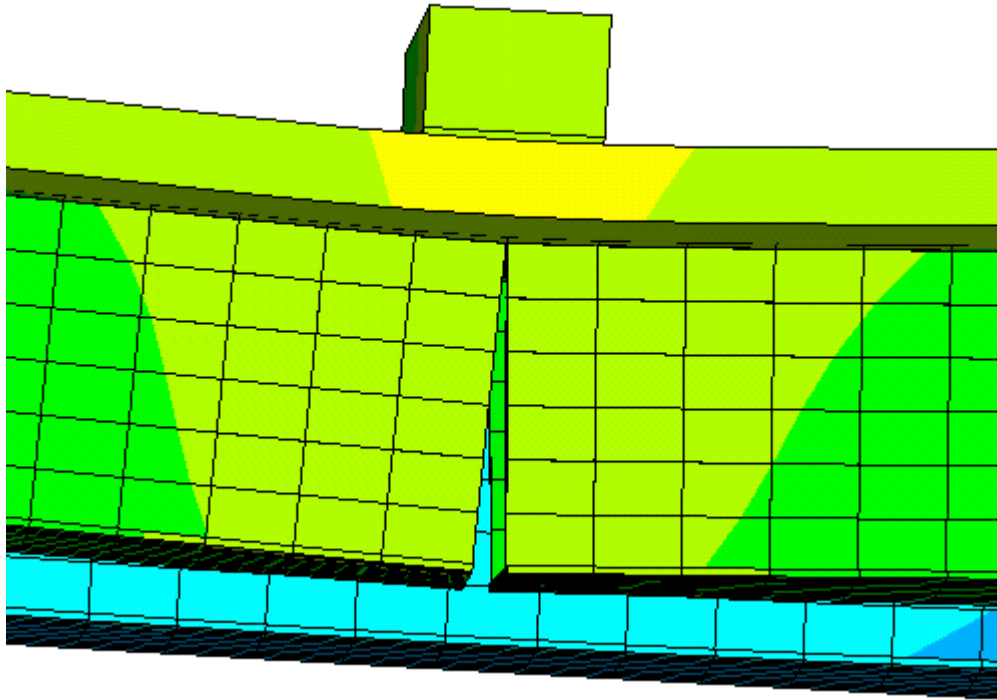


**Figure 5-3 Finite element model with full-web fracture condition.**

Since the subject of this study only focused on the inelastic behavior of the twin steel box-girder bridge under the worst-damage condition, which is full-web fracture condition, the need to simulate the crack propagation was eliminated.

### **5.3 Steel Behavior Modeling**

The inelastic behaviors of steel plates, steel brace members, and steel reinforcement were modeled as a multi-linear inelastic model with isotropic hardening (Dassault Systemes, 2007). Von Mises plasticity was incorporated, which means the material was assumed to yield when the equivalent stress exceeded the von Mises yield criterion, and the perfectly plastic behavior was assumed when the stress exceeded yield stress. This

research used available data rather than testing to verify the steel material properties and behavior. The steel plates and bracing members used to construct this small-scaled specimen were A709 Grade 50 steel while the steel reinforcement bars were A706 Grade 60 reinforcement. The stress-strain curves of the steel plates and rebars shown in Figure 5-4 are approximations of typical stress-strain curves of A709 Grade 50 steel and A706 Grade 60 steel reinforcements under uniaxial tension load.

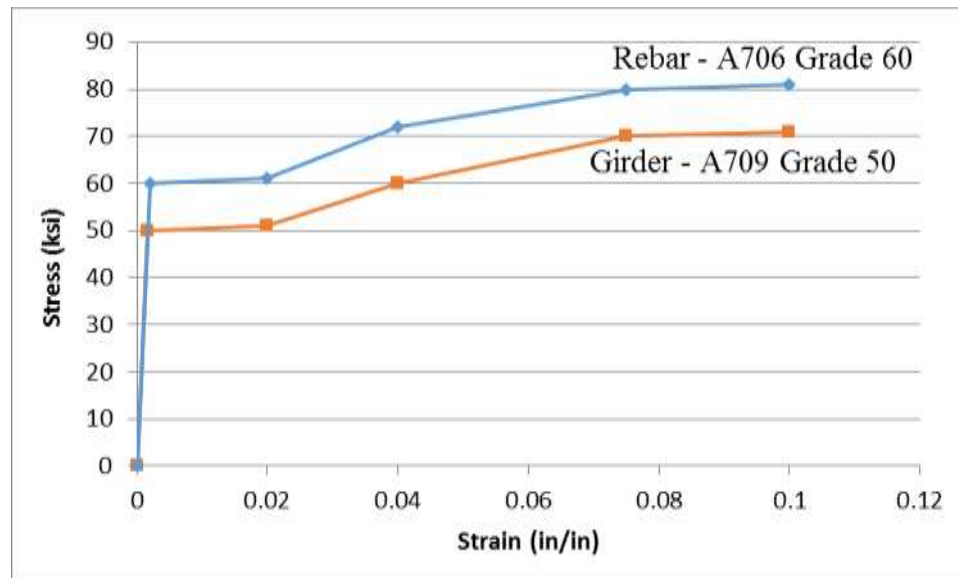


**Figure 5-4 Stress-strain behavior of steel girder and rebars.**

All the bolts that were used for connections in external and internal cross-frames are A325 Type 1 steel with 5/8-in. diameter. These bolts are supposed to have a minimum yield strength of 92 ksi and a minimum tensile strength of 120 ksi according to ASTM A325-14. To simplify the model, these bolt connections were modeled assuming full connections. This assumption was reasonable as the failure modes observed in the laboratory tests indicated that the failure of cross-frame connections did not significantly affect the capacity of the specimen.

## 5.4 Concrete Material Properties

FDOT uses Class II concrete mix with 28-day strength of 4,500 psi, 3-in. slump and ¾-in. maximum aggregate size. This is also the concrete that was used for the deck of bridge in this project. The concrete cylinder strengths were tested for the first specimen as well as the reconstructed specimen. The results of concrete compressive strengths for the first specimen are summarized in Table 5-1. The average of all concrete cylinder tests was 7,829 psi, and this is the final value used in respective simulated finite element models.

**Table 5-1 Concrete Cylinder Strengths for First Specimen**

| Specimen ID | Date Poured | Specimen Age (days) | Avg. Diameter (in)              | Avg. Length (in)                 | Weight (lb) | Ultimate Load (lb) | Strength (psi) |
|-------------|-------------|---------------------|---------------------------------|----------------------------------|-------------|--------------------|----------------|
| C1-1        | 7/29/13     | 120                 | 5 <sup>15</sup> / <sub>16</sub> | 11 <sup>7</sup> / <sub>8</sub>   | 27.44       | 218560             | 7893           |
| C1-2        | 7/29/13     | 120                 | 5 <sup>15</sup> / <sub>16</sub> | 11 <sup>7</sup> / <sub>8</sub>   | 27.50       | 203850             | 7361           |
| C1-3        | 7/29/13     | 120                 | 5 <sup>15</sup> / <sub>16</sub> | 11 <sup>7</sup> / <sub>8</sub>   | 27.32       | 216480             | 7818           |
| C1-4        | 7/29/13     | 120                 | 5 <sup>15</sup> / <sub>16</sub> | 11 <sup>13</sup> / <sub>16</sub> | 27.32       | 221220             | 7989           |
| C1-5        | 7/29/13     | 150                 | 5 <sup>15</sup> / <sub>16</sub> | 11 <sup>5</sup> / <sub>8</sub>   | 26.74       | 226110             | 7997           |
| C1-6        | 7/29/13     | 150                 | 5 <sup>15</sup> / <sub>16</sub> | 11 <sup>11</sup> / <sub>16</sub> | 26.96       | 217050             | 7677           |
| C1-7        | 7/29/13     | 150                 | 5 <sup>15</sup> / <sub>16</sub> | 11 <sup>9</sup> / <sub>16</sub>  | 26.92       | 228090             | 8067           |
| Average     |             |                     |                                 |                                  |             |                    | <b>7829</b>    |

The reconstructed specimen used the same concrete mix as mentioned above. The concrete cylinder strengths at test day are summarized below in Table 5-2. Please note that in the first four cylinder tests, the average diameter and length of the cylinders were assumed to be 6” and 12” respectively, because the measurements were not taken that day.



The average concrete compressive strength for the reconstructed specimen was approximately 7,135 psi.

**Table 5-2 Concrete Cylinder Strengths for Reconstructed Specimen**

| Specimen ID | Date Poured | Specimen Age (days) | Avg. Diameter (in)              | Avg. Length (in)                 | Weight (lb) | Ultimate Load (lb) | Strength (psi) |
|-------------|-------------|---------------------|---------------------------------|----------------------------------|-------------|--------------------|----------------|
| C2-1        | 12/22/14    | 49                  | 6                               | 12                               | 28.56       | 207530             | 7340           |
| C2-2        | 12/22/14    | 49                  | 6                               | 12                               | 28.54       | 199120             | 7043           |
| C2-3        | 12/22/14    | 49                  | 6                               | 12                               | 28.58       | 201270             | 7118           |
| C2-4        | 12/22/14    | 49                  | 6                               | 12                               | 28.54       | 199220             | 7046           |
| C2-5        | 12/22/14    | 52                  | 5 <sup>15</sup> / <sub>16</sub> | 11 <sup>5</sup> / <sub>8</sub>   | 27.04       | 197780             | 7143           |
| C2-6        | 12/22/14    | 52                  | 5 <sup>7</sup> / <sub>8</sub>   | 11 <sup>11</sup> / <sub>16</sub> | 27.26       | 193030             | 7121           |
| Average     |             |                     |                                 |                                  |             |                    | <b>7135</b>    |

A tensile splitting test were also performed on two concrete cylinders. The cylinders were loaded at a rate of 106 psi/min and the results are shown below in Table 5-3. The average tensile strength of concrete was found to be 545 psi. Although this tensile strength might be slightly different for the first specimen, this value was used for all finite element models.

**Table 5-3 Concrete Tensile Strengths for Reconstructed Specimen**

| Specimen ID | Date Poured | Specimen Age (days) | Avg. Diameter (in)              | Avg. Length (in)                 | Weight (lb) | Ultimate Load (lb) | Strength (psi) |
|-------------|-------------|---------------------|---------------------------------|----------------------------------|-------------|--------------------|----------------|
| T2-1        | 12/22/14    | 49                  | 5 <sup>15</sup> / <sub>16</sub> | 11 <sup>15</sup> / <sub>16</sub> | 27.04       | 58885              | 529            |
| T2-2        | 12/22/14    | 49                  | 5 <sup>15</sup> / <sub>16</sub> | 11 <sup>15</sup> / <sub>16</sub> | 27.08       | 62340              | 560            |
| Average     |             |                     |                                 |                                  |             |                    | <b>545</b>     |

In this study, concrete was modeled using a multi-linear isotropic hardening material. Concrete compressive behavior was constructed using EQ 5-1 as suggested by Hognestad (1951). With the ultimate strain ( $\epsilon_0=0.003$ ) and concrete compressive strength that was found earlier from concrete cylinder tests, the stress-strain curve of concrete under uniaxial compressive force is graphically illustrated in Figure 5-5. On the tension side of the stress-strain curve, the concrete is assumed to have the same initial stiffness as it has initially for the compression strength under uniaxial force as mentioned in finite element software package such as ANSYS or ABAQUS.

$$f_c = f'_c * \left( 2 * \frac{\epsilon}{\epsilon_0} - \left( \frac{\epsilon}{\epsilon_0} \right)^2 \right)$$

**EQ 5-1**

where  $f_c$  = concrete compressive stress at given strain (ksi)

$f'_c$  = concrete compressive strength (ksi)

$\epsilon_0$  = ultimate strain (in/in)

$\epsilon$  = strain (in/in)

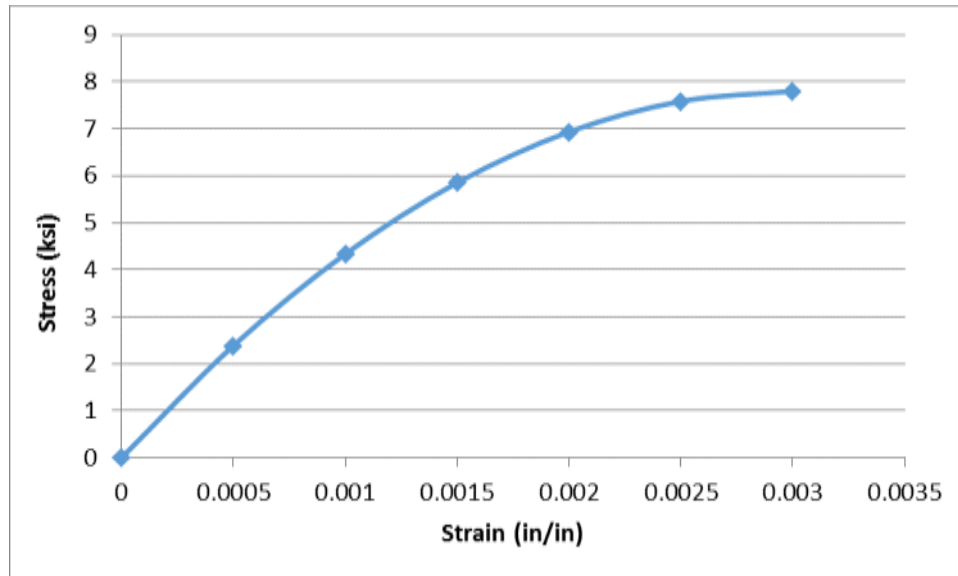


Figure 5-5 Modeling of stress-strain curve of concrete in compression.

## 5.5 Concrete and Reinforcement Behavior Modeling

Concrete was modeled in ANSYS by SOLID65, a three dimensional eight-node isotropic solid element as shown in Figure 5-6. The SOLID65 element is capable of plastic deformation, creep, cracking in three orthogonal directions, and crushing. SOLID65 has one solid element and up to three rebar materials. Rebar specifications are input as real constants, including material properties, volume ratio with respect to the solid element volume, and the orientations as denoted by  $\theta$  and  $\Phi$  in Figure 5-6. The material properties of the steel reinforcement bars are discussed in the section above. The steel bars are capable of tension, compression but no shear. The reinforcement bars are modeled to be “smeared” throughout the elements. Figure 5-7 shows the smeared steel reinforcement inside the SOLID65 elements. In this specimen, the concrete is reinforced in both longitudinal and transverse directions.

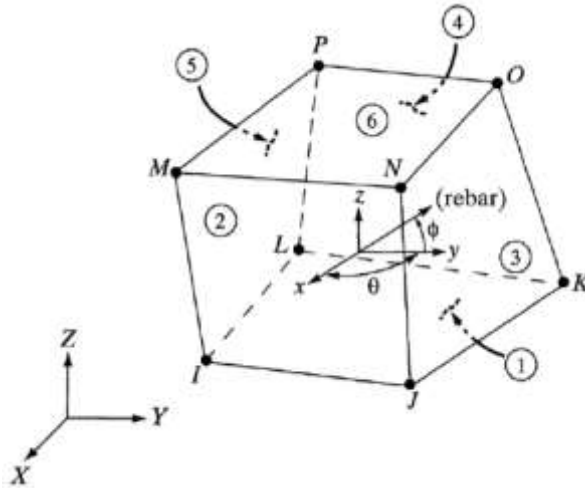


Figure 5-6 SOLID65 concrete element in ANSYS.

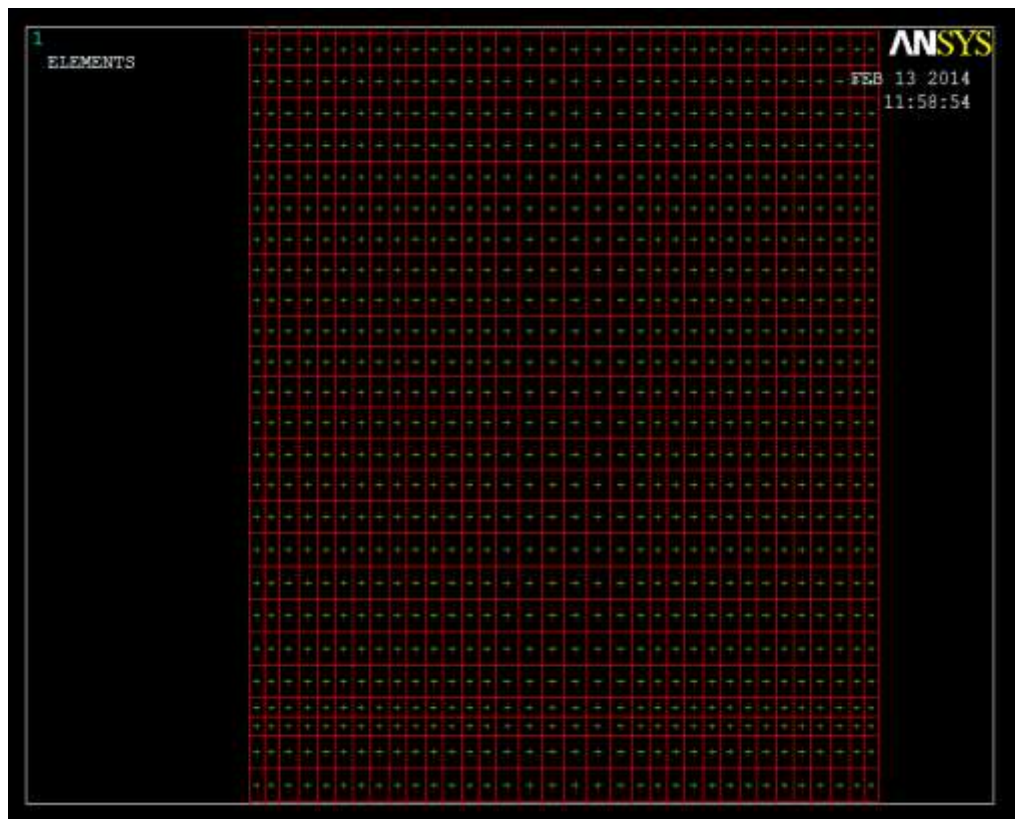


Figure 5-7 Smearred reinforcement bars.

Concrete material data are input through nine constants, which are summarized in Table 5-4, for SOLID65 elements. The first two constants are shear transfer coefficients for open and closed cracks. These shear transfer coefficients can vary from zero to one.

Zero represents a smooth crack with no shear transfer and one represents a rough crack with full shear transfer. Previous studies have shown that if the shear transfer coefficient for an open crack is below 0.2 (Kachlakev et al., 2001), the model might face convergence issues. In this study, only the first four constants are input while the last five constants are left at their default values. In this study, the shear transfer coefficients are assumed to be 0.35 for an open crack and 1.0 for a closed crack. The uniaxial tensile cracking stress limit, which corresponds to the constant number 3, is assumed to be 0.55 ksi based on the results of cylinder splitting tests. The uniaxial crushing stress limit is assumed to be the same with the average concrete cylinder compressive strength that were found from concrete cylinder tests.

The Willam and Warnke (1975) yield criterion was used to define a failure surface of concrete material. The biaxial and triaxial failure surfaces of concrete material are illustrated in Figure 5-8. In this model, the concrete element is defined as cracked when a principal stress exceeds the ultimate tensile strength. The cracking plane is perpendicular to the direction of principal stress which tensile stress exceeded. The crack can occur in all three principal directions. If the material at an integration point fails in uniaxial, biaxial, or tri-axial compression, the material is assumed to crush at that point. This means the concrete is assumed to be crushed when one or all principal stresses lie outside the failure surface. When crushing occurs, strength of concrete is assumed to degrade to an extent such that the contribution to the stiffness of an element at the integration point in question can be ignored.

**Table 5-4 Input Parameters for Properties of Concrete Materials**

| <b>Constant</b> | <b>Meaning</b>   |
|-----------------|--|
| 1               | Shear transfer coefficients for an open crack.   |
| 2               | Shear transfer coefficients for a closed crack.  |
| 3               | Uniaxial tensile cracking stress.  |
| 4               | Uniaxial crushing stress (positive).   |
| 5               | Biaxial crushing stress (positive).  |
| 6               | Ambient hydrostatic stress state for use with constants 7 and 8.                             |
| 7               | Biaxial crushing stress (positive) under the ambient hydrostatic stress state (constant 6).  |
| 8               | Uniaxial crushing stress (positive) under the ambient hydrostatic stress state (constant 6). |
| 9               | Stiffness multiplier for cracked tensile condition, used if KEYOPT(7) = 1 (defaults to 0.6). |

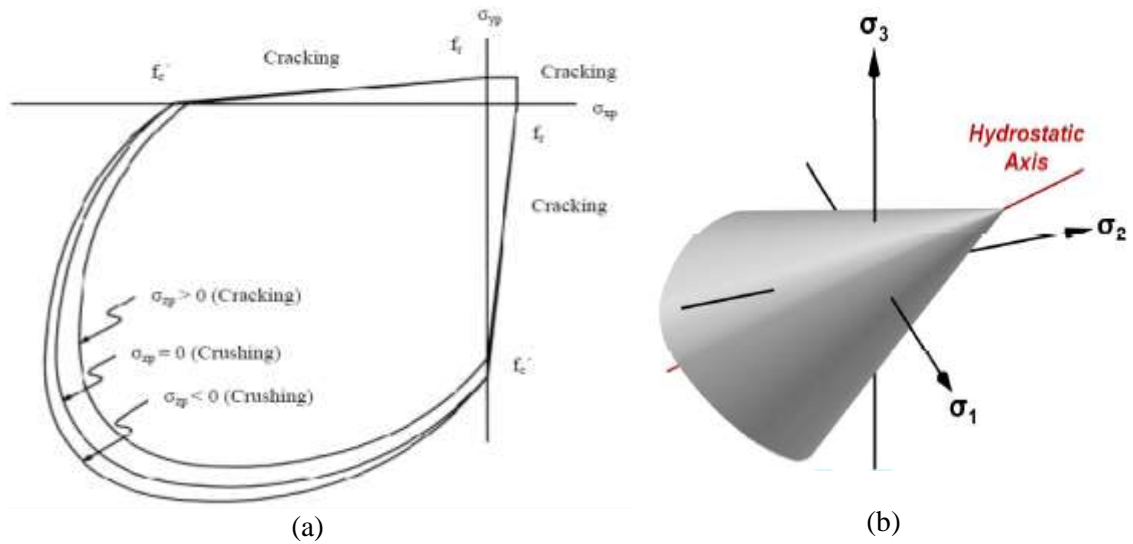


**Figure 5-8 Failure surfaces of concrete under (a) biaxial and (b) triaxial loading states (Willam and Warnke, 1975).**

This concrete model is known to be sensitive to mesh density, especially at contact surfaces (Dassault Systemes, 2007). Material properties and the element size through thickness of the deck were also found to affect the convergence of the simulated models.

## 5.6 Bearing Pad and Contact Surface Modeling

The bearing pads that were used in this experiment were steel reinforced elastomeric pads with a durometer hardness range of 50. The dimension of the bearing pads is 1 in. x 24 in. x 2 in. Based on the provided durometer hardness, the shear modulus of the pads, at room temperature, ranges from 85 psi to 110 psi, according to FDOT Structure Specifications for Road and Bridge Construction, or 95 psi to 130 psi according to *AASHTO LRFD Bridge Design Specification*. In this study, the shear modulus was assumed to be 100 psi. According to Lee (1994), the bulk modulus for 50 Shore hardness elastomeric bearings is assumed to be 2,060 MPa, which is equivalent to 290 ksi. The typical Young's modulus for 50 Shore hardness is approximately 320 psi. Young's modulus of elastomeric bearings for different Shore hardness was provided by Podolny

and Muller (1982). The typical stress-strain curve for steel reinforced bearing pads based on the hardness and the shape factor is shown in Figure 5-9.

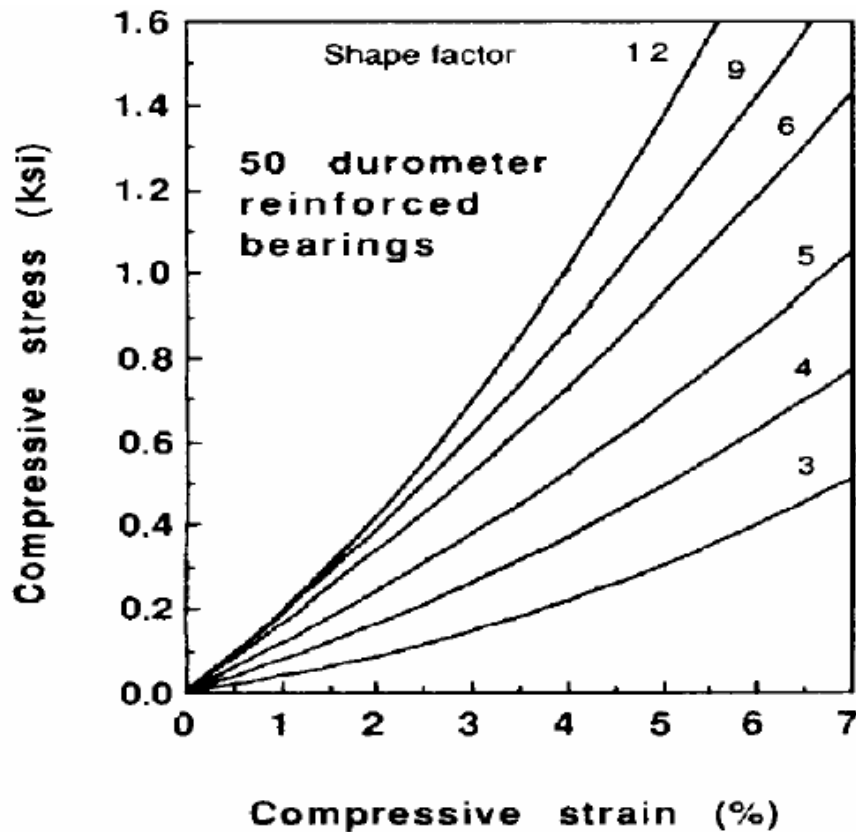
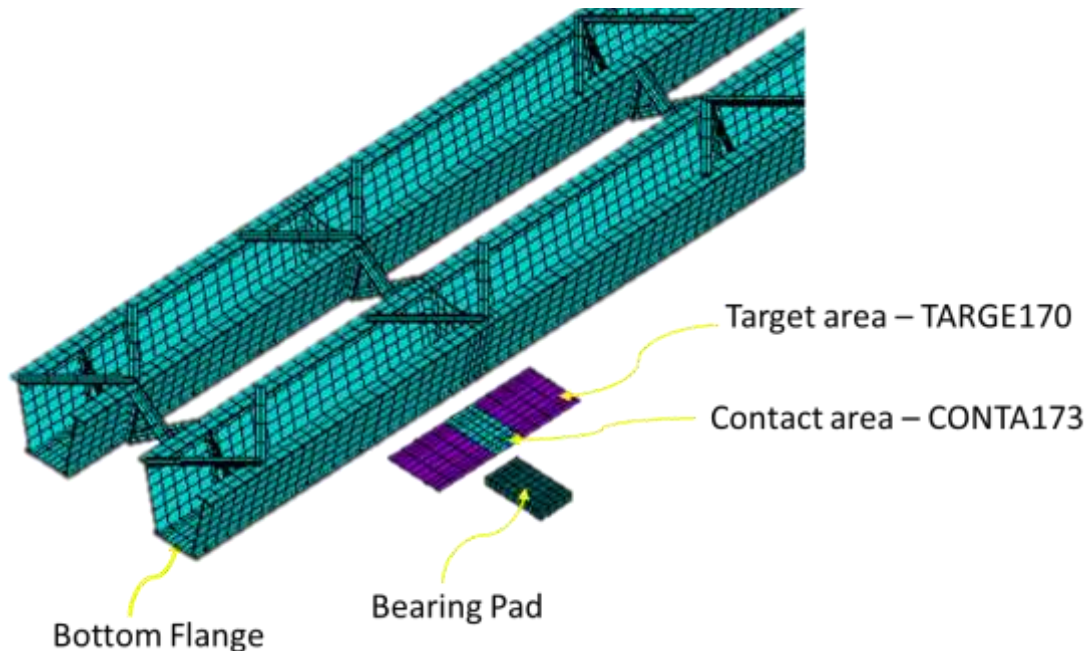


Figure 5-9 Typical stress-strain curve for steel-reinforced bearings (AASHTO-C14.7.6.3.3-1).

These bearing pads were simulated using SOLID185 elements. The material nonlinearity of the pads was modeled using three-parameter Mooney-Rivlin hyper-elastic material model. The input data for Mooney-Rivlin model requires three parameters, which are  $C_{10}$ ,  $C_{01}$  and  $C_{11}$ . These three parameters are material constants characterizing the deviatoric deformation of the material. These constants are usually determined by curve-fitting the experimental data. It was suggested to use 0.044, 0.011 for the first two parameters for 50 shore hardness bearings (Altidis and Adams, 2005). The third parameter  $C_{11}$  was determined to be 100 based on parametric studies. This parameter will take into account the fact that the effective shear modulus also increases as compression increases.



In addition to the bearing pad models, the contact surfaces between the bearing pads and bottom flange of the girders were also modeled to capture the uplift incident that occurred during the test. The contact surface was modeled using a combination of TARGE170 element and CONTA173 element as shown in Figure 5-10. TARGE170 element is used to model a 3-D target surface where the contact occurs while CONTA173 is surface-to-surface contact element without mid-side node which is used to model contact and sliding between target surface and a deformable body. If the beneath solid or shell element surface do have mid-size node, CONTA174 will be used. The target surface is paired with its associated contact surface via a shared real constant set. As illustrated in the figure, the target area could be larger than the contact area.



**Figure 5-10 Contact surface between the bearing pad and bottom flange of girder.**

In ANSYS, the behavior of CONTA173 element can be controlled or characterized through a set of KEYOPTs and real constants. The default KEYOPTs and used KEYOPTs

are summarized in Table 5-5. Depending on which KEYOPT option is used, the properties of the contact element then will be determined by a set of real constants such as contact stiffness, limit of initial penetration, friction coefficient damping factor and so on. The default values of these real constants are provided by ANSYS unless they are manually specified by the users. In some cases, the default values of a real constant will vary depending on the option selected for KEYOPTs. The parameters for the contact elements for both default KEYOPTs and used KEYOPTs are summarized in Table 5-6.

There were 3 KEYOPTs that were manually input (not by default) for the nonlinear finite element analyses performed in this study including KEYOPTs 2, 4 and 12. The default option for KEYOPT 2 is to use the augmented Lagrangian method as a contact algorithm. This method requires an iteration in which the contact tractions (pressure and frictional stresses) are augmented during the equilibrium iteration so that the final penetration is smaller than the allowable tolerance. This option is less sensitive to the magnitude of the contact stiffness; however, it requires additional iterations especially for nonlinear analyses with large deformation and high level of element distortion which is also the case for this study. Therefore, the pure Lagrange multiplier method was used instead in this study. This method does not require normal, tangent penalty stiffness factors and allowable elastic slip (FKN, FKT and SLTO respectively). But instead, it requires penetration tolerance factor (FTOLN) which was set as 0.1 (10% of the element thickness) and maximum allowable tensile contact pressure (TNOP) which was automatically determined by the program by dividing the force convergence tolerance by the contact area. The force convergence tolerance was set as 2.5% in these analyses.

KEYOPT 4 by default uses Gauss integration points which are located inside the element surface as contact detection points. However, several analyses with different options were performed and the results indicated that the nodal detection which uses the nodes themselves as the integration points was more suitable for this model because the need of having very fine mesh at contact area to capture uplift accurately (which is not the objective of this study) could be eliminated which in turn reduced computational time. However, one of the disadvantage of using nodes as contact detection points can cause some convergence issues such as “node slippage” where the node slips off the edge of the target surface. In order to prevent such issues, ANSYS uses real constant TOLS, which is determined as a percent of the target edge length, to add a small tolerance that will internally extend the edge of the target surface.

KEYOPT 12 by default uses standard unilateral contact model in which the normal pressure equals zero if separation between two nodes occurs. However, after performing several trial analyses, the results indicated that using perfectly rough frictional contact where no sliding was allowed (only vertical separation is allowed) was adequate and required much less computational time. All of KEYOPTs that were used in all nonlinear analyses in this study is illustrated in **Error! Reference source not found.**

In general, most of the parameters characterizing the behavior and properties of contact element CONTA173 were used by the default values. Most of parameters are interpreted by ANSYS as a scaling factor without units except maximum friction stress (TAUMAX) and contact cohesion (COHE). Beside normal, tangent penalty stiffness and allowable elastic slip factors (FKN, FKT and SLTO respectively), the coefficient of

restitution (COR) for impact between rigid bodies is also not required. It is only required when the impact constraints is activated by KEYOPT 7 with a transient dynamic analysis.

**Table 5-5 Summary of KEYOPTs Defaults in ANSYS.**

| <b>KEYOPT</b> | <b>Description</b>                         | <b>ANSYS Default</b>           | <b>Selected Options</b>                    |
|---------------|--|--------------------------------|--|
| 1             | Selects DOF                                | UX/UY/UZ                       | UX/UY/UZ                                   |
| 2             | Contact Algorithm                          | Augmented Lagrange             | Pure Lagrange Multiplier                   |
| 3             | Stress state when super element is present | No super element               | No super element                           |
| 4             | Location of contact detection point        | Gauss Integration Points       | Nodal Points – Normal from Contact Surface |
| 5             | CNOF/ICONT adjustment                      | No adjust                      | No adjust                                  |
| 6             | Contact stiffness variation                | Use default range              | Use default range                          |
| 7             | Element level time increment control       | No control                     | No control                                 |
| 8             | Asymmetric contact selection               | No action                      | No action                                  |
| 9             | Effect of initial penetration or gap       | Include all                    | Include all                                |
| 10            | Contact stiffness update                   | Between load steps             | Between load steps                         |
| 11            | Beam/shell thickness effect                | Exclude                        | Exclude                                    |
| 12            | Behavior of contact surface                | Standard                       | Rough                                      |
| 14            | Behavior of fluid penetration load         | Iteration-based                | Iteration-based                            |
| 15            | Effect of stabilization damping            | Active only in first load step | Active only in first load step             |
| 16            | Squeal damping controls                    | Damping scaling factor         | Damping scaling factor                     |

**Table 5-6 Summary of Default and Input Real Constants.**

| <b>Real Constant Name</b> | <b>Description</b>                         | <b>ANSYS Default</b>                                | <b>Used Value</b>         |
|---------------------------|--|---|---------------------------|
| FKN                       | Normal penalty stiffness factor            | 1   | N/A                       |
| FTOLN                     | Penetration tolerance factor               | 0.1%  | 0.1%                      |
| ICONT                     | Initial contact closure                    | 0   | 0                         |
| PINB                      | Pinball region                             | 2   | 2                         |
| PMAX                      | Upper limit of initial penetration         | 0   | 0                         |
| PMIN                      | Lower limit of initial penetration         | 0   | 0                         |
| TAUMAX                    | Maximum friction stress                    | 1.00E+20<br>(Pressure)                              | 1.00E+20<br>(ksi)         |
| CNOF                      | Contact surface offset                     | 0   | 0                         |
| FKOP                      | Contact opening stiffness factor           | 1   | 1                         |
| FKT                       | Tangent penalty stiffness factor           | 1   | N/A                       |
| COHE                      | Contact cohesion                           | 0 (Pressure)  | 0 (ksi)                   |
| FACT                      | Static/dynamic ratio                       | 1   | 1                         |
| DC                        | Exponential decay coefficient              | 0   | 0                         |
| SLTO                      | Allowable elastic slip                     | 1%  | N/A                       |
| TNOP                      | Maximum allowable tensile contact pressure | Force<br>Convergence<br>Tolerance /<br>Contact Area | 2.5% /<br>Contact<br>Area |
| TOLS                      | Target edge extension factor               | 2%  | 2%                        |
| PPCN                      | Pressure-penetration criterion             | 0   | 0                         |
| FPAT                      | Fluid penetration acting time              | 0.01  | 0.01                      |
| COR                       | Coefficient of restitution                 | 1   | N/A                       |
| FDMN                      | Normal stabilization damping factor        | 1   | 1                         |
| FDMT                      | Tangential stabilization damping factor    | 0.001   | 0.001                     |
| FDMD                      | Destabilizing squeal damping factor        | 1   | 1                         |
| FDMS                      | Stabilizing squeal damping factor          | 0   | 0                         |

The comparison between the mid-span displacements, before and after the bearing pads and contact elements were modeled, and one of the test results is illustrated in Figure 5-11. This indicated that modeling the bearing pad and contact surface helped the model to have a better agreement with the test results. It should be noted that modeling contact

surface might make these FE models more prone to non-convergence issues. The results from this study suggest that refining mesh density and reducing time step are possible solutions for this problem. In general, the computational time for each nonlinear analysis varied from 6 to 12 hours depending on the tests.

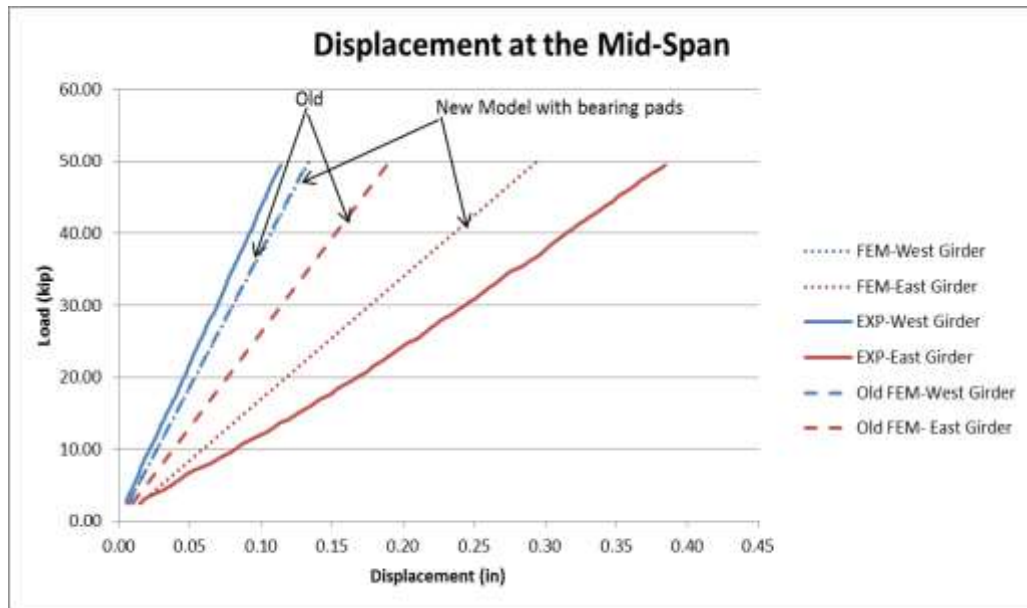


Figure 5-11 Mid-span displacement before and after modeling the bearing pads.

## **Chapter 6 Validating FE Models with Experimental Data**

For verification purposes, the finite element analysis results are compared to the experimental data on selected tests. The verifications will be made in both elastic and inelastic ranges. Due to a high number of elastic tests carried out, only a few tests are selected for the comparison purposes for each damage condition. The experiment data used for the comparison purposes in Section 6.1, 6.2 and 6.3 was extracted from the third ramp in the loading history. Although data from third loading cycle is expected to present the most accurate behavior of the specimen, the specimen might not be completely unloaded at the beginning of the third loading cycle as illustrated in Figure 3-23. That is the reason, the experimental data might not start from zero in some comparison plots.

### **6.1 Undamaged Bridge Specimen**

For the undamaged specimen, the comparison between experimental data and finite element analysis results were made for Test 1, 2, and 3 and presented in the following sections. The comparison includes the longitudinal strain and displacement, at the mid-span section.

#### **6.1.1 Test 1 - No Rail, No Continuity, Symmetric Loading (NNS)**

The first test had NNS characteristics. Figure 6-1 provides a schematic description of the test.

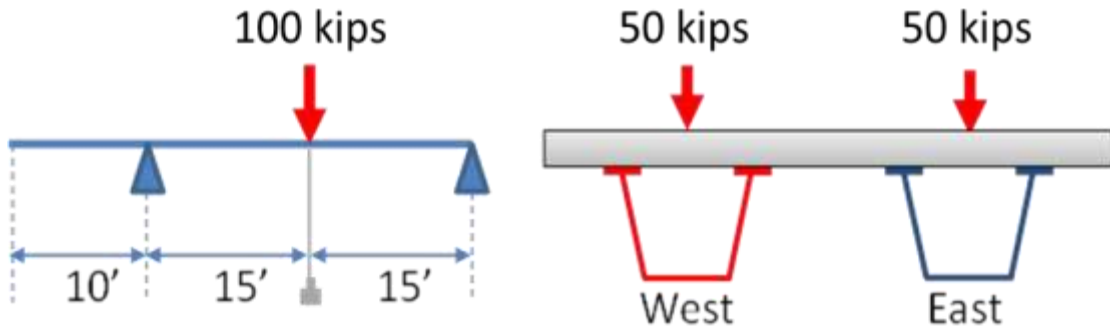


**Figure 6-1 Schematic description of Test 1.**

The vertical displacements at the center of the bottom flange of both girders at the mid-span section are compared with those obtained from FEM in Figure 6-2. The longitudinal strains in the bottom flange and top flange at the mid-span section are compared in Figure 6-3 and Figure 6-4, respectively. In Figure 6-4, only the exterior top flange of EG and the interior top flange of WG were compared, and the same comparison was made in subsequent tests.

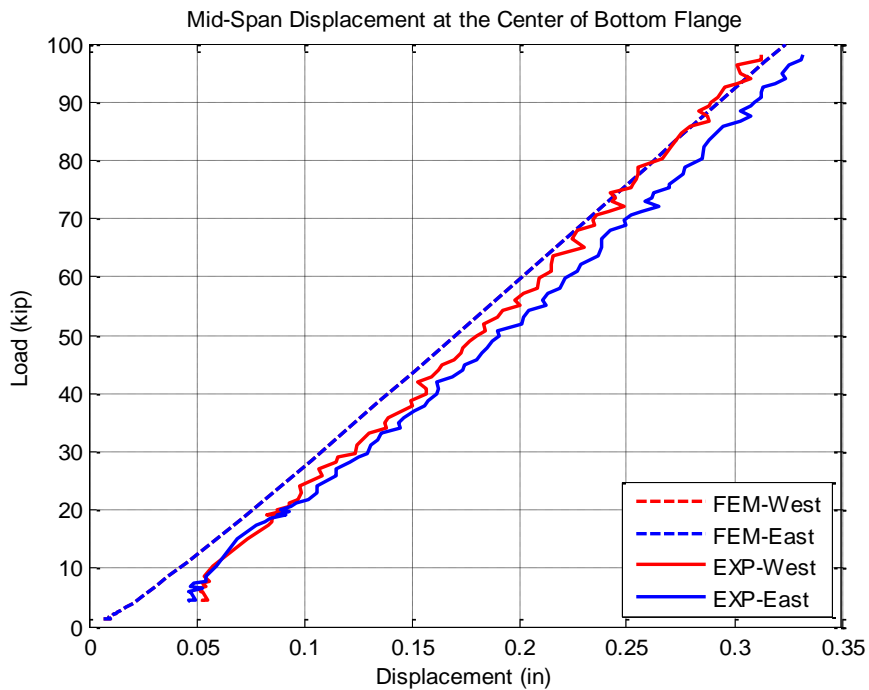


**Figure 6-2 Comparison of vertical displacement at the bottom flange of each girder in Test 1.**



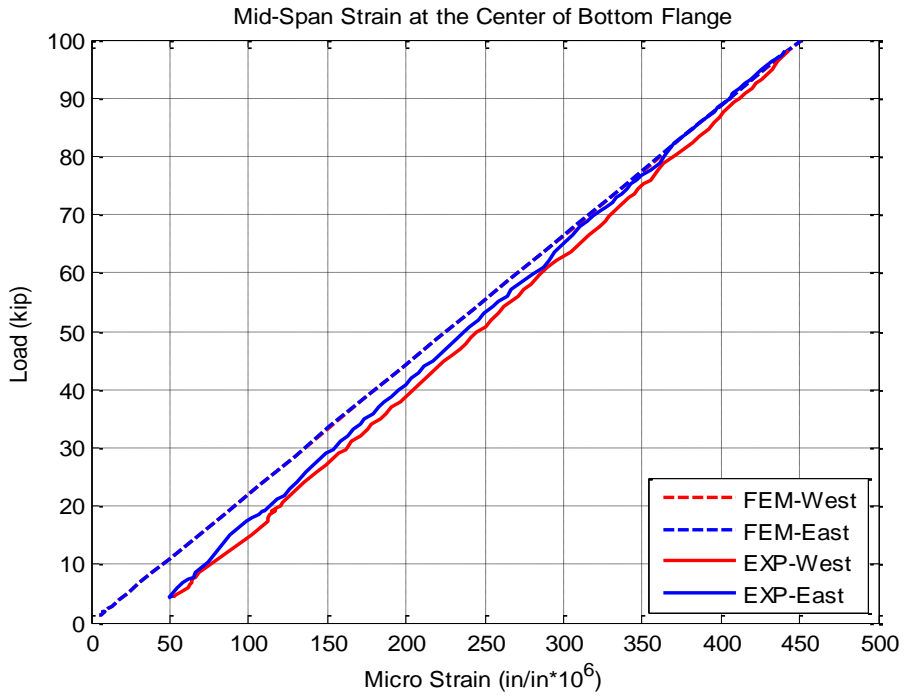


Figure 6-3 Comparison of longitudinal strain at the bottom flange of each girder in Test 1.

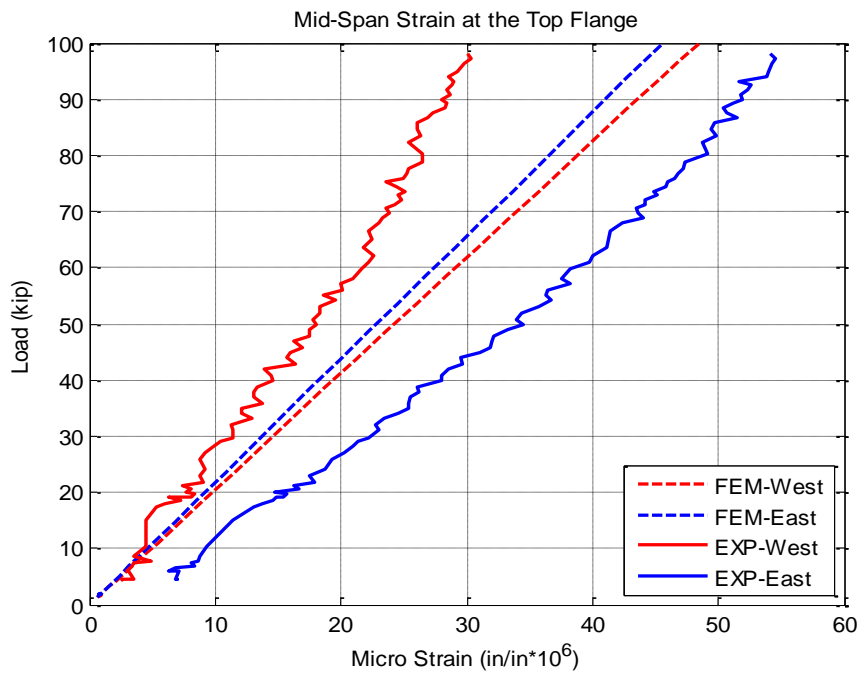
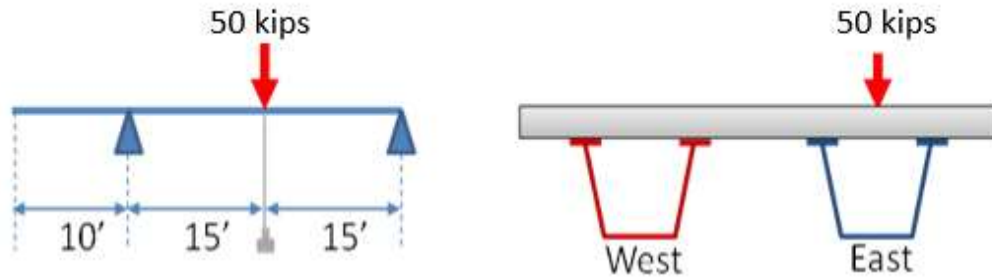


Figure 6-4 Comparison of longitudinal strain at the top flange of each girder in Test 1.

### 6.1.2 Test 2 - No Rail, No Continuity, Unsymmetrical Loading (NNU)

Test 2 NNU was carried out without railing and continuity installed. Schematic drawing of the test is shown in Figure 6-5.



**Figure 6-5 Schematic description of Test 2.**

Figure 6-6 compares the vertical displacement measured at the center of bottom flange of each girder at mid-span to the one obtained from results of FEA. Figure 6-7 provides a comparison of measured and calculated longitudinal strains at the center of the bottom flange at the mid-span section, while Figure 6-8 compares measured and calculated longitudinal strains in the top flanges.

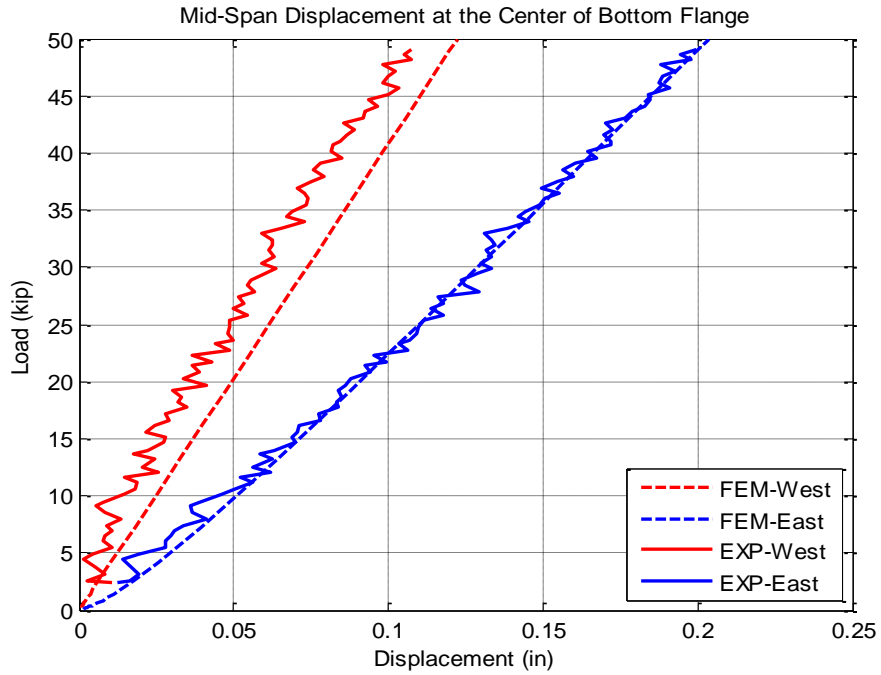


Figure 6-6 Comparison of vertical displacement at the bottom flange of each girder in Test 2.

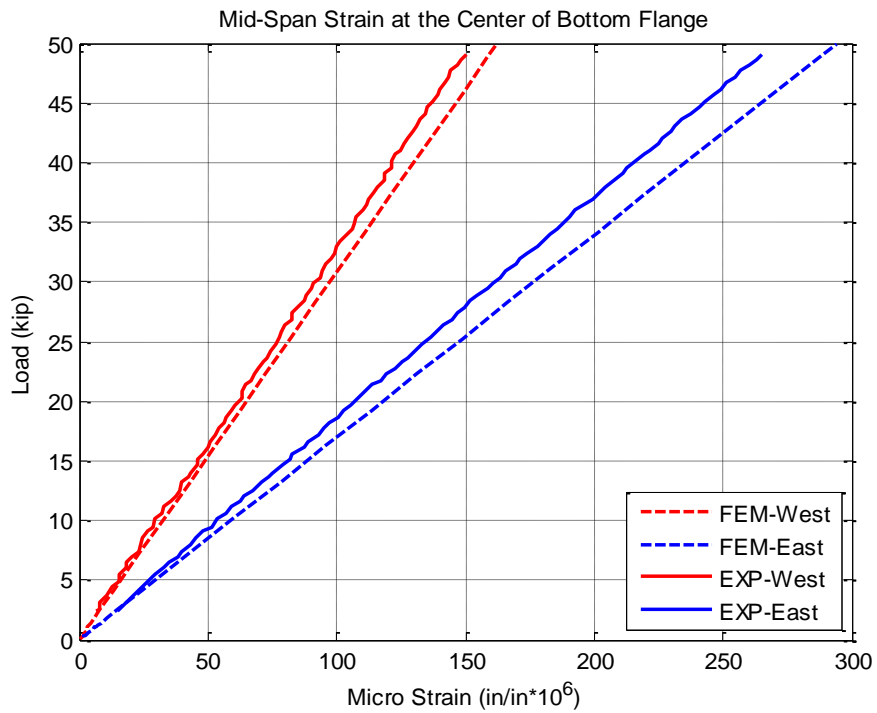


Figure 6-7 Comparison of longitudinal strain at the bottom flange of each girder in Test 2.

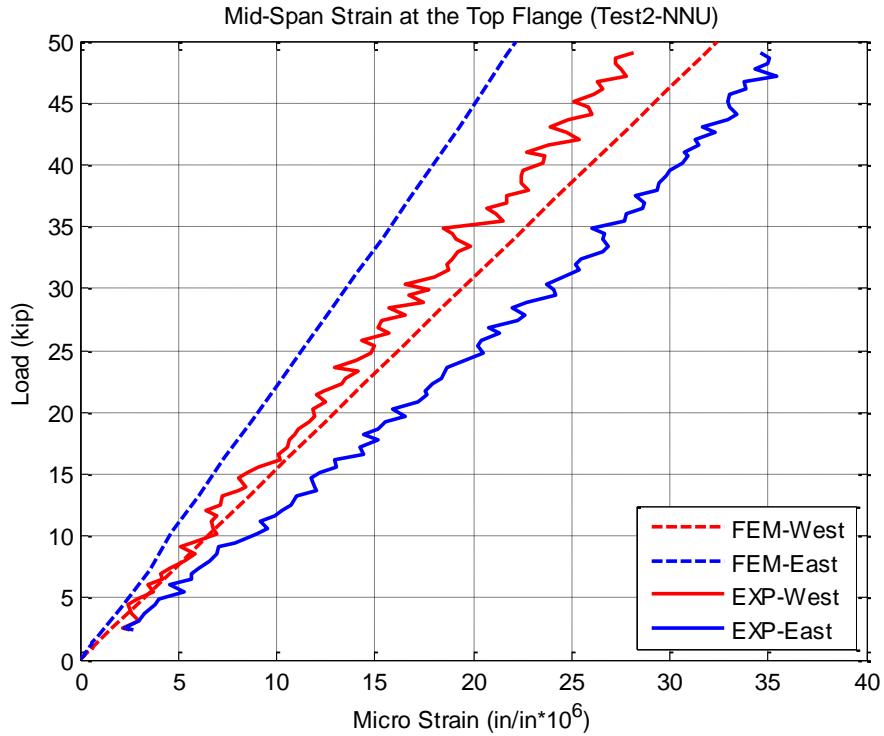


Figure 6-8 Comparison of longitudinal strain at the top flange of each girder in Test 2.

### 6.1.3 Test 3 - No Rail, with Continuity, Unsymmetrical Loading (NYU)

In Test 3 NYU, the cantilever end was restrained from moving up vertically to provide continuity effect. Its schematic description is shown in Figure 6-9.

The vertical displacements of the center of the bottom flange of both girders at the mid-span obtained from the experiment and FEA are compared in Figure 6-10. Similarly, the longitudinal strains in bottom flange and top flange at the mid-span section are compared in Figure 6-11 and Figure 6-12, respectively.

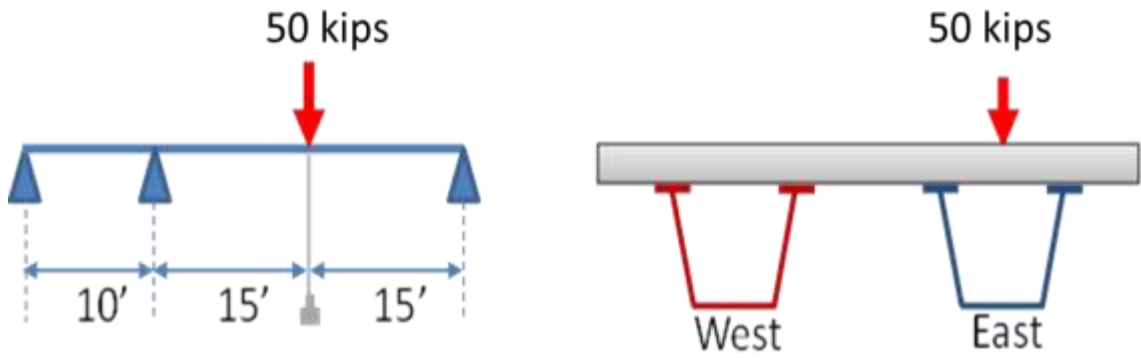


Figure 6-9 Schematic description of Test 3.

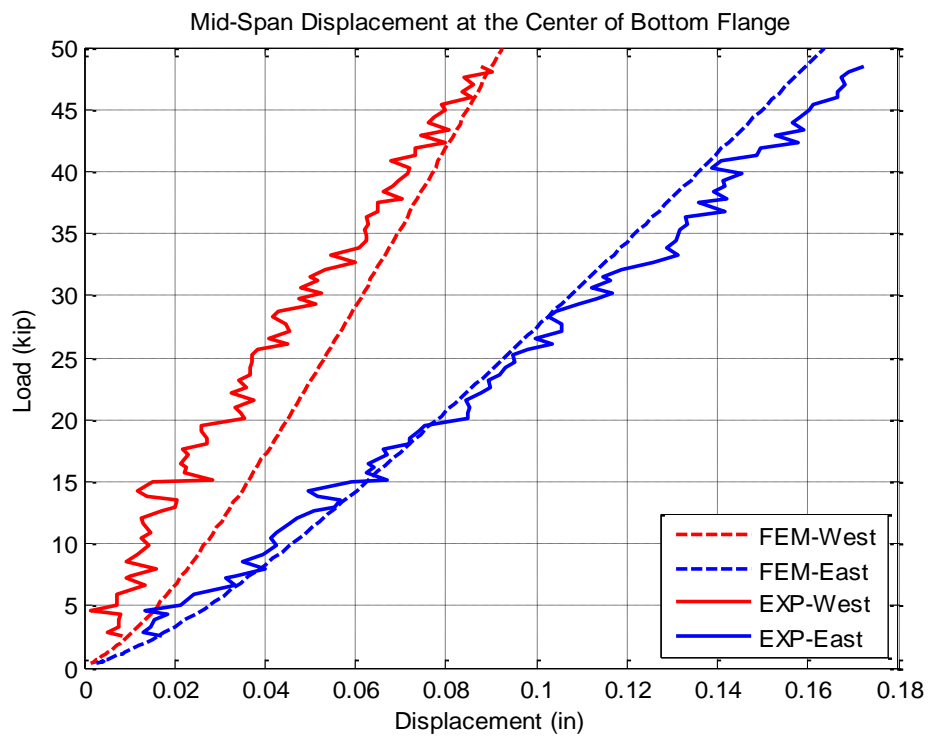


Figure 6-10 Comparison of vertical displacement at the bottom flange of each girder in Test 3.

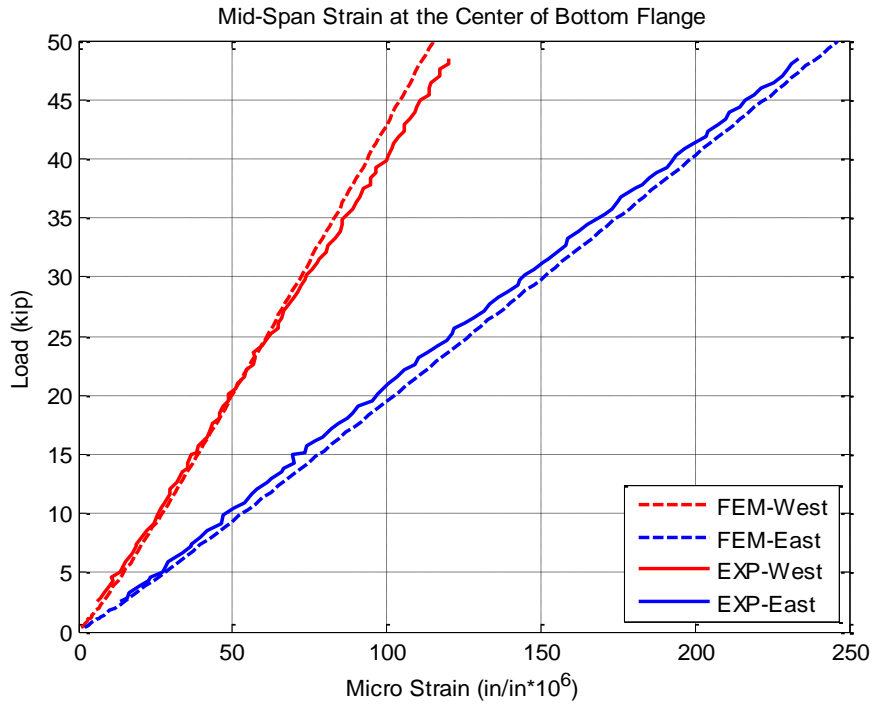


Figure 6-11 Comparison of longitudinal strain at the bottom flange of each girder in Test 3.

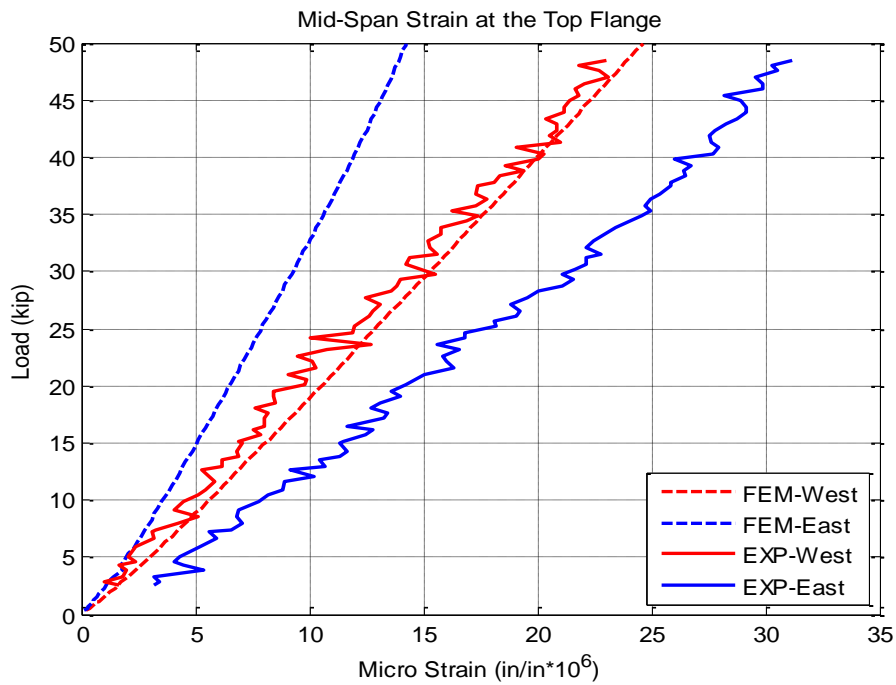


Figure 6-12 Comparison of longitudinal strain at the top flange of each girder in Test 3.

In general, the FEA results showed reasonable agreement with the experimental data for the tests on undamaged specimen, especially in the bottom flanges. In Test 3, the top flange strains showed some discrepancy between FEA and experiment.

## 6.2 Bridge Specimen with Bottom Flange Fractured in One Girder

FEA results and experimental data for Test 9 and Test 10 are compared to verify the FE modeling techniques for the series of tests with the bottom flange fractured in one girder.

### 6.2.1 Test 9 - with Rail, No Continuity, Unsymmetrical Loading (YNU)

Test 9 was YNU with bottom flange fractured in EG as illustrated in Figure 6-13. The mid-span vertical displacements at the center of bottom flange of both girders from the experiment and FEA are compared in Figure 6-14. The longitudinal strains in bottom flange and top flange at mid-span section are compared in Figure 6-15 and Figure 6-16, respectively.

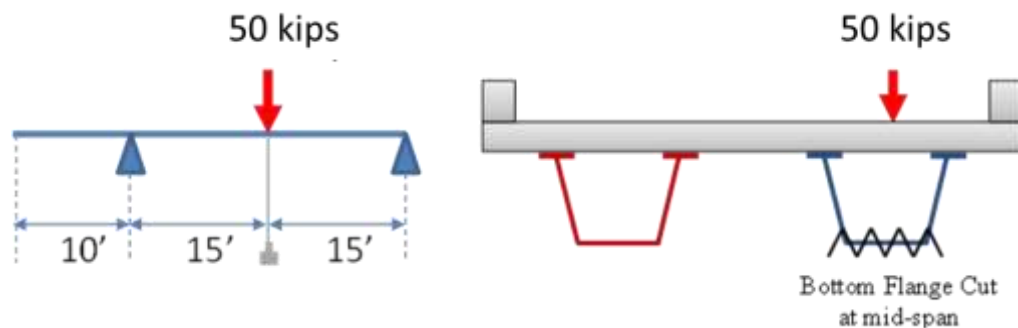


Figure 6-13 Schematic description of Test 9.

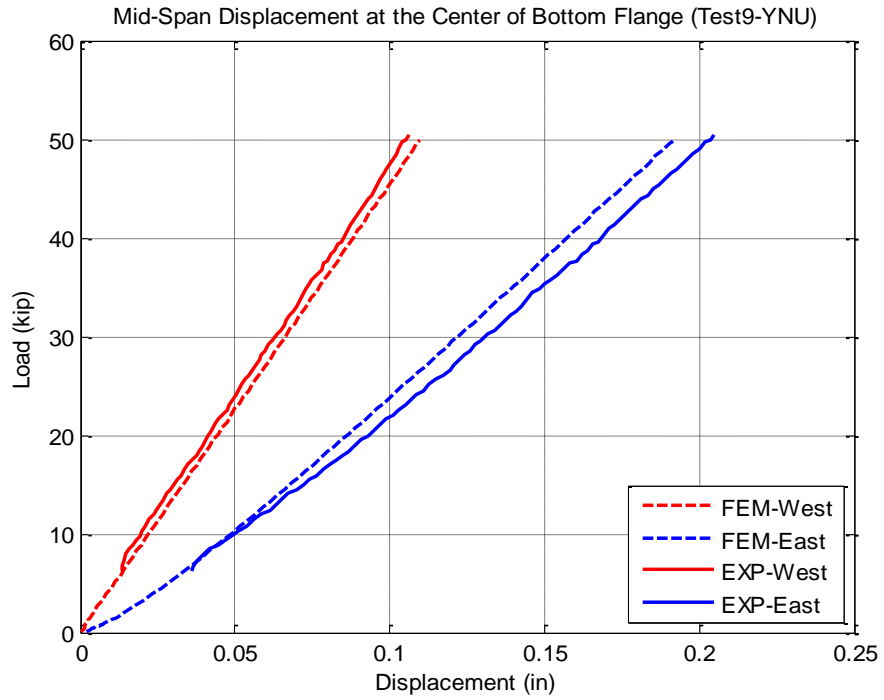


Figure 6-14 Comparison of vertical displacement at the bottom flange of each girder in Test 9.

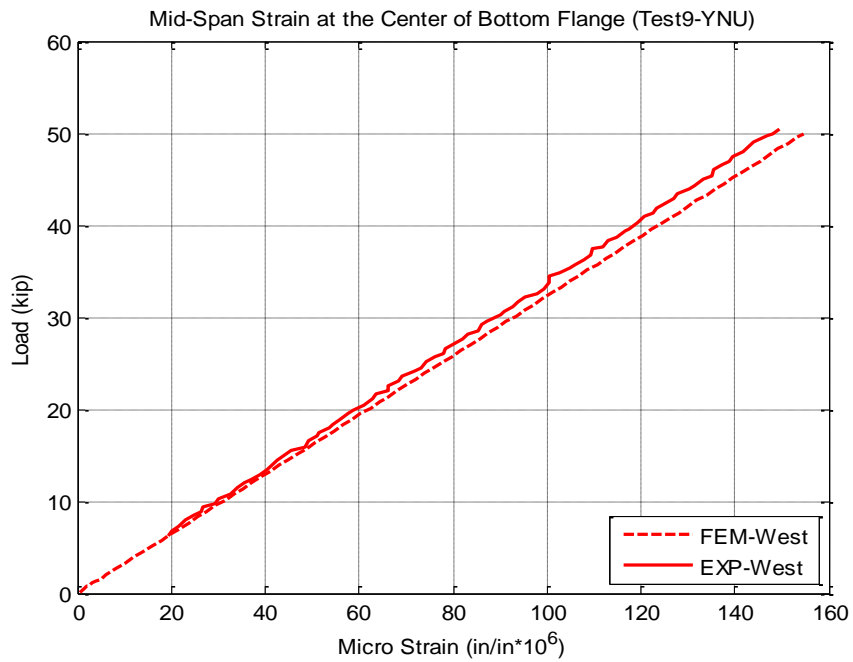


Figure 6-15 Comparison of longitudinal strain at the bottom flange of each girder in Test 9.



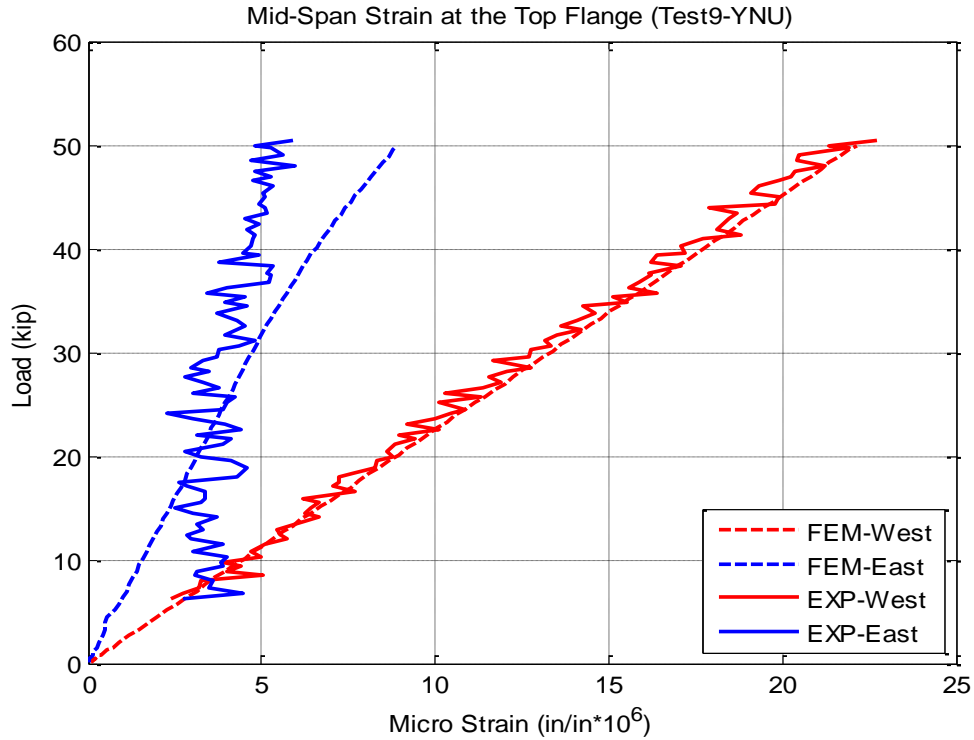


Figure 6-16 Comparison of longitudinal strain at the top flange of each girder in Test 9.

### 6.2.2 Test 10 - No Rail, No Continuity, Symmetric Loading (NNS)

Test 10 was carried out without rail, without continuity and symmetrical load applied and is illustrated in Figure 6-17.

The vertical displacements of the center of bottom flange at mid-span from the experimental data and FEA are compared in Figure 6-18. Similarly, the longitudinal strains in the bottom flange and top flanges at the mid-span section are compared in Figure 6-19 and Figure 6-20, respectively.

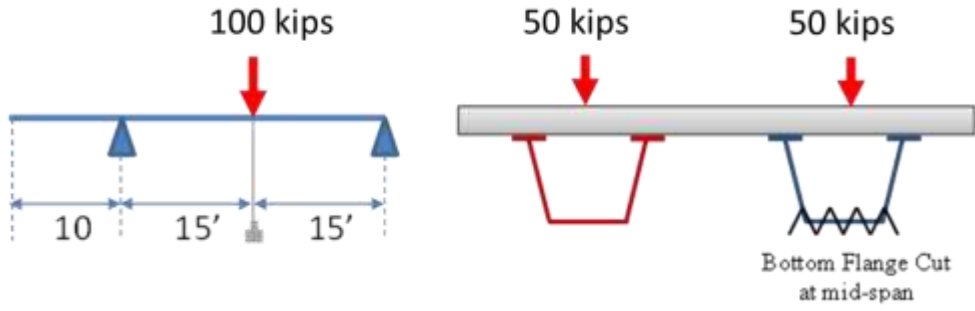


Figure 6-17 Schematic description of Test 10.

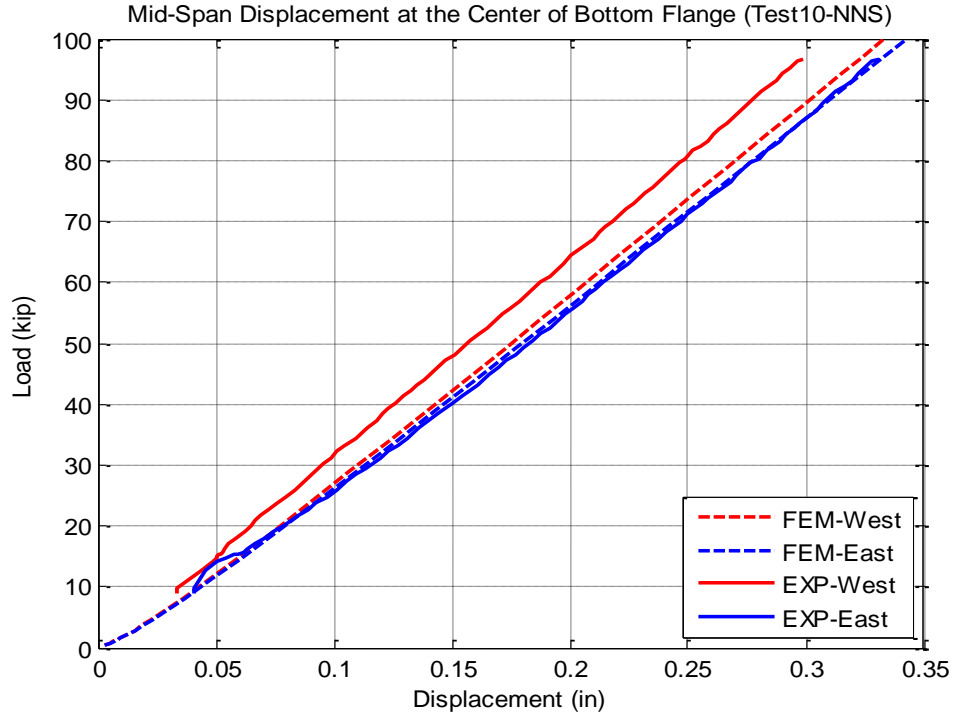


Figure 6-18 Comparison of vertical displacement at the bottom flange of each girder in Test 10.

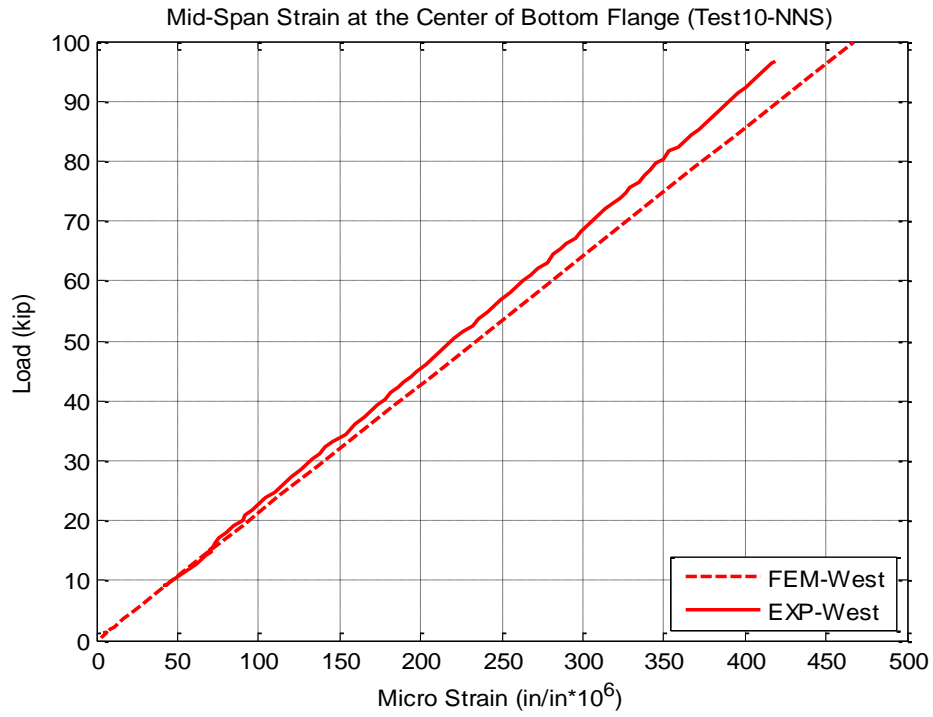


Figure 6-19 Comparison of longitudinal strain at the bottom flange of each girder in Test 10.

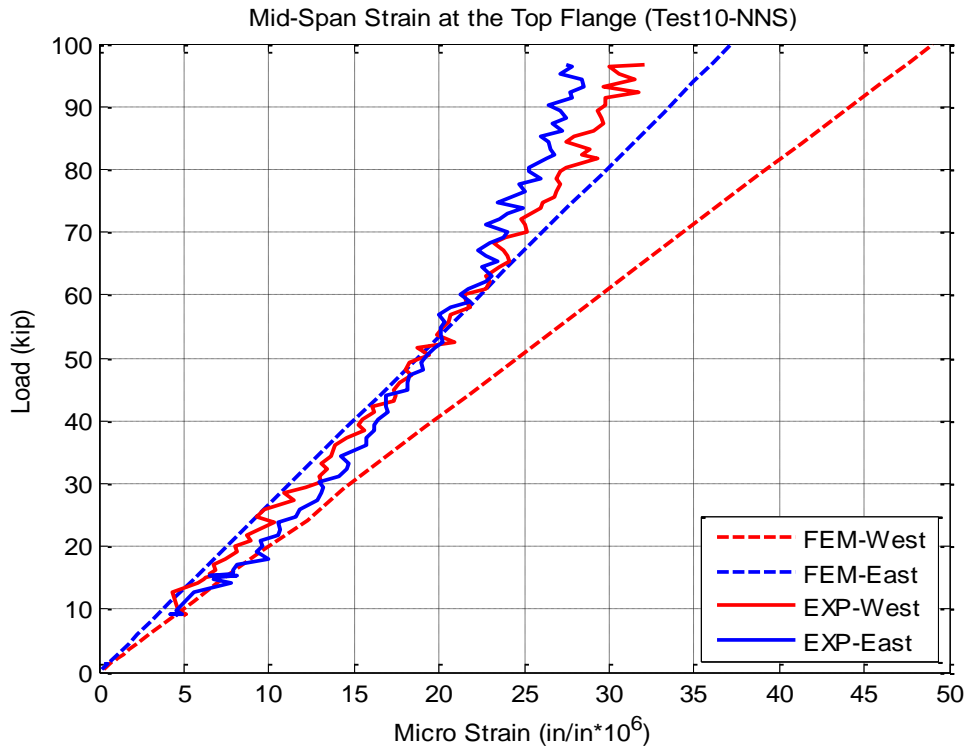


Figure 6-20 Comparison of longitudinal strain at the top flange of each girder in Test 10.

Overall, the FEM results showed reasonable agreement with the experimental data in both local and global responses for bottom flange fractured specimen.

### 6.3 Bridge Specimen with Full-Web Fractured in One Girder

With the web and bottom flange completely fractured in one girder, the FEA results from Test 16 and Test 17 are compared to the experimental data. Test 16 and Test 17 have characteristics similar to Test 9 and Test 10 except the web in EG was now fractured in addition to the bottom flange.

#### 6.3.1 Test 16 - with Rail, No Continuity, Unsymmetrical Loading (YNU)

The specimen was tested with the railings but no continuity, and 50 kips of load was applied to the damaged girder. A schematic of Test 16 is shown in Figure 6-21.

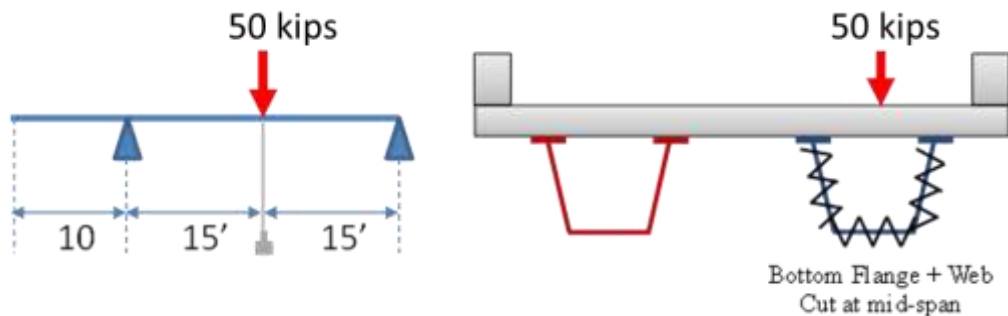


**Figure 6-21 Schematic description of Test 16.**

The vertical displacements of center of bottom flange at the mid-span from the experimental data and FEA are compared in Figure 6-22. Similarly, the longitudinal strain comparison in bottom flange at mid-span section is plotted in Figure 6-23. Both sets of data showed similar slopes. However, the experimental data showed bottom flange had some initial strains because the specimen wasn't completely unloaded in the third loading cycle.

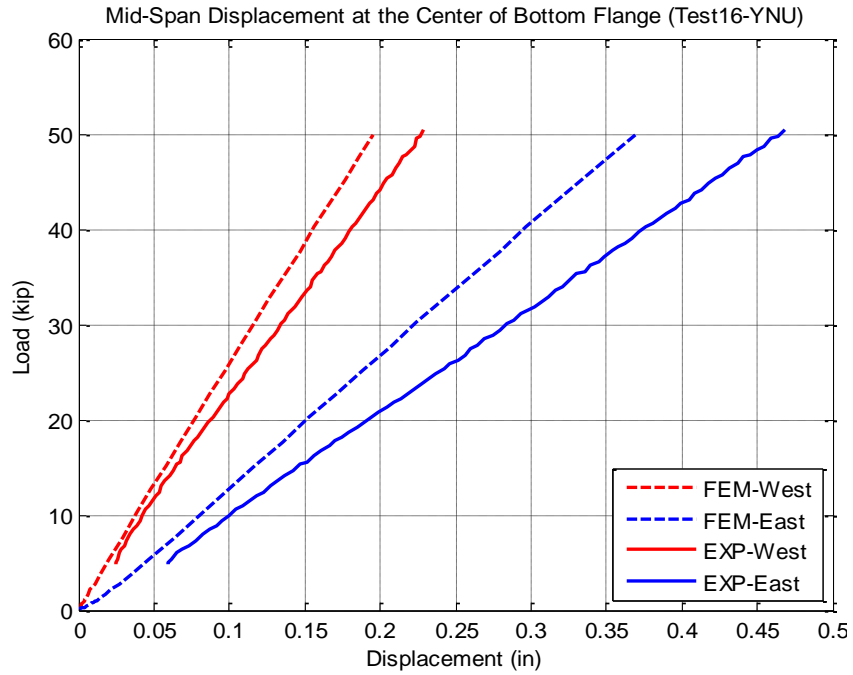


Figure 6-22 Comparison of vertical displacement at the bottom flange of each girder in Test 16.

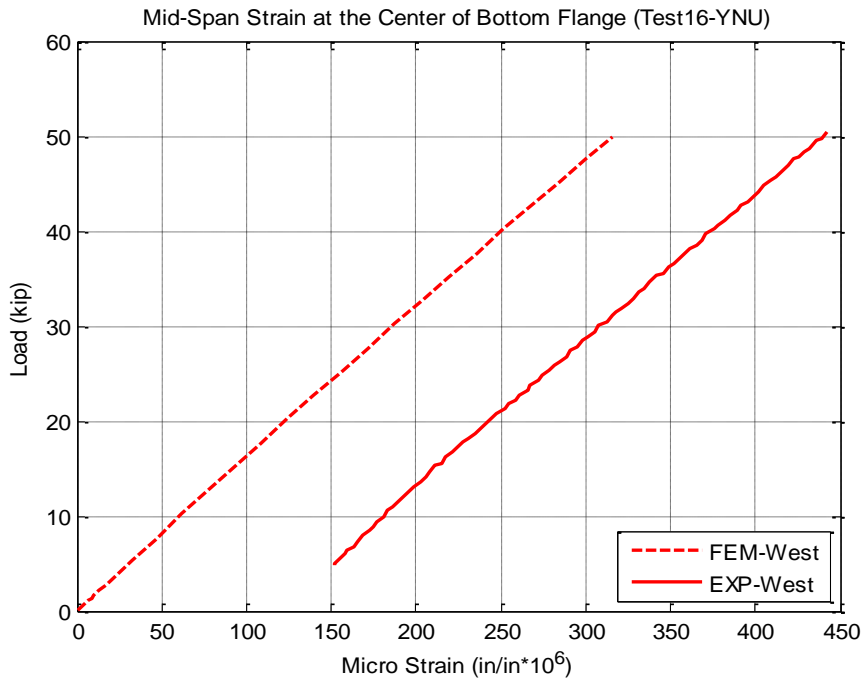


Figure 6-23 Comparison of longitudinal strain at the bottom flange of undamaged girder in Test 16.

### 6.3.2 Test 17 - No Rail, No Continuity, Symmetric Loading (NNS)

In Test 17, the bridge was tested without rail and continuity and under symmetrical loading. A schematic of Test 17 is shown in Figure 6-24.

The vertical displacements of the center of the bottom flange at the mid-span obtained from the experimental data and FEM analysis are compared in Figure 6-25. Similarly, the longitudinal strain in the bottom flange at the mid-span section is compared in Figure 6-26.

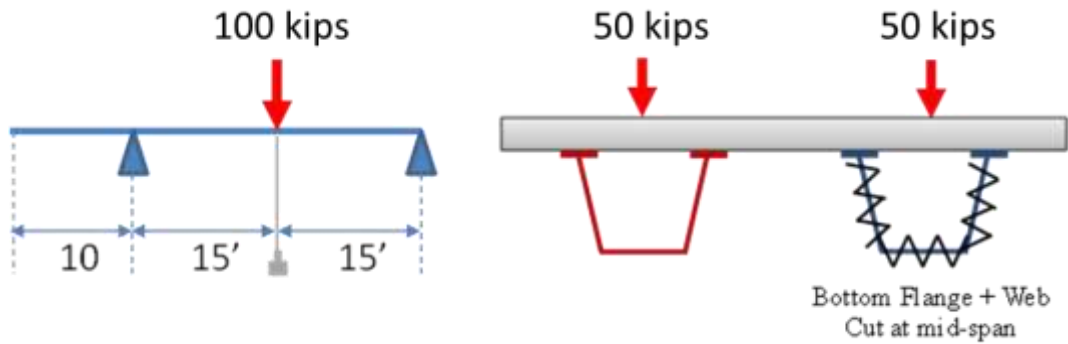


Figure 6-24 Schematic description of Test 17.

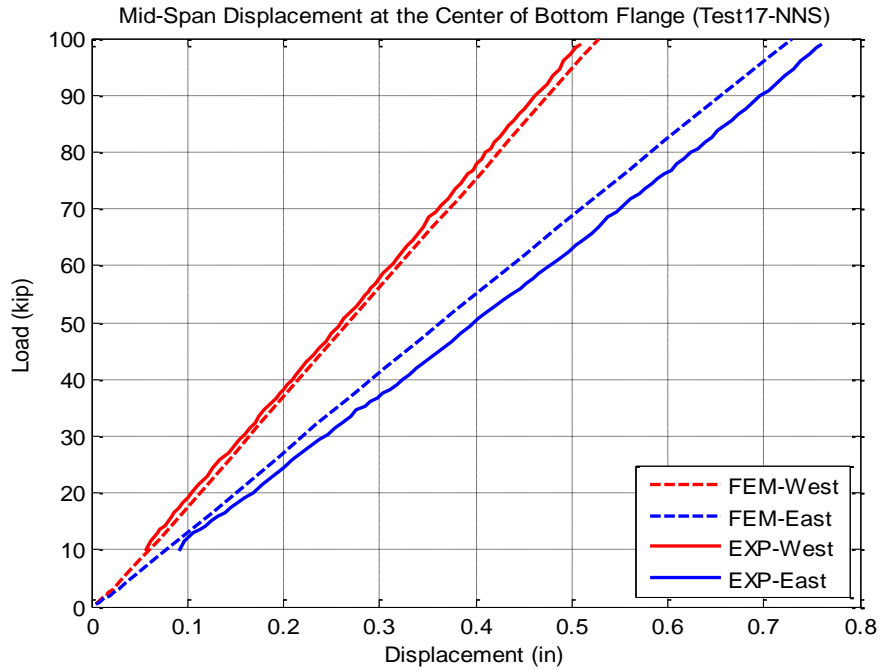


Figure 6-25 Comparison of vertical displacement at the bottom flange of each girder in Test 17.

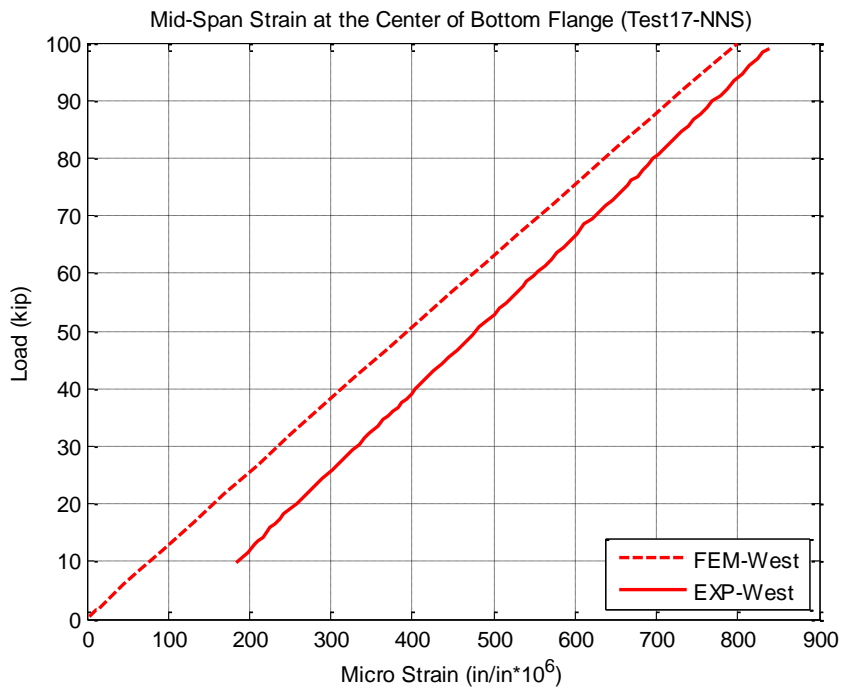


Figure 6-26 Comparison of longitudinal strain at the bottom flange of undamaged girder in Test 17.

In general, the finite element model is capable of reasonably predicting the linear responses of the specimen under the full-web fracture damage condition.

#### **6.4 Verification of FEMs with Ultimate Test A**

Both load-control and displacement control approaches were utilized to predict the ultimate load capacity of the specimen. The ultimate capacity of the specimen was predicted to be between 143 kips and 153 kips from FEA using the displacement-control method, for 7.8 ksi and 8.0 ksi concrete compressive strength, respectively, as a lower bound and upper bound. This method allows us to capture the capacity drop in the bridge after crushing of the concrete, as shown in Figure 6-27. The ultimate load, predicted from FEA using the load-control method, was 148 kips with concrete compressive strength of 7.8 ksi and was 163 kips with concrete compressive strength of 8.0 ksi. In FEA with load control method, after the ultimate capacity was reached, that load value then held nearly constant with increasing displacement for a short increment until the analysis was automatically terminated by the program, which can be seen in Figure 6-28. Since the ultimate capacity of the specimen in ultimate Test A was 156 kips, this suggests that the FE models provided good estimations of the ultimate capacity of tested specimen in either approach. Moreover, the FE models showed good agreements with experimental data on predicting when the ultimate capacity of the specimen will be reached.



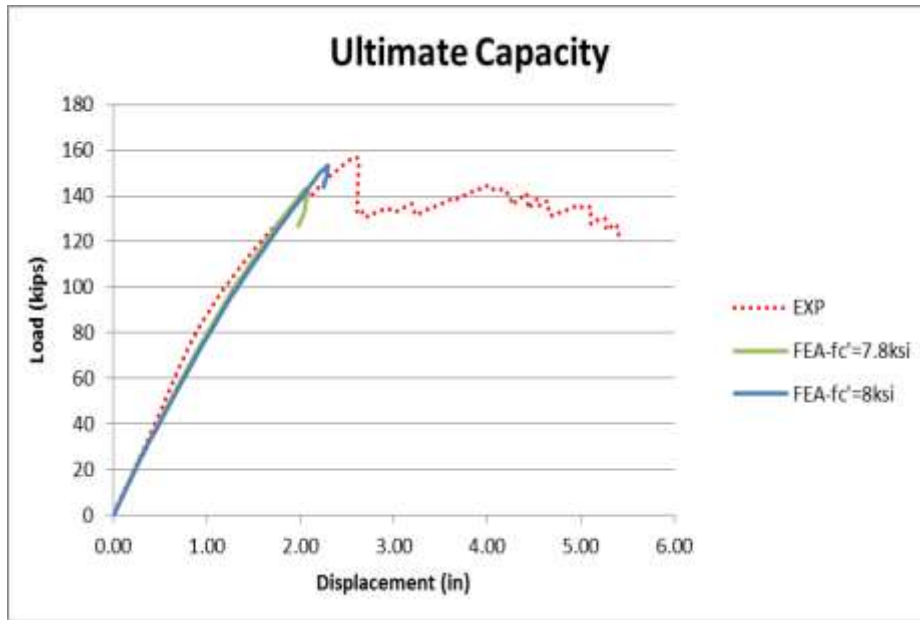


**Figure 6-27 Comparison of load vs. vertical deflection curves using displacement-control analysis.**

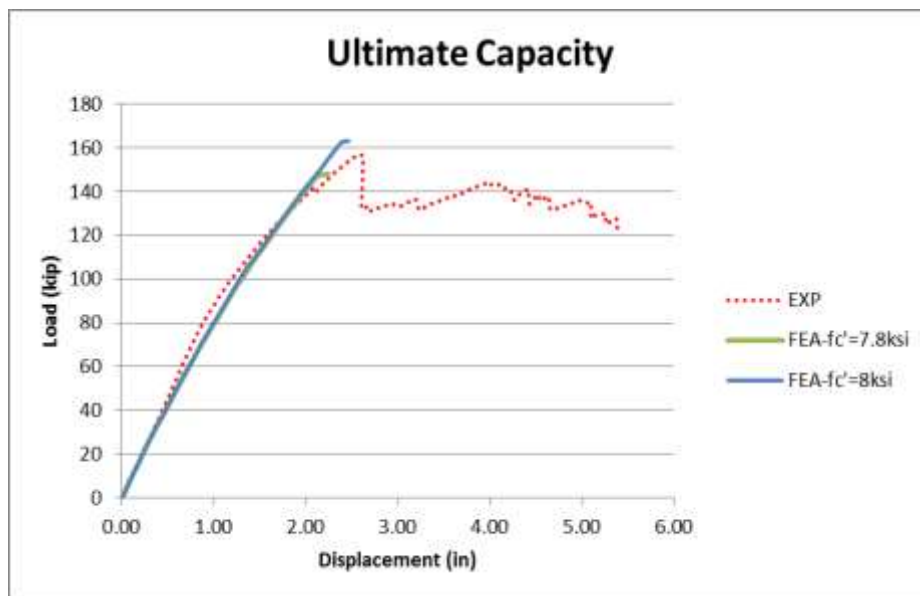


**Figure 6-28 Comparison of load vs. vertical deflection curve using load-control analysis.**

The capability of the FE model in capturing the behavior of the concrete deck and steel girders is also verified below.

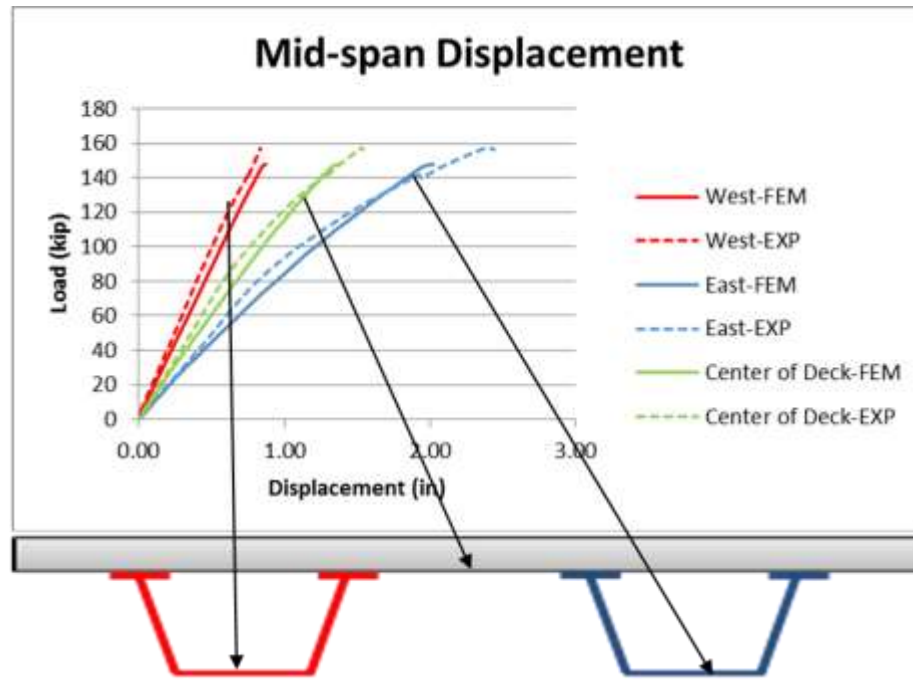


**Figure 6-29 Vertical displacements at the bottom flange of each girder and at center of the deck at mid-span.**

The FE models predicted very well the displacement of the laboratory specimen at mid-span, the most critical section, as shown in Figure 6-29. The difference between FEM and experimental data for mid-span displacement was less than 5%. In addition, the FE models well predict the uplift of the bridge that occurred in experiment. Figure 6-30a-b indicate that the WG was the only one that experienced uplifting in the experiment. This uplift occurred at the south support location when the applied load was around 80 kips (the blue dot in Figure 6-31a represents where and when the uplift occurred). The curve also shows that the uplift of the undamaged girder at the south support location might not have lifted completely until after the ultimate capacity was reached.

By using contact elements to model the interface between the supports and the bottom flanges, the FEM was also able to capture correctly the support location that will have uplift as shown in Figure 6-31. With negative reaction, the south-west support

location was predicted as the location, which will experience uplifting. It is important to note that tolerance in the contact algorithm and deviation of contact normal at large deflections allow us to capture the apparent small negative reaction force.

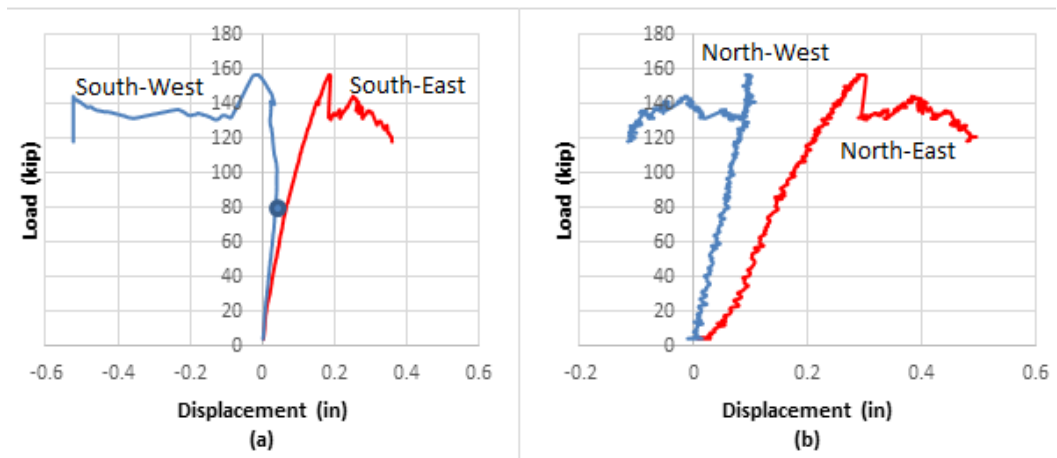


Figure 6-30 Reactions vs. EG vertical displacement.

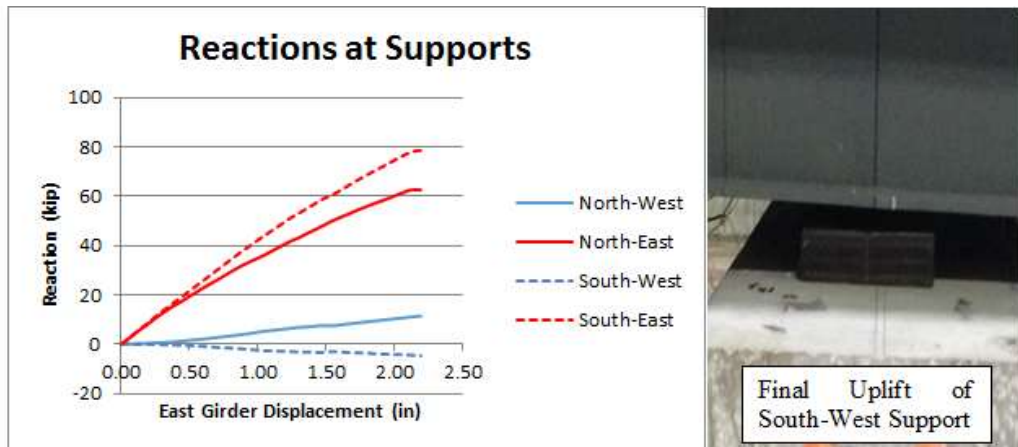


Figure 6-31 Prediction of uplift in finite element analysis.

Local behaviors of both the steel girders and deck were validated. Comparisons of longitudinal strain of top flanges and bottom flange of the undamaged WG, between FEA results and experimental data, are illustrated in Figure 6-32 and Figure 6-33, respectively. The transverse strains in the deck are verified in Figure 6-34.

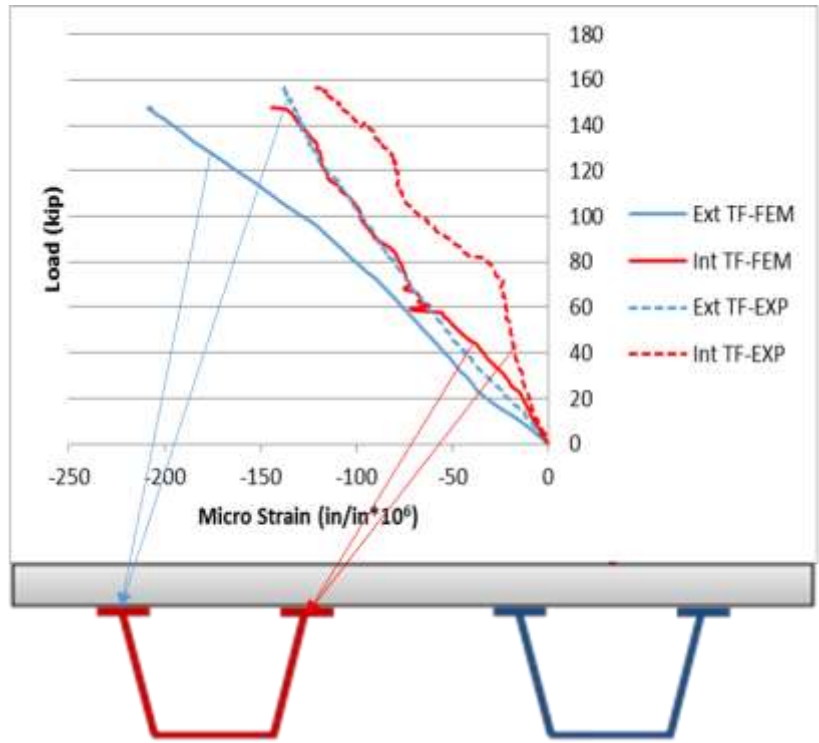


Figure 6-32 Comparison of longitudinal strains at the top flange of WG at mid-span.

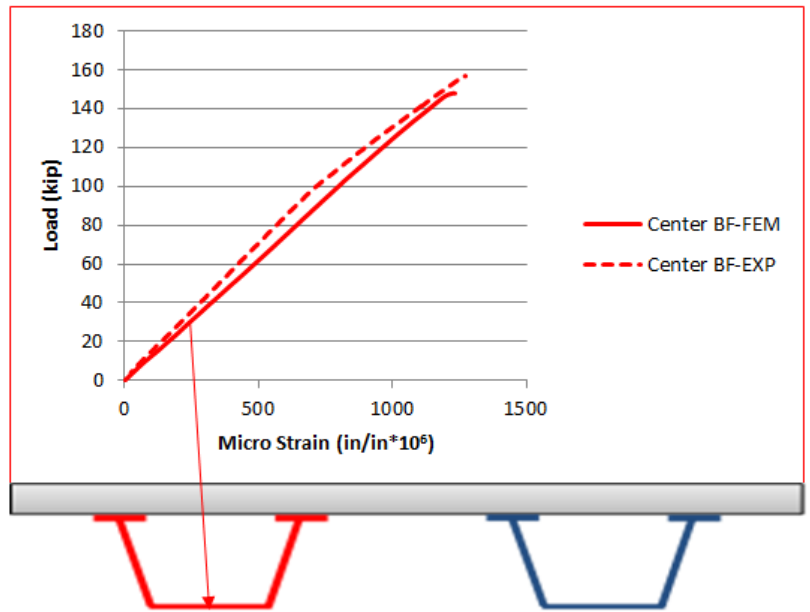
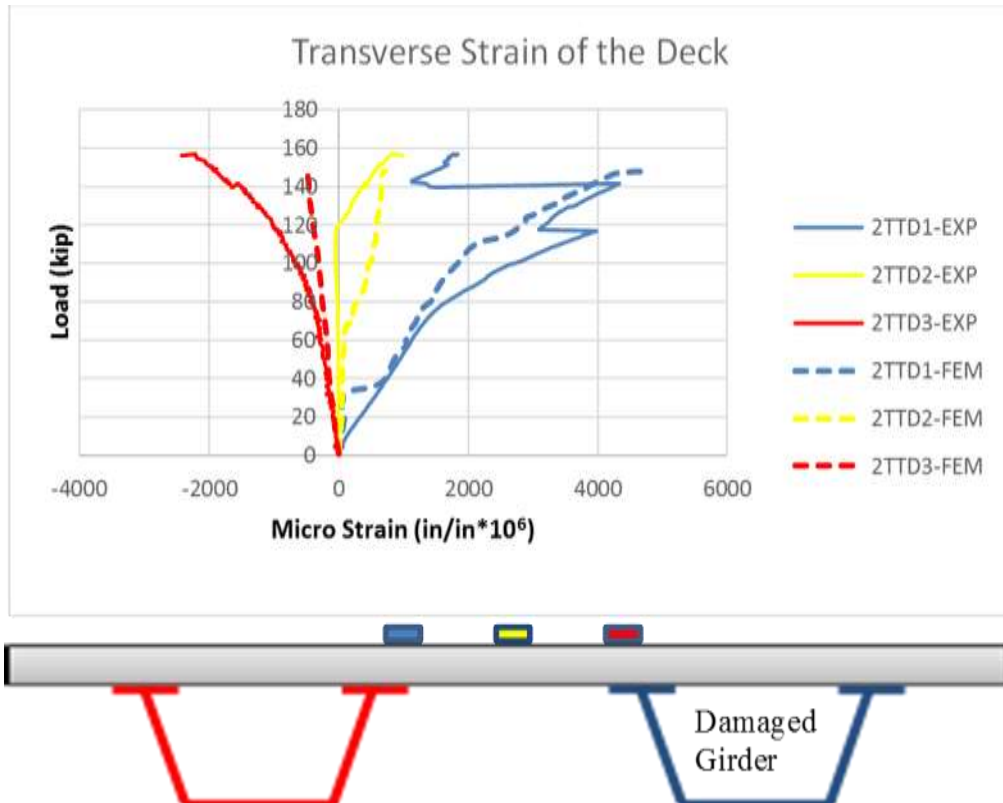


Figure 6-33 Comparison of longitudinal strain at bottom flange at mid-span.



**Figure 6-34 Comparison of transverse strain on the top of deck.**

The FEM models provided a good prediction of the location where concrete crushing would occur. Figure 6-35 compares the location of concrete crushing in the analytical model and experiment. Figure 6-36 compared experimental results to finite element analysis results regarding cracks at the ends of specimen. Finite element analysis results in Figure 6-36 predicted the shear cracks and tensile cracks would occur at the ends of the bridge.

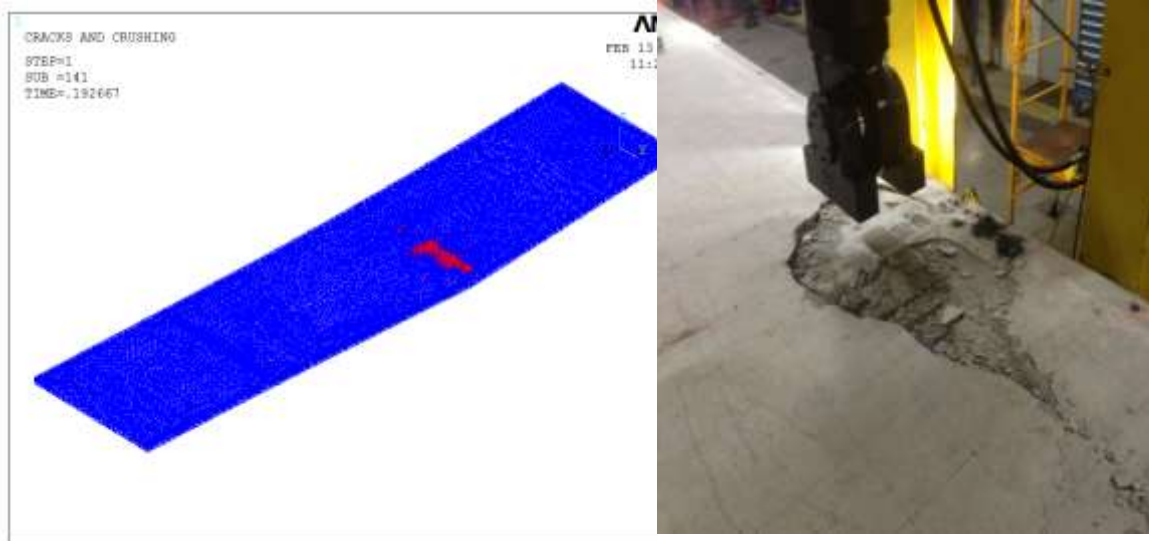


Figure 6-35 Location of concrete crushing in FEA and in experiment.

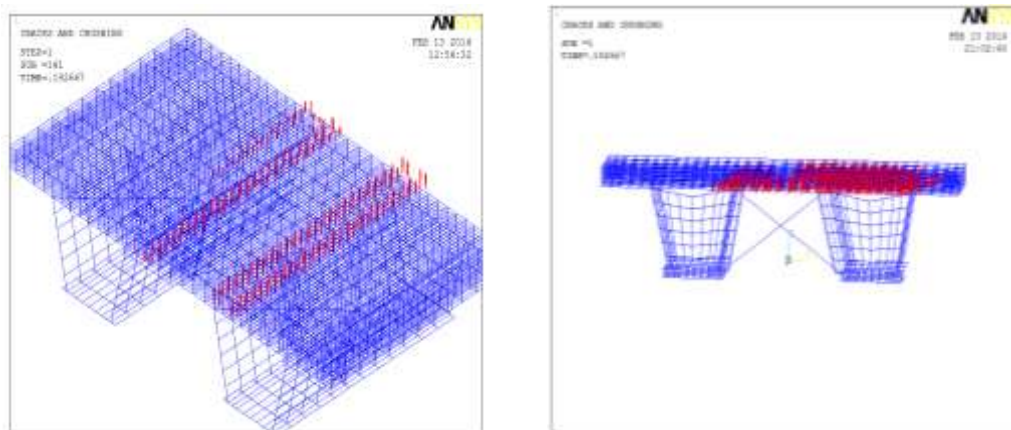
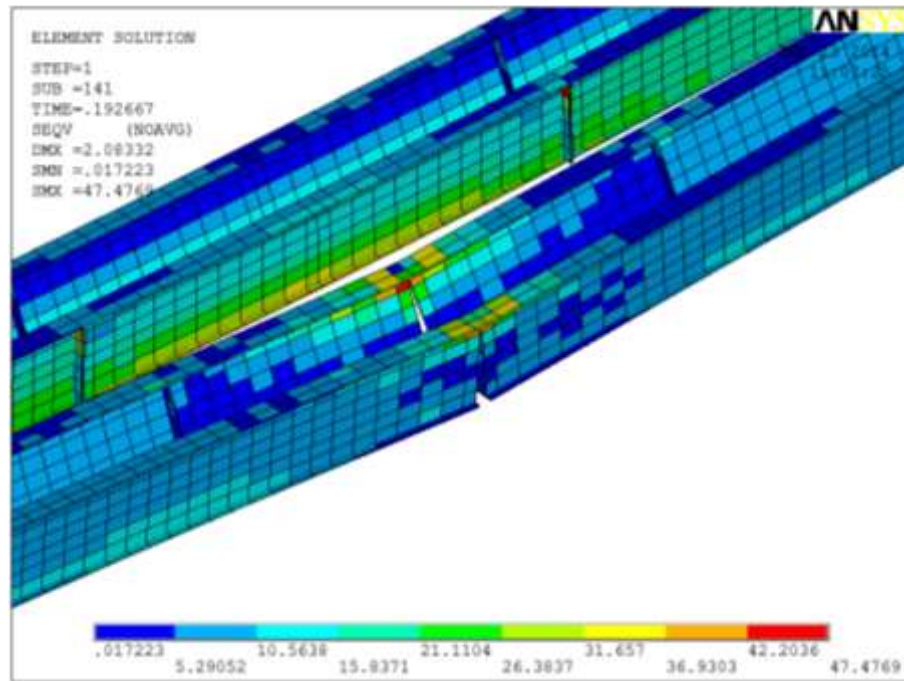


Figure 6-36 Shear cracking in south (left) and north (right) supports.

Figure 6-37 shows that the maximum von Mises stress in the steel girder was

around 48 ksi, which was less than 50 ksi, the assumed yielded stress of the material. In other words, the steel girder had not yet yielded when the ultimate capacity of the model was reached and this matches with what was observed from the experimental data. The FEA results also showed a similarity with experimental tests in the stress distribution along the length of both intact and damaged girders.



**Figure 6-37 Stress contour at mid-span in the steel girders.**

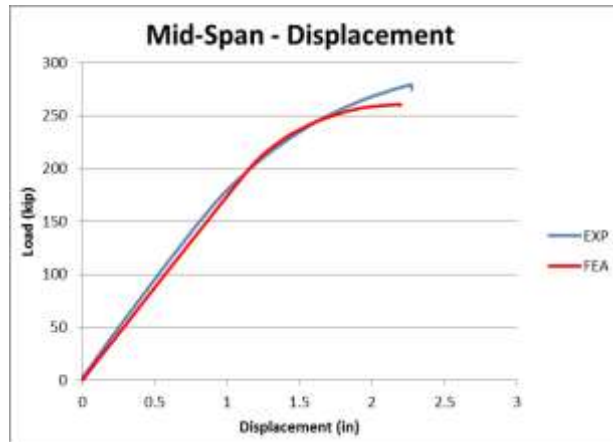
Overall, the FE model was able to capture behavior of concrete, steel girder, and major damages that were observed during the test such as shear failures of concrete deck at the loading point and at both ends as well as the uplift of the intact girder.

## 6.5 Verification of FEMs with Ultimate Test B

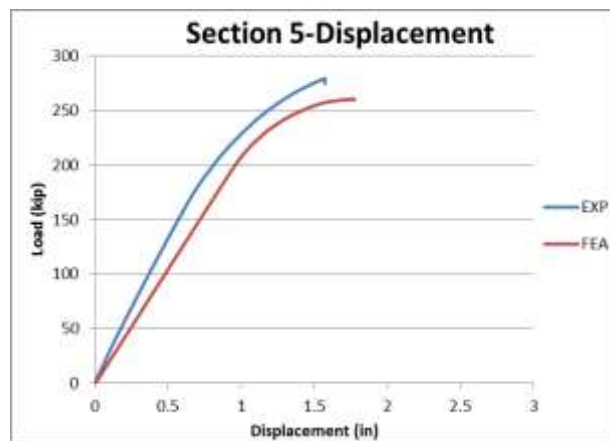
Since both girders experienced similar displacements as illustrated in Section 4.5, the average vertical displacements are used to present the displacement of both girders. The average vertical displacements of both girders along the length of the specimen were compared in Figure 6-38. In this figure, the agreements were observed not only in the

vertical displacements of the girders along the length but also in the capacity of the specimen. The capacity obtained from the test was 275 kips while the capacity obtained from FEA as 260 kips.

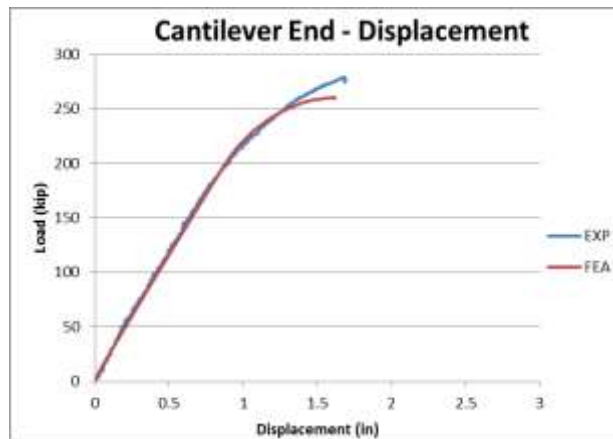




(a)



(b)



(c)

Figure 6-38 Load vs average vertical displacements at (a) mid-span, (b) Section 5, and (c) cantilever end.

In addition, Figure 6-39 and Figure 6-40 compare test data and FEA results on longitudinal strains of the intact girder and on the transverse strain of the deck at mid-span.

The comparison indicates that the FEMs were to predict and capture the behavior of both deck and steel girder. However, the comparison on steel girders had better agreement than it was on the deck. This could be due to several assumptions that was made when modeling the concrete, such as stress-strain material model, crushing stress, cracking stress and shear transfer coefficients.

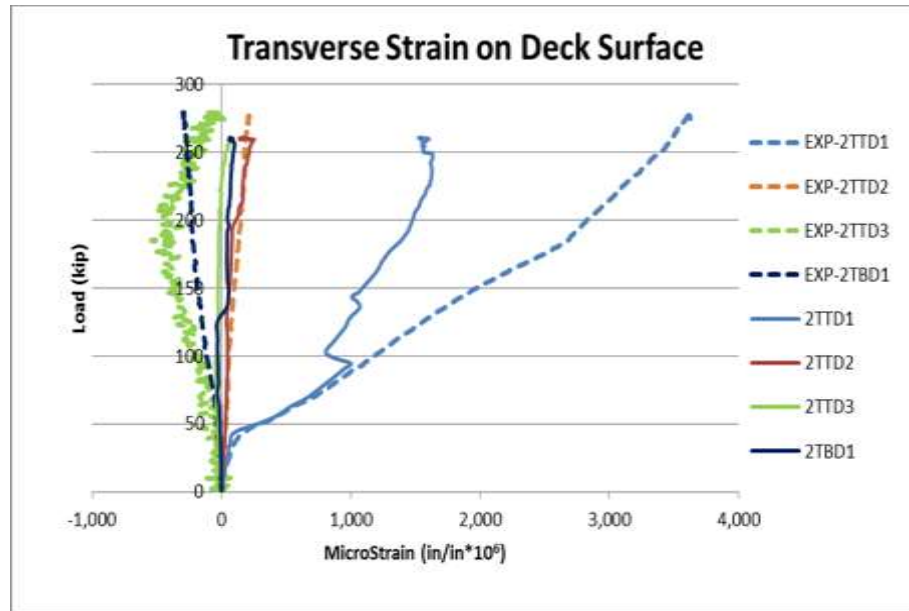
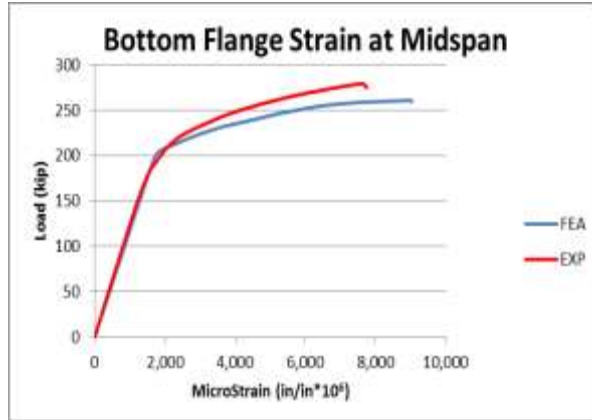
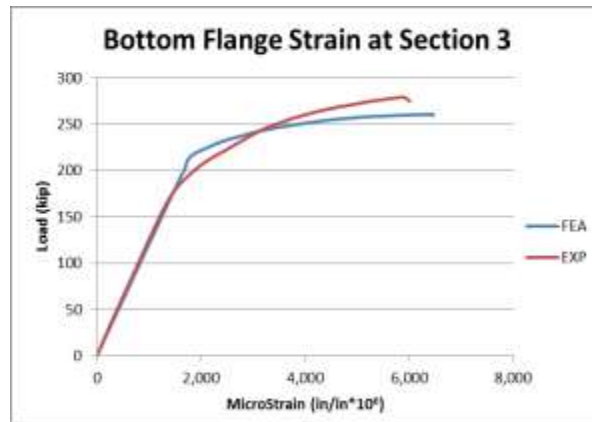


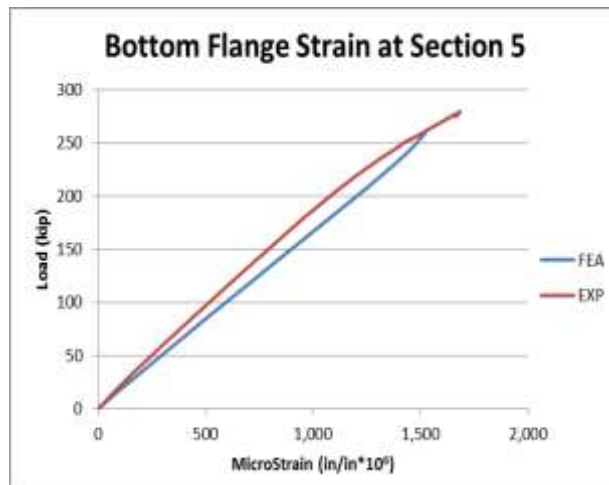
Figure 6-39 Transverse strain on the deck at mid-span.



(a)



(b)



(c)

Figure 6-40 Comparison of longitudinal strains at the bottom flange of the intact girder at (a) mid-span, (b) Section 3, and (c) Section 5.

Overall, the capacity and displacements produced by the FEM were in good agreement with those observed in the test. The FEM was also able to predict the responses in both steel girders and the concrete deck.

## 6.6 Summary

Overall, the predictions from finite element analyses were in good agreement with experimental data in both elastic and inelastic ranges. The maximum vertical displacements in each elastic test obtained from experimental data and FEM analysis results are listed in Table 6-1. Percentage difference in the last column of the table is calculated by dividing the difference of experimental and FEM deflection with the experimental deflection and multiplying by 100. The percentage differences between FEM analysis results and test data was 5.1% on average ranging from 0.03% for Test 2 (NNU) on undamaged system to 19.8% for Test 16 (YNU) on damaged system.

It should be noted that the high percentage of difference resulted primarily from the tests that have the rail system. This could be because the connection between the rail and the deck was assumed to be a full connection in the finite element models and the contact area between rail segments weren't modeled. This suggested that the rail were modeled stiffer than they actually were in the tests; therefore, the deflections for these tests with rails obtained from FEA were smaller than those obtained in the tests. Since in all ultimate tests, the specimen was tested without the rail, these assumptions were made to simplify the finite element modeling, and it was expected that they would not affect findings of this study.

From ultimate Tests A and B, it can be concluded that the finite element models were able to capture the inelastic responses of the specimen. For example, the finite element models were able to predict the modes of failure, the maximum capacity as well as damages observed in the experiment such as uplift of the intact girder, deck cracks at both ends and shear damage on the deck in ultimate Test A.

A good agreement between finite element analyses and experimental data in both elastic and inelastic ranges for several experiments indicates that the finite element models used in this study have been fully calibrated.

**Table 6-1 Comparison of Displacement between FEA Results and all Elastic Tests.**

| Test #         | Characteristics | Experimental Deflection (in) | FEM Deflection (in) | % Difference |
|----------------|-----------------|------------------------------|---------------------|--------------|
| 1              | NNS             | 0.333                        | 0.324               | 2.7          |
| 2              | NNU             | 0.203                        | 0.203               | 0.03         |
| 3              | NYU             | 0.179                        | 0.189               | 5.8          |
| 4              | YNS             | 0.303                        | 0.285               | 6.0          |
| 5              | YYU             | 0.174                        | 0.171               | 1.6          |
| 6              | YNU             | 0.194                        | 0.182               | 6.2          |
| 7              | YNS             | 0.337                        | 0.300               | 11.1         |
| 8              | YYU             | 0.180                        | 0.180               | 0.2          |
| 9              | YNU             | 0.206                        | 0.192               | 6.7          |
| 10             | NNS             | 0.337                        | 0.342               | 1.6          |
| 11             | NNU             | 0.218                        | 0.215               | 1.3          |
| 12             | NYU             | 0.188                        | 0.200               | 6.1          |
| 14             | YNS             | 0.573                        | 0.575               | 0.3          |
| 15             | YYU             | 0.378                        | 0.330               | 12.8         |
| 16             | YNU             | 0.460                        | 0.369               | 19.8         |
| 17             | NNS             | 0.741                        | 0.730               | 1.6          |
| 18             | NNU             | 0.503                        | 0.465               | 7.6          |
| 19             | NYU             | 0.401                        | 0.403               | 0.7          |
| Avg Difference |                 |                              |                     | 5.1          |

## **Chapter 7    Field Testing of Ft. Lauderdale Twin Box-Girder Bridge 860600**

Florida International University (FIU) contracted Bridge Diagnostics, Inc. (BDI) to conduct a field test on Ramp Bridge 860600 located in Ft. Lauderdale, Florida. This structure is a multiple- span bridge and the test was performed on the north module, which is a three-span continuous bridge. The bridge has two separate superstructures. Each superstructure consists of two steel box-girders composite with a concrete deck. In this project, only the west superstructure that provides the access ramp from SW 1<sup>st</sup> street to I-95 South was tested. Figure 7-1 and Figure 7-2 show the pictures of the first two spans of the bridge.

Tasks began on May 22, 2012, when FIU staff began preliminary work on the bridge including marking the exact spot for each instrument and preparing the surface of the steel box-girders for installation of instruments. That task was completed on May 23, 2012, and then BDI started its job on the bridge site on May 30, 2012. The BDI services included providing testing equipment and instruments, installation, data collection and preliminary data processing. Loading trucks were provided by FDOT District 4 and were weighed at a nearby certified scale. The loading started around 9:00 p.m. on May 30, 2012. Eight different moving load scenarios were applied and testing finished at 11:30 p.m. that night. After that, removing the instruments, wiring and equipment, and restoring the instrumentation spots on the steel girders to their initial state, including cleaning, sanding, zinc coating and painting was done until 3:00 am on May 31, 2012 when the field job was accomplished.

The acquired data was first reviewed and analyzed by BDI, which showed the structure was behaving in a linear elastic manner. A slight thermal drift was detected during the test, which is typical for long-duration tests. The drift was corrected with a linear offset. BDI reported the overall data to be of good quality.

FIU analyzed the data provided by BDI using finite element analysis of the bridge under different loading scenarios. In general, the deflection results match with the test data with good precision. The collected strain data are also in good agreement with the finite element analysis results. A partial fixity in the abutment of the bridge is observed from the strain data compared to ideal finite element model, which is in agreement to observations of past researchers. This partial fixity causes slightly greater stresses in the superstructure close to the abutment and reduces the magnitude of stresses in the mid-span region to some extent.

This chapter provides details regarding the instrumentation, load test procedures and response plots. The processed data from each path has been formatted as a function of longitudinal truck position. In general, the good match of the analysis results and test data verifies the accuracy of the finite element models that FIU researchers have constructed to study the behavior of twin box-girder bridges.

It should be noted that the test results presented in this chapter correspond to the properties of the structure at the time of testing. Any further structural aging, degradation, damage, or retrofits must be taken into account for future analysis or rating purposes.



**Figure 7-1 First two spans of the ramp bridge - underneath view.**



**Figure 7-2 First span of the ramp bridge 860600 - elevation view from west.**



## 7.1 Objective

The main goal of this field testing was to calibrate the finite element models and verify the accuracy of the modeling techniques that are used in the redundancy analysis of twin box-girder bridges in elastic range. Another target was to observe the behavior of an existing two girder bridge under actual truck loading.

## 7.2 Bridge Configuration

The Ft. Lauderdale Ramp Bridge 860600 has a twin box-girder superstructure that is continuous over three spans. The lengths of the spans are 144, 163 and 148 ft and the bridge total length is 455 ft. Figure 7-3 shows the elevation view of the bridge.

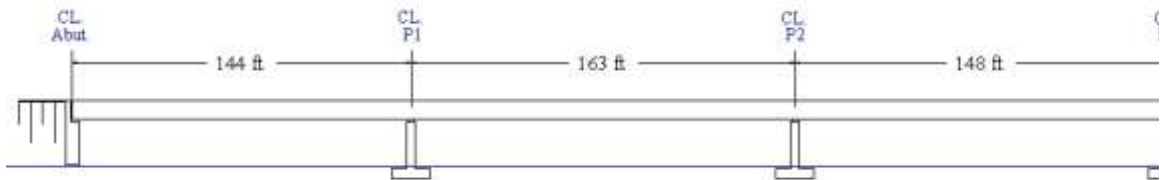


**Figure 7-3 Elevation view of the bridge.**

The box-girders of the superstructure are composite with a concrete deck of 8-in thickness. The depth of the box-girders is 6 ft - 4 in. The width of the roadway is 28ft and there are two railings with a width of 1 ft - 6.5 in. at each side of the roadway. Figure 7-4 shows the bridge superstructure cross-section.

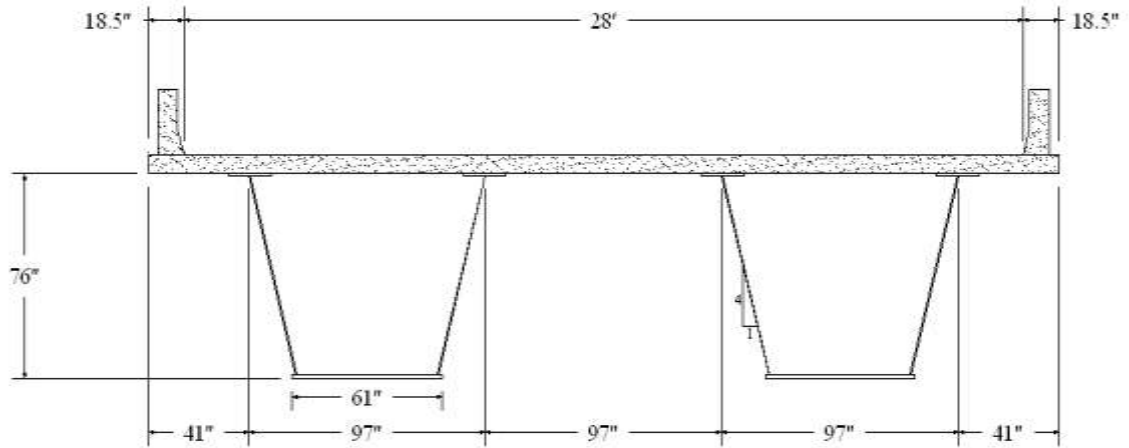


**Figure 7-4 Cross-section of the Ft. Lauderdale bridge 860600.**

The width of the bottom flange of each box-girder is 5 ft and 1 in. and the center-to-center distance of the top flanges is 8 ft and 1 in. The thickness of girder webs is equal to 0.6875 in. and they are inclined with a slope of 4:1. The width of the top flange and the thickness of the top and bottom flanges of the girders are changing throughout the length of the girders and are tabulated in Table 7-1.

**Table 7-1 Thickness of Top and Bottom Flanges of the Bridge Girders**

| Plate Length |       | Top Flange  |                 | Bottom Flange |                 |
|--------------|-------|-------------|-----------------|---------------|-----------------|
| Plate #      | (ft)  | Width (in.) | Thickness (in.) | Width (in.)   | Thickness (in.) |
| 1            | 128.5 | 12          | 1               | 61            | 5/8             |
| 2            | 25    | 16          | 15/8            | 61            | 9/8             |
| 3            | 40    | 16          | 1               | 61            | 7/8             |
| 4            | 72    | 12          | 1               | 61            | 5/8             |
| 5            | 22.5  | 12          | 5/4             | 61            | 7/8             |
| 6            | 45    | 24          | 2               | 61            | 13/8            |
| 7            | 31    | 16          | 1.5             | 61            | 7/8             |
| 8            | 72.5  | 16          | 1.5             | 61            | 5/8             |
| 9            | 17.5  | 12          | 5/4             | 61            | 5/8             |

The internal bracing of the box-girders are made of an L5x5x3/8 angle for the top chord and an inverted V bracing with L3.5x3.5x1/2 sections for each leg. These elements are connected to the box-girder by means of web transverse stiffeners with 5-in. width and 0.5-in. thickness. There are 11, 13 and 12 of such internal braces in the first, second and third spans, respectively. These braces are approximately equally spaced in each span. Figure 7-5 depicts the internal braces that are used in the box-girders.

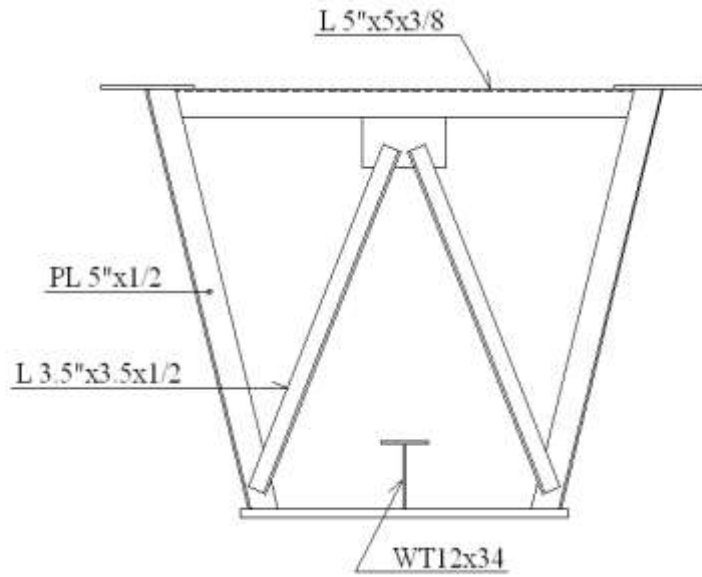


**Figure 7-5 Internal bracing of superstructure girders.**

Table 7-2 presents some general information about the bridge and the testing procedure.

**Table 7-2 General Structure and Testing Specifications**

| ITEM                                    | DESCRIPTION   |
|---|---|
| STRUCTURE NAME                          | Park and Ride Outbound Ramp to Southbound I-95      |
| CITY/STATE                              | Ft. Lauderdale, FL                                  |
| TESTING DATE                            | May 22 to 31, 2012                                  |
| CLIENT'S STRUCTURE ID #                 | Ramp Bridge 860600                                  |
| STRUCTURE TYPE                          | Steel Twin Box-girder                               |
| TOTAL NUMBER OF SPANS TESTED            | 2   |
| SPAN LENGTH(S)                          | Span 1: 144'-0" , Span 2: 163'-0"                   |
| ROADWAY WIDTH                           | 28'-0"  |
| SKEW                                    | 0   |
| WEARING SURFACE                         | Concrete  |
| SPANS TESTED                            | 2   |
| TEST REFERENCE LOCATION (X=0,Y=0) - BOW | CL of North Abutment at the inside face of the East |
| NUMBER/TYPE OF SENSORS                  | Strain Transducers – 28, Displacement Sensors – 8   |
| SAMPLE RATE                             | 40 Hz – Semi-Static and Normal Speed                |
| NUMBER OF TEST VEHICLES                 | 2   |
| STRUCTURE ACCESS TYPE                   | Bucket Truck  |
| STRUCTURE ACCESS PROVIDED BY            | FDOT  |
| TRAFFIC CONTROL PROVIDED BY             | FDOT  |
| TOTAL FIELD TESTING TIME                | 4 Days  |

### 7.3 Instrumentation

The instrumentation of the bridge was performed using the BDI wireless structural testing system. In this system, the transducers are connected to a wireless data acquisition

device which collects the structure response data at a predefined frequency. In this project, the bridge is instrumented in two locations to gather the displacement data and in three sections for strain data. The following two subsections describe the details of the instrumentation at each section.

### 7.3.1 Potentiometers (Displacement Sensors)

To measure the deflections of the bridge under live load, eight potentiometers are installed below the superstructure of the bridge at two locations, named locations 1 and 2. A side view of the bridge showing these two locations is illustrated in Figure 7-6.

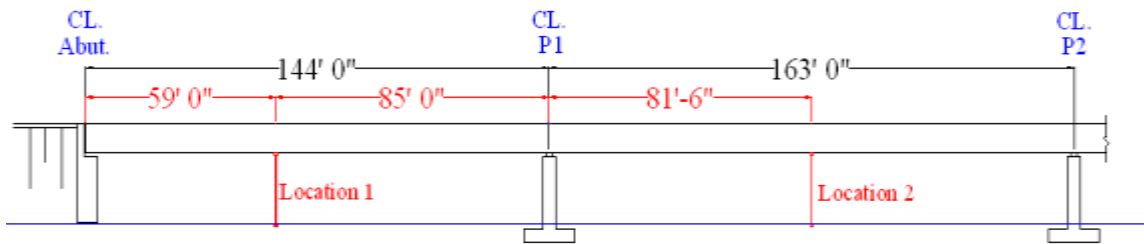


**Figure 7-6 Locations of potentiometers in the first two spans.**

Location 1 is in the first span at a distance of 85 ft from the first pier. At this location, there are four potentiometers, two of them below the edges of the bottom flange of the west box-girder, one in middle of the concrete deck between the steel girders and the other one below the west edge of the EG. Figure 7-7 displays the arrangement of the potentiometers in the first span. The gauge and channel ID's (in parentheses) of these displacement sensors are shown in Figure 7-8. A typical photo of the assembly of these displacement sensors is in Figure 7-9. As stated earlier to measure the displacement of the concrete deck between the girders, a sensor is attached to it. As the structural insulated panel (SIP) is used for the concrete, the transducer should be attached to the SIP form

instead of the concrete face. Figure 7-10 shows the transducer attached to formwork below the concrete slab.

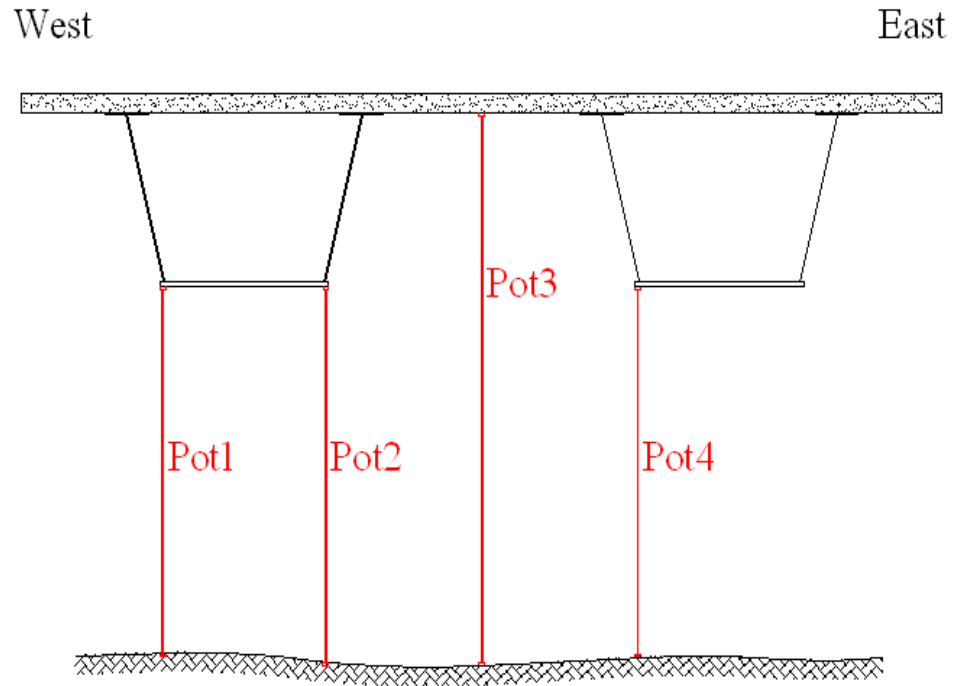


Figure 7-7 Arrangement of potentiometers at Location 1 in the first span.

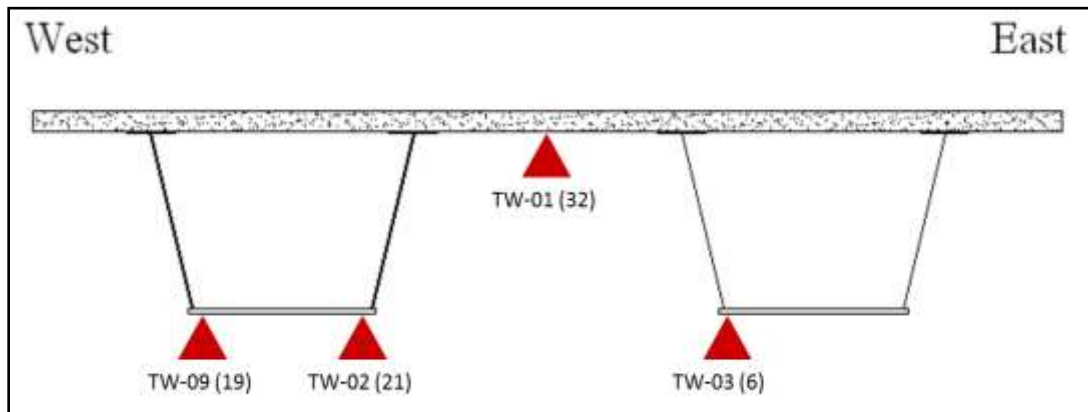
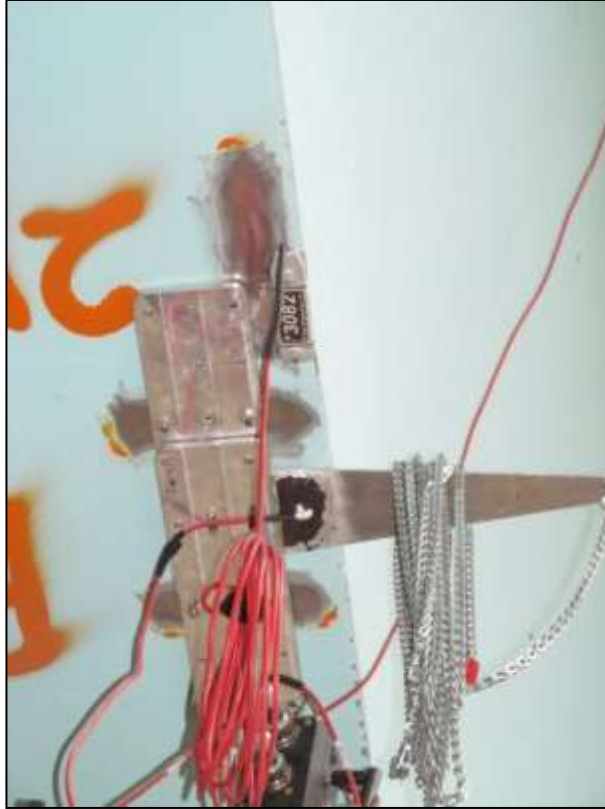


Figure 7-8 Gauge and channel ID of first span displacement sensors.



**Figure 7-9 Displacement sensor beneath bottom flange of box-girder (typical).**





**Figure 7-10 Displacement sensor on SIP form below concrete deck.**

In the second span, four potentiometers are installed in the middle of the span which has a distance of 81'-6" from the adjacent piers. At this location, one potentiometer is attached to each edge of the bottom flange of each box-girder. Figure 7-11 shows the configuration of the potentiometers at middle of the second span. The gauge and channel ID's (in parentheses) of these potentiometers are indicated in Figure 7-12.

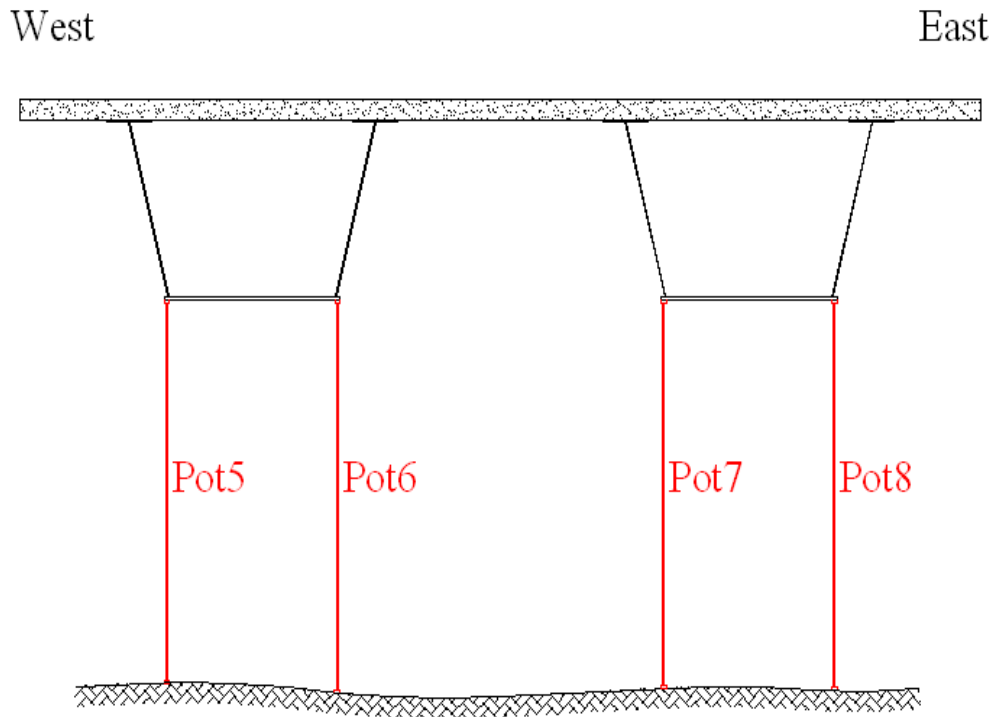


Figure 7-11 Arrangement of the potentiometers at Location 2 in the second span.

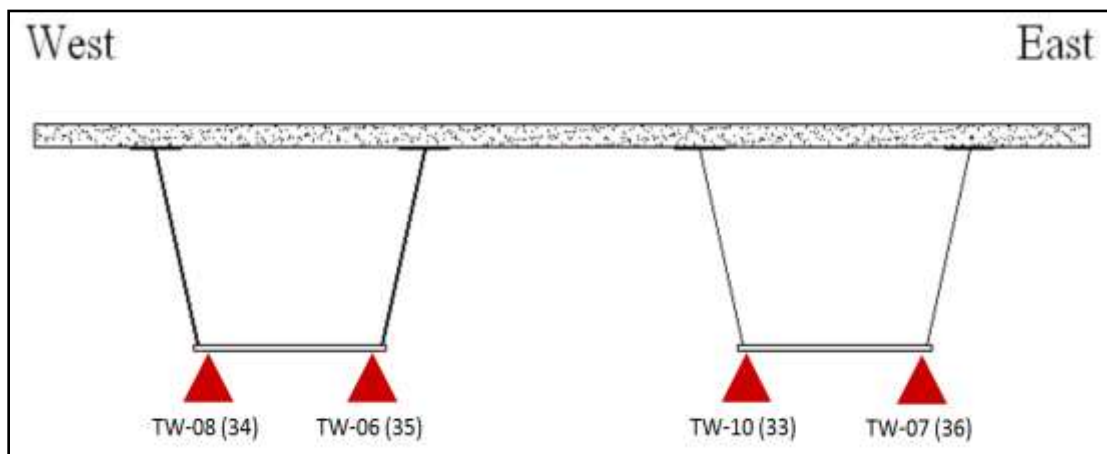


Figure 7-12 Gauge and channel ID of displacement sensors at Location 2.

### 7.3.2 Strain Gauges

In order to measure longitudinal strains in the steel girders of the bridge superstructure under live load, 28 strain gauges are installed in the first span of the bridge at three sections, named sections 1, 2, and 3. The distances of these sections from the end of the superstructure are 6, 58 and 138 ft, respectively. Figure 7-13 shows the location of these sections in an elevation view of the bridge. The strain gauges are attached to the outer surface of the steel box-girders at different places of each section. Figure 7-14 shows two pictures of typical strain transducers attached for the steel girders in this project.

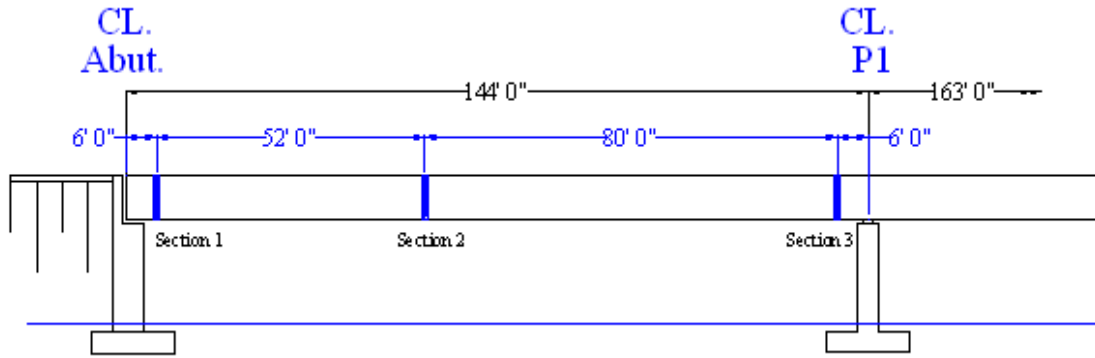
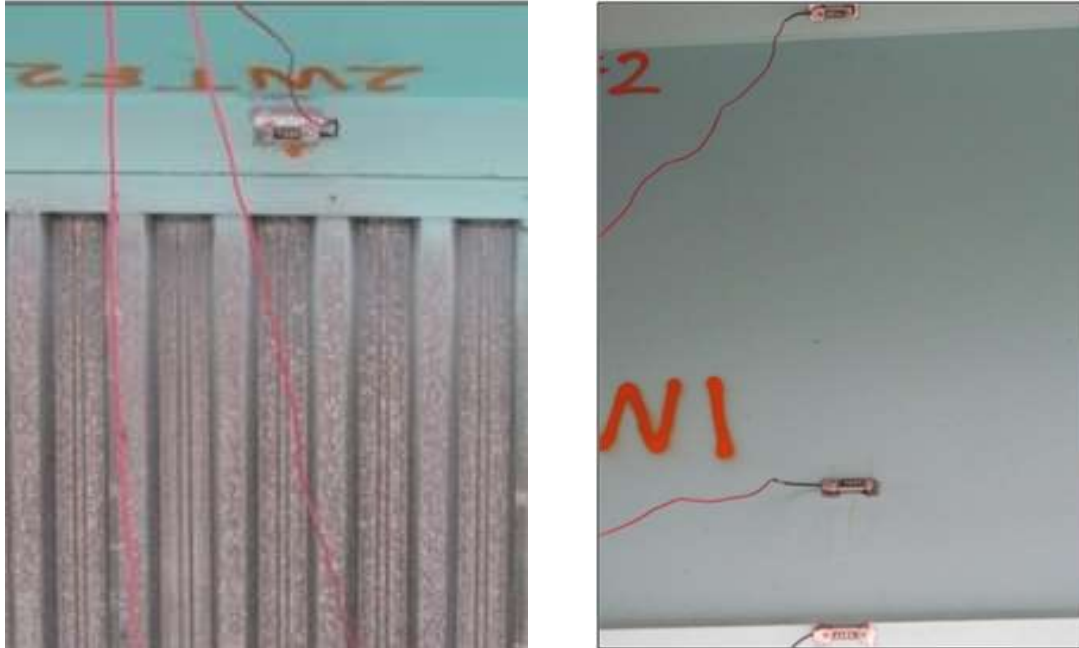


Figure 7-13 Locations of strain gauges in the first span.



**Figure 7-14 Strain transducers on box-girders (typical).**

In section 1, nine strain gauges are installed on the girders. The WG has one strain gauge attached to the lower surfaces of its east top flange. That strain gauge is placed in the middle of the outstanding length of the top flange. This girder has one strain gauge installed on its west web, 15 in. above the bottom flange. The bottom flange has two strain gauges, 2 in. from the flange edges. The WG has a total of four strain gauges.

At this section, the EG has five strain gauges, two of them on the lower surface of its top flanges, similar to that of the WG. The west web of the EG has one strain gauge attached to its outer surface, 10 in. below the top of flange. The bottom flange of this girder has two strain gauges located 2 in. away from the edges. Figure 7-15 shows the arrangement of the strain gauges at this section of the bridge.

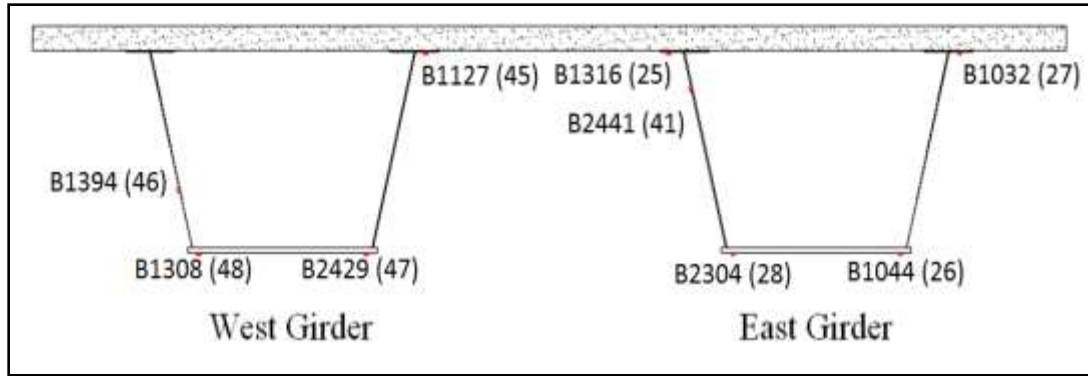


**Figure 7-15 Gauge and channel ID's of strain gauges at Section 1.**

Section 2, which is located 58 ft from the abutment, has nine strain gauges, five of them installed on the WG and four of them on the EG. In this section, both girders have one strain gauge under the lower surface of the top flanges, and two strain gauges at the edges of the bottom flange. The WG has one strain gauge on the east web, 10 in. above the bottom flange. Figure 7-16 displays the arrangement of the strain gauges at Section 2.

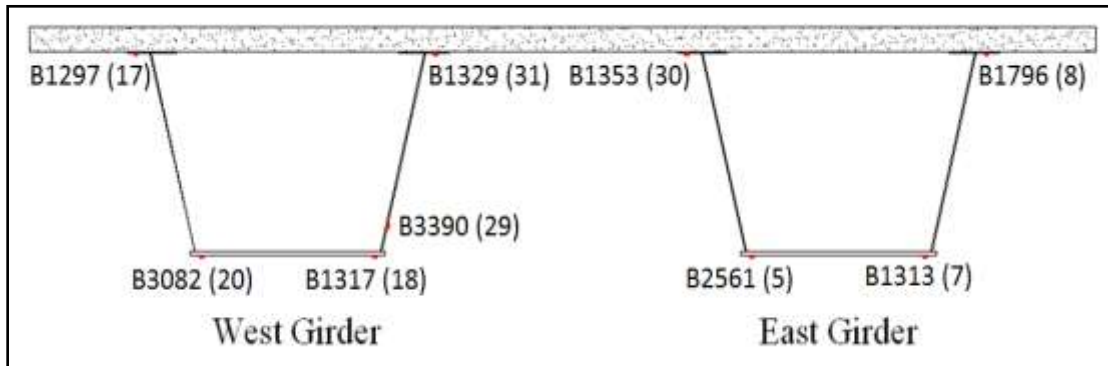


**Figure 7-16 Gauge and channel ID's of strain gauges at Section 2.**

Section 3, which is located 6 ft from the center line of the first pier (or 138 ft from the abutment) has ten strain gauges, five of them installed on the WG and the other five on the EG. In this section, both of the girders have a strain gauge under each of their top flanges. In addition, both have two strain gauges at the edges of their bottom flanges. The east web of the WG and the west web of EG have one strain gauge, 12 in. above the bottom flange. Figure 7-17 displays the arrangement of the strain gauges at section 3.

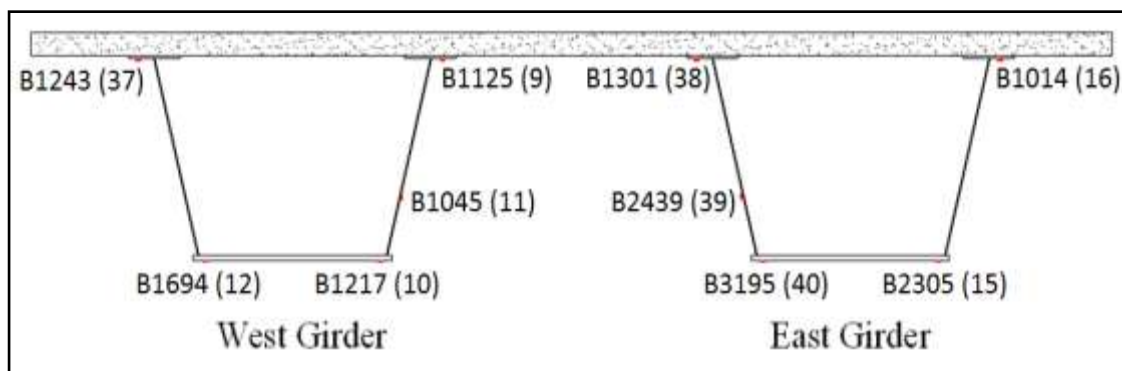


Figure 7-17 Gauge and channel ID's of strain gauges at Section 3.

#### 7.4 Loading

Loading of the bridge was done by two trucks which were provided by District 4 of the Florida DOT. Those 10-wheel trucks, named Truck-1 and Truck-2, were weighed in a certified weigh station close to the bridge site about an hour before the testing. The weights of Truck-1 and Truck-2 were 62560 and 59940 pounds, respectively. Other specifications of the test trucks are tabulated in Table 7-3 and Table 7-4. In addition, the spacing of the axles of these trucks is illustrated in Figure 7-18 and Figure 7-19.

**Table 7-3 Test Truck-1 Specifications**

| <b>VEHICLE TYPE</b>                      | <b>TANDEM REAR AXLE DUMP TRUCK</b> |       |
|--|------------------------------------|-------|
| GROSS VEHICLE WEIGHT (GVW)               | 62,560 lbs                         |       |
| WEIGHT/WIDTH - AXLE 1                    | 13,320 lbs                         | 7'-2" |
| WEIGHT/WIDTH - AXLE 2 - REAR TANDEM PAIR | 49,240 lbs                         | 7'-2" |
| SPACING: AXLE 1 - AXLE 2                 | 13'-3"                             |       |
| SPACING: AXLE 2 - AXLE 3                 | 4'-8"                              |       |
| WEIGHTS PROVIDED BY                      | Certified Weight Station           |       |
| AUTOClicker POSITION                     | Driver - 3 <sup>rd</sup> axle      |       |
| WHEEL ROLLOUT 5 REVS                     | 53'-0"                             |       |
| WHEEL CIRCUMFERENCE                      | 10.6'                              |       |
| # SEMI-STATIC PASSES                     | 10                                 |       |
| # NORMAL SPEED PASSES                    | 1                                  |       |
| VEHICLE PROVIDED BY                      | FDOT                               |       |

**Table 7-4 Test Truck-2 Specifications**

| <b>VEHICLE TYPE</b>                      | <b>TANDEM REAR AXLE DUMP TRUCK</b> |       |
|--|------------------------------------|-------|
| GROSS VEHICLE WEIGHT (GVW)               | 59,940 lbs                         |       |
| WEIGHT/WIDTH - AXLE 1                    | 11,380 lbs                         | 7'-2" |
| WEIGHT/WIDTH - AXLE 2 - REAR TANDEM PAIR | 48,560 lbs                         | 7'-2" |
| SPACING: AXLE 1 - AXLE 2                 | 12'-8"                             |       |
| SPACING: AXLE 2 - AXLE 3                 | 4'-6"                              |       |
| WEIGHTS PROVIDED BY                      | Certified Weight Station           |       |
| AUTOClicker POSITION                     | Driver - 3 <sup>rd</sup> axle      |       |
| WHEEL ROLLOUT 5 REVS                     | 52'-7"                             |       |
| WHEEL CIRCUMFERENCE                      | 10.52'                             |       |
| # SEMI-STATIC PASSES                     | 4                                  |       |
| # NORMAL SPEED PASSES                    | 0                                  |       |
| VEHICLE PROVIDED BY                      | FDOT                               |       |

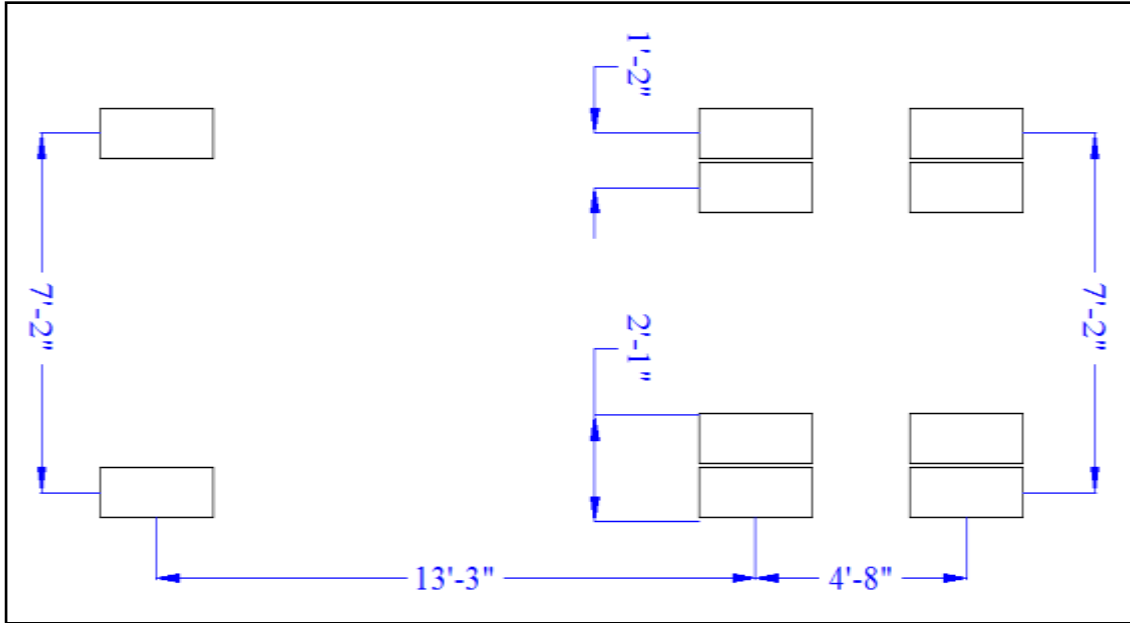


**Figure 7-18 Test Truck-1 axle spacing.**

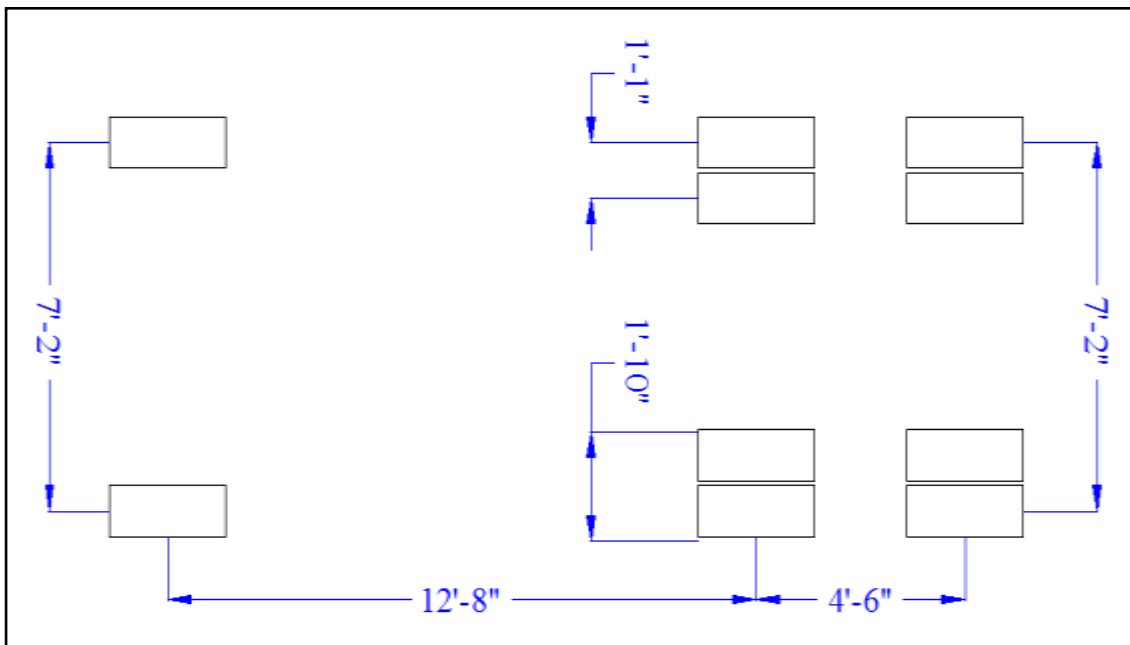


**Figure 7-19 Test Truck-2 axle spacing.**

Trucks were moved along three paths over the bridge. Each path is defined based on the distance of the driver side wheels from the inner face of the east railing of the bridge. This distance was equal to 2 ft, 10 ft - 5 in. and 18 ft -10 in. for the three paths. These loading paths are defined in Figure 7-20 and



Table 7-5.

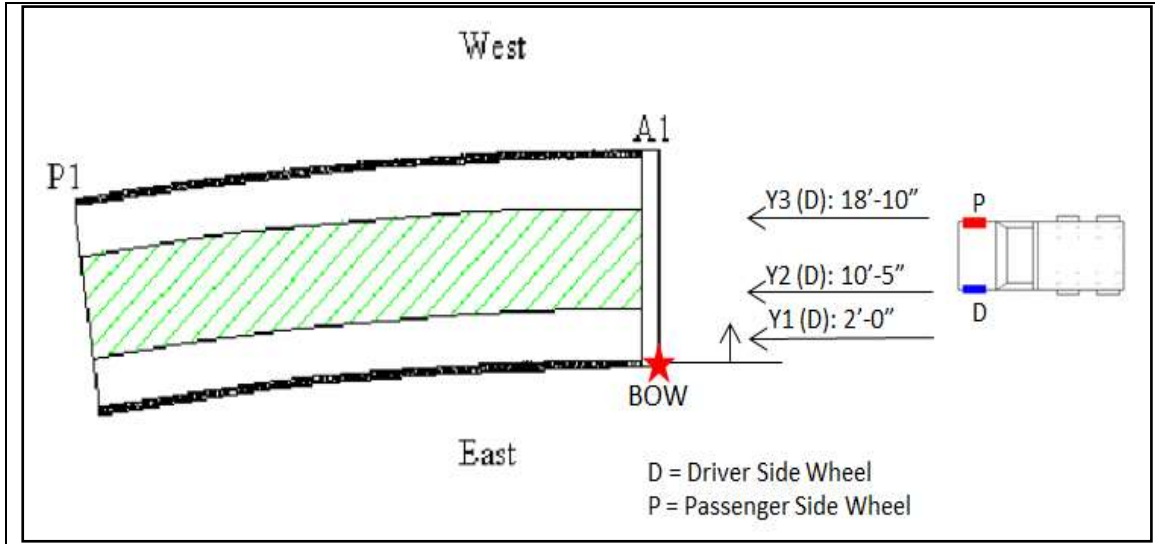


Figure 7-20 Test truck path locations.

Table 7-5 Loading Path Definitions

|   |  |
|---|--|
| TEST VEHICLE DIRECTION                                  | From North to South  |
| TEST BEGINNING POINT                                    | Front axle at $X = \sim 21' - 3'' (\pm 1')$                          |
| LATERAL LOAD POSITIONS<br>(PERPENDICULAR TO<br>ROADWAY) | $Y1 (D) = 2' - 0''$<br>$Y2 (D) = 10' - 5''$<br>$Y3 (D) = 18' - 10''$ |

The loading was done in eight different scenarios. In scenarios 1, 2, and 3, Truck-1 was run over path-1, path-2 and path-3, respectively with a slow (crawling) speed. In scenario-4, Truck-2 moved along path-1. In scenario-5, Truck-1 and Truck-2 traveled side by side on path-3 and path-1, respectively. In scenario-6, Truck-1 ran on path-2 with a speed of 30 MPH. In scenarios 7 and 8, Truck-1 followed by Truck-2 moved along path-1

and path-2, respectively. Therefore, the only high speed loading was at scenario-6 while all other loading scenarios conducted in a very low speed.

**Table 7-6 Loading Scenario Definitions**

| TEST SCENARIO       | LOADING CONFIGURATION           | <i>LATERAL POSITION</i>    |         |
|---------------------|---------------------------------|----------------------------|---------|
| 1                   | Truck-1                         | Y1                         |         |
|                     |                                 | Y1                         |         |
| 2                   |                                 | Y2                         |         |
|                     |                                 | Y2                         |         |
| 3                   |                                 | Y3                         |         |
|                     |                                 | Y3                         |         |
| 4                   |                                 | Truck-2                    | Y1      |
| 5                   |                                 | Truck-2 (Y1), Truck-1 (Y3) | Y1 & Y3 |
| 6                   | Truck-1 (Y2) Roadway Speed Test | Y2                         |         |
| 7                   | Truck-1 followed by Truck-2     | Y1                         |         |
| 8                   | Truck-1 followed by Truck-2     | Y2                         |         |
|                     | Truck-1 followed by Truck-2     | Y2                         |         |
| ADDITIONAL COMMENTS |                                 | Weather: High 70's, humid  |         |

## 7.5 Finite Element Modeling

The main objective of this field testing was to calibrate the finite element models. These calibrated finite element models are required for further understanding of the behavior of twin box-girder bridges. Therefore, the finite element model of the Bridge 860600 is used to evaluate the responses of the bridge under the defined loading scenarios. The ABAQUS FEA software package is used for this purpose. The results of the analyses are compared with the field testing data.

An attempt was made to include all possible details in the finite element model. Therefore, the top flange, web, and bottom flange of the box-girders, web transverse stiffeners, internal and external diaphragms, concrete deck, and railings of the bridge are modeled using shell elements. The only elements that are modeled using beam elements are the internal bracings of the girders. Then, the footprints of the trucks in each loading scenario are applied to the concrete deck of the bridge. This is done using surface pressure feature in Abaqus FEA. Figure 7-21 shows the model with and without the concrete deck, so that the modeling details can be more visible. The meshed model shows meshing of the cracked zone of a damaged girder.

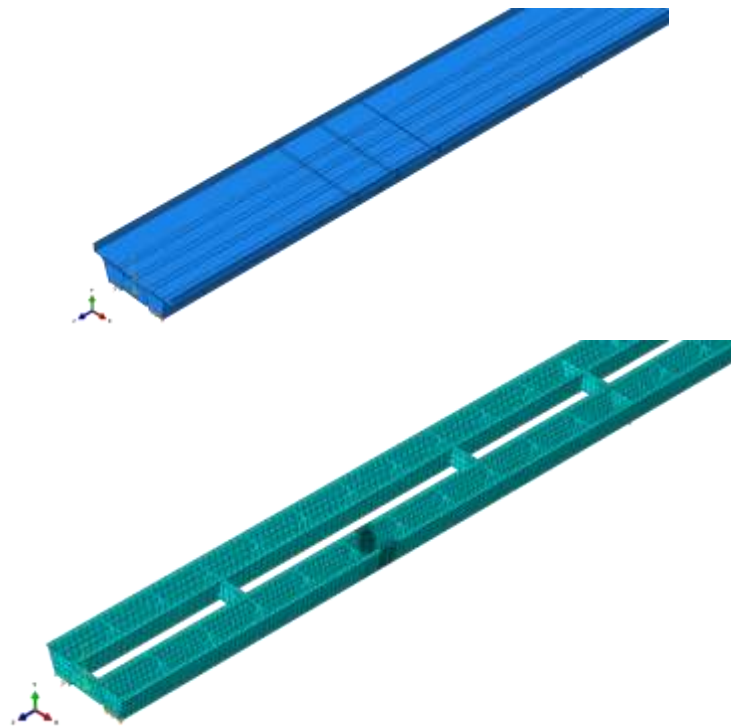


**Figure 7-21 Finite element model of the first span of Ft. Lauderdale bridge 860600.**

## 7.6 Qualitative Review of Test Data

Field data was examined graphically first by BDI and then by FIU to determine its quality and usefulness for analytical comparisons. Some of the typical indicators of data quality include reproducibility between identical truck crossings, elastic behavior (strains returning to zero after truck crossing), and observation of any unusual responses that might indicate possible gauge malfunctions.

### Responses as a Function of Load Position:

Data recorded from the wireless truck position indicator (BDI Autoclicker) was processed so that all of the corresponding response data could be presented as a function of vehicle position. This was done so that during analytical modeling, important measurement responses could be directly related to a specific load location rather than an arbitrary point in time.

### Reproducibility and Linearity:

Responses from identical truck passes were very reproducible, as shown in Figure 7-22 and Figure 7-23. In addition, all response data was linear with respect to load magnitude and truck position. Note that the majority of responses returned to zero (barring thermal drift for strains – see next item), indicating elastic behavior. All of the response histories had a similar degree of reproducibility and linearity, indicating that the data collected was of good quality.

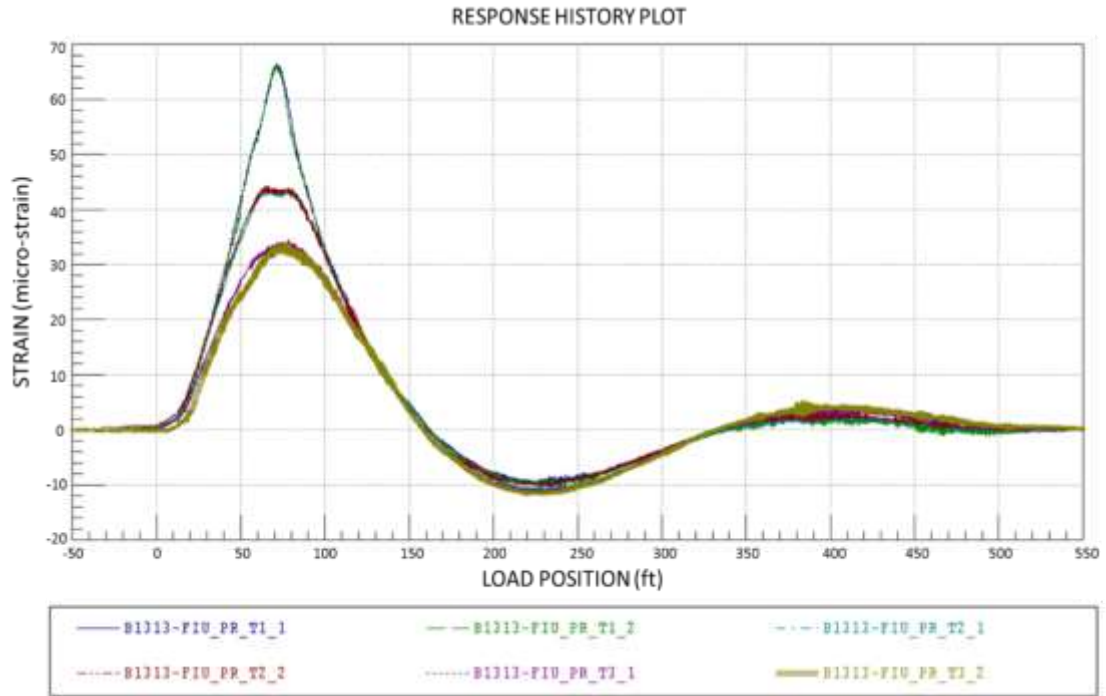


Figure 7-22 Reproducibility of strain response histories (typical).

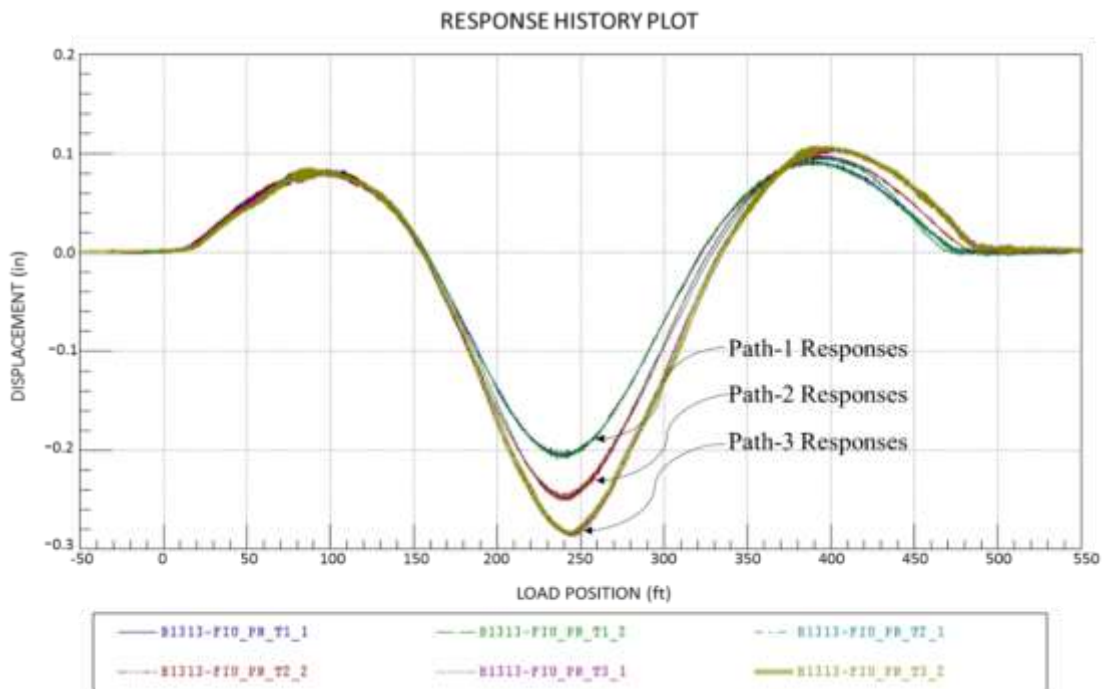
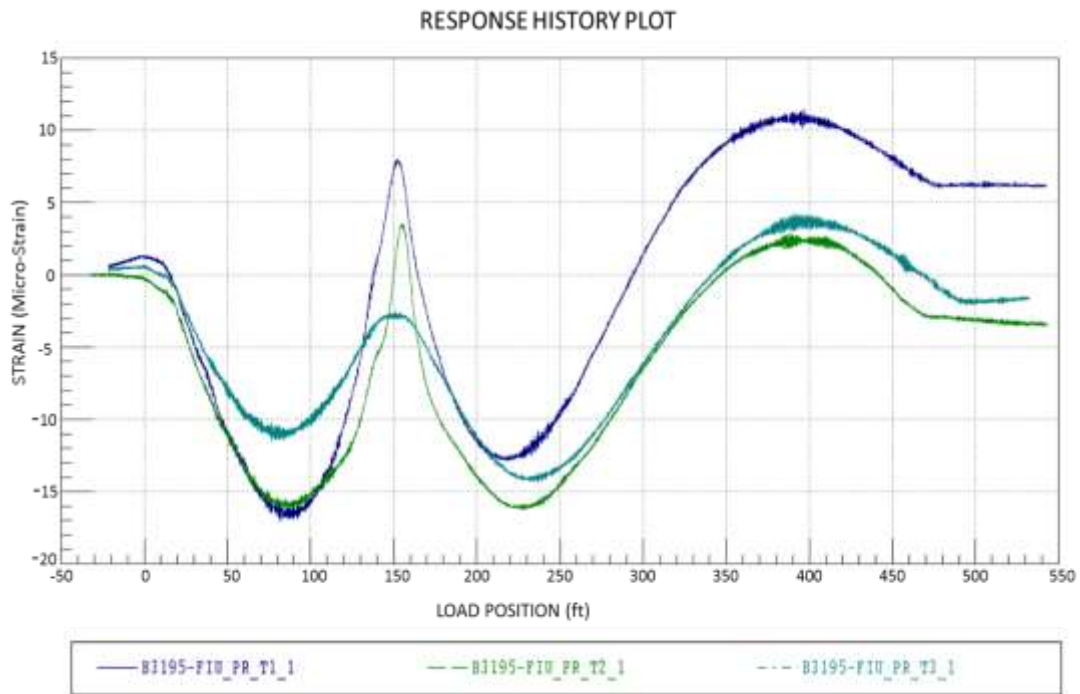


Figure 7-23 Reproducibility of displacement response histories (typical).

### Thermal Drift:

During the initial data investigation, it was observed that the majority of the strain response data tended to drift throughout the load tests, as shown in Figure 7-24. This is a common occurrence with strain transducers since they have very little mass and react to temperature changes very rapidly compared to the structure to which they are attached to. Generally, temperature drift is not a concern for short duration load tests because the magnitude of the drift is very small compared to the live-load responses. However, due to the extended duration of the tests (greater than 4 minutes) some of the strain measurements were able to drift by as much as  $6 \mu\epsilon$ . To account for the drift, a linear offset was assumed for the duration of each load test and subtracted from each sensors' output. This is illustrated in Figure 7-25, where the raw response and corrected response for Truck-1 load along path-1 are shown on the same plot.



**Figure 7-24 Example of variable thermal drift observed during testing.**

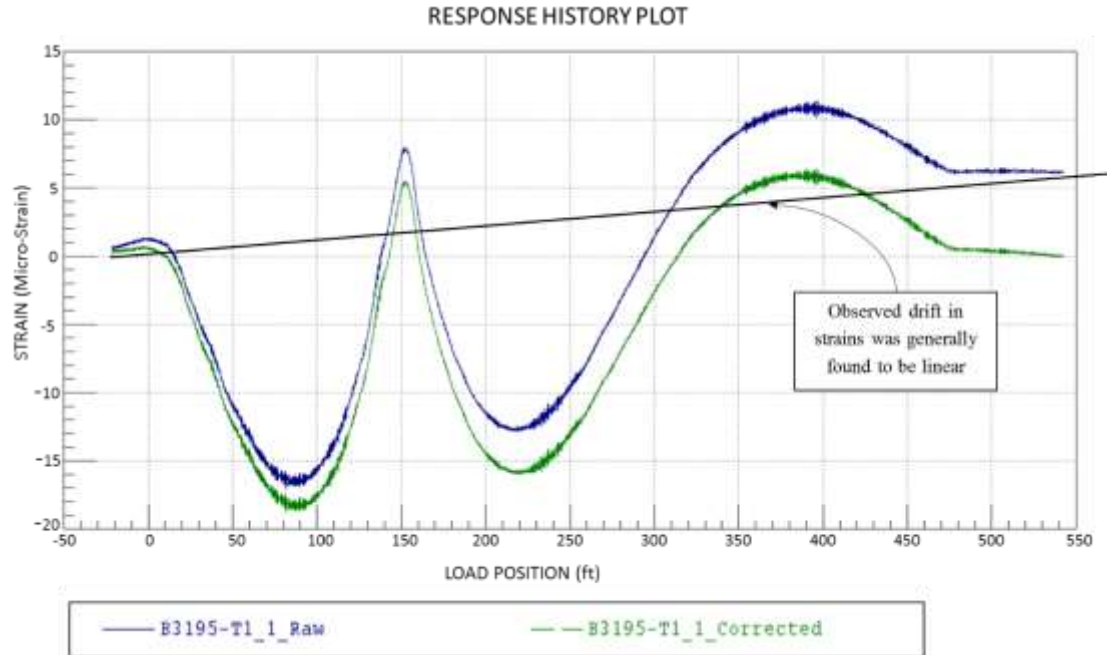


**Figure 7-25 Comparison of raw and thermally corrected strain data.**

Dynamic Component of Response:

Tests at both crawl speed (~3 mph) and roadway speed (~30 mph) were performed along path-2 using test Truck-1. When comparing strain responses from the two different tests, a fairly significant dynamic effect was observed in the roadway speed test as compared to the crawl speed test, seen in Figure 7-26. In this figure the blue response is from the crawl speed test while the green response is from the roadway speed test. Comparing with the crawl speed test, the roadway speed test saw a dynamic effect of approximately 12%. It is important to note that this impact factor is less than the impact factor of 33% specified in AASHTO *LRFD Bridge Design Specifications* due to dynamic loading. This difference is because the dynamic impact factor specified in AASHTO *LRFD Bridge Design Specifications* is defined as the ratio of peak response to static response,

while the dynamic effect found here are calculated based on the peak responses between two dynamic loading tests.

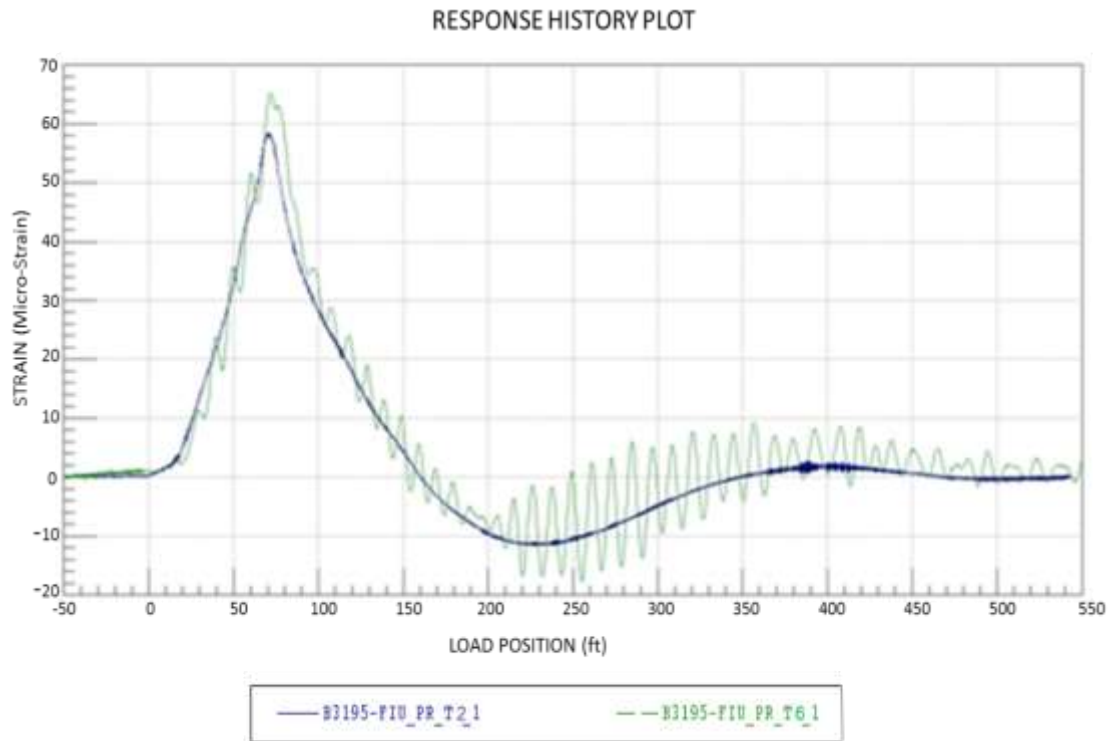


Figure 7-26 Strain history comparison – crawl speed vs. roadway speed at Section 2.

## 7.7 Comparison of Field Test Data and FEA Results

In general, the results of field testing were in good agreement with the results of finite element analysis. In this section, some of the results of finite element analysis of the bridge under loading scenarios are compared to the field test data. The selected loading scenarios include scenario-3 which has Truck-1 on path-3, scenario-5 which has Truck-2 on path-1 and Truck-1 on path-3 and loading scenario-7 which has Truck-1 followed by Truck-2 on path-1. Figure 7-27 through Figure 7-32 compare the deflection of the girders in first and second spans due to application of selected loading scenarios.



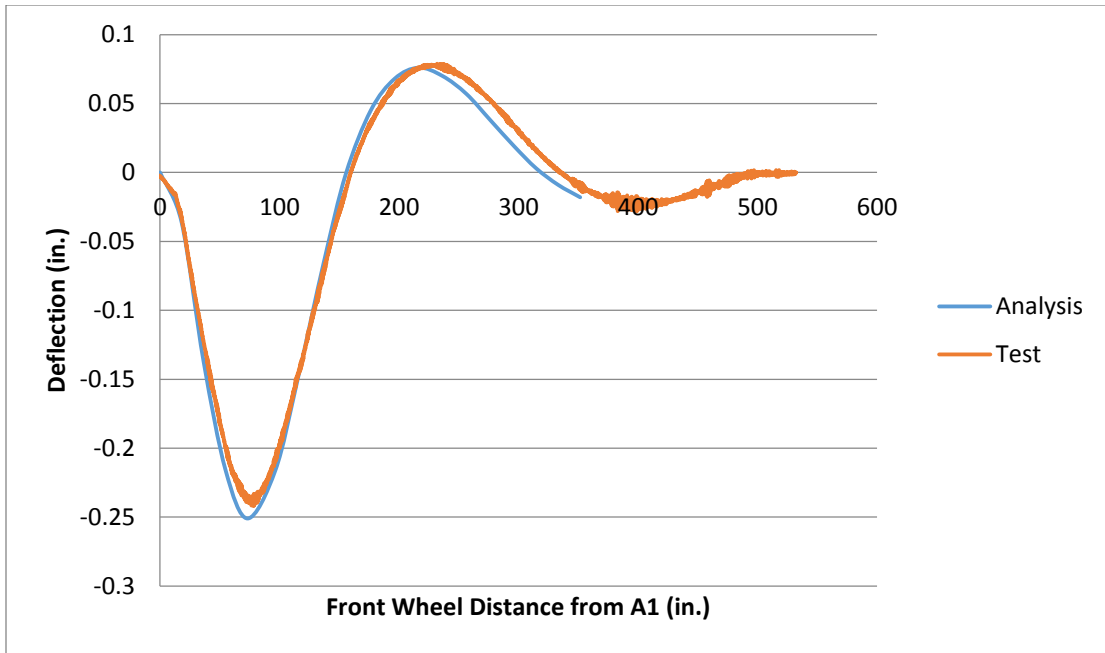


Figure 7-27 Vertical deflection of west edge of WG: 59 ft from north abutment, Truck-1 on path-3.



Figure 7-28 Vertical deflection of west edge of WG: 225.5 ft from north abutment, Truck-1 on path-3.

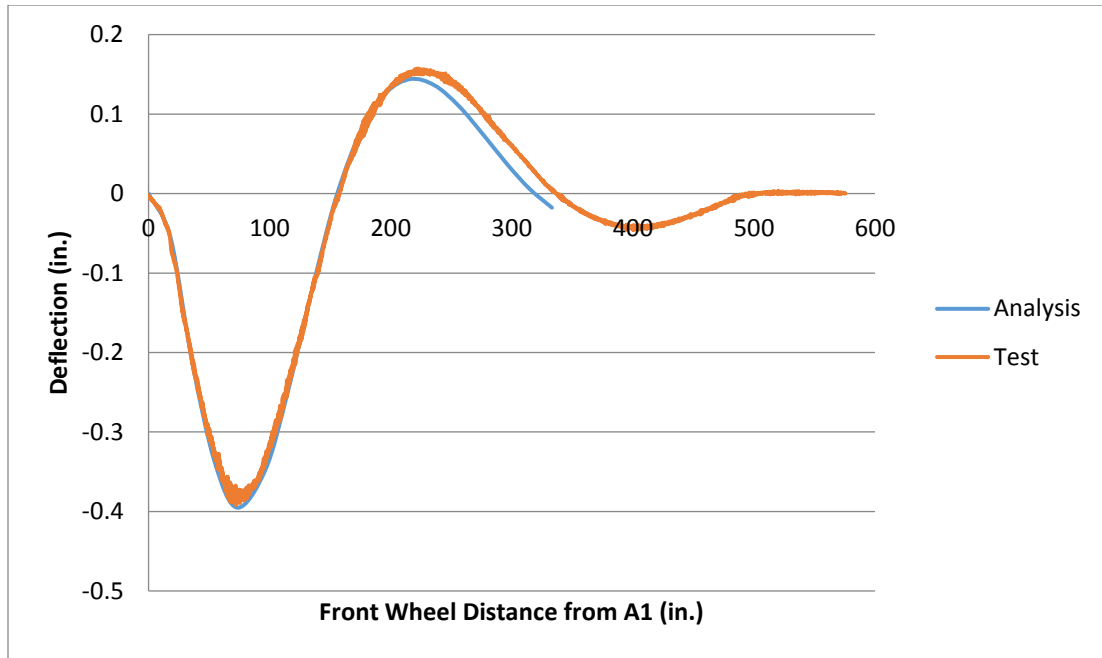


Figure 7-29 Vertical deflection of west edge of EG: 59 ft from north abutment, Truck-1 on path-3 and Truck-2 on path-1.

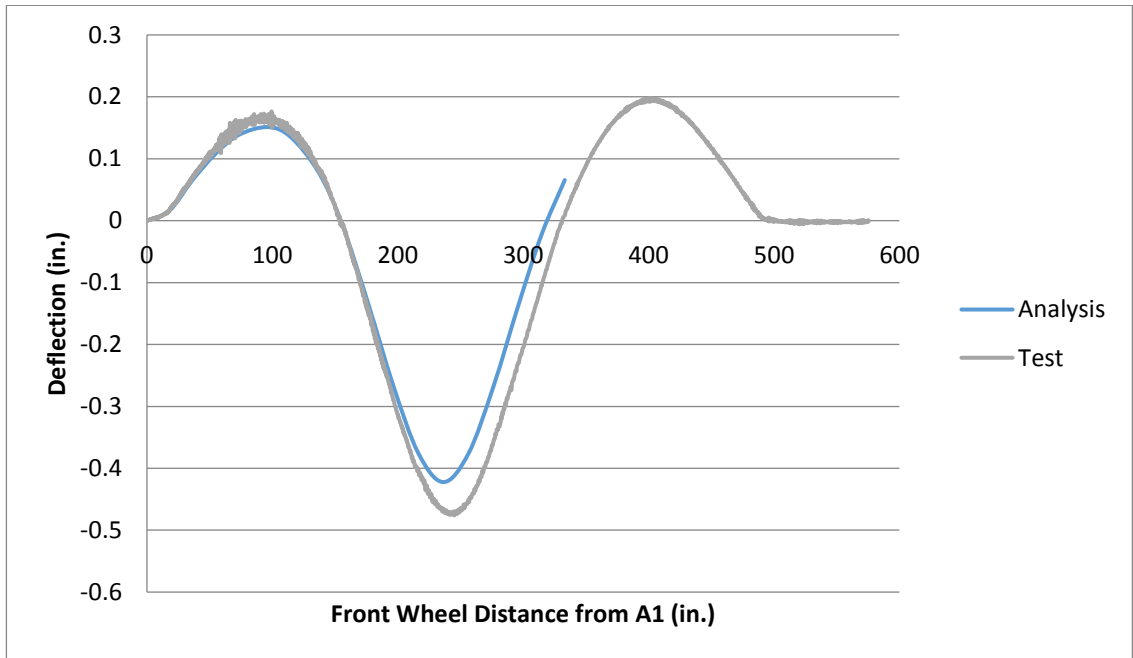
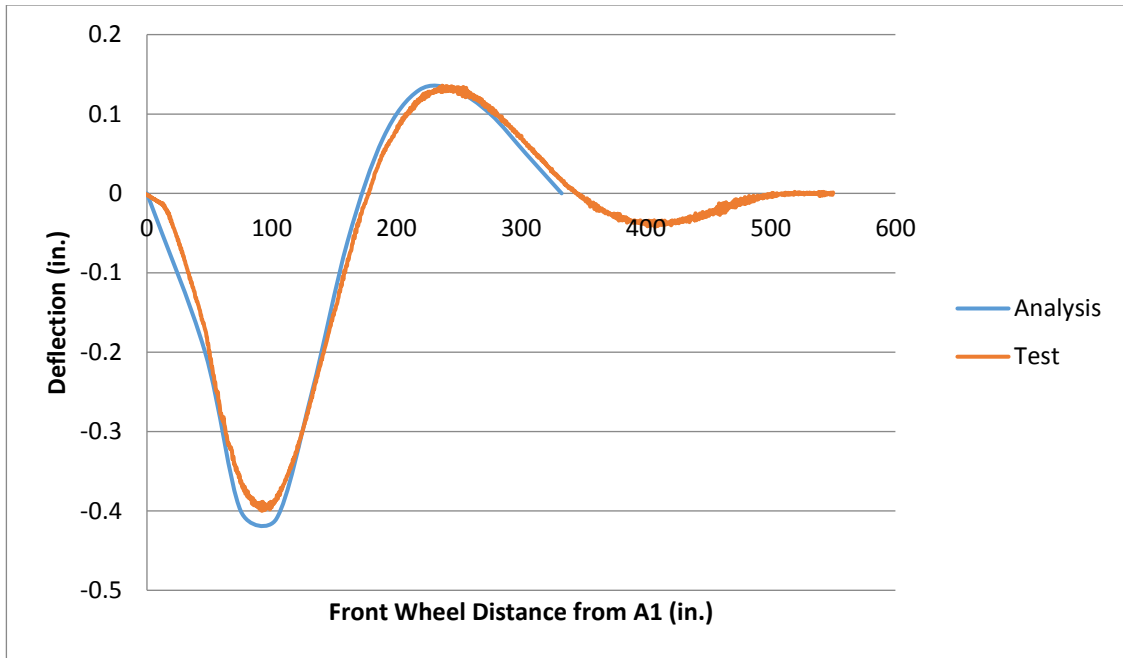
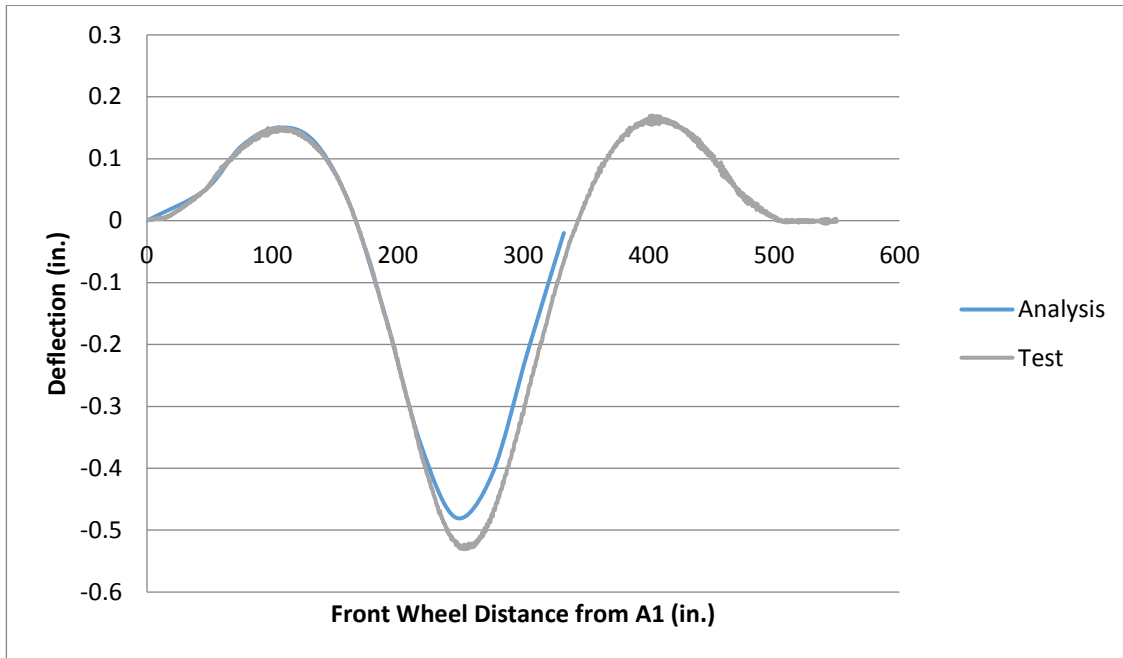


Figure 7-30 Vertical deflection of west edge of WG: 225.5 ft from north abutment, Truck-1 on path-3 and Truck-2 on path-1.



**Figure 7-31 Vertical deflection of west edge of EG: 59 ft from north abutment, Truck-1 followed by Truck-2 on path-1.**



**Figure 7-32 Vertical deflection of east edge of EG: 225.5 ft from north abutment, Truck-1 followed by Truck-2 on path-1.**

It is observed that the field test deflections are in agreement with computer model deflections. Figure 7-33 through Figure 7-38 illustrate the longitudinal stresses of the bottom flange of the box-girders due to application of loading scenario-3 to the bridge.

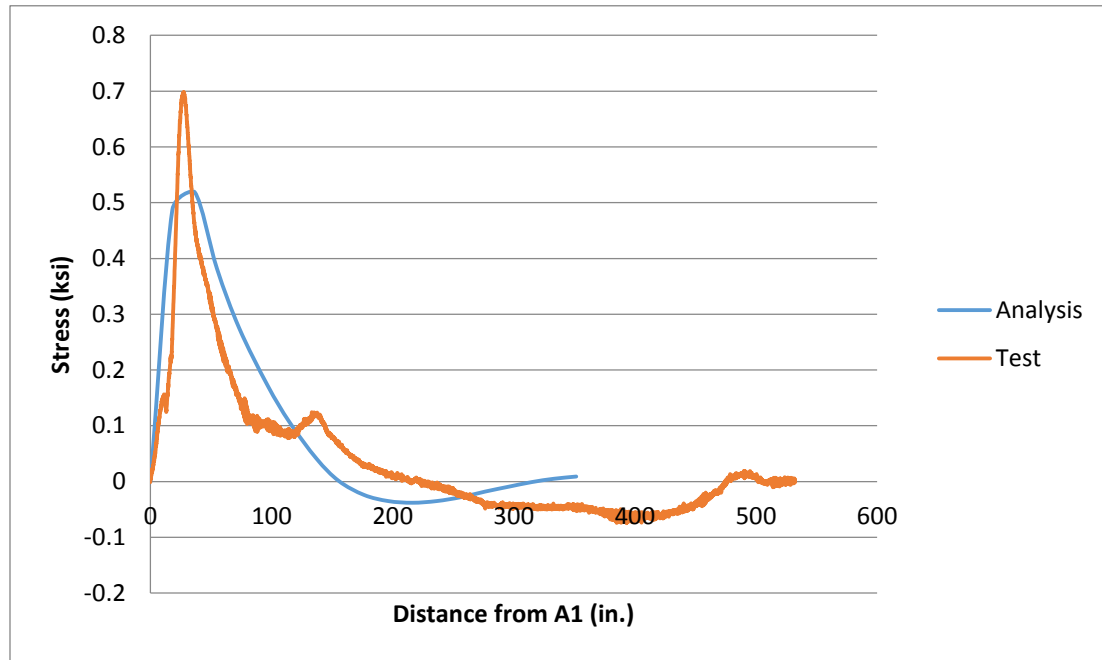


**Figure 7-33 Longitudinal stress at 6 ft from north abutment in the west edge of bottom flange of WG: Truck-1 on Path-3.**

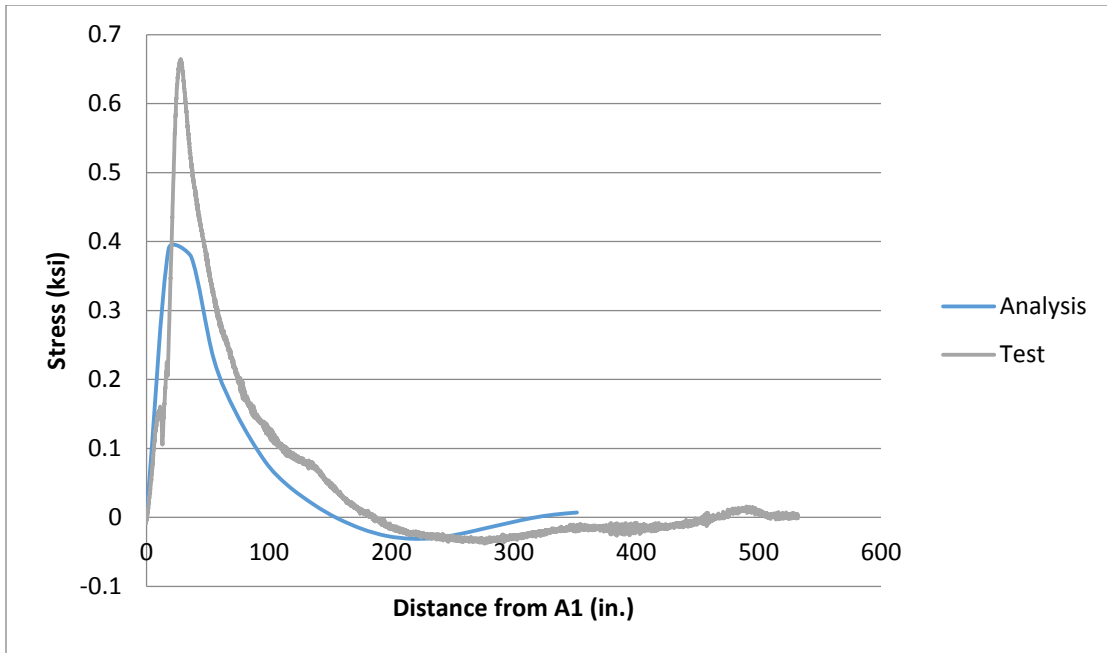


**Figure 7-34 Longitudinal stress at 6 ft from North Abutment in the west edge of bottom flange of EG: Truck-1 on path-3.**

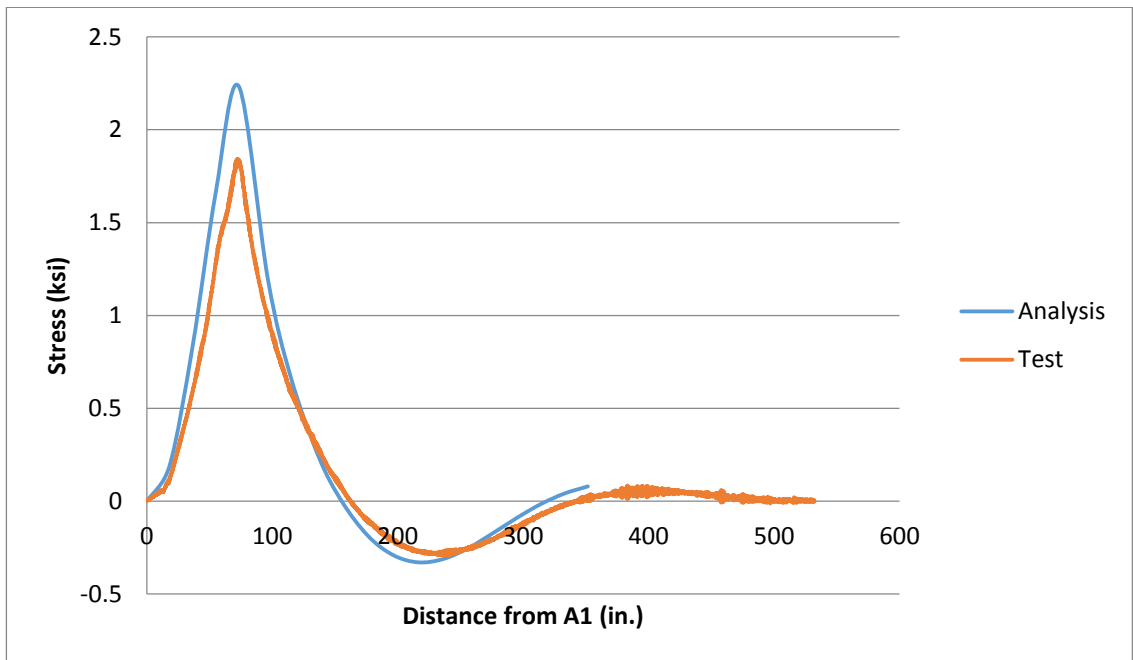


**Figure 7-35 Longitudinal stress at 58 ft from north abutment in the west edge of bottom flange of WG: Truck-1 on path-3.**

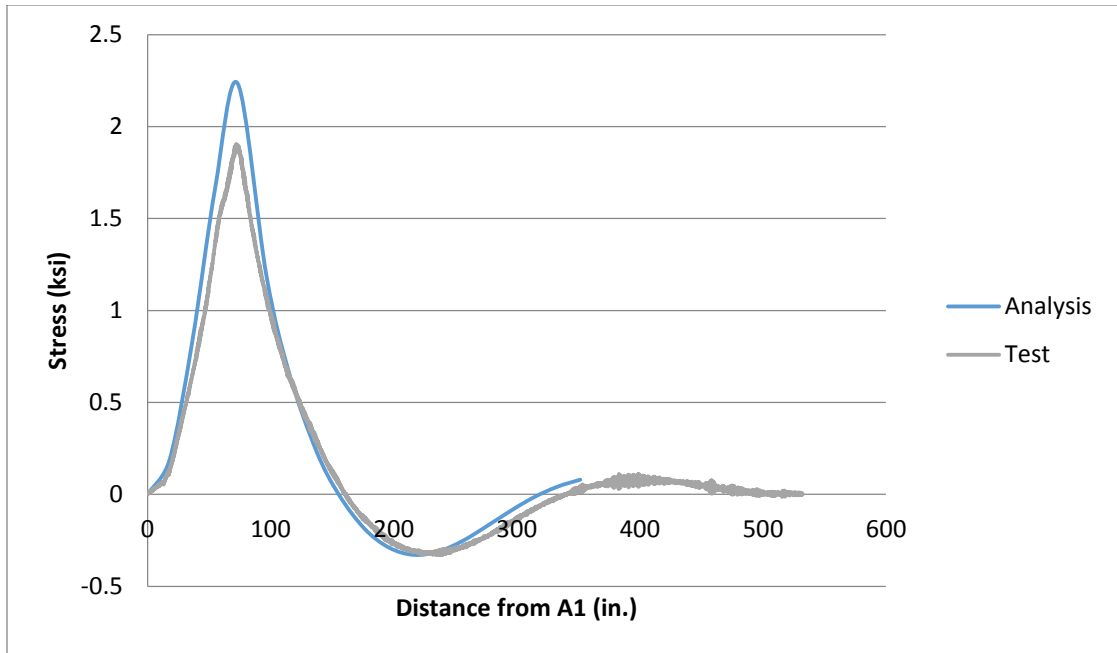


**Figure 7-36 Longitudinal stress at 58 ft from north abutment in the east edge of bottom flange of WG: Truck-1 on path-3.**

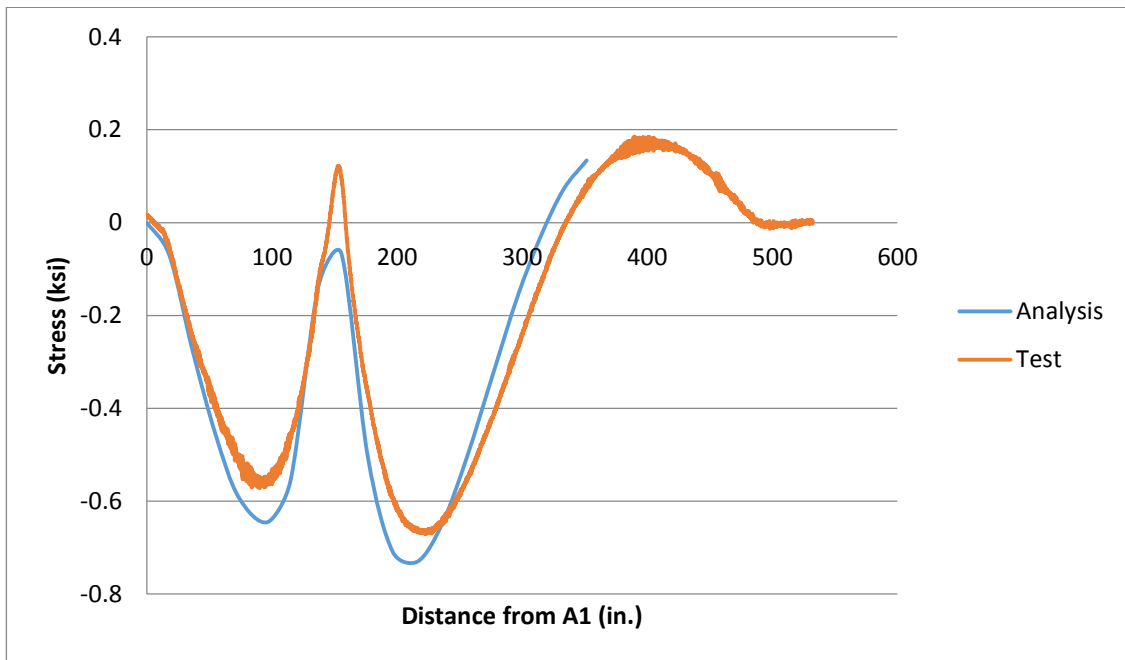


**Figure 7-37 Longitudinal stress at 138 ft from north abutment in the west edge of bottom flange of WG: Truck-1 on path-3.**

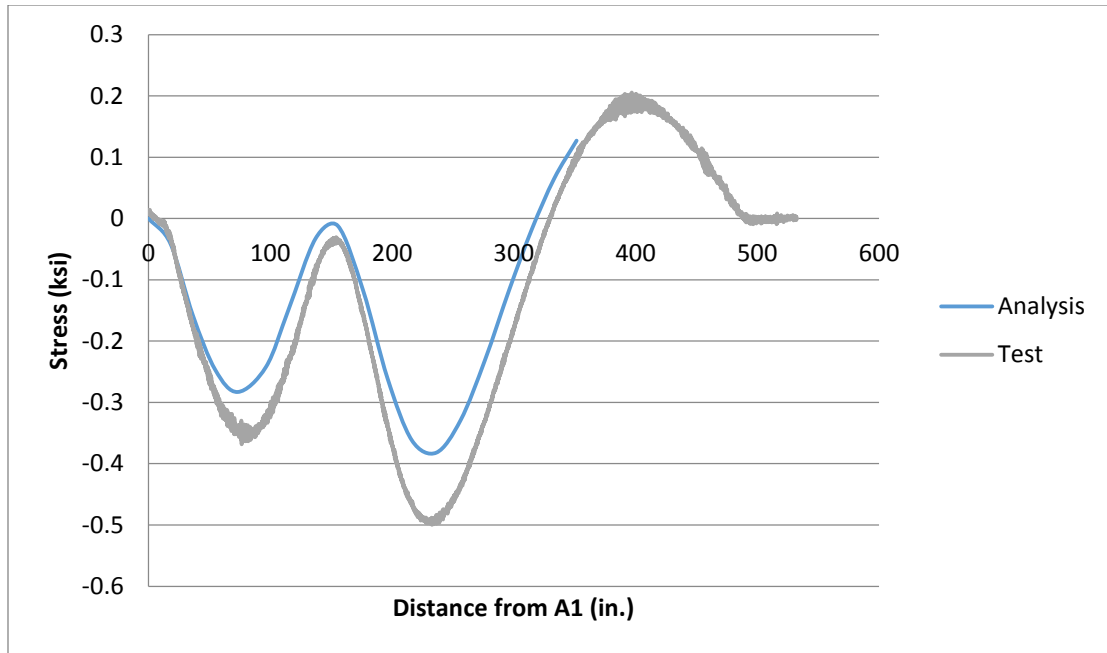


**Figure 7-38 Longitudinal stress at 138 ft from north abutment in the east edge of bottom flange of WG: Truck-1 on path-3.**

Figure 7-39 through Figure 7-44 compare the longitudinal stresses of the bottom flange of the box-girders due to application of loading scenario-5 to the bridge.

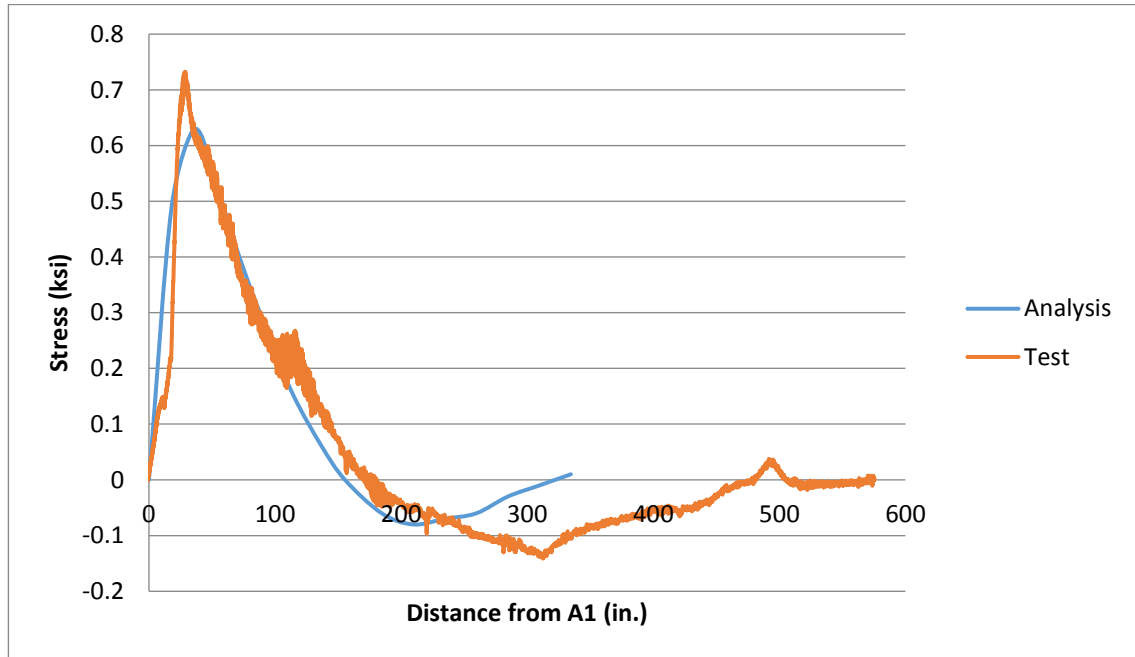


**Figure 7-39 Longitudinal stress at 6 ft from north abutment in the west edge of bottom flange of WG: loading scenario-5.**

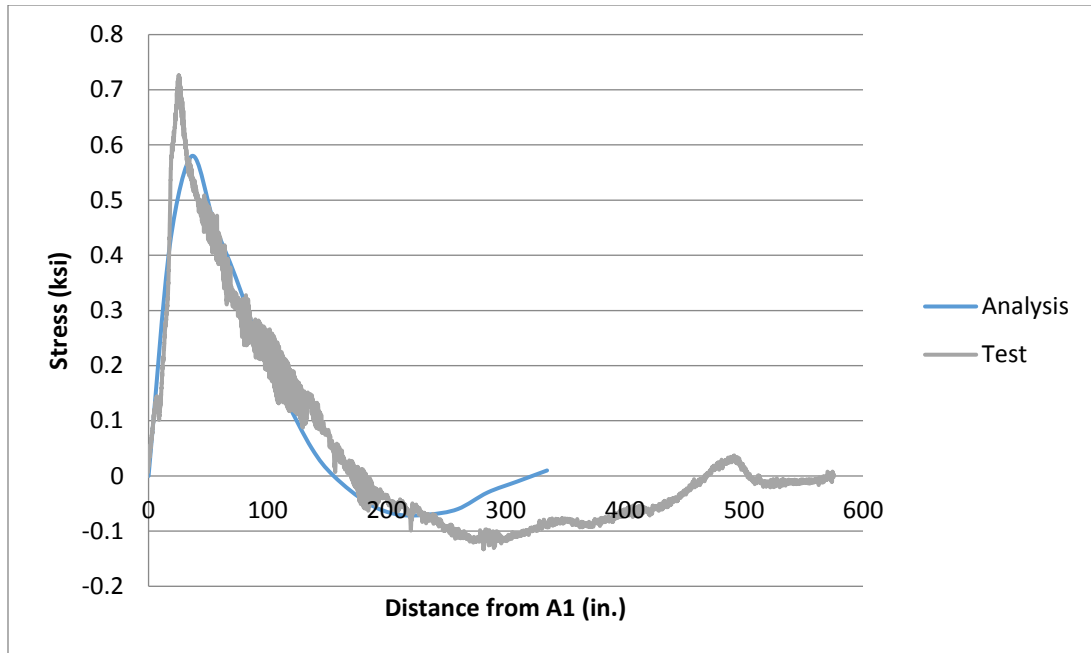


Figure 7-40 Longitudinal stress at 6 ft from north abutment in the west edge of bottom flange of EG: loading scenario-5.

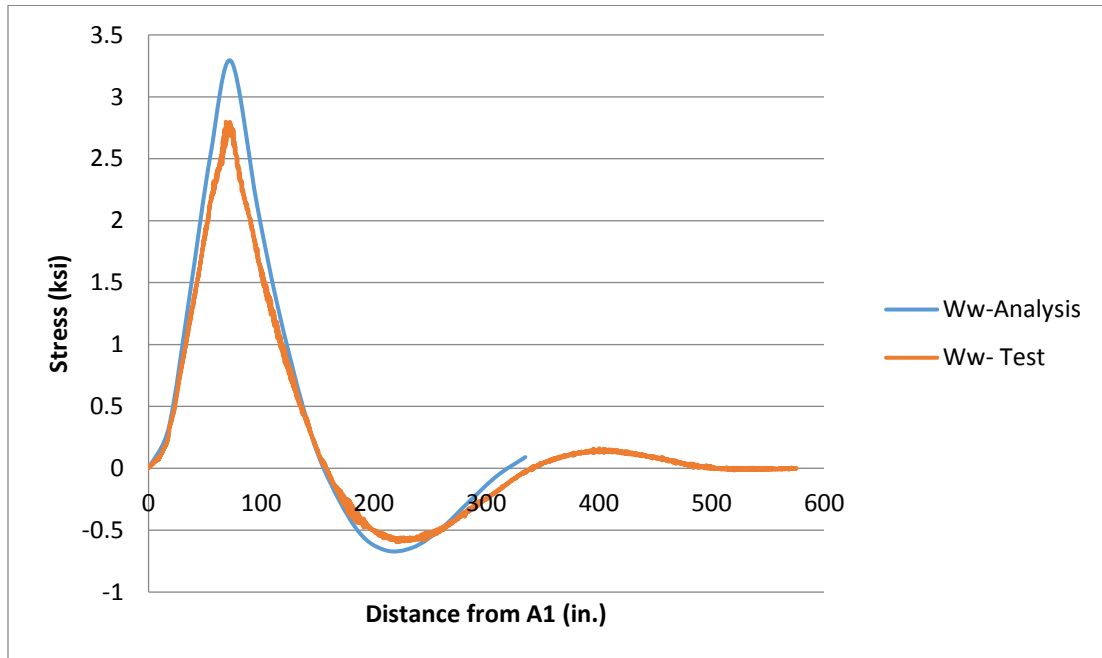


Figure 7-41 Longitudinal stress at 58 ft from north abutment in the west edge of bottom flange of WG: loading scenario-5.



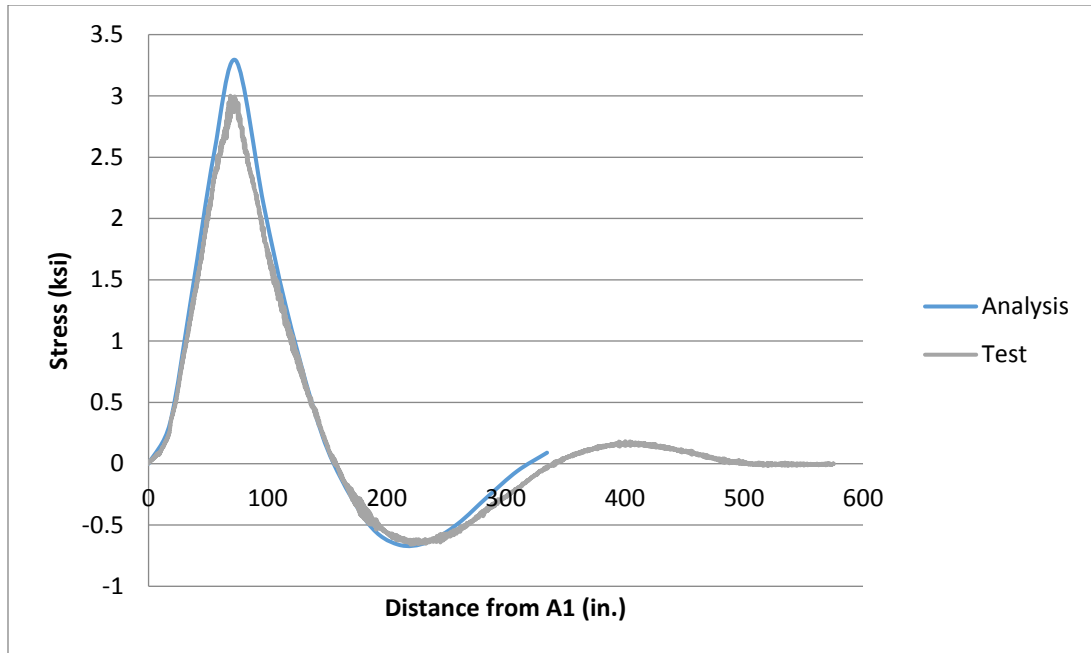


Figure 7-42 Longitudinal stress at 58 ft from north abutment in the east edge of bottom flange of WG: loading scenario-5.

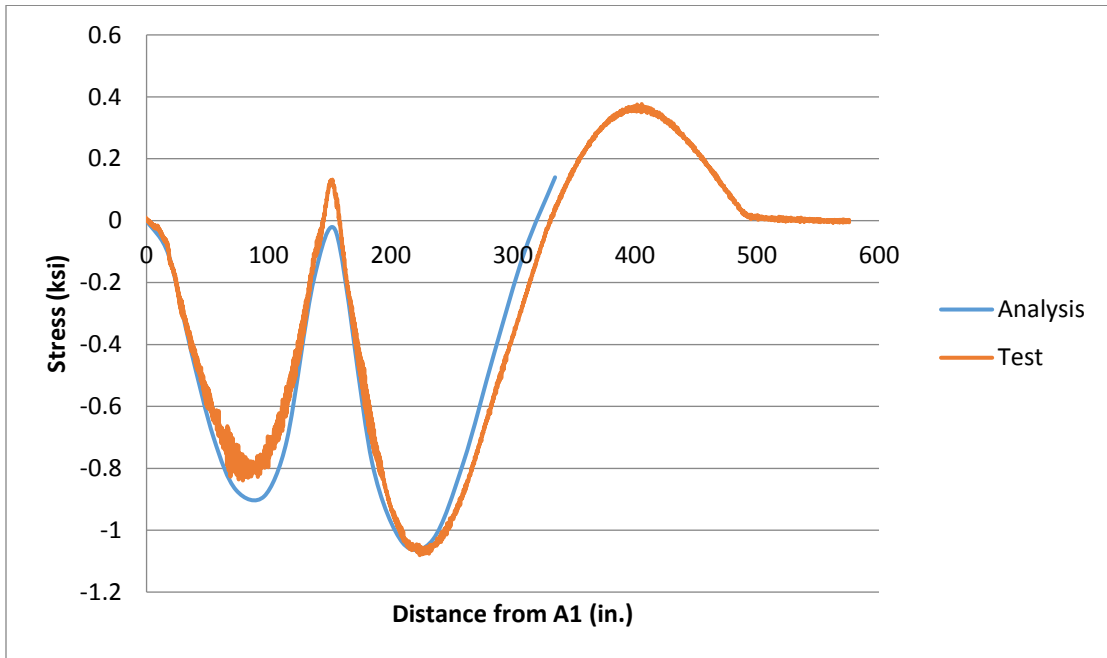
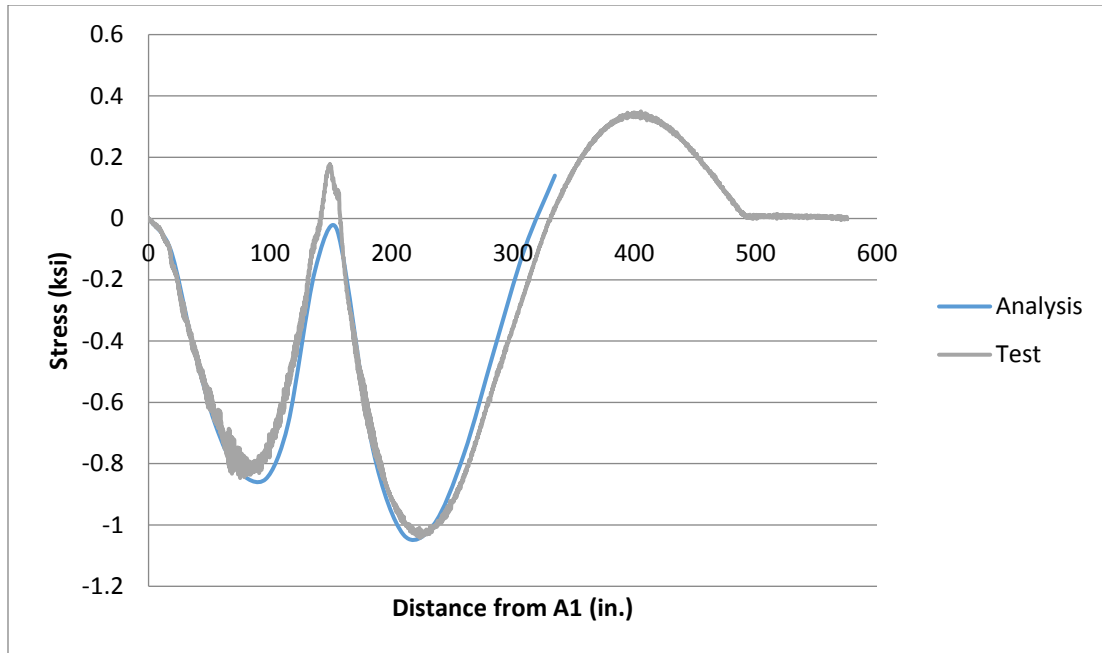


Figure 7-43 Longitudinal stress at 138 ft from north abutment in the west edge of bottom flange of WG: loading scenario-5.



**Figure 7-44 Longitudinal stress at 138 ft from north abutment in the east edge of bottom flange of WG: loading scenario-5.**

In Figure 7-45 to Figure 7-50, the longitudinal stress of the bottom flange of the box-girders that resulted from finite element analysis of loading scenario-7 are compared to the test data.

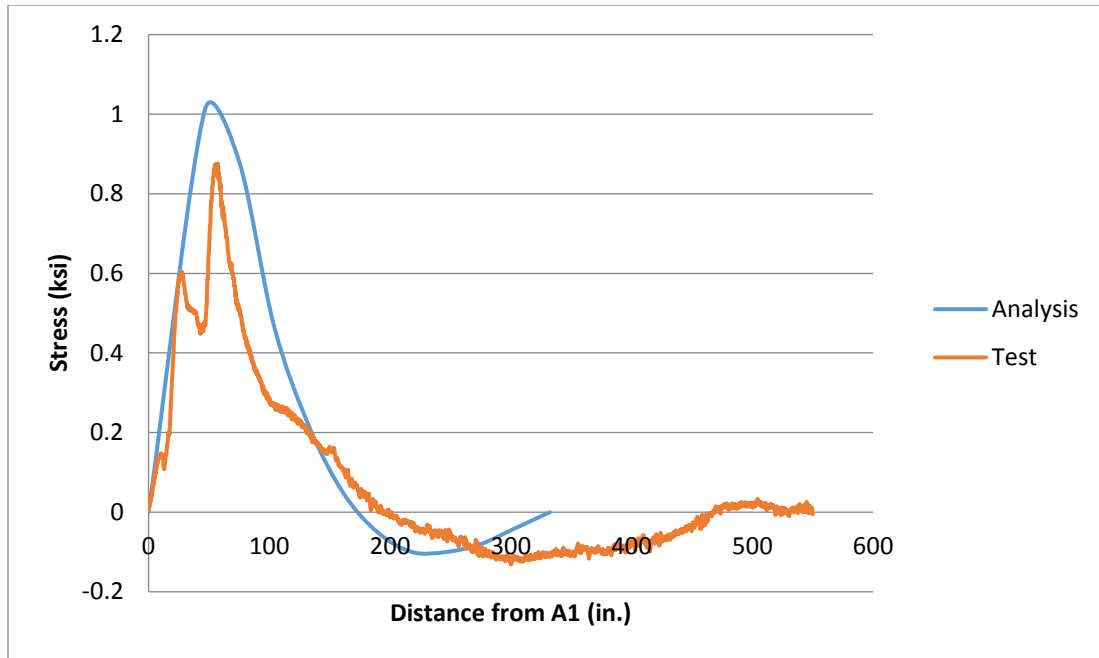


Figure 7-45 Longitudinal stress at 6 ft from north abutment in the west edge of bottom flange of EG - Truck-1 followed by Truck-2 on path-1.

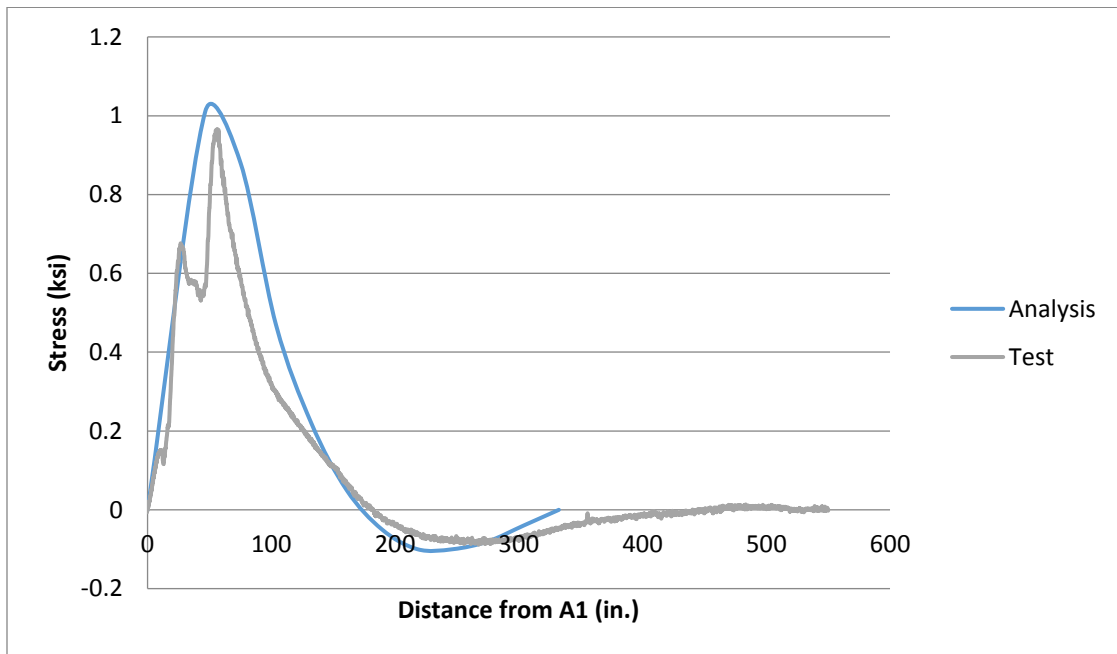


Figure 7-46 Longitudinal stress at 6 ft from north abutment in the east edge of bottom flange of EG: Truck-1 followed by Truck-2 on path-1.

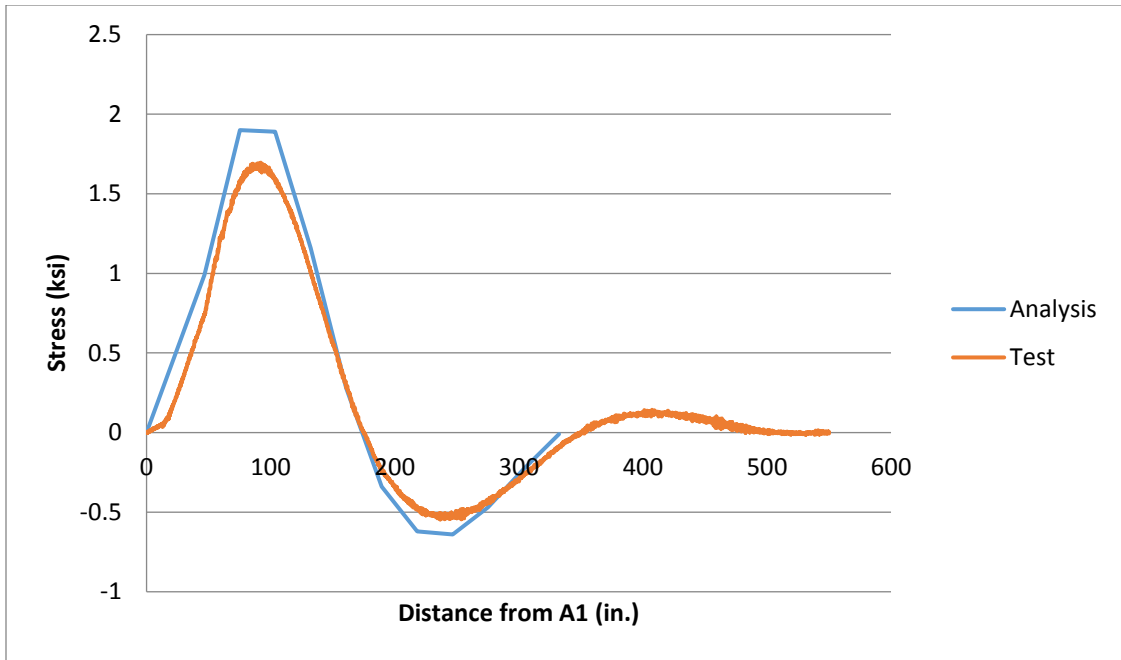


Figure 7-47 Longitudinal stress at 58 ft from north abutment in the west edge of bottom flange of EG: Truck-1 followed by Truck-2 on path-1.

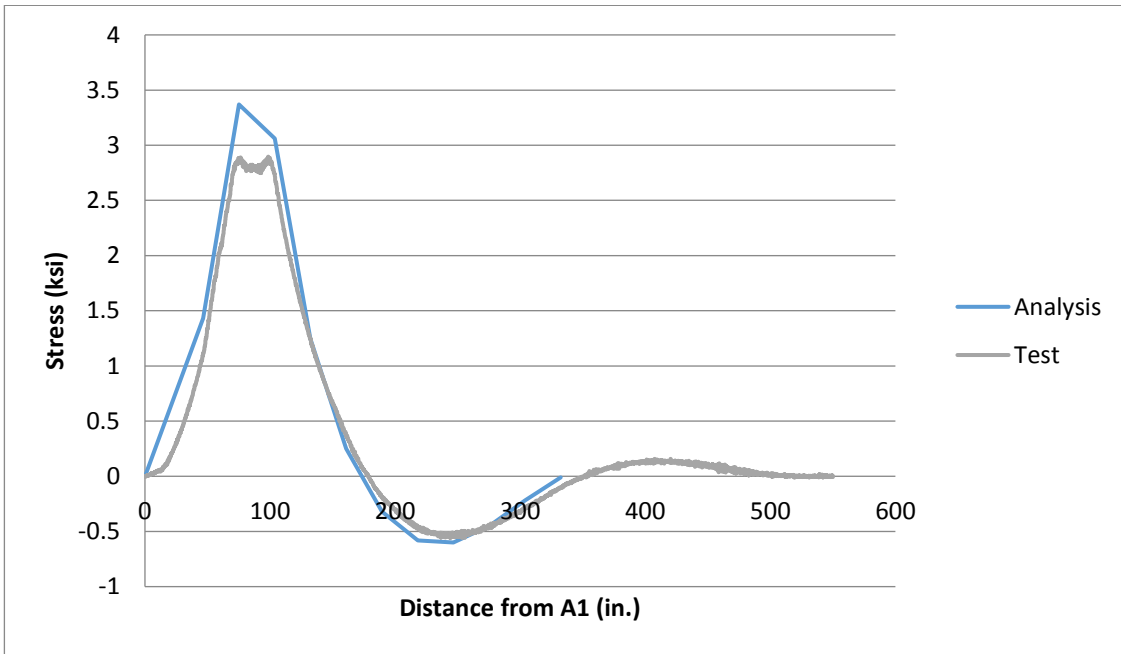
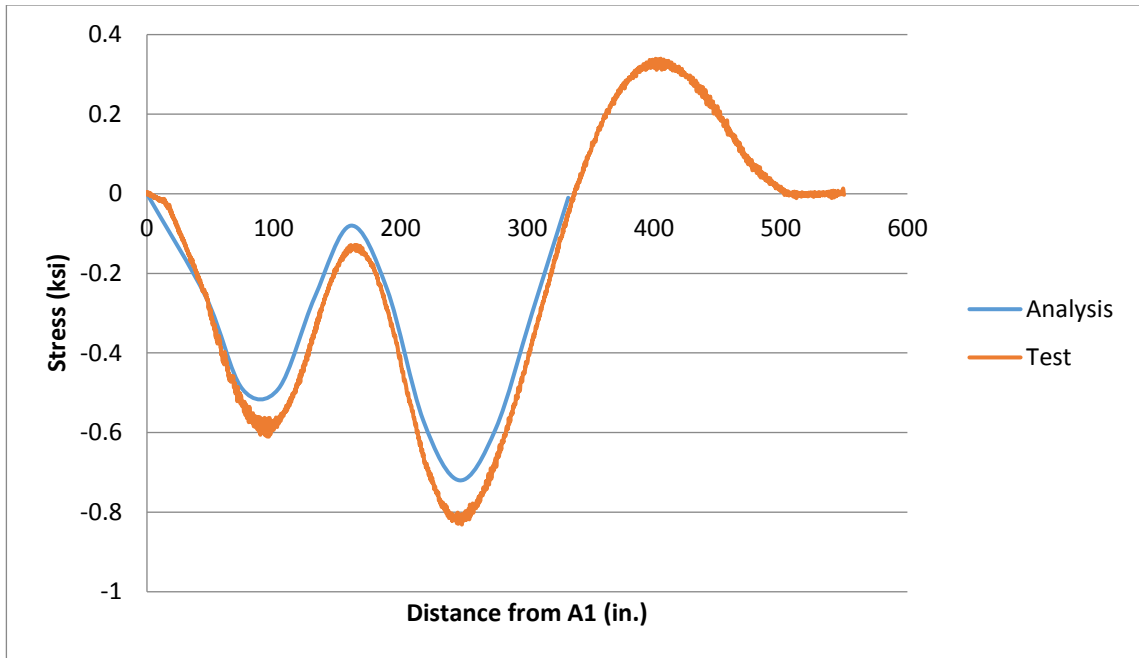
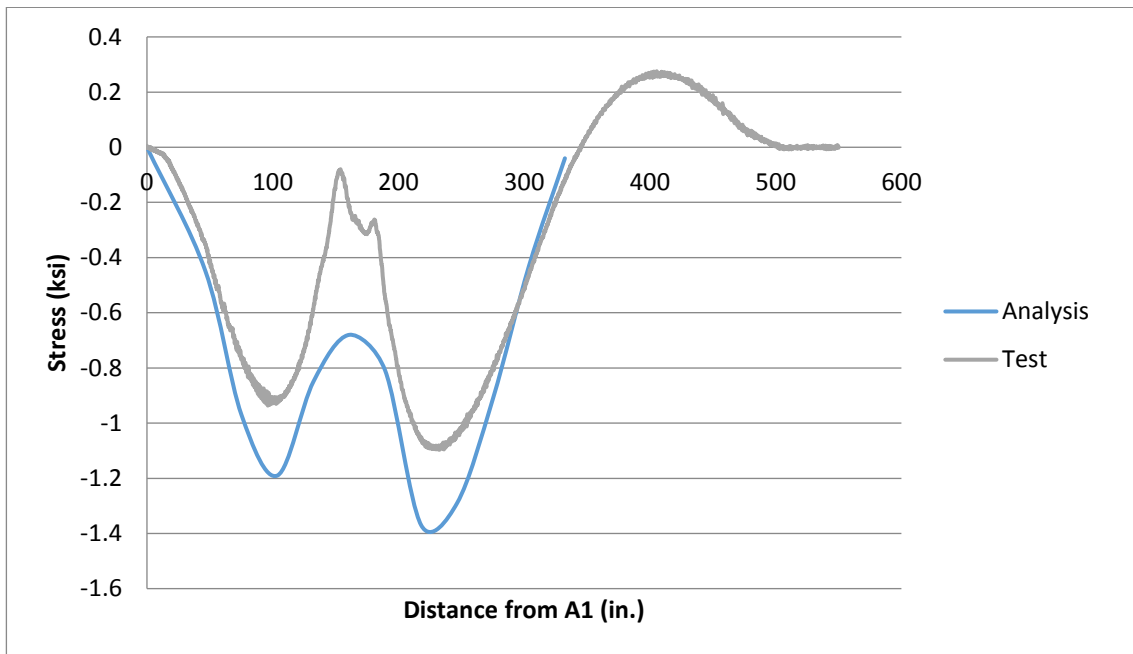


Figure 7-48 Longitudinal stress at 58 ft from north abutment in the east edge of bottom flange of EG: Truck-1 followed by Truck-2 on path-1.



**Figure 7-49 Longitudinal stress at 138 ft from north abutment in the west edge of bottom flange of WG: Truck-1 followed by Truck-2 on path-1.**



**Figure 7-50 Longitudinal stress at 138 ft from north abutment in the east edge of bottom flange of EG: Truck-1 followed by Truck-2 on path-1.**

It is observed from the stress results that the analytic and observed stresses match each other in most of the points of the curve. The maximum tensile stresses from finite element analysis in the section close to north abutment (Section-1) are greater than the field test maximum stresses. This can be attributed to the partial fixity over the abutment in the real life structure compared to that of the computer model which assumes a perfect pin in the abutments. That is why the finite element stresses at the section 58ft from the north abutment are smaller than those of field test.

## Chapter 8 Redundancy Analysis of Ft. Lauderdale Twin Box-Girder Bridge 860600

In this chapter, the redundancy of Ft. Lauderdale Bridge, which was discussed earlier in Chapter 7, will be assessed using direct analysis approach that was proposed by Ghosn and Moses in NCHRP Report 406. Please refer to Section 1.3.1 for the overview description of this approach and to Chapter 7 for the detailed information on the bridge geometry and configuration.

### 8.1 Bridge Girder Flexural Capacity

The first needed parameter for redundancy analysis of the bridge is the flexural capacity of the composite box-girder section. A summary of the dimensions of the composite section at the middle of the span is shown in Figure 8-1.

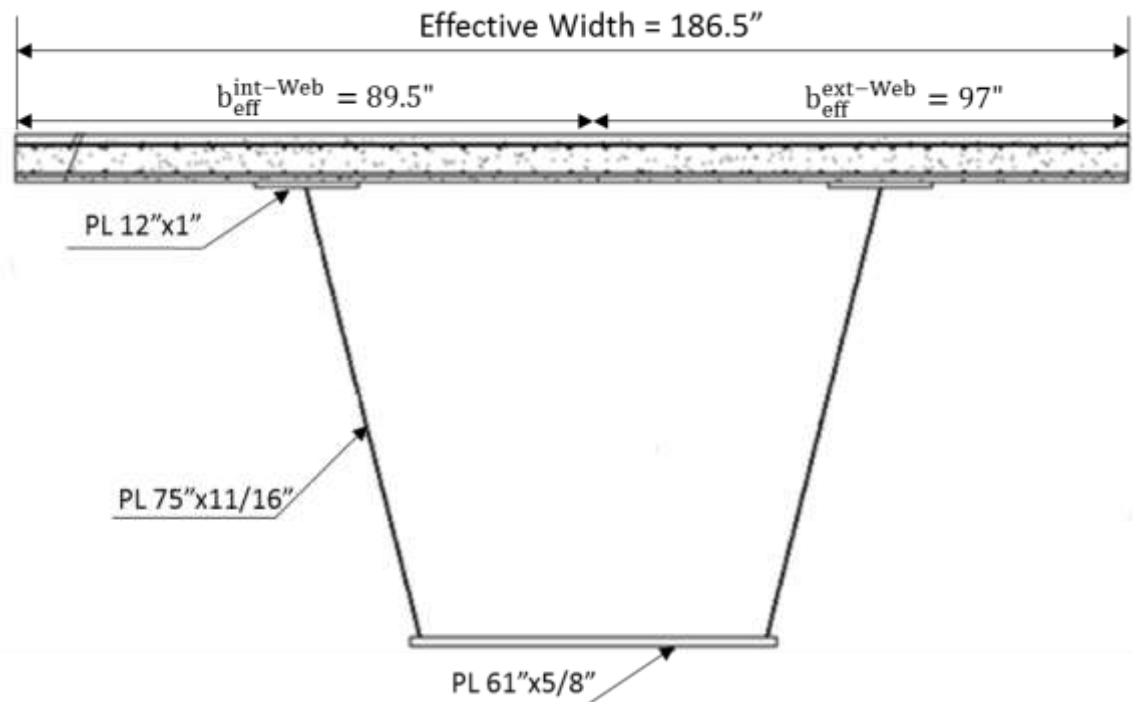


Figure 8-1 Box-girder composite section, Ft Lauderdale bridge.

### 8.1.1 Effective Width of Concrete Deck

Based on the provisions of AASHTO *LRFD Specifications*, the effective width of concrete deck for the composite action of each girder of a two-girder bridge can be calculated as follows:

$$b_{\text{eff}} = b_{\text{eff}}^{\text{int-Web}} + b_{\text{eff}}^{\text{ext-Web}}$$

Where:

$b_{\text{eff}}^{\text{int-Web}}$  = Effective concrete deck width for an interior web

$b_{\text{eff}}^{\text{ext-Web}}$  = Effective concrete deck width for an exterior web

And the effective width of concrete deck for the interior web of the girder is calculated as the minimum of the following three values:

$$12t_s + \frac{1}{2}b_{\text{TF}} = 12 \times 8 + \frac{1}{2} \times 12 = 102 \text{ in}$$

$$\frac{\text{Span Length}}{4} = \frac{1716}{4} = 429 \text{ in}$$

$$\text{Avg. Girder Spacing} = 97 \text{ in}$$

Therefore, the effective width of concrete deck for the interior web of the girder is equal to 97 in. For the exterior web of the girder, the effective width of concrete deck will be equal to half of the effective width for the interior web plus the minimum of the following three values:

$$6t_s + \frac{1}{4}b_{\text{TF}} = 6 \times 8 + \frac{1}{4} \times 12 = 51 \text{ in}$$

$$\frac{\text{Span Length}}{8} = \frac{1716}{8} = 214.5 \text{ in}$$



Overhang length = 41 in.

Hence

$$b_{\text{eff}}^{\text{ext-Web}} = \frac{97}{2} + 41 = 89.5 \text{ in}$$

And

$$b_{\text{eff}}^{\text{Box}} = b_{\text{eff}}^{\text{int-Web}} + b_{\text{eff}}^{\text{ext-Web}} = 97" + 89.5 = 186.5 \text{ in}$$

Therefore, it is concluded that the effective width for each girder is one-half of the total width of the concrete deck.

### 8.1.2 Section Compactness

Based on AASHTO *LRFD Bridge Design Specifications*, the following criteria should be met so that the girder section can be considered a compact section.

1. Web and flanges yield stress:

$$F_{yf} = F_{yw} = 50 \text{ ksi} < 70 \text{ ksi}$$

2. For webs without longitudinal stiffener (AASHTO LRFD 6.11.2.1.2):

$$\frac{D}{t_w} = \frac{77}{\frac{11}{16}} = 112 < 150$$

3. Top flange width limit (AASHTO LRFD 6.11.1.1):

$$b_f = 12 \text{ in.} < \frac{\text{Span Length}}{5} = \frac{143 \text{ ft}}{5} = 343.2 \text{ in}$$

4. Limit for depth of web in compression at plastic moment:

$$\frac{2D_{cp}}{t_w} \leq 3.76 \sqrt{\frac{E}{F_y}}$$

### 8.1.3 Nominal Moment Capacity

The nominal moment capacity of the composite section is obtained as follows:

$$M_n = M_p \left( 1.07 - 0.7 \frac{D}{D_t} \right) \leq 1.3M_y \quad \text{EQ 8.1}$$

Where:

$M_p$  = Plastic moment capacity

$M_y$  = Yield moment

$D$  = Distance from top fiber of the composite section to the plastic moment neutral axis

$D_t$  = Total depth of the composite section

#### 8.1.3.1 Plastic Moment

To calculate the plastic moment capacity, first the location of the neutral axis when the section bears the plastic moment should be determined. Based on the cross-section shown in Figure 8-1 and the details shown in Figure 8-2, the forces of each element of the section under plastic moment are calculated as follows:

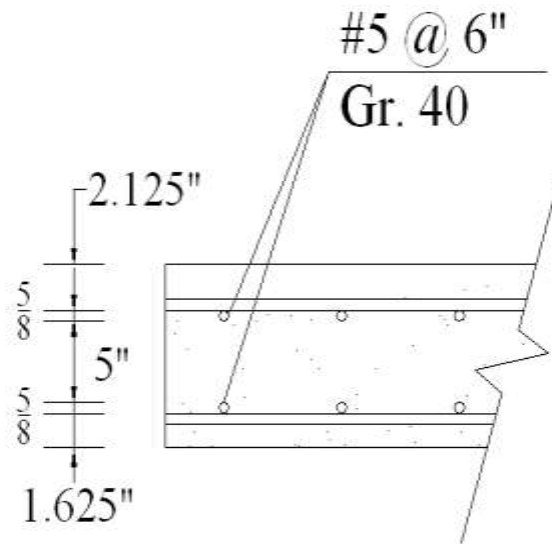


**Figure 8-2 Rebar layout in concrete slab.**

$$f'_c = 4.5 \text{ ksi}$$

$$F_y = 60 \text{ ksi}$$

$$A_{\text{rebar}} = \frac{186}{6} \times \frac{\pi}{4} \times \left(\frac{4}{8}\right)^2 = 6.09 \text{ in}^2$$

$$P_{rt} = 60 \times 6.09 = 365.4 \text{ kips (Top layer of rebar)}$$

$$P_c = 0.85 \times 4.5 \times 186.5 \times 8 = 5,707 \text{ kips (Concrete)}$$

$$P_{rb} = 60 \times 6.09 = 365.4 \text{ kips (Bottom layer of rebar)}$$

$$P_b = 2 \times 12 \times 1 \times 50 \text{ ksi} = 1,200 \text{ kips (Bottom flange of girder)}$$

$$P_w = 2 \times \frac{78 \times 11}{16} \times 50 \text{ ksi} = 5,363 \text{ kips (Webs of girder)}$$

$$P_t = \frac{61 \times 5}{8} \times 50 \text{ ksi} = 1,906 \text{ kips (Top flanges of girder)}$$

And

$$P_t + P_w + P_s = 8,469 \text{ kips} > P_{rb} + P_c + P_{rt} = 6,438 \text{ kips}$$

Therefore, the neutral axis under plastic moment is located in the top flange of the steel girder and its distance to the top fiber of the steel girder is calculated using the following equation

$$\bar{Y} = \frac{t_c}{2} \times \left( \frac{P_t + P_w - P_c - P_{rt} - P_{rb}}{P_s} + 1 \right) = 0.846 \text{ in}$$

It can also be concluded that total web depth would be in tension at plastic moment and so the depth of web in compression would be equal to zero:

$$D_{cp} = 0$$

$$\frac{2D_{cp}}{t_w} = 0 < 3.76 \sqrt{\frac{E}{F_y}}$$

So the section under consideration is compact and the nominal moment capacity is calculated using the EQ 8.1 and the plastic moment is calculated as follows:

$$M_p = \frac{P_c}{2t_c} \times [\bar{Y}^2 + (t_c - \bar{Y})^2] + \sum P_i d_i \quad \text{EQ 8.2}$$

The value of the plastic moment from the previous equation will be equal to:

$$M_p = 381,524 \text{ kips} \cdot \text{in}$$

### 8.1.3.2 Yield Moment

To calculate the yield moment,  $M_y$ , the composite section, shown in Figure 8-1 is analyzed to find the location of the neutral axis for the elastic flexural member, and therefore to find the yielding moment. For the elastic analysis, the concrete material is transformed to its steel equivalent. The modular ratio is found as follows:

$$n = \frac{E_s}{E_c} = \frac{29,000}{1822\sqrt{4.5}} = 7.5$$

And so the equivalent width of the concrete slab and also the rebars for each girder will be:

$$b_{\text{eff,conc}} = \frac{186.5}{7.5} = 24.87 \text{ in}$$

$$b_{\text{eff,rebar}} = \frac{186.5}{6} \times \left( \frac{\pi}{4} \times 0.5^2 \right) \times \frac{6.5}{7.5} = 10.66 \text{ in}$$

The result of this elastic analysis indicates that the neutral axis and moment of inertia of the section will be equal to:

$$\bar{Y}_{\text{top}} = 24.62 \text{ in}$$

$$I_x = 340,968 \text{ in}^4$$

The steel material yield stress is equal to 50 ksi and the maximum stress capacity of concrete material is 4.5 ksi. Setting the values of stresses in the top fiber of the concrete equal to the maximum stress and in the top and bottom flanges of steel box-girder equal to yield stress gives three values for the moment which the minimum of those three moments is the yielding moment of the section. This analysis results in a yielding moment equal to 280,217 k-in.

$$M_y = 279,421 \text{ kips} - \text{in}$$

Based on the calculated plastic and yield moment capacities for the composite section, the nominal flexural capacity will be equal to

$$\begin{aligned} M_n &= 381,524 \left( 1.07 - 0.7 \frac{8.846''}{85.46''} \right) = 380,587 \text{ kips} - \text{in} > 1.3M_y \\ &= 1.3 \times 280,217 = 364,282 \text{ kips} - \text{in} \end{aligned}$$

Hence,

$$M_n = 364,282 \text{ kips} - \text{in}$$

## 8.2 Linear Elastic Analysis of the Bridge

In this redundancy analysis study, two different cases for the Ft. Lauderdale bridge are considered. In one case, just the first span of the bridge is studied and in the other case, the continuous three-span bridge is investigated. For this purpose, in addition to the moment capacity of the composite girder obtained in the previous section, the maximum moment in the girders due to dead load and HS-20 truck load using a linear elastic analysis is needed.

First, the single span bridge is modeled and analyzed using SAP2000 structural analysis software. For live load analysis, two HS-20 trucks are placed so that the moments in one of the girders are maximized. In order to generate the maximum moment in one girder, both trucks should be placed as close to that girder as possible. The most severe loading condition to create the maximum moment in one of the girders is shown in Figure 8-3.

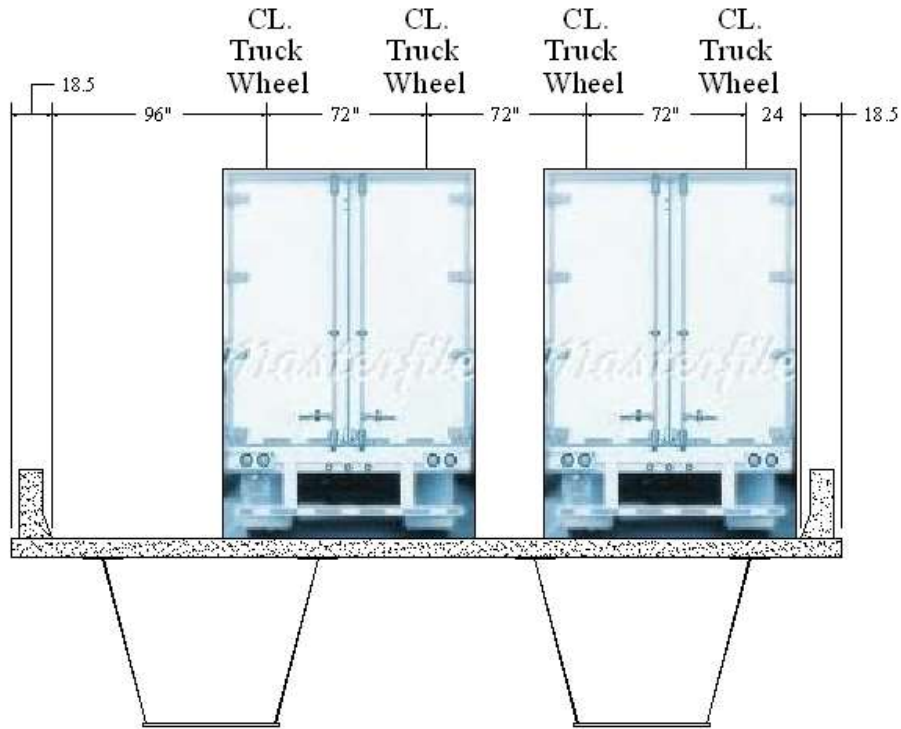


**Figure 8-3 Worst case scenario for HS-20 loading of the bridge.**

The results of a linear elastic analysis in SAP2000 show that the maximum flexural moment in the girders of the single-span bridge is equal to 34,637 kips-in. To verify the results of SAP2000 analysis, the maximum bending moment in the composite girders of the bridge is approximated by hand calculations. For this purpose, two trucks with unit weight are applied to a 2D model of the bridge cross-section to find the transverse distribution of loads between the girders. Figure 8-4 shows the point loads representing the truck wheels applied to the bridge deck.

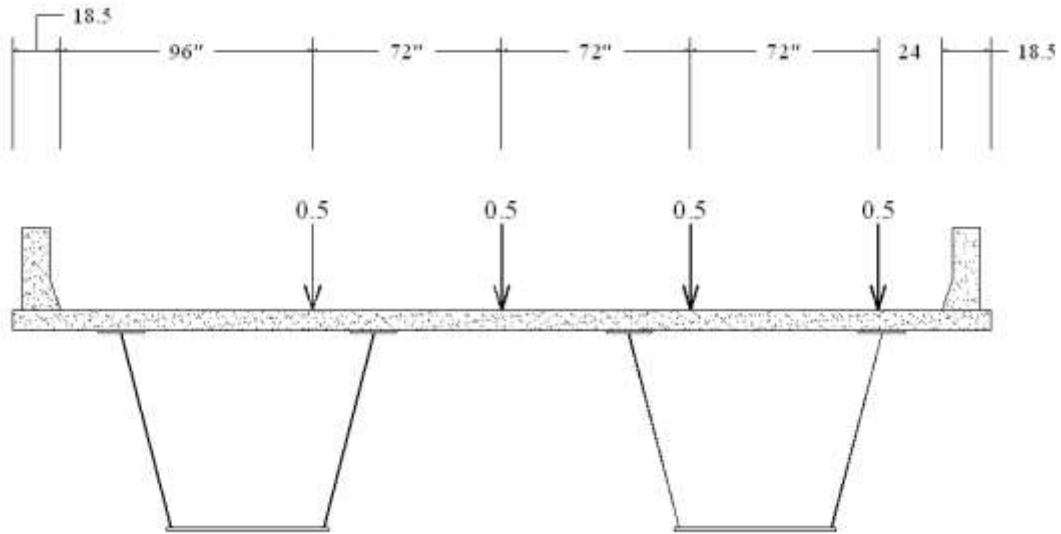


**Figure 8-4 Worst case scenario of loading for two trucks with unit weight.**

Assuming the webs of the girders act like a pin support for the concrete deck, the reactions of the supports are found through 2D analysis of the continuous deck. Figure 8-5 shows the reaction forces that are developed in the girder webs.

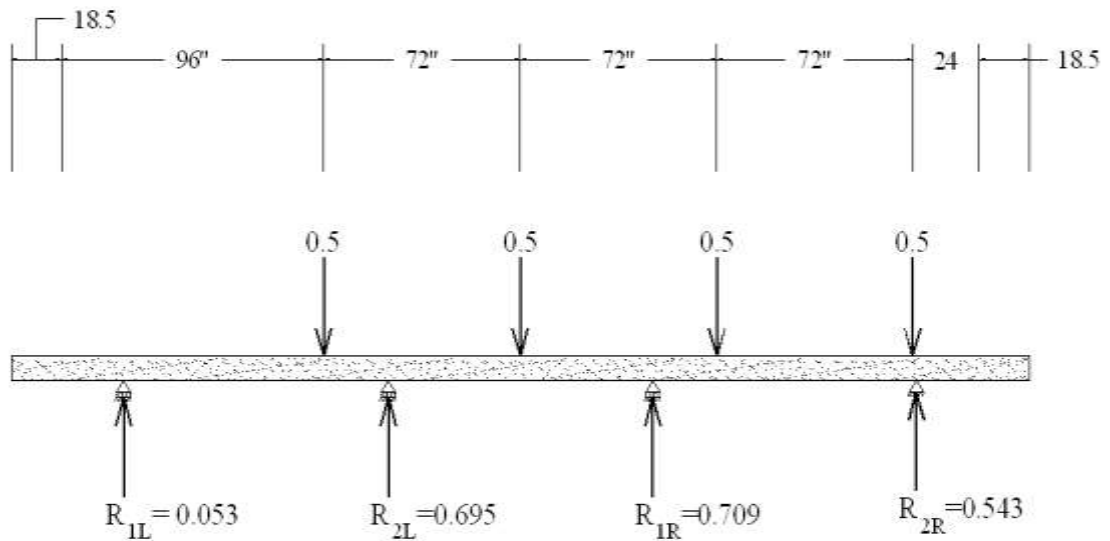


**Figure 8-5 Web reactions due to application of two trucks with unit weight.**

Therefore, the maximum reaction force which is developed in the right girder will be equal to:



$$R_R = R_{1R} + R_{2R} = 1.252$$

And it can be concluded that due to positioning of two HS-20 trucks on the bridge in the most severe location, 1.252 times of the weight of one of the trucks is carried by one of the girders. At this point, the girder should be analyzed in the longitudinal direction, so that the maximum moment in the girder is obtained. If the distance of the front axle of the truck and the support is set equal to the unknown parameter,  $x$ , maximizing the girder moment, which would be a function of  $x$ , shows that the value of  $x$  equal to 55 ft results in the maximum moment in the girder. The position of the truck, which creates the maximum moment is illustrated in Figure 8-6. This maximum moment is equal to 27,564 kips-in. due to one HS-20 truck. Based on the transverse analysis results that showed one of the girders may carry up to 1.252 times the truck weight, it is concluded that the maximum moment in the composite girders due to weight of two HS-20 trucks will be equal to 34,510 kips-in. This maximum moment is in agreement with the maximum moment obtained from SAP2000 linear elastic analysis which was equal to 34,637 kips-in. Therefore, the maximum moment in the girders due to application of two HS-20 trucks is chosen to be equal to 34,637 kips-in.

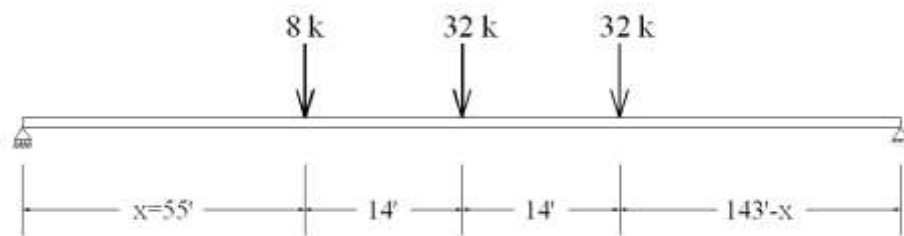


**Figure 8-6 Position of the HS-20 truck for maximum moment in girders.**

The other parameter needed for the redundancy analysis of the bridge is the moment due to dead weight of the bridge in single span and continuous bridge and also live load

moment in the continuous structure. The results of SAP2000 analysis show that the dead load moments are equal to 83,676 and 49,780 kips-in. in single span and continuous bridges, respectively. The moment due to HS-20 loading in the continuous bridge is equal to 27,765 kips-in. With the moments produced by dead and live loads and the nominal moment capacity of the bridge, the only remaining part of the analysis is the nonlinear finite element analysis of the bridge in different limit states.

### **8.3 Nonlinear Finite Element Analysis**

For redundancy analysis of the bridge, the live load capacity of the structure in three different limit states is required: the ultimate capacity of the undamaged bridge, the capacity of the damaged structure, and the capacity of the bridge corresponding to a live load deflection equal to the span length/100. To find these load carrying capacities, the single span and continuous bridges are modeled. Figure 8-7 and Figure 8-8 show the state of the von Mises stresses in the single-span bridge under maximum bending moment in undamaged and full-web cracked conditions, respectively. Figure 8-9 shows the load-deflection curves of the single-span and three-span bridges under different conditions.

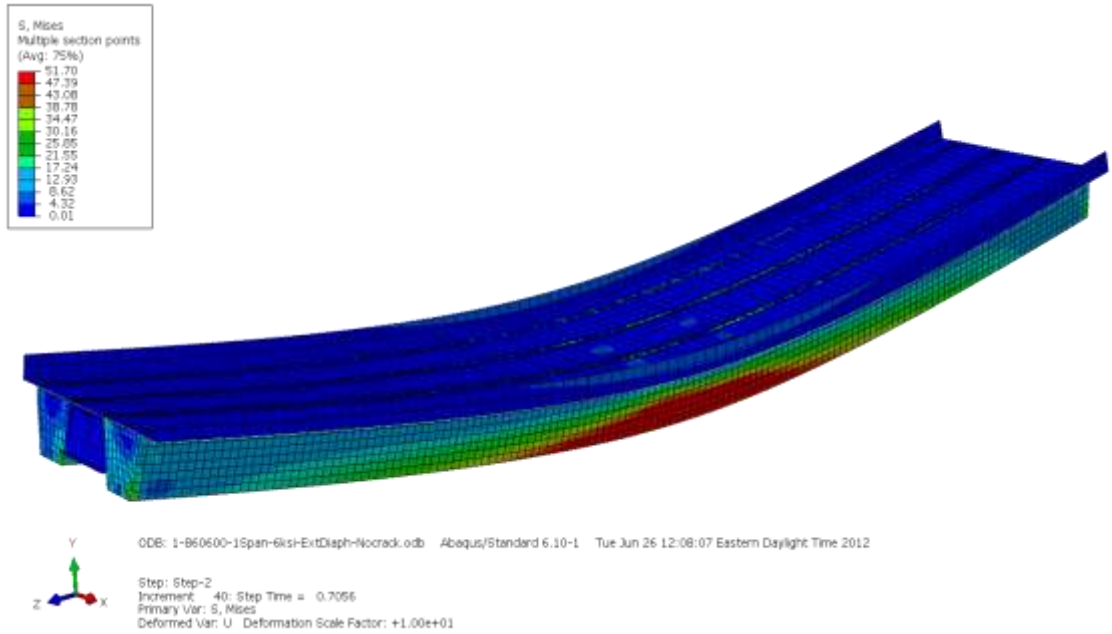


**Figure 8-7 Von Mises stresses in single-span bridge under maximum moment, undamaged condition.**

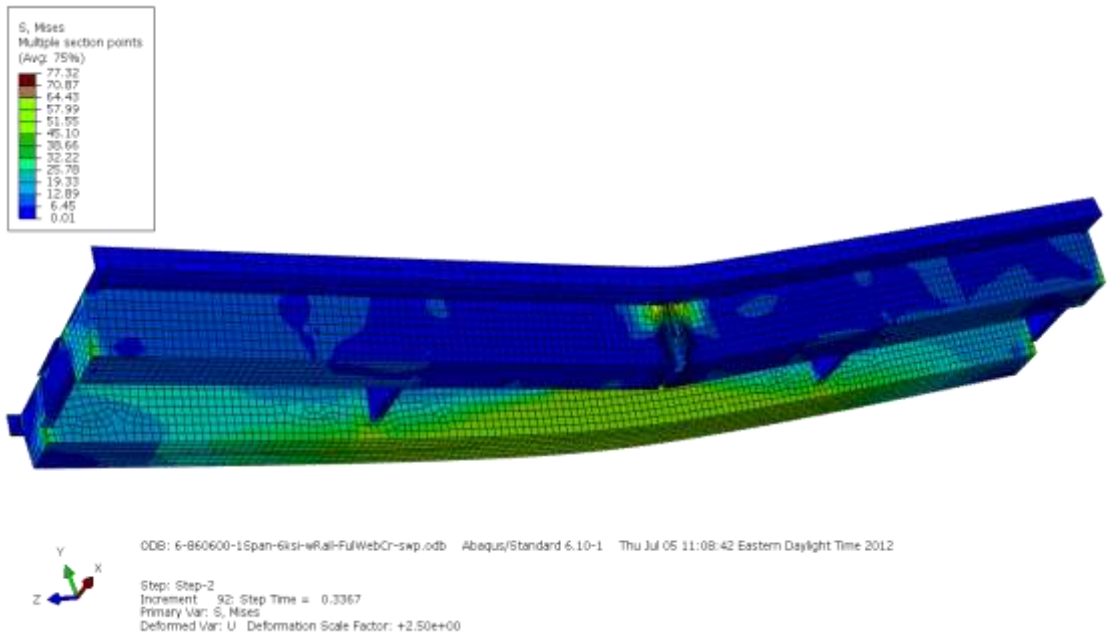


**Figure 8-8 Von Mises stresses in single-span bridge under maximum moment, full-web cracked condition.**

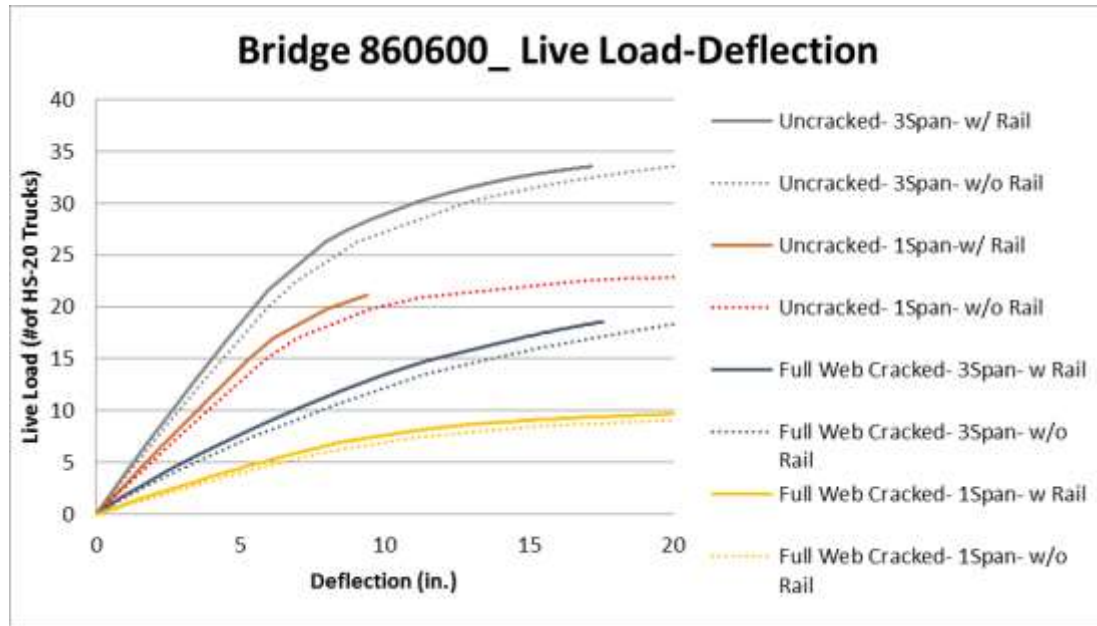


**Figure 8-9 Load vs. vertical deflection of single- and three-span bridges with different conditions.**

The live load capacities from nonlinear finite element analysis of the undamaged and cracked bridges in different limit states are tabulated in Table 8-1. As seen in Figure 8-9, the Ft. Lauderdale bridge is predicted to fail in flexural mode in all the cases under the HS-20 loading configuration. However, it is important to note that the finite element model that was used to analyze the Ft. Lauderdale bridge was only calibrated in the linear range, plus the crushing capabilities of concrete wasn't activated.

**Table 8-1 Live Load Capacity of the Bridge as a Multiplier of HS-20 Trucks**

|                          | Undamaged | Full-Web Cracked | Corresponding to $d=L/100$ |
|--------------------------|-----------|------------------|----------------------------|
| Single Span Bridge       | 22.68     | 9.90             | 9.55                       |
| Continuous 3-Span Bridge | 33.54     | 18.60            | 18.39                      |

The other factor that is studied in the finite element analyses is the effect of the railing. Both single- and three-span bridges in undamaged and damaged conditions are analyzed under live loads with and without railing. The results show that the existence of

a concrete railing, integrally connected to the superstructure deck, will not change the capacity of the structure drastically. From the load deflection curves, it is observed that the ductility of the bridge is reduced due to existence of such railings. However, it should not be a major concern because after brittle failure of the railing at mid-span under compression, the bridge behavior tends to be similar to a bridge without railing.

## 8.4 Redundancy Analysis

Using the results of the linear elastic analysis for dead and live loads, the nonlinear finite element analysis of live load and the calculated flexural capacity of the bridge composite girders, the system redundancy factors of the bridge are obtained using the direct analysis approach. For that purpose, first the load factors recommended by NCHRP Report 406 are evaluated as follows.

### 8.4.1 Member Failure ( $LF_1$ )

Member failure limit state is a check of individual member safety using elastic analysis or the capacity of the structure to resist its first member failure.

$$LF_1 = \frac{R - D}{L} \leftarrow \text{Linear Elastic Analysis} \quad \text{EQ 8.3}$$

Where:

$R$  = Resistance

$D$  = Dead load effects

$L$  = Live load effects

If moment values are implemented in EQ 8.3, it will convert to:

$$LF_1 = \frac{M_n - M_{DL}}{M_{LL,2HS-20}} \leftarrow \text{Linear Elastic Analysis}$$

Where:

$M_n$  = Nominal moment capacity based on AASHTO LRFD

$M_{DL}$  = Dead load moment

$M_{LL,2HS-20}$  = Live load moments due to two HS-20 trucks

For single span bridge, the  $LF_1$  will be equal to:

$$LF_{1,single-span} = \frac{364,282 - 83,676}{34,637} = 8.10$$

And for the continuous three-span bridge the load factor will be equal to:

$$LF_{1,three-span} = \frac{364,282 - 49,780}{27,780} = 11.32$$

#### 8.4.2 Ultimate Limit State ( $LF_u$ )

Ultimate limit state factor is defined as the ultimate capacity of the undamaged bridge system or the load required for the formation of a collapse mechanism in the bridge system divided by the weight of two HS-20 trucks. In mathematical format, this definition yields in:

$$LF_u = \frac{\text{Ultimate Load Capacity of Undamaged Bridge from Nonlinear FEA}}{2 \times 72 \text{ kips}} \quad \text{EQ 8.4}$$

Where:

$72 \text{ kips}$  = Weight of one HS-20 Trucks

Based on the results of the conducted finite element analysis, the capacities of the undamaged single-span and three-span bridges are equal to 22.68 and 33.54 time HS-20, respectively. Therefore, the ultimate limit state load factors for single span bridge will be equal to:

$$LF_{u,single-span} = \frac{22.68 \times 72 \text{ kips}}{2 \times 72 \text{ kips}} = 11.34$$

And this load factor for the three-span bridge will be:

$$LF_{u,three-span} = \frac{33.54 \times 72 \text{ kips}}{2 \times 72 \text{ kips}} = 16.77$$

The redundancy reserve ratio for the undamaged condition is defined as the ratio of the ultimate limit state load factor and the member failure factor. This factor for the single span bridge will be as follows:

$$R_{u,single-span} = \frac{LF_u}{LF_1} = \frac{11.34}{8.10} = 1.40 > 1.30$$

So, the capacity of the single span bridge in its ultimate limit state is satisfactory. For the three span bridge, the redundancy reserve ratio will be evaluated as follows:

$$R_{u,three-span} = \frac{LF_u}{LF_1} = \frac{16.77}{11.32} = 1.48 > 1.30$$

Therefore, the three-span bridge is also passing the redundancy criterion in the undamaged condition.

### 8.4.3 Damage Condition Limit State (LF<sub>d</sub>)

Damage condition limit state is defined as the ultimate capacity of the bridge system after removal or cracking of one load carrying component from the structure model.

$$LF_d = \frac{\textit{Ultimate Load Capacity of Damaged Bridge}}{2 \times 72 \text{ kips}} \quad \text{EQ 8.5}$$

The limiting value for the redundancy reserve ratio in this limit state is defined as follows:

$$R_d = \frac{LF_d}{LF_1} \geq 0.50$$

This factor and the relevant criterion for single- and three-span bridges are evaluated as follows:

$$LF_{d,single-span} = \frac{9.9 \times 72 \text{ kips}}{2 \times 72 \text{ kips}} = 4.95$$

$$R_{d,single-span} = \frac{LF_d}{LF_1} = \frac{4.95}{8.10} = 0.61 > 0.50$$

$$LF_{d,three-span} = \frac{18.60 \times 72 \text{ kips}}{2 \times 72 \text{ kips}} = 9.30$$

$$R_{d,three-span} = \frac{LF_d}{LF_1} = \frac{9.30}{11.32} = 0.82 > 0.50$$

It is observed that both single- and three-span bridges meet the redundancy criterion in their damaged conditions.

#### 8.4.4 Functionality Limit State (LF<sub>f</sub>)

Functionality limit state is defined as the capacity of the structure to resist a live load displacement in a main longitudinal member equal to the span length/100. The functionality limit state load factor is obtained from dividing this capacity by the weight of two HS-20 trucks.

$$LF_f = \frac{\text{Load Capacity corresponding to } \frac{L}{100} \text{ deflection}}{2 \times 72 \text{ kips}} \quad \text{EQ 8.6}$$

And the reserve ratio criterion for this limit state is:

$$R_f = \frac{LF_f}{LF_1} \geq 1.10$$

This factor and the relevant criterion for single- and three-span bridges are evaluated as follows:

$$LF_{f,single-span} = \frac{9.55 \times 72 \text{ kips}}{2 \times 72 \text{ kips}} = 4.78$$

$$R_{f,single-span} = \frac{LF_f}{LF_1} = \frac{4.78}{8.10} = 0.59 < 1.10$$



$$LF_{f,three-span} = \frac{18.39 \times 72 \text{ kips}}{2 \times 72 \text{ kips}} = 9.20$$

$$R_{f,three-span} = \frac{LF_f}{LF_1} = \frac{9.20}{11.32} = 0.81 < 1.10$$

It is observed that neither single-span bridge nor three-span one meets the functionality redundancy criterion in their damaged condition.

## 8.5 Summary

The redundancy analysis results for the Ft Lauderdale twin steel box-girder bridge is summarized in Table 8-2. The results indicate that both the single-span and three-span bridge satisfy the redundancy criteria for the ultimate limit state and damaged limit state, but not for the functionality limit state. This suggests that the bridge has enough ultimate capacity to be classified as redundant; however, the intensive deformation that the bridge will experience makes the bridge unsafe to use even at loads lower than the ultimate capacity. The continuity was observed to improve the redundancy of the bridge significantly.

**Table 8-2 Summary of Redundancy Analysis Results on the Ft. Lauderdale Bridge**

| Models      | $R_u = \frac{LF_u}{LF_1} (1.30)$ | $R_d = \frac{LF_d}{LF_1} (0.5)$ | $R_f = \frac{LF_f}{LF_1} (1.10)$ |
|-------------|----------------------------------|---------------------------------|----------------------------------|
| Simple Span | 1.40 (OK)                        | 0.61 (OK)                       | 0.59 (NG)                        |
| 3-Span      | 1.48 (OK)                        | 0.82 (OK)                       | 0.81 (NG)                        |

## **Chapter 9    Simplified Methods of Predicting Remaining Capacity of Damaged Twin Steel Box-Girder Bridges under Concentrated Loads**

As mentioned earlier in Chapter 2, FHWA and AASHTO *LRFD Bridge Design Specifications* require the redundancy of twin steel box-girder bridges to be assessed by means of refined finite element analysis. However, performing finite elements analysis for every single twin steel box-girder bridge in the inventory can be costly and time-consuming. One of the goals of this research was to develop simplified methods that could provide a reasonable estimation of the remaining capacity of a damaged twin steel box-girder bridges under concentrated loads. The simplified methods could serve as a first-level check in the redundancy evaluation assessment procedure that this research is aiming to develop eventually.

Observations from the performed experiments from Tests A to E, except Test B, showed that twin steel box girder bridges subjected to concentrated loads would fail in either one-way or two-way shear failure mode, or a combination of both. Under four-point loading configuration, a damaged twin steel box-girder bridge tends to fail in one-way shear failure mode while under single concentrated load it tends to fail in two-way (punching) shear failure mode.

Comparison of the ultimate capacities obtained from the experiment indicated that the punching shear failure would be the controlling mode of failure. In this chapter, both one-way and punching shear practice codes will be reviewed and used to predict the test results. Where the codes are not applicable, different methods will be proposed and discussed.

## 9.1 One-Way Shear Provision for Bridge Slabs

In general, shear in reinforced concrete slabs that failed in one-way shear manner can be checked by two approaches. The first approach is to calculate the beam shear capacity over a certain effective width of the support. The second approach is to calculate the punching shear capacity of the slabs over the critical perimeter around the load.

For the first approach, two beam shear provisions including BS 8110 and ACI 318-08, will be utilized in this study to predict the shear resistance of a damaged twin steel box-girder bridge that predominantly in one-way shear failure mode as in Test E. It should be noted that these shear resistance expressions are derived based on results from beam tests. For beams, the effective width is considered as the entire width of the beam. For the slabs, however, the shear resistance should not be calculated over its entire width, but over a certain effective width  $b_{eff}$ . Determination of the effective width  $b_{eff}$  of one-way slab under a concentrated load can be either a fixed width or a horizontal load spreading methods depending local practice. Few common load spreading methods to determine the effective width of slabs under single concentrated load are illustrated Figure 9-1 including (a) Dutch practice and (b) French practice.

$$V_{ACI\ 318-08} = 2\sqrt{f'_c}b_{eff}d \text{ (US units: psi and in)}$$

ACI 318-08

$$V_{ACI\ 318-08} = 0.167\sqrt{f'_c}b_{eff}d \text{ (SI units: MPa and mm)}$$

BS 8110

$$P_{BS\ 8110} = 7.45^3\sqrt{100\rho f_{cu}}\sqrt{\frac{15.75}{d}}b_{eff}d \text{ (US units: psi and in)}$$

$$P_{BS\ 8110} = 0.27^3\sqrt{100\rho f_{cu}}\sqrt{\frac{400}{d}}b_{eff}d \text{ (SI units: MPa and mm)}$$

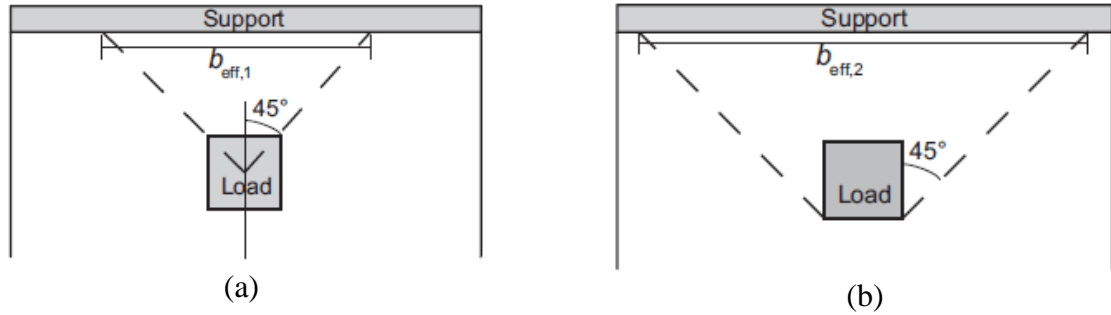


**Figure 9-1** Determination of effective width (a) assuming 45° horizontal spreading from the center of the load in Dutch practice, (b) assuming 45° horizontal spreading from the far corner of the load in French practice (Adopted from Lantsoght, 2015).

When the slabs are subjected to multiple concentrated loads the effective width can be considered for each wheel load separately or by each axle as shown in Figure 9-2. If the effective width of each wheel load overlaps, it is conservative to use the effective width of the entire axle.

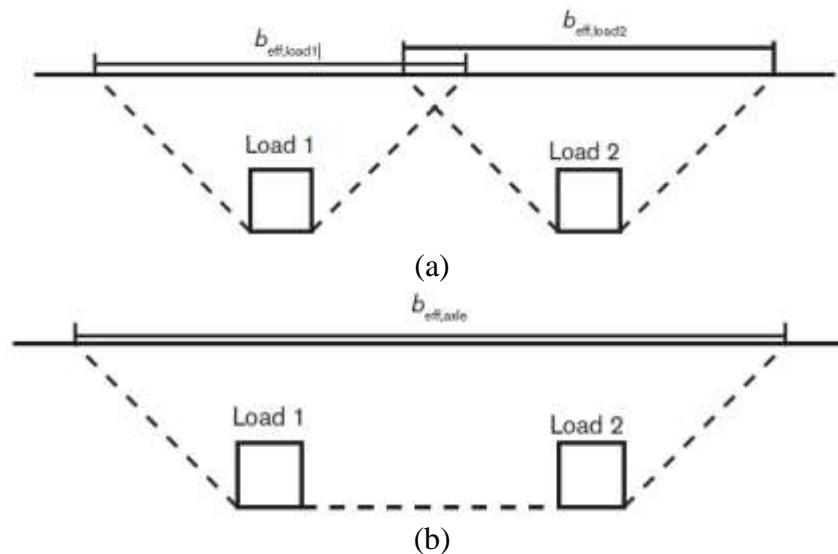


**Figure 9-2** The method to determine effective width (a) per load print and (b) per axle.

## 9.2 Two-Way (Punching) Shear Provision for Bridge Slabs

Punching shear provisions from ACI 318-08 and BS 8110 will also be used to predict the test results in which the specimen failed in punching shear. The formulas for punching shear resistance of slabs for each provisions are given:

$$P_{ACI} = 4\sqrt{f'_c}b_o d \text{ (US units: psi and in)}$$

ACI 318-08

$$P_{ACI} = 0.33\sqrt{f'_c}b_o d \text{ (SI units: MPa and mm)}$$

$$P_{BS8110} = 7.45\sqrt[3]{100\rho f_{cu}}\sqrt{\frac{15.75}{d}}b_o d \text{ (US units: psi and in)}$$

BS 8110

$$P_{BS8110} = 0.27\sqrt[3]{100\rho f_{cu}}\sqrt{\frac{400}{d}}b_o d \text{ (SI units: MPa and mm)}$$

These equations are developed for two-way slabs and derived from test results on slab-column connections. In ACI 318-08 provision, the punching shear stress is determined to be twice greater than the one-way beam shear stress. The punching shear resistance of the slabs, according to ACI 318-08, is calculated over a critical perimeter located at a distance  $d/2$  away from the loading area. In BS 8110, the design punching shear stress is assumed to be the same as one-way shear stress. However, the punching shear resistance of the slabs is calculated over a larger critical perimeter which is located at a distance  $1.5d$  from the loading area.

However, it is important to note that the punching shear resistance of the bridge slabs are also dependent on the supporting condition and loading configuration. For instance, the ultimate punching shear capacity of the bridge specimen in ultimate Test C, where the load was applied over the intact girder, was significantly greater than the one obtained in ultimate Test D, where the load was applied over the damaged girder. Unlike this observation in the test results, both ACI 318-08 and BS 8110 punching shear provisions

resulted in similar predictions for both tests as shown in Figure 9-3. This significant difference between these two tests, even though they had a similar loading configuration, is attributed to the effects of compressive membrane action and direct load transfer which are currently not considered in these codes. For these reasons, both compressive membrane action and direct load transfer effects on the shear resistance of bridge slabs will be reviewed as subsequent sections. Finally, a simplified method will be proposed to take both effects into consideration when predicting the punching shear resistance of a damaged twin steel box-girder bridges.

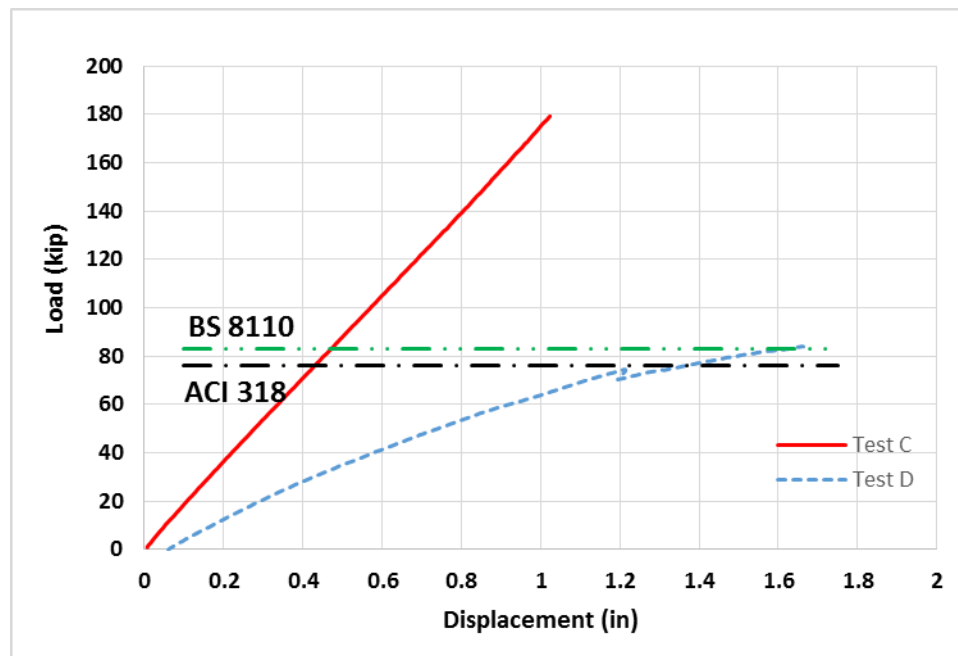


Figure 9-3 Comparison between results from Tests C and D and predictions from design provisions.

### 9.3 Literature Review on Compressive Membrane Action

Compressive membrane action (CMA) in reinforced concrete slabs occurs as a result of the great difference between the tensile and compressive strength of concrete. Once the concrete cracks, the neutral axis will migrate upward and concrete tends to move

outward at the edges. If this tendency of expanding outward of the slabs is restrained, CMA will develop as shown by thrust in Figure 9-4. As a result it will enhance the capacity of the slabs. The typical load versus deflection curve for a laterally restrained reinforced concrete slab is shown in Figure 9-5.

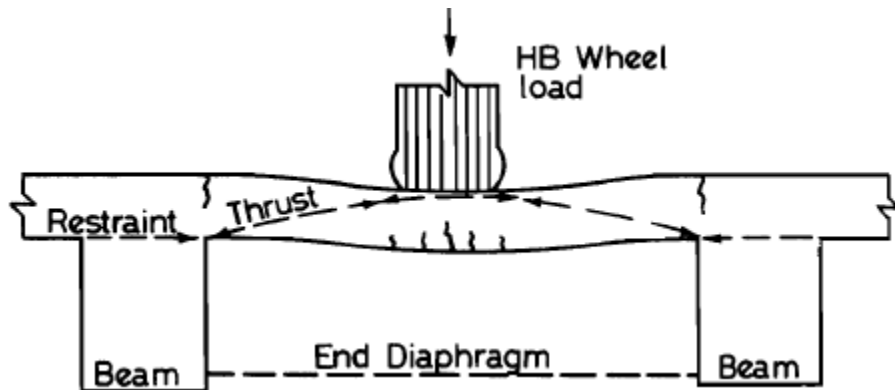


Figure 9-4 Compressive membrane action in laterally restrained reinforced concrete slabs (adopted from Kirkpatrick et al. 1984).

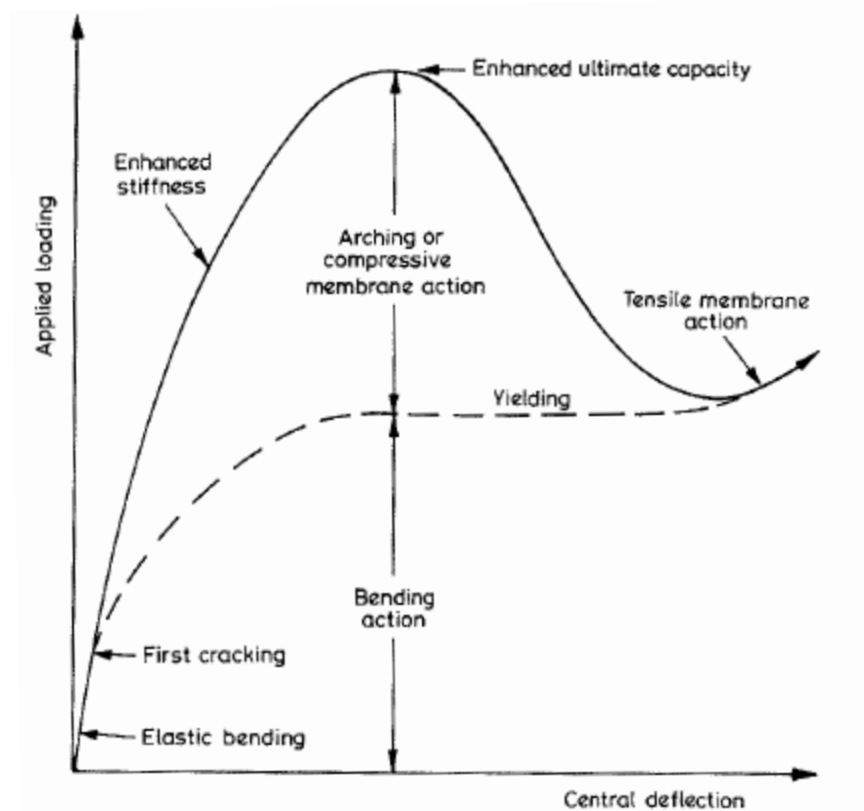


Figure 9-5 Typical load vs. deflection for restrained reinforced concrete slab (adopted from Rankin et al. 1991).

CMA effect was first recognized by Westergaard and Slater (1921) in reinforced concrete floors. However, this finding was not appreciated until when Ockleston (1955 and 1958) observed this CMA effect on uniformly loaded panel of full-scale reinforced concrete slabs and floor beams. In these tests, ultimate load-carrying capacities were found to be significantly greater (two to four times) than those predicted by Johansen's yield-line theory. After that extensive experimental and analytical studies on CMA effect in uniformly loaded reinforced concrete slabs have been carried out such as Park (1964), Liebenberg (1966), Gamble (1969), Christiansen (1963), Brothie et al. (1971), Rankin et al. (1991) and others. Moreover, in order to investigate the effect of edge restraint on ultimate capacity of the slabs, several experimental and analytical studies on both rigidly



and elastically restrained reinforced concrete slabs under concentrated loads also have been carried out including Taylor and Hayes (1965), Aoki and Seki (1971), Tong and Bachelor (1971), Kuang and Morley (1992), Kuang and Morley (1993), Azad et al. (1994), Mufti and Newhook (1998), Kirkpatrick et al. (1984), Rankin and Long (1997), Taylor et al. (2001), Salim and Sebastian (2003), Hon et al. (2005), Zheng et al. (2010) and others. These studies have not only shown that the ultimate load-carrying capacity of bridge slabs under both uniform loading and concentrated loading increased significantly due to the CMA effect but also indicated that effect of CMA is dependent on the degree of lateral restraint of the slabs. Several of them have proposed different approaches to predict the enhanced punching strength of laterally restrained reinforced concrete slabs with reasonable accuracy. However, the elastic-plastic method developed by researchers at the Queen's University at Belfast is best suited for this study because it allows for the different degree of lateral restraint in bridge slabs to be taken into account and is simple to use and has been validated with a wide range of test results. A review of major research carried out by Queen's University related to effects of CMA on the shear strength of laterally restrained bridge deck slabs are summarized below:

**Kirkpatrick, Rankin and Long (1984)**

Kirkpatrick, Rankin and Long (1984) proposed a semi-empirical formula for predicting the ultimate capacity of M-beam bridge decks assuming the bridge decks were rigidly-restrained laterally. The maximum arching moment of resistance  $M_{ar}$  was expressed in term of concrete compressive strength, depth of slab and arching moment resistance  $M_r$  by the following equation.

$$M_{ar} = 0.85f'_c \left(\frac{h}{2}\right)^2 \times \frac{M_r}{4} = kf'_c h^2 \quad \text{where } k = \frac{0.21M_r}{4}$$

The arching moment ratio  $M_r$  was first derived by McDowell et al. (1956) based on the geometry of deformation of a rigidly restrained unreinforced masonry wall constrained between rigid supports. The idealized geometry of deformation for rigidly restrained unreinforced strip and idealized stress-strain relationship for concrete is shown in Figure 9-6. Figure 9-7 illustrates the arching moment ratio curves in term of two non-dimensional parameters,  $R$  and  $u$ . These two parameters are used to express the stress distribution at the contact areas under different span-to-depth ratio and material plastic strains and defined below:

$$R = \frac{\epsilon_c L_r}{4d_1^2} \quad \text{and} \quad u = \frac{w}{2d_1^2}$$

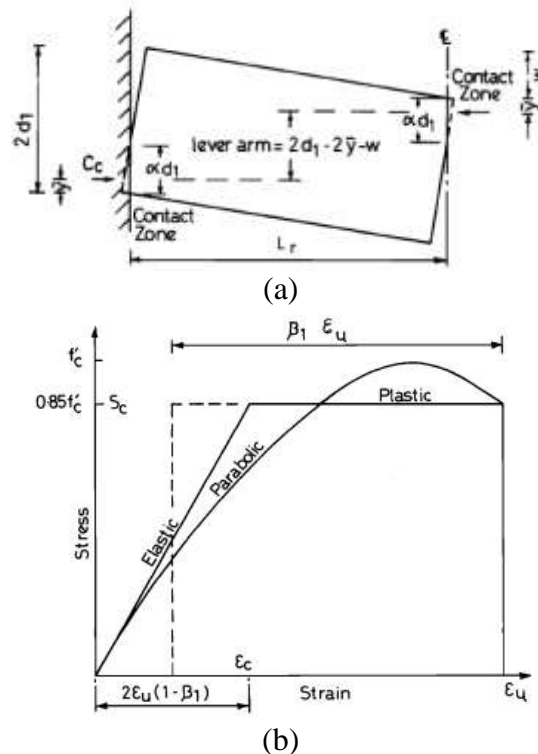


Figure 9-6 (a) Idealized geometry of deformation of half span of laterally rigidly-restrained strip and (b) idealized stress-strain relationship of concrete.

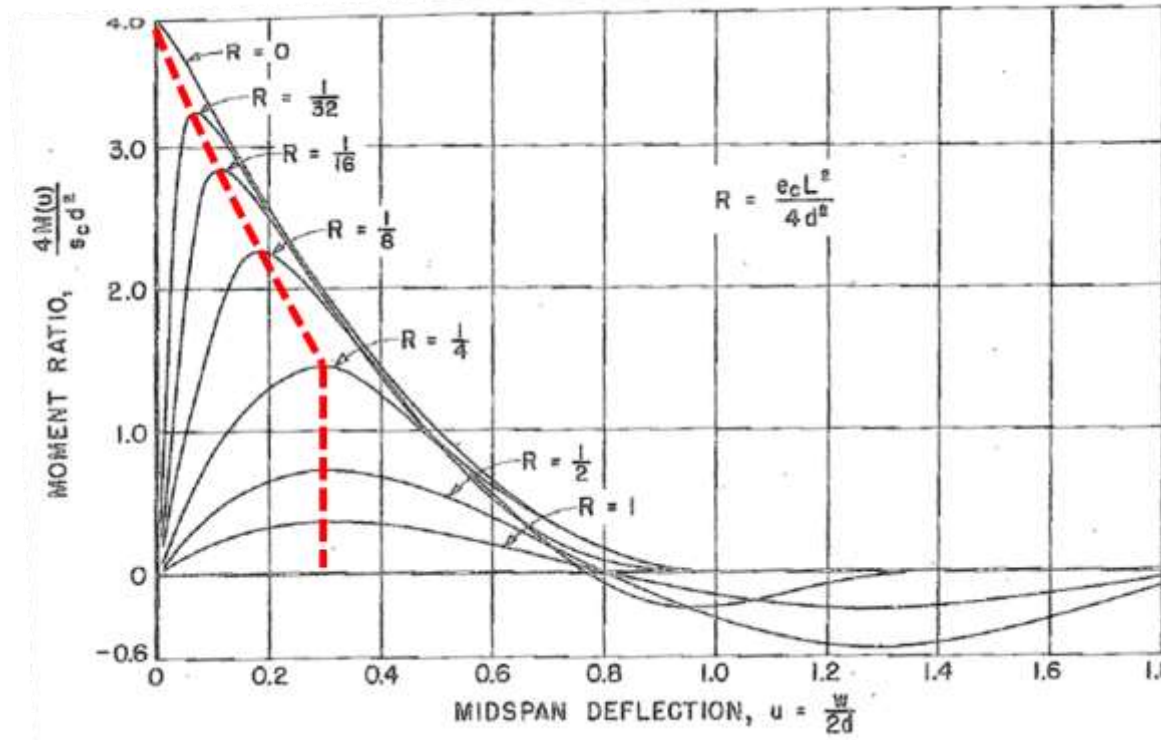


Figure 9-7 (a) Idealized geometry of deformation of half span of laterally rigidly-restrained strip and (b) variation of arching moment ratio with mid-span deflection.

This McDowell et al.'s expression for  $M_r$  was taken a step further so that the need for prediction of the critical deflection was eliminated (Rankin (1982) and Kirkpatrick (1984)). In order to do that, the  $M_r$  was first differentiated with respect to parameter  $u$  and then solved numerically for  $u$  at a range of  $R$  less than 0.26, which is usual for bridge slabs. The value of  $u$  is then substituted back into the original expression of  $M_r$ . The resulting equation provides the maximum value of the arching moment ratio for any value of  $R$  and is also graphically illustrated by the red dash curve superimposed on the original arching moment resistance ratio curves in Figure 9-6(b). The mathematical expression for the maximum arching moment ratio for any value  $R$  is given:

$$\text{For } R > 0.26 \quad M_r = \frac{0.3615}{R}$$

$$\text{For } 0 < R < 0.26 \quad M_r = 4.3 - 16.1\sqrt{(3.3 \times 10^{-4} + 0.1243R)}$$

Kirkpatrick et al. (1984) also proposed a design chart in Figure 9-8 in which the arching moment coefficient,  $k$ , was plotted in term of concrete compressive strength and the span to depth ratio.

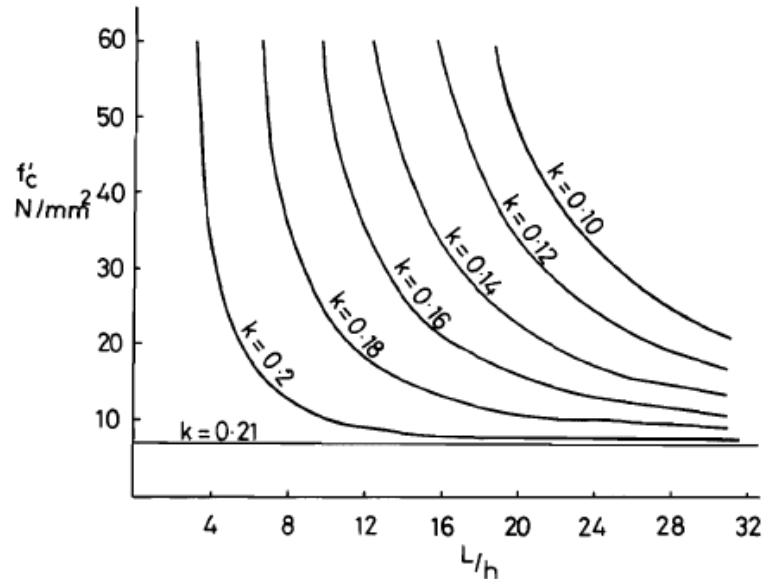


**Figure 9-8 Curves of arching moment coefficient ( $k$ ).**

Once the maximum arching moment is calculated, it is converted to an equivalent area of flexural reinforcement by using the following equation:

$$\rho_e = \frac{kf'_c h^2}{240d^2}$$

It should be noted that in the equation above, the yield strength of this equivalent steel reinforcement is taken as  $320 \text{ N/mm}^2$  based on a study of Long (1975), the lever arm of arching action is assumed to be 75% of the effective depth of the section, and the existing flexural reinforcement of the slabs is neglected.

This equivalent area of reinforcement is then substituted into the following punching shear equation (general form) which was developed by Long (1975).

$$P_p = \frac{0.47}{r_f} \sqrt{f'_c} \times (\text{critical perimeter})d \times (100\rho_e)^{0.25}$$

$$P_p = \frac{0.43}{r_f} \sqrt{f_{cu}} \times (\text{critical perimeter}) \times (100\rho_e)^{0.25}$$

Where  $r_f$ , a shape factor = 1.0 (circular load) or 1.15 (rectangular load). The critical perimeter is taken at 0.5d from the face of loaded area.

### **Rankin and Long (1997)**

Rankin and Long (1997) represented their approach for the strength of laterally restrained slab strips. The method separates the bending and arching components of punching shear strength of slabs. The maximum arching moment of resistance was somewhat similar to one proposed by Kirkpatrick et al. (1984). However, instead of assuming the depth of arching section ( $2d_1$ ) to be the full depth of the slab, the depth of arching section was calculated by Christiansen's (1963) equation by assuming the maximum arching moment develops after yielding of the reinforcement and the bending deformation necessary to cause yield can be neglected. It means some of the compression zone is required to balance the tensile force in the reinforcement; therefore, the depth of section available for arching action should be smaller than the full depth of the slab. The depth of section available for arching and the maximum arching moment resistance are given by:

$$d_1 = h - (\rho + \bar{\rho}) \frac{f_y d}{0.85 f'_c}$$

$$M_a = \frac{M_r \times 0.85 f'_c d_1^2}{4}$$

The ultimate bending moment resistance is calculated by the following equation which was given by Mattock et al (1961).

$$M_b = \rho f_y d^2 \left(1 - \frac{0.59 \rho f_y}{f'_c}\right)$$

In this study, Rankin and Long (1997) also proposed a three-hinged arch approach so that the CMA effect can be evaluated on elastically restrained (less than rigidly restrained) slab strips. This approach converts a shorter elastically restrained slab strip to a longer equivalent rigidly restrained slab strip as shown in Figure 9-9. The relationship between the span length of elastically-restrained slab strip and that of the equivalent rigidly-restrained one is given by the following equation:

$$L_r = L_e \times \left(\frac{E_c A}{K L_e} + 1\right)^{1/3}$$

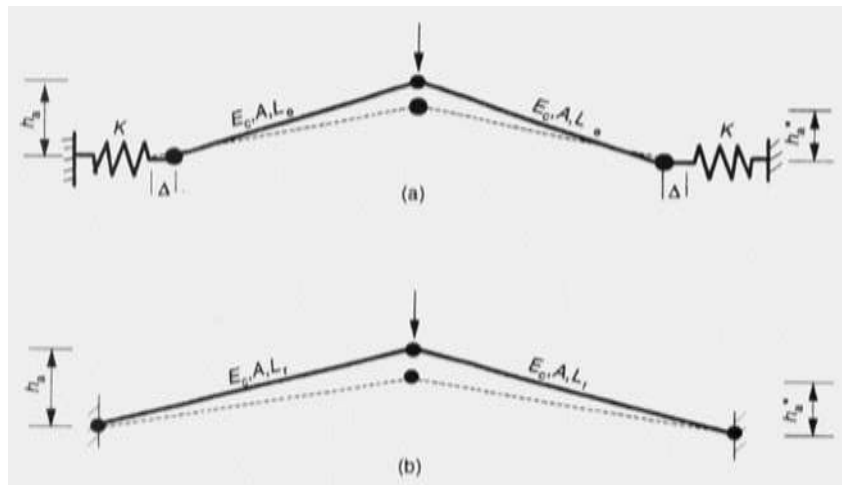


**Figure 9-9 Analogy of three-hinged arch.**

### **Taylor, Rankin and Cleland (2002)**

In 2002, Taylor, Rankin and Cleland put all the works done related to CMA effects on bridge slabs together for a “Guide to Compressive Membrane Action”. In this guide, the ultimate shear capacity of the slabs will be determined as the lesser value between the flexural shear capacity and punching shear capacity. The flexural shear capacity is

calculated using Rankin and Long (1997) method while the punching shear capacity is calculated using Kirkpatrick et al.'s (1984) method. In this guide, Taylor et al. (2002) made few modifications to the previous methods.

The first modification is a new stress-strain relationship that could be used for both normal and high strength concrete. This stress-strain relationship was first proposed by Taylor, Rankin, and Cleland (2001a). It is suggested that the ultimate compressive strain of concrete  $\varepsilon_u$  could be related to the cube compressive strength of concrete  $f_{cu}$  (or  $1.25 f'_c$ ) using the following equation:

$$\varepsilon_u = 0.0043 - ((f_{cu} - 60) \times 2.5 \times 10^{-6})$$

The depth of the stress block is also given by:

$$\beta = 1 - 0.003f_{cu}$$

Moreover, Taylor (200) also proposed a restraint model where the bridge slabs' lateral stiffness provided by supporting beams/girders, end diaphragms and unloaded portion of slab was estimated. In this restraint model, the lateral stiffness of bridge slabs is calculated based on the idea of effective width. It was assumed that the influence of the arching force was negligible after a distance equal to the effective span plus the depth of the slab ( $L_e + h$ ) from the face of the loaded area as shown in Figure 9-10. The effective width that shows the portion of a bridge deck slab being influenced by arching forces is illustrated in Figure 9-11.

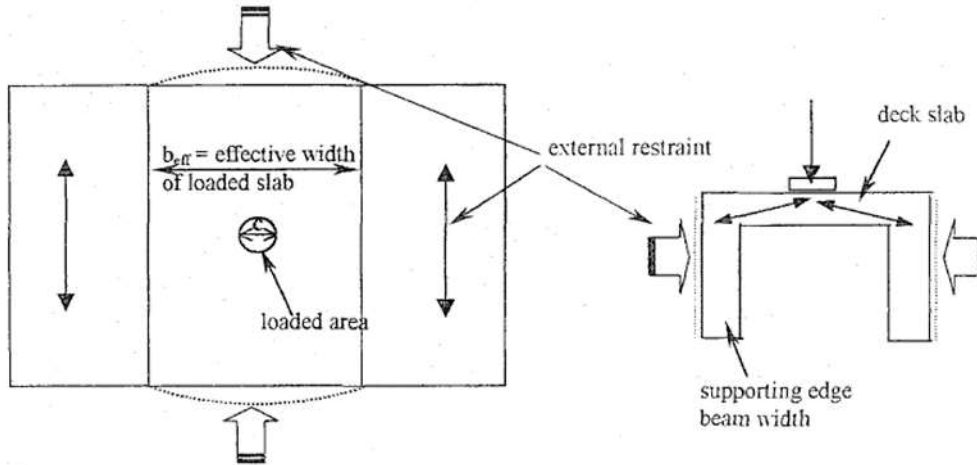


Figure 9-10 Restraint model proposed by Taylor (2000).

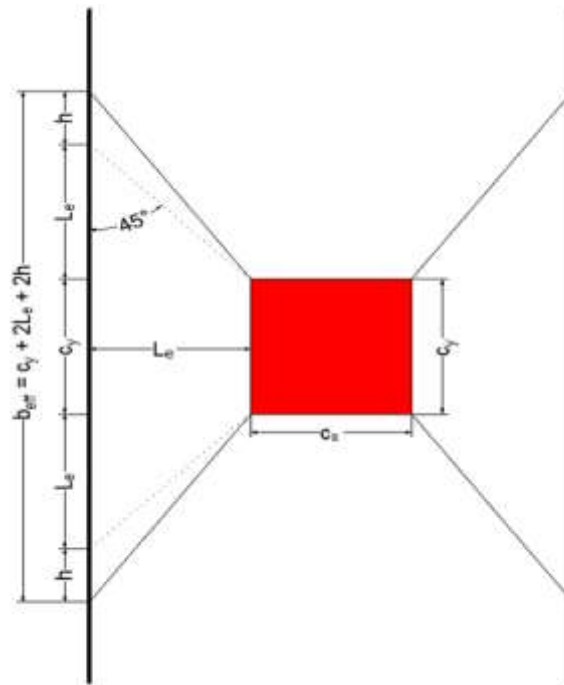


Figure 9-11 Effective width for slabs subjected CMA.

Based on the definition of effective width, Taylor (2000) suggested that the edge beam or supporting beam is equal to a spring with equivalent stiffness that has an axial area described by:

$$A_b = \frac{\zeta L_e I_{yb}}{b_{eff}^3}$$



$\zeta$  is a constant for support conditions of edge beam (range from 115 for simple support condition to 985 for fixed support condition) and it is 550 for most bridges. The average axial stiffness of the edge beam over the effective width was described by:

$$K_b = \frac{A_b E}{L_e}$$

The slab outside the effective width and end diaphragms act together to resist the outward arching thrust. Then, the axial stiffness of these two components is cumulative and is calculated as follows:

$$K_d = \frac{A_{slab} E_{slab}}{L_e} + \frac{A_{diaphragm} E_{diaphragm}}{L_e}$$

The combined flexibility of the system is found by adding each component's flexibility as follows:

$$\frac{1}{K_r} = \frac{1}{K_b} + \frac{1}{K_d}$$

With the calculated lateral restraint stiffness of the system  $K_r$ , assumed to be the same for the entire effective width, the Rankin and Long's (1997) method now can be applied directly. Using this method, the bridge slab can be converted to an equivalent rigidly-restrained slab strip and the flexural punching capacity of the bridge slab can be calculated as suggested in the procedure.

Lastly, Taylor suggests the effect of existing flexural reinforcement that was neglected in Kirkpatrick et al.'s (1984) method should be included. The equivalent area of reinforcement due to both bending and arching actions is estimated using the following equation:

$$\rho_e = (\rho_a + \rho) \times \left( \frac{f_y}{320} \right) = \left( \frac{M_a + M_b}{M_b} \right) \times \left( \frac{f_y}{320} \right) \times \rho$$

Once the equivalent area of steel reinforcement is determined, the punching shear capacity of the bridge slab can be calculated using the same equation that was previously reported by Long (1975).

### **Complete Queen's University Method for Predicting Punching Shear Capacity of Bridge Slabs under CMA effect**

The complete procedure to calculate the flexural and shear punching strengths of laterally restrained slabs is summarized in the following flow chart and the equations (in SI units: MPa and m) needed for each step are presented as follows:

1. Effective width of loaded slab:

$$L_e = \frac{L}{2} - \frac{c_x}{2}$$

$$b_{eff} = c_y + 2L_e + 2h$$

2. Stiffness parameters:

$$E_c = 4.23f_{cu}^{0.5}$$

$$K_s = \frac{E_c A_{sl}}{L_e} \text{ where } A_{sl} = h \times b_{eff}$$

$$I_{yb} = \frac{BD^3}{12} \text{ or transformed I-beam}$$

$$A_b = \frac{\zeta L_e I_{yb}}{b_{eff}^3}$$

$$K_b = \frac{A_b E_c}{L_e} \text{ (axial stiffness of supporting beam)}$$

$A_d$  = area of diaphragms + area of slab outside the effective width

$$K_d = \sum \frac{A_d E_d}{L_e} \text{ (axial stiffness of unloaded deck portion and end diaphragms)}$$

$$K_r = \frac{1}{\frac{1}{K_b} + \frac{1}{K_d}} \text{ (total lateral stiffness of the system)}$$

3. Bending capacity:

Depth of stress block,  $\beta = 1 - 0.003f_{cu}$  but  $< 0.9$

$$\text{Depth of neutral axis, } x = \frac{f_y A_s}{0.67f_{cu}\beta b_{eff}}$$

Lever arm,  $z = d - 0.5\beta x$

$$M_b = f_y A_s z$$

$$P_b = k_b M_b$$

4. Arching section:

$$d_1 = \frac{(h-2\beta x)}{2} \text{ where } d_1 \text{ is half of depth of arching section.}$$

Assume  $\alpha = 1$  for the first iteration, where  $\alpha$  is a proportion of half depth of arching action in contact with the lateral restraint.

5. Affine Strip:

$$A = \alpha b_{eff} d_1$$

$$L_r = L_e \sqrt[3]{\left(\frac{E_c A}{K_r L_e} + 1\right)}$$

6. Arching parameters:

$$\varepsilon_u = 0.0043 - ((f_{cu} - 60) \times 2.5 \times 10^{-5}) \text{ but } < 0.0043$$

$$\varepsilon_c = 2\varepsilon_u(1 - \beta)$$

$$R = \frac{\varepsilon_c L_r^2}{4d_1^2}$$

7. Deformation:

$$R > 0.26 : u = 0.31 \text{ (Constant)}$$

$$0 < R < 0.26 : u = -0.15 + 0.36\sqrt{0.18 + 5.6R}$$

8. Contact depth:

$$\alpha = 1 - \frac{u}{2}$$

Use  $\alpha d_1$  for refined arching section above until value remains constant

9. Arching capacity:

$$R > 0.26 : M_r = \frac{0.3615}{R}$$

$$0 < R < 0.26 : M_r = 4.3 - 16.1\sqrt{3.3 \times 10^{-4} + 0.1243R}$$

$$M_a = 0.168b_{eff} f_{cu} d_1^2 M_r \left(\frac{L_e}{L_r}\right)$$

$$P_a = k_a M_a$$

10. Flexural punching capacity:

$$P_{pf} = P_a + P_b$$

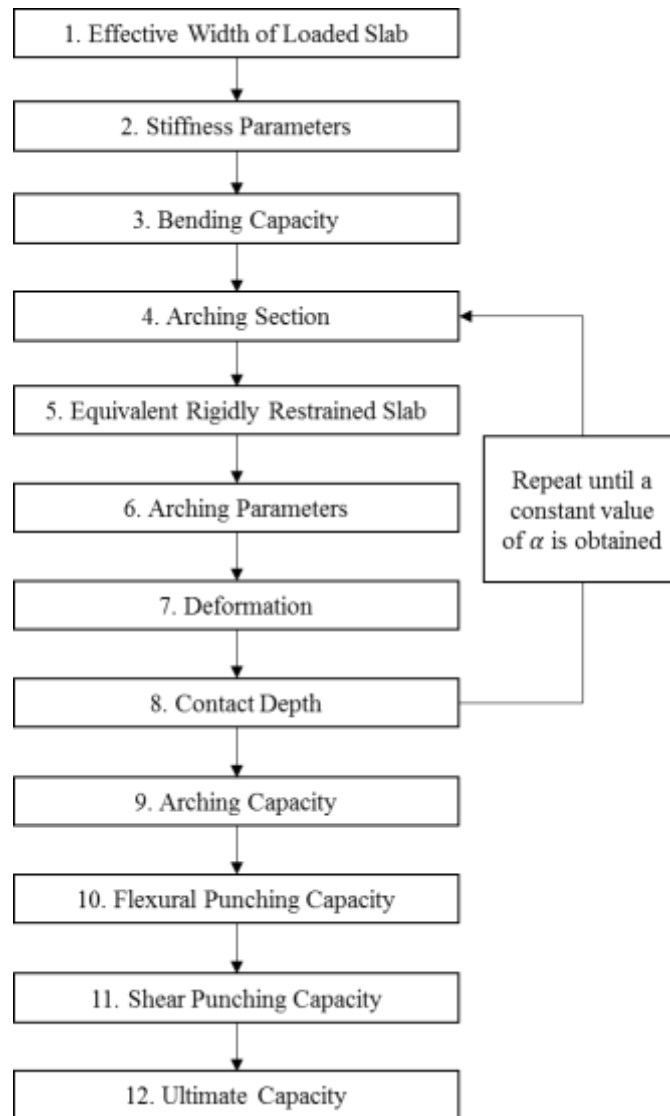
11. Shear punching capacity:

$$\rho_e = (\rho_a + \rho) \left(\frac{f_y}{320}\right) = \left(\frac{M_a + M_b}{M_b}\right) \left(\frac{f_y}{320}\right) \rho$$

$$P_{pv} = \frac{0.43}{r_f} \sqrt{f_{cu}} (\text{critical perimeter}) d (100\rho_e)^{0.25}$$

12. Ultimate Capacity:

$$P_{p\_CMA} = \min(P_{pf}, P_{pv})$$



#### 9.4 Literature Review on Direct Load Transfer

This effect was first recognized from beam shear tests (Kani, 1964) when the shear resistance of the beam will increase significantly when the load is applied close to the support as the shear span-to-depth ratio ( $a/d$ ) less than 2.5. This effect is due to the formation of a direct compression strut between the load and the support. As the strut becomes steeper, the load-carrying capacity of the compression strut will increase, hence

will increase the shear resistance of the beam. For slabs, this is called direct transfer effect. While for beams, only one straight strut develops over the distance,  $a$ , as shown in Figure 9-12, in slabs, a fan of strut can develop as illustrated in Figure 9-14 (b). It means that under the same distance,  $a$ , from the center of load to the center of support, the average shear span-to-depth ratio ( $a/d$ ), in slabs, is larger than what it has in beams. Therefore,  $a/d$  will have smaller influence on the shear resistance of the slab than it has on the beam.

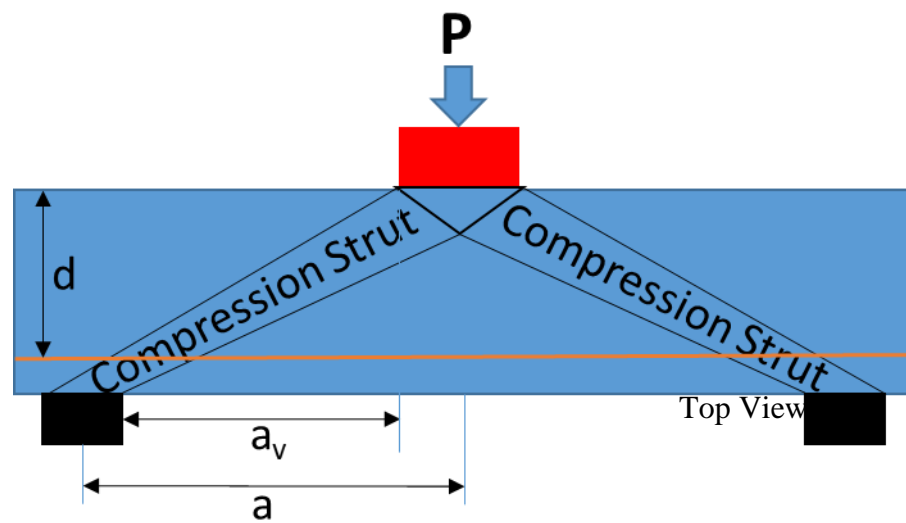


**Figure 9-12 Formation of direct compression strut in beam.**

Back to the experiments performed in this study, in addition to the CMA effect, the direct load transfer effect was also believed to be responsible for the enhancement in the punching shear capacity of the tested specimen. Particularly for Tests C and D, the load was applied so close to the top flanges and the webs of the box-girder with  $a/d$  of 1.75. Therefore, a certain amount of the applied load might be transferred directly the girder top flanges; hence, increased the punching shear resistance of the specimen.

Although most of empirical methods that were developed to predict the shear resistance of slabs subjected concentrated loads close to supports were based on studies on

one-way slabs, the method that was proposed by Regan (1982) could be extended easily for two-way slabs. Regan's method also has been found to give very close predictions to the experimental data for one-way slabs (Lantsoght, 2013). This approach also been implemented in many practice codes such as British punching shear provision and EN 1992-1-1:2000. For instance, BS 8110 shear provision allows the enhancement of shear resistance of beam section, when subjected to concentrated loads with shear span-to-depth ratio ( $a/d$ ) less than 2.5, to be taken into account by multiplying the design shear stress,  $v_c$ , of the beam by  $2d/a_v$ . For a slab, BS 8110 also allows the shear stress to increase by a factor of  $1.5d/a_v$  when it is desired to check perimeters closer to the loaded area than  $1.5d$ . The review of Regan's method is provided in below.

#### **Regan's Method to Account for Direct Load Transfer Effect (1982)**

Regan (1982) developed a method to predict punching shear resistance of reinforced concrete one-way slabs under concentrated load near the supports. This method is based on the critical perimeter around the concentrated load and takes into account the clear span distance ( $a_v$ ) between the face of the support to the face of the load. This method is summarized as follows:

- 1) A critical perimeter around the concentrated load is selected at a distance of  $1.5d$  from the periphery of the load as shown in Figure 1.
- 2) For any part of the critical perimeter which is parallel to the support and has clear span distance,  $a_v$ , less than  $1.5d$  as illustrated by the part  $u_2$  of the perimeter in Figure 2. Its shear resistance is multiplied by a shear span factor of  $\frac{2d}{a_v}$  as follows:

$$P_{R2} = \left(\frac{2d}{a_v}\right)\xi_s v_c u_2 d < \frac{\sqrt{f_{cu}}}{\gamma_m} u_2 d$$

Where  $\xi_s = \sqrt[4]{\frac{500}{d}}$

$$v_c = \frac{0.27}{\gamma_m} \sqrt[3]{100\rho f_{cu}}$$

It is important to note that the shear resistance For the remainder  $\sum u = u_1$  of the perimeter, the punching shear resistance is calculated as follows:  $P_{R1} = \sum \xi_s v_c u_1 d$

For each part of the calculation, the local values of the effective depth  $d$  ( $d_t$  for transverse reinforcement and  $d_l$  for and the ratio of flexural reinforcement  $\rho$  ( $\rho_t$  for the transverse reinforcement and  $\rho_l$  for the flexural reinforcement). The total punching shear resistance is given by:  $P_R = P_{R1} + P_{R2}$

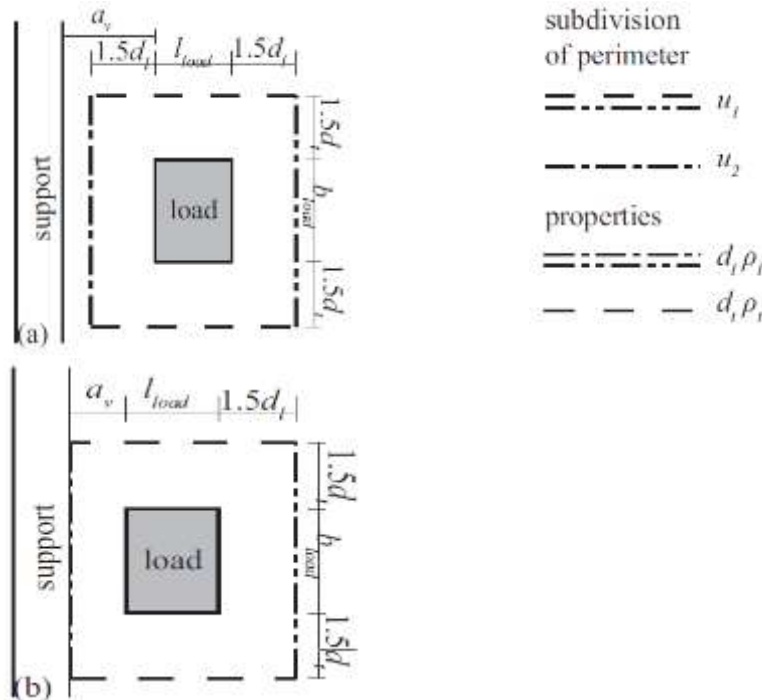


Figure 9-13 Subdivision of perimeter and slab properties to be used for parts of perimeter: (a) for  $2d_t > a_v > 1.5d_t$ ; (b) for  $a_v < 1.5d_t$  (Adopted from Lantsoght (2013) based on Regan (1982)).

## **9.5 Methods for Predicting Punching Shear Capacity of Damaged Twin Steel Box-Girder under Single Concentrated Load**

The experimental results have shown that under single concentrated load, the punching shear is likely to be the governing failure mode for twin steel box-girder bridges. However, current punching shear provisions seems to be inadequate in predicting the punching shear resistance of the bridge specimens in this study. It was because the effects of CMA and direct load transfer are not considered in these punching shear provisions. Although several methods have been proposed to capture these effects on the shear resistance of bridge slabs separately (Sections 9.3 and 0), there is a need to develop a simple and versatile approach that could take these effects into consideration. Moreover, this study will also propose a new shear span factor that can adequately capture the direct load transfer effect in two-way slabs.

### **9.5.1 Proposed New Shear Span Factor for Two-Way Slabs Subjected to Concentrated Load**

Due to the presence of diaphragms, external cross-frames connecting two box-girders and internal cross-frames connecting the webs of the box-girder together, the bridge slabs should be considered as a two-way slabs. Since two-way slabs are restrained in both longitudinal and transverse directions, the fan of compression struts should form with a larger angle than it does in one-way slab as illustrated in Figure 9-14. This results in a larger average  $a/d$  and therefore, the influence of  $a/d$  will be smaller in two-way slabs than in one-way slabs. However, in two-way slabs, the influence of  $a/d$  on the shear resistance of a two-way slab should exist in a larger range of  $a/d$ . For these reasons, the shear span factor which was proposed for one-way slabs by Regan (1982) and is being adopted in BS



8110 shear provision should be modified. In general the effect of direct load transfer is expressed in term of clear shear span to effective depth ratio,  $a_v/d$  as in Regan's method (1982) and BS 8110 or EN 1992-1-1:2005 shear provisions.

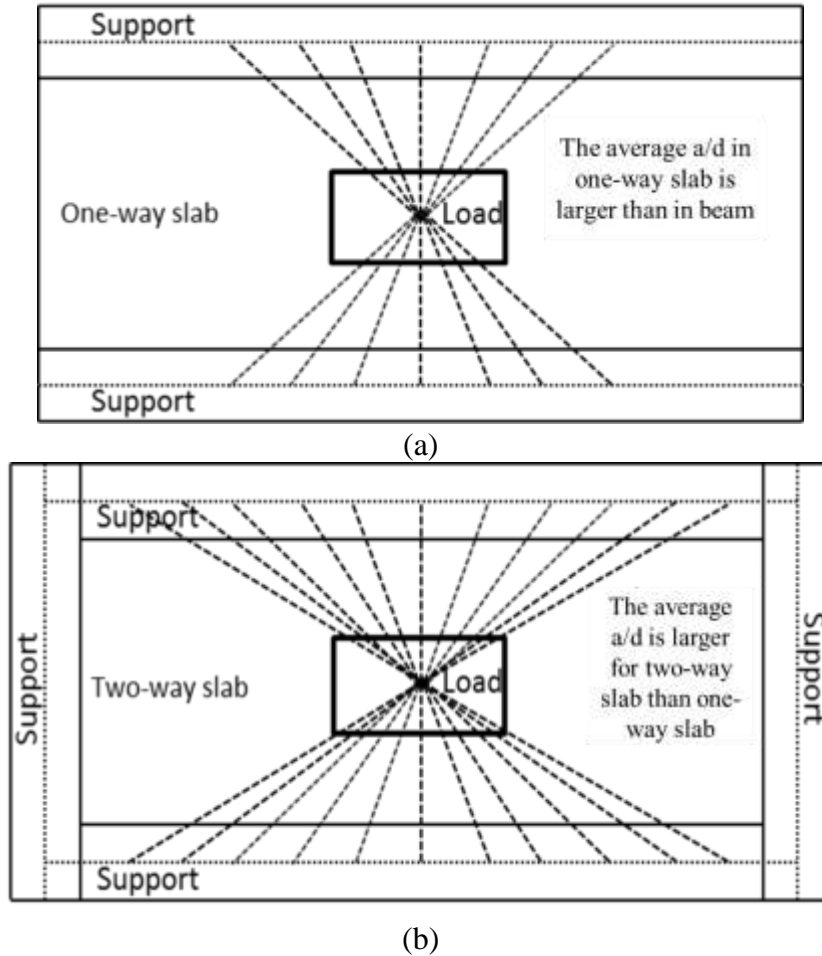


**Figure 9-14: Schematic drawings of strut formation in (a) one-way and (b) two-way slabs.**

In order to investigate the direct load transfer effect occurred in Tests C and D, two series of nonlinear finite element analyses was performed using the experimentally validated and calibrated 3D finite element model. The load was applied through a 10x10-in. loading pad as in the experiments. In the first series of FE analysis, the effect of direct load transfer effect on the shear resistance of bridge slabs over the intact girder will be

investigated by varying the clear shear span,  $a_v$ , as shown in Figure 9-15 (a) until no further increase in the slabs' capacity is observed. Similarly, in the second series of the analysis the effect of direct load transfer on the shear resistance of bridge slabs over the damaged girder will be investigated by varying the clear shear span,  $a_v$ , as shown in Figure 9-15 (b) until no further increase in the slabs' capacity is observed. The analysis results from these two series of analysis are expected to not only show the relationship between the influence of  $a_v/d$  and the punching shear capacity of the slab but also reveal how the fracture damage affects the influence of  $a_v/d$  and the punching shear capacity of the slab. It should be noted that the clear shear span is determined as a distance from face of the load area to the interior face of the closest top flange and the effective depth,  $d$ , of the slab of the tested specimens was 4 in. Then in each finite element analysis, the ultimate load-carrying capacity and load distribution at the critical perimeter determined at  $0.5d$  distance from the face of loaded area will be investigated.

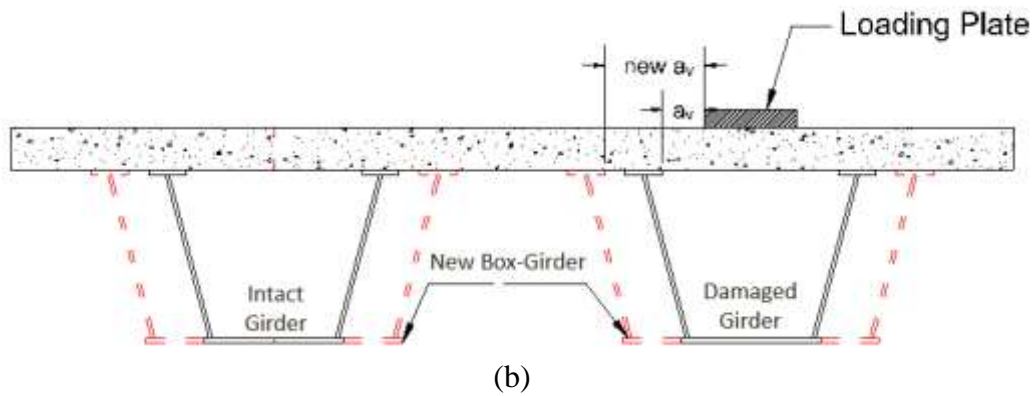
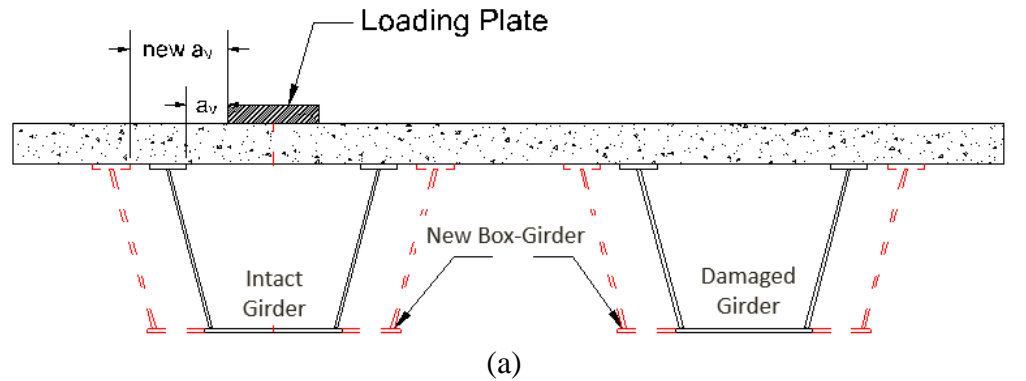


**Figure 9-15 Approaches of investigating the direct load transfer effects for bridge slabs subjected to concentrated load over (a) the intact girder and (b) the damaged girder.**

### **Shear Span Factor for Bridge Slab Portion over the Intact Girder of Twin Steel Box-Girder Bridge**

In this first series of analysis, the load was applied through a 10-in.-square loading pad placed at the center of the intact girder with a clear shear span distance,  $a_v$  increasing from  $1.125d$  to  $6.25d$ . The influence of clear shear span distance,  $a_v$ , on shear resistance of bridge slab portion over the intact girder is summarized in Table 9-1. The results clearly show that as the distance between the load and the top flange increases, the ultimate punching shear capacity of the specimen decreases.

Especially, when  $a_v$  distance increases from  $1.125d$  to  $4d$ , the capacity of the slab decreases significantly from 172 kips to 124 kips. As seen in the fourth column in Table

9-1, the decrease in the ultimate capacity of the specimen was due to the decrease of shear resistance of slabs along the parts of the critical perimeter that are parallel and close to the top flanges of the girder. As the  $a_v$  distance increases from  $1.125d$  to  $6.25d$ , the shear resistance of the slab along these parts decreases from 52 kips to 30 kips. In contrast, the shear resistance of the slab along the parts of the critical perimeter that are perpendicular with the top flanges decreases slightly from 36 kips to 30 kips. Since that the distance between the face of the load and the internal cross-frame of the box-girder, remains constant and very large in these analysis and in the tests, the direct load transfer effect in longitudinal direction should be zero. It suggests that this decrease from 36 kips to 30 kips could be due to the influence of the clear shear span distance onto the shear resistance of the parts of the critical perimeter that are perpendicular to the top flanges. In a graphical explanation, the fan of struts, which is developed due to the load is applied close to the top flange, crosses with the parts of the critical perimeter that are perpendicular to the top flanges. A further study might be necessary to investigate how the clear shear span distance influences the shear resistance of the slabs along parts of the critical perimeter that are perpendicular to the supports. Different parameters such as reinforcement ratio, concrete strength, the ratio of clear shear span distance in one direction to clear shear span distance in other direction might be considered. In this study, it is conservative to consider only the influence of  $a_v/d$  on the shear resistance of the parts of the critical perimeters that are parallel and close to the top flanges.

When the  $a_v$  distance increases from  $4d$  to  $6.25d$  the punching shear capacity of the slab decreases only 2 kips. The shear resistance of the slabs are along the critical perimeter

are observed to be quite similar and uniform along the critical perimeter for these analysis. It is important to note that punching shear is still the mode of failure in all of analyses.

Based on the analysis results, a relationship between the shear resistance along parts of the critical perimeter that are parallel and close to the top flanges and the clear shear span distance  $a_v$  is proposed through a shear span factor defined as  $\omega$ . By selecting  $a_v = 6.25d$  as a base-line model where the shear resistance of slabs are not influenced by the distance  $a_v$ , the shear span factor  $\omega$  for each distance  $a_v$  can be calculated by taking average load carried by parts of the critical perimeter that are parallel and close to the top flanges divided by the shear resistance of the slab that are parallel and close to the top flanges obtained from the base-line mode. The shear span factor for each value of  $a_v$  is reported in the last column in Table 9-1. With the calculated shear span factor for each value of  $a_v$ , the suggested relationship between the shear span factor,  $\omega$ , and  $a_v$  is illustrated in Figure 9-16. In fact, in Figure 9-16 the shear span factor is plotted in term of  $a_v/4d$  because the punching shear capacity of the slab is observed to be almost the same when  $a_v$  greater than  $4d$  as discussed above. By fitting these data, equations for predicting shear span factors for two-way slabs are given below. These equation limits the maximum shear span factor to be 2.

$$\text{For } a_v \leq 4d \quad \psi = 2 - \frac{a_v}{4d}$$

$$\text{For } a_v > 4d \quad \psi = 1$$

**Table 9-1 Influence of  $a_v/d$  on Shear Resistance of Bridge Slab Portion over Intact Girder**

| $a_v$ (in.) | $\frac{a_v}{d}$ | $P_u$ (kips) | Load Distribution at Critical Perimeter | Shear Span Factor, $\Psi$ |
|-------------|-----------------|--------------|---|---------------------------|
| 4.5         | 1.125           | 172          |   | 1.69                      |
| 8           | 2               | 169          |   | 1.59                      |
| 9.5         | 2.375           | 161          |   | 1.48                      |
| 12          | 3               | 155          |   | 1.36                      |
| 14.5        | 3.625           | 136          |   | 1.11                      |
| 16          | 4               | 124          |   | 1.03                      |
| 25          | 6.25            | 122          |   | 1.0                       |

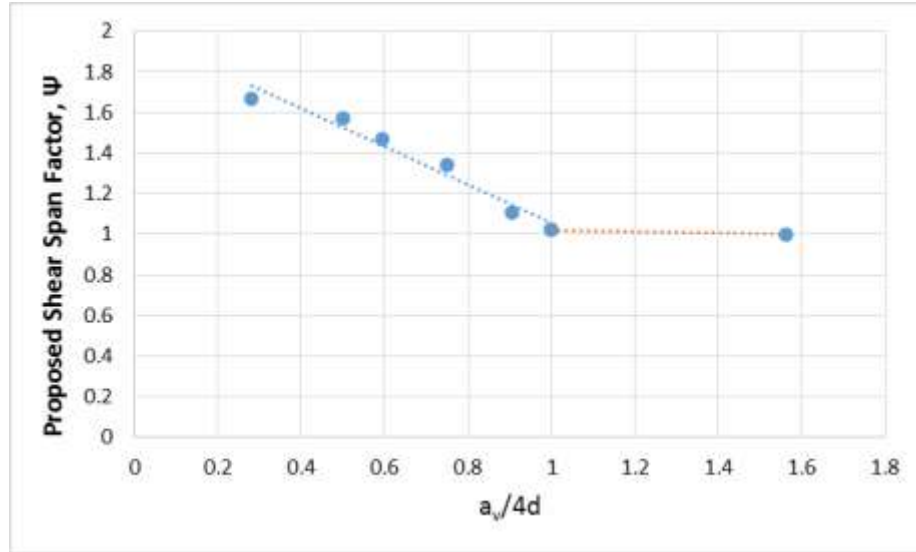


Figure 9-16 Shear span factor for slab portion over the intact girder.

### Shear Span Factor for Bridge Slab Portion over the Damaged Girder of Twin Steel Box-Girder Bridge

In the second series of finite element analysis, the influence of clear shear span distance,  $a_v$ , on shear resistance of bridge slab portion over the damaged girder will be investigated. Similar to the first series of analysis, the clear shear span distance,  $a_v$  will be varying from  $1.125d$  to  $6.25d$  with the load is applied at the center of the damaged girder through 10x10-in. loading pad. The analysis results are summarized in Table 9-2. As  $a_v$  decreases from 4.5 in. to 8 in., the ultimate load-carrying capacity of the slabs decreases 15 kips. However, for further increase in  $a_v$  the decrease in the ultimate punching shear capacity of the bridge slab is very small. The results also show that the load is distributed quite uniformly around the critical perimeter for this range of  $a_v$  considered in the analysis. Overall, the influence of  $\frac{a_v}{d}$  or direct load transfer effect on shear resistant of the slabs over the damaged girder along the critical perimeter is negligible. It could be due to the fact that

the flexural stiffness of the damage girder at this particular location is insignificant which eventually prevents compression struts to be developed. Therefore, the punching shear resistance of the bridge slabs over the damaged girder at the fracture location could be conservatively assumed to be constant for all range of  $a_v$ . The suggested relationship between shear span factor  $\psi$  and  $\frac{a_v}{4d}$  is shown in Figure 9-17. As explained, this relationship shows that the shear span factor  $\omega$  can be assumed to be 1 when the load is applied over the damaged girder regardless how close the load is applied to the top flanges. It should be noted that this proposed shear span factor is only applicable when the load is applied over the fractured location. When the load is applied over the damaged girder but far away from the fracture location, the direct compression struts can develop and the shear resistance of the slabs can be increased significantly even to the extent that is observed in the intact girder.



**Table 9-2 Influence of  $a_v/d$  on Shear Resistance of Bridge Slab Portion over Damaged Girder**

| $a_v$ (in.) | $\frac{a_v}{d}$ | $P_u$ (kips) | Load Distribution at Critical Perimeter | Shear Span Factor, $\Psi$ |
|-------------|-----------------|--------------|---|---------------------------|
| 4.5         | 1.125           | 104          |   | 1.27                      |
| 8           | 2               | 88           |   | 0.98                      |
| 9.5         | 2.375           | 89           |   | 1.09                      |
| 12          | 3               | 88           |   | 1.07                      |
| 14.5        | 3.625           | 86           |   | 0.95                      |
| 16          | 4               | 86           |   | 1.0                       |
| 25          | 6.25            | 85           |   | 1.0                       |

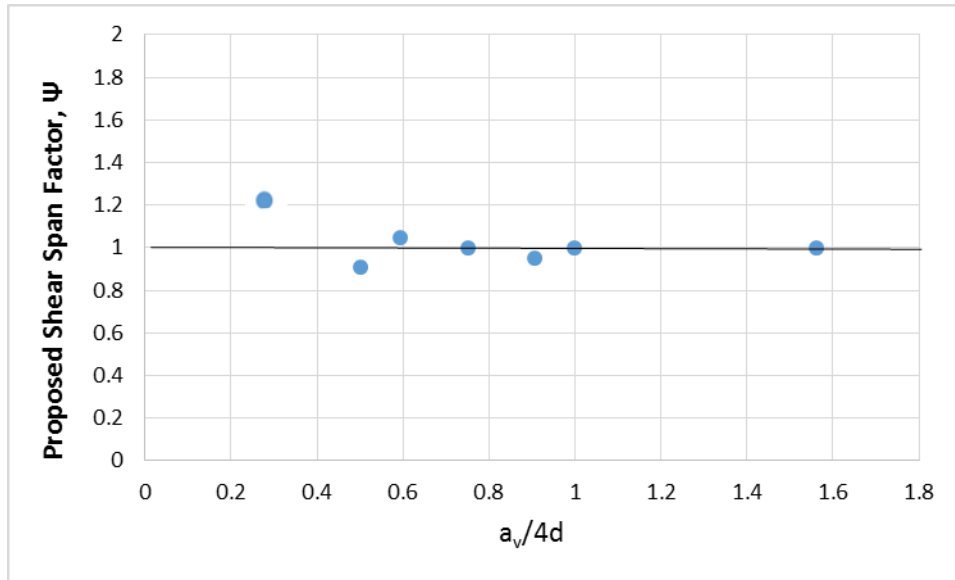


Figure 9-17 Shear span factor for slab portion over the damaged girder.

### 9.5.2 Proposed Method for Predicting Punching Shear Resistance of Bridge Slabs under CMA and Direct Load Transfer Effects

Even though the shear span factor is now developed, there is still a need to develop a simple and versatile method that could take both CMA and direct load transfer effects into consideration when predicting punching shear resistance of bridge slabs. For this reason, the proposed shear span factor will be incorporated into Queen's University method which is summarized previously in Section 9.3. Combining this Queen's University method with the proposed shear span factor, both effects of CMA and direct load transfer can be both captured. The incorporating process can be done as following: 1) Assuming the punching capacity of the slabs calculated from Step 12 in Queen's University approach is distributed uniformly along the critical perimeter, 2) Calculate the load carried by each part of the critical perimeter, 3) For any part of the critical perimeter that is close and parallel to the support, the load will be multiplied by the proposed shear span factor  $\psi$ , 4)

Finally, the final ultimate punching capacity of the slab is the summation of the load carried by all parts of the critical perimeter. The modifications to the method developed by Queen's University is expressed below.

**Step 12: Ultimate Capacity**

$$P_{p\_CMA} = \min(P_{pf}, P_{pv})$$

Assuming the punching capacity of the slabs considering only CMA effects is uniformly distributed along the critical perimeter.

For any part of the critical perimeter that parallel and close to the supporting girder's top flange.

$$P_{u2} = u_2 \times \frac{P_{p\_CMA}}{\text{critical perimeter}} \times \omega$$

Where  $\psi = 2 - \frac{a_v}{4d}$  For  $a_v \leq 4d$

$\psi = 1$  For  $a_v > 4d$

$u_2$  is the length of the part of critical perimeter that parallel and close to the top flanges

For the remaining parts of the critical perimeter

$$P_{u1} = u_1 \times \frac{P_{p\_CMA}}{\text{critical perimeter}}$$

$u_1$  is the length of the part of critical perimeter that parallel and close to the top flanges

The final ultimate punching capacity is given by:

$$P_p = P_{u1} + P_{u2}$$

If the supporting girder is fully fractured, the effects of CMA and direct load transfer can be neglected at the fracture location as explained previously. The arching moment resistance of the slabs can be assume to be zero and then the calculations from Steps 4 to 9 can be skipped and the shear span factor can be taken as 1 for all range of  $a_v$ .

## 9.6 Methods for Predicting Shear Capacity of Damaged Twin Steel Box-Girder under Four Concentrated Loads

As illustrated by the Test E results, under four concentrated loads that were used to represent a truck load, the damaged twin steel box-girder bridge specimen had its slab failed predominantly in one-way failure mode. As discussed previously, the shear resistance of the bridge slabs failing in one-way shear in general could be predicted by checking beam shear capacity of the slab over a certain effective width of the support and calculating the punching shear capacity of the slab over the critical perimeter around the load. In this section, procedure for using each approach will be discussed and the test results will be compared with the prediction values from both approaches in Section 9.7.2.

In the first approach, the beam shear provisions ACI 318-08 and BS 8110 will be utilized in combination with shear span factor and effective widths. The shear span factors that was proposed by Regan and is proposed in this study will be incorporated into these provisions to account for the enhancement of shear resistance of the slabs with loads close to the supports. The effective widths will be determined from two horizontal load spreading methods. The first method (Dutch practice) determines the effective width,  $b_{\text{eff1}}$ , assuming 45° horizontal load spreading from the center of the load as shown in Figure 9-1 (a). The effective width,  $b_{\text{eff2}}$ , determined in the second method (French practice) is assumed to have 45° horizontal load spreading from the far side of the load. An example showing how to determine the effective width for each concentrated load with French method of horizontal load spreading is shown in Figure 9-18. As mentioned earlier, if the effective

width of each load overlaps, the effective width of the entire axle will be used to be conservative.

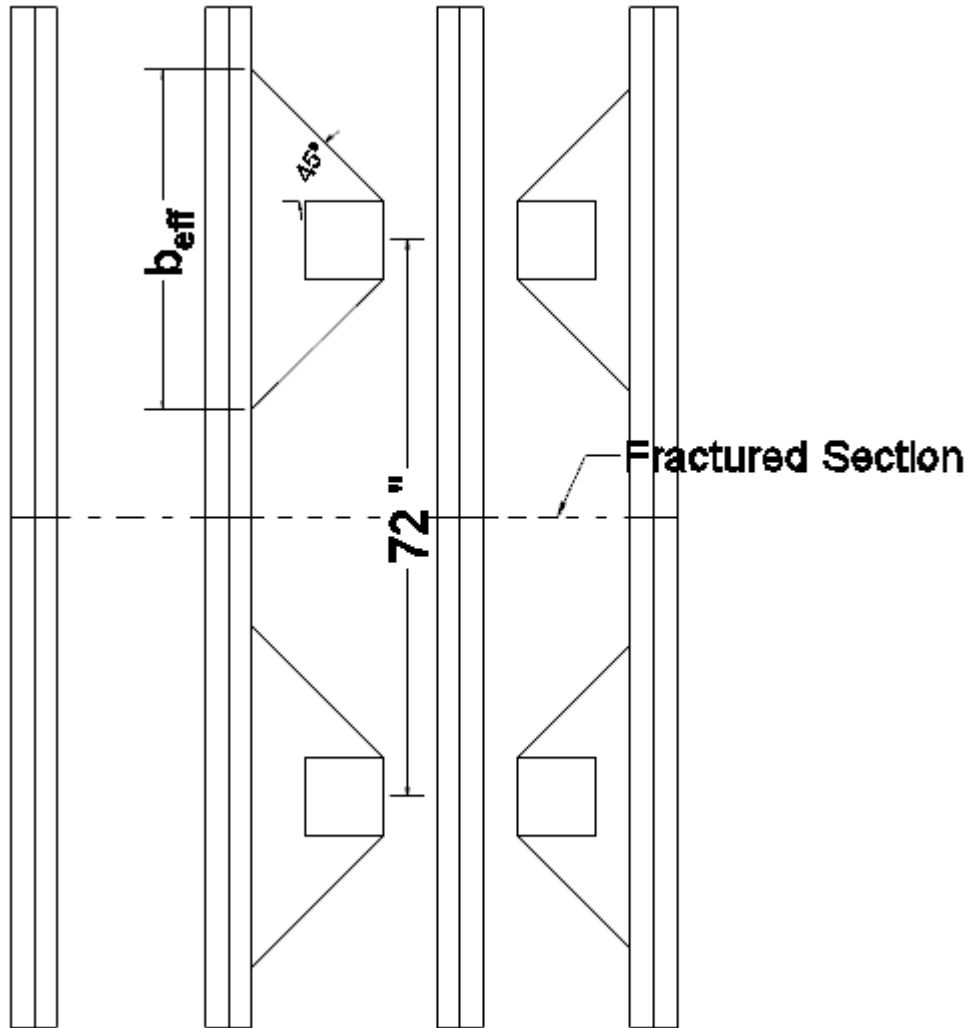


**Figure 9-18 Determination of effective width using French horizontal load spreading.**

In the second approach, the method proposed earlier for predicting the punching shear resistance of the slab under single concentrated load will be used to check the punching shear capacity of the slabs at the critical perimeter around the load. However, the critical perimeter will not be taken as a full rectangular but instead only half of the perimeter will be used. As shown in Figure 9-19, it shows that unlike other tests with single

concentrated load, the load is not distributed uniformly under each loading pad when four concentrated loads are applied in the configuration that was used in Test E. In fact, the load is distributed over only one half of the loading pad toward to the supports. The other half of the loading pad that is closer to the fractured location showed uplift with negative reaction. It is because concave-down deflection profile of the damaged girder and this causes the deflection at one side of the loading pad is greater than the deflection at the other side of the pad. In addition, the loading beams on the top of the loading pads are so stiff so that they remained nearly straight during the test; therefore, the load was mainly applied to the further edge of the loading pad as illustrated by the blue line in Figure 9-20. For these reasons, the critical perimeter will be also taken as one-half of the original critical perimeter.

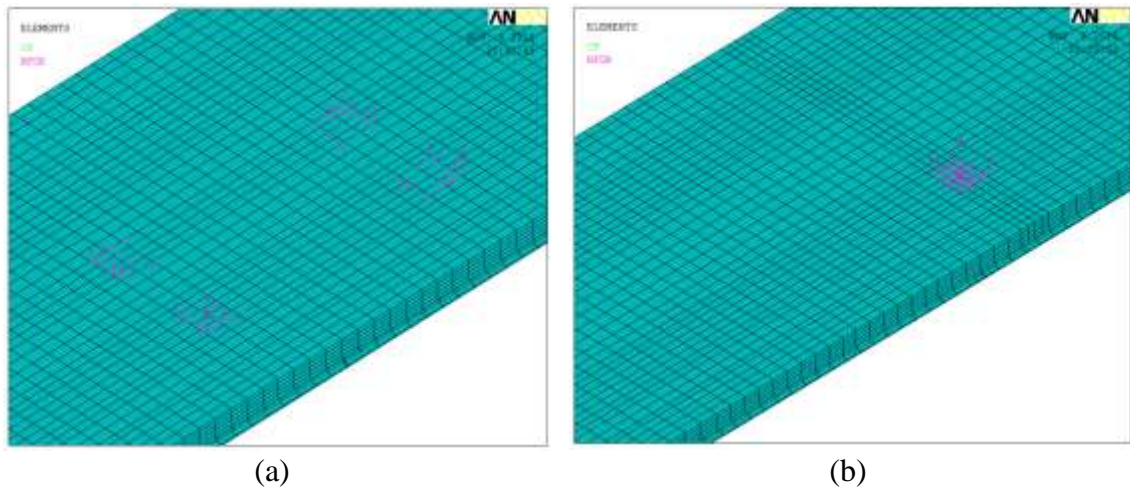
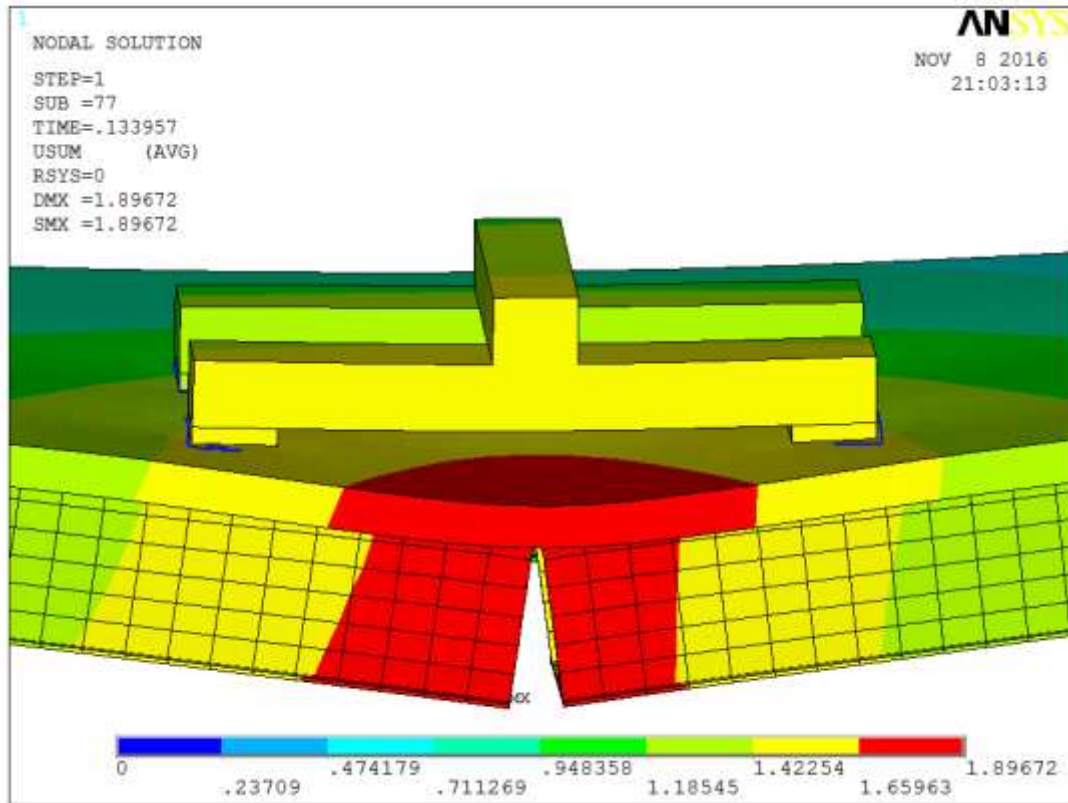


**Figure 9-19 Load distribution (a) under 4-point loading and (b) single concentrated loading configuration.**



(a)

Figure 9-20 Deflection of the specimen under 4-point loading configuration.

### 9.7 Comparisons between Predictions and Experimental Results for Damaged Twin Steel Box-Girder under Single Concentrated Load

In this section, comparisons between the experimental results and the predicting values from different methods will be provided and discussed. It should be noted that only the results from Tests A, C, D and E will be considered. Test B in this experimental program basically was a flexural test and the capacity of the specimen in this test could be predicted by simply calculating the plastic moment of the composite section of a half of bridge specimen as explained previously. All of the comparisons are made based on the measured

mean material properties and all safety factors are assumed to be 1. Where the properties are not measured, the data provided from manufactures will be used.

### **9.7.1 Under Single Concentrated Load – Tests A, C, and D**

Although in ultimate Test A the specimen had a complex failure/damage sequence, the punching shear damage in the concrete deck around the loading pad was the major cause for the largest drop in the load-deflection curve when the specimen reached its maximum load-carrying capacity at 156 kips. It should be noted that the specimen was loaded over the entire width of the damaged girder. Therefore, the compression struts didn't develop, and therefore the effect of direct load transfer was neglected. As a result, the shear span factor is taken as 1 in the comparison. Moreover, the damaged girder was observed to response as two cantilevers joining by a hinge and experienced a concave down deflection shape which suggested the majority of the top of bridge slab portion over the damaged girder was in tension. Therefore the effect of CMA can be neglected as well. As both effects are neglected, the proposed method will turn into the simple punching shear equation that was developed by Long (1975). The predicted values from ACI 318, BS 8110 punching shear provisions and the proposed method were 150, 120 and 164 kips respectively while the test result was 156 kips. The ratios between the predicted values to the experimental results are shown in Table 9-3. Among all the methods, BS 8110 was the most conservative one. Both ACI 318-08 and the proposed method resulted in good agreements with the experimental result with less than 5% of difference.

For ultimate Test C, the punching shear capacities of the specimen predicted from the codes are highly conservative. The experimental result is more than two times greater



than the predictions obtained from the codes. However, ACI 318-08 is the most conservative one because it doesn't include both effects of CMA and direct load transfer in consideration and predicts only inclined cracking load instead of an ultimate load in shear. As mentioned earlier, ACI 318-08 recommends to use nonlinear strut-and-tie model for slabs with loads applied close to the supports. The BS 8110 provision with direct load transfer effect taken into consideration provides better prediction than the ACI 318-08 provision but still highly conservative. It is because the CMA effect is not taken into account and the shear span factor that is recommended in BS 8110 for slabs is the lower bound value compared to those recommended by Regan (1982). The proposed method with both effects taken into consideration provides the closest estimate. The ratio between the predicted value from the proposed method and the test value was 0.86.

For Test D, ACI 318-08 and BS 8110 punching shear provisions and the proposed method provides good estimates of the experimental result. The ratios between the predicted values and the experimental result is 0.92, 0.90 and 1.07 respectively for ACI 318-08, BS 8110 and the proposed method. Both code provisions result in slightly smaller values than the proposed method. It is because Long's equation in the proposed method allows slightly greater shear stress to be developed around the critical perimeter. However, it should be noted that Test D was conducted after Test C on the same specimen without any repair, any damage and residual deformation inherited from Test C could have an influence on the results of Test D. Therefore the punching shear capacity of the slab in Test D predicted from finite element analysis could be used as another reference data. Comparing between Test A and Test D, ACI 318-08 provision seems to have a better accuracy than BS 8110 provision.

**Table 9-3 Comparison between Test Results and Predicting Methods.**

|        | Loading Area (in. x in.) | Loading Location | $\rho$ (%) | $f'_c$ (ksi) | $P_{Exp}$ (kip) | $P_{ACI}/P_{Exp}$ | $P_{BS\ 8110}/P_{Exp}$ | $P_p/P_{Exp}$ |
|--------|--------------------------|------------------|------------|--------------|-----------------|-------------------|------------------------|---------------|
| Test A | 9x36                     | DG               | 0.9        | 7.8          | 156             | 0.96              | 0.77                   | 1.05          |
| Test C | 10x10                    | IG               | 0.9        | 7.2          | 180             | 0.43              | 0.49                   | 0.86          |
| Test D | 10x10                    | DG               | 0.9        | 7.2          | 83              | 0.92              | 0.90                   | 1.07          |

Another comparison between predictions from the proposed method and data obtained from punching shear tests on steel girder bridge performed by Kathol et al. (1995) is shown in Table 9-4. The proposed method results in good agreement with the test data. The ratio between the predicted values and the test values is 0.95 on average with 0.09 standard deviation.

**Table 9-4 Comparison of between Punching Shear Test Results (Kathol et al., 1995) and the Proposed Method's Predictions.**

| Tests              | Loading Area | $a_v$ (in.) | $a_v/4d$ | $P_{Azizinamini}$ (kip) | $P_p$ (kip) | $P_p/P_{Azizinamini}$ |
|--------------------|--------------|-------------|----------|-------------------------|-------------|-----------------------|
| UT                 | 20x8         | 21.5        | 0.83     | 129                     | 137         | 1.06                  |
| PS1                | 10x4         | 26.5        | 1.02     | 156                     | 128         | 0.82                  |
| PS2                | 10x4         | 26.5        | 1.02     | 122                     | 128         | 1.04                  |
| PS3                | 10x4         | 26.5        | 1.02     | 147                     | 128         | 0.87                  |
| PS4                | 10x4         | 26.5        | 1.02     | 132                     | 128         | 0.97                  |
| Average            |              |             |          |                         |             | 0.95                  |
| Standard Deviation |              |             |          |                         |             | 0.09                  |

### 9.7.2 Under Four Concentrated Loads – Test E

The comparisons between predicted values utilizing beam shear capacity approach over an effective width and the test results are provided in Table 9-5. It should be noted that the effective width  $b_{eff1}$  is determined assuming 45° load spreading from the center of the loading pad (Dutch method) while the effective width  $b_{eff2}$  is determined assuming 45° load spreading from the far side of the loading pad (French method). Since the Dutch

method results to smaller effective widths than the French method does as shown in Figure 9-21; the predictions using  $b_{eff1}$  are more conservative than those using  $b_{eff2}$ . In fact, the total effective width determined by assuming  $45^\circ$  horizontal load spreading from the center of the load is 88 in. This is approximately 52% smaller than the effective width determined by French method of horizontal load spreading (168 in.). The comparison between Figure 9-21 and Figure 9-22 indicates that the effective width determined by the French method of horizontal spreading is in a good agreement with the finite element results.

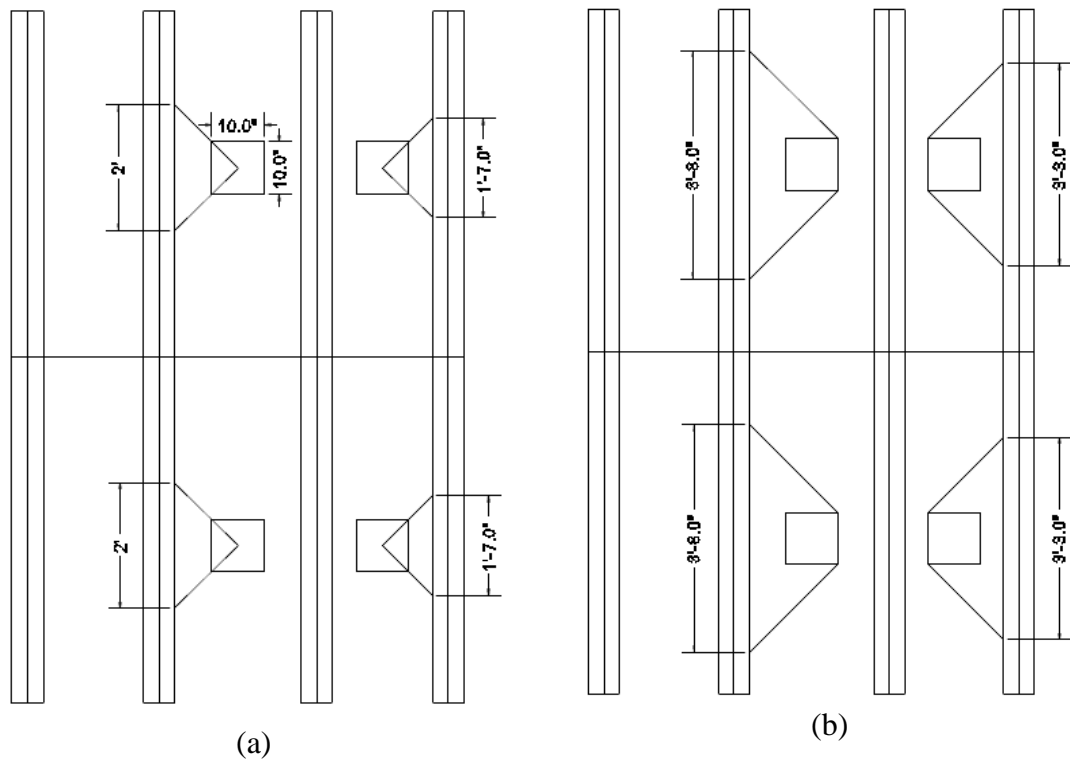


**Figure 9-21 Effective width determined (a) assuming  $45^\circ$  horizontal spreading from the center of the load, (b) assuming  $45^\circ$  horizontal spreading from the far corner of the load.**

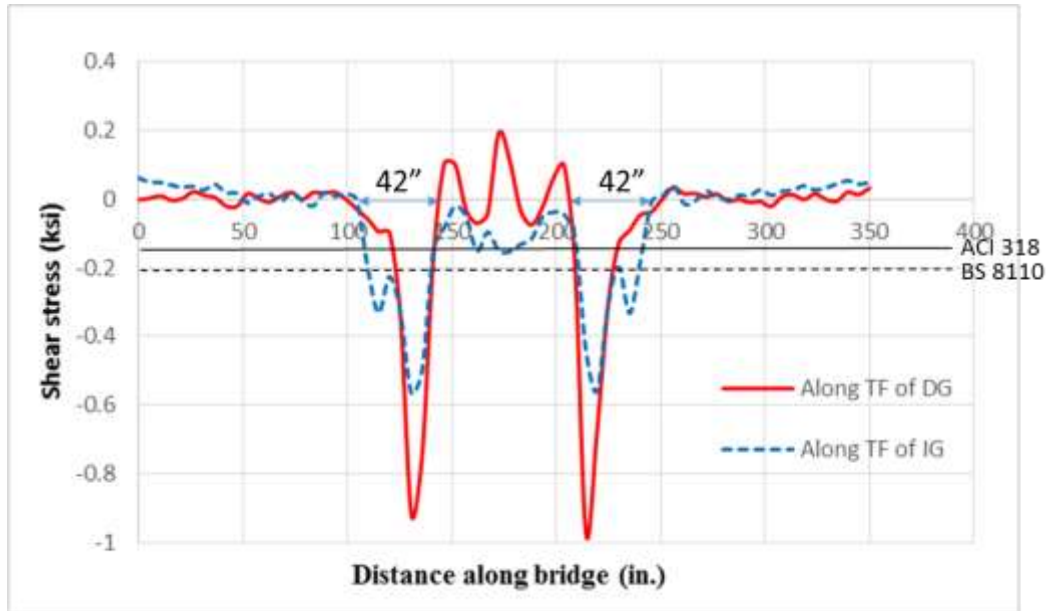


Figure 9-22 Shear stress in the slab along the main span of the bridge specimen.

Similar to punching shear provisions, the ACI 318-08 beam shear provision seems to lead to more conservative predictions than the BS 8110 provision. It was because the ACI 318-08 has lower design beam shear stress than BS 8110 does. As discussed previously the one-way shear expression in ACI 318-08 provision was developed based on the inclined cracking load of concrete. Both shear provisions when is used in combination with  $b_{eff2}$  results in less conservative predictions than using  $b_{eff1}$ . A combination of BS 8110 shear provision with  $b_{eff2}$  and the proposed shear span factor ( $\omega_{proposed}$ ) results in a closest prediction with 3% less than the test result. The most conservative prediction is the combination of ACI 318-08 shear provision with  $b_{eff1}$  and Regan's shear span factor ( $\omega_{Regan}$ ) with 65% smaller than the test value.

Although both shear span factors, when incorporated, improved the predicted capacity,  $\omega_{proposed}$  results in better correlation with the test and finite element analysis results. While the factor,  $\omega_{Regan}$ , increases the shear resistance of the slab along the top

flange of the intact girder and the damaged girder by 15% and 78%, respectively, these numbers are 56% and 72% when using  $\omega_{\text{proposed}}$ . Comparison between the shear stress distributions along the intact girder and damaged girder and the design beam shear stresses suggested ACI 318-08 and BS 8110, the factor proposed by Regan for one-way slab seems to underestimate the enhancement of the shear resistance of the slab along the top flange of the intact girder as compared with the shear span factor proposed in this study (Figure 9-22). The main difference between these shear span factors was already explained previously in Figure 9-14. It should be noted that the comparison results reported in Table 9-5 were calculated by magnifying the design code beam shear stress by the shear span factors throughout the entire effective width. In general, the predictions using the proposed shear span factor are 14% greater than the predictions using the Regan's factor; therefore are less conservative and closer to the test values.

**Table 9-5 Comparison of between Test E and Predictions Using Beam Shear Approach.**

| Predictions using one-way shear approach with effective width (kips) |                            |  |   |   |  |  |   |   |  |
|--|----------------------------|--|---|---|--|--|---|---|--|
| $V_{\text{exp}}$<br>(kips)   | $V_{\text{FEA}}$<br>(kips) | $b_{\text{eff1}}$ ,<br>ACI,<br>$\omega_{\text{Regan}}$ | $b_{\text{eff1}}$ ,<br>BS,<br>$\omega_{\text{Regan}}$ | $b_{\text{eff1}}$ ,<br>ACI,<br>$\omega_{\text{proposed}}$ | $b_{\text{eff1}}$ ,<br>BS,<br>$\omega_{\text{proposed}}$ | $b_{\text{eff2}}$ ,<br>ACI,<br>$\omega_{\text{Regan}}$ | $b_{\text{eff2}}$ ,<br>BS,<br>$\omega_{\text{Regan}}$ | $b_{\text{eff2}}$ ,<br>ACI,<br>$\omega_{\text{proposed}}$ | $b_{\text{eff2}}$ ,<br>BS,<br>$\omega_{\text{proposed}}$ |
| 235  | 262                        | 82   | 103   | 95  | 118  | 163  | 202   | 184   | 229  |

As mentioned earlier, another way to predict the shear resistance of a slab failing in one-way shear manner is calculating the punching shear capacity over the critical perimeter around load. By using the modified critical perimeter which is only one half of the original critical perimeter, the proposed method with the new shear span factor

incorporated along the critical perimeter, in Section 9.5, results in a predicted value of 234 kips. The predictions when using ACI 318-08 and BS 8110 punching shear provisions with the modified critical perimeter and without the shear span factor is 152 kips and 149 kips, respectively. These predictions indicate that these current shear provisions are highly conservative when the enhancement of shear resistance of the slabs due to the direct load transfer effect is not taken into account. When these provisions are used in combination with the shear span factor  $\omega_{\text{proposed}}$ , they results in better predictions with the ratios between the code predictions and the test value increasing from 65% to 85% for ACI 318-08 and 63% to 84% for BS 8110.

**Table 9-6 Comparison of between Test E and Predictions Using Punching Shear Approach.**

| $V_{\text{Test}}$<br>(kips) | $V_{\text{ACI}}$<br>(kips) | $V_{\text{BS}}$<br>(kips) | $V_{\text{ACI}, \omega_{\text{proposed}}}$<br>(kips) | $V_{\text{BS}, \omega_{\text{proposed}}}$<br>(kips) | $V_{\text{proposed}}$<br>(kips) |
|-----------------------------|----------------------------|---------------------------|--|---|---------------------------------|
| 235                         | 152                        | 149                       | 200  | 197   | 234                             |

It is important to note that unlike predictions for punching shear capacity of slab over the fracture location, in this test the shear resistance of the slab along the top flanges of the damaged girder was assumed to have a full enhancement due to direct load transfer effect because the load was applied far away from the fracture location. The effect of CMA is also neglected in this comparison because of the concave-down deflection shape of the specimen which was observed in the test and finite element analysis.

## **9.8 Investigation of Punching Shear Resistance of Slabs across the Bridge in Transverse Direction**

Another important parameter that influences the load-carrying capacity of a damaged twin steel box-girder bridge is the location where the load is applied. Although

the responses of a damaged twin steel box-girder bridge under a concentrate load applied over the center of the intact girder and damaged girder, have been investigated experimentally in Tests C and D, respectively, there is a need to investigate how the responses of the damaged twin steel box-girder bridges vary as the load is moved cross the bridge in transverse direction. For this reason, two additional finite element analyses with the load applied over the center of the deck and over the overhang were performed. Summary of all loading locations considered are shown in Figure 9-23. The loading area is 10 in. x 10 in. in all cases and the load is applied at mid-span section where the fracture occurs. The results presented here are all from finite element analyses.

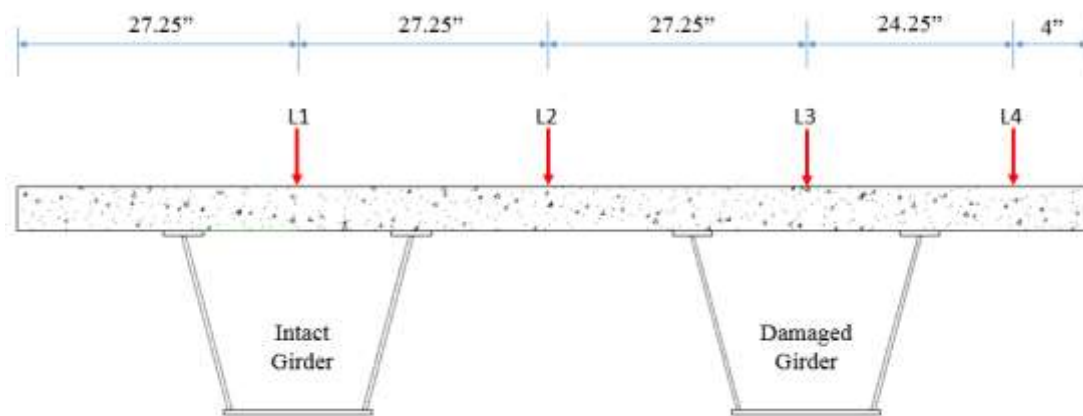


**Figure 9-23 Locations across the bridge investigated for the punching shear capacity.**

The comparison of the ultimate load-carrying capacities obtained from each load case is illustrated in Figure 9-24. As the loading location moves further toward the damaged side of the specimen the capacity of the specimen decreases significantly. At location L1, the punching shear capacity was 172 kips obtained at 1-inch displacement. This predicted capacity is approximately 4.4% smaller than the actual capacity of the specimen, which was 180 kips, obtained in Test C. When the load was moved to the center of the deck at location L2, the specimen reached its ultimate capacity at 160 kips at 1.3-in. displacement.

With load applied at location L3 which is the center of the damaged girder, the specimen's ultimate capacity reduced to 104 kips at 1.4-in. displacement. This value is greater than what obtained experimentally from Test D which was 80 kips. This difference could be attributed to the initial deck cracks and the girder residual deformation that the specimen experienced as a result of Tests B and C. When the load is moved over the overhang of the damaged girder, the ultimate capacity decreased significantly to 68 kips with a displacement of 1.4 in.

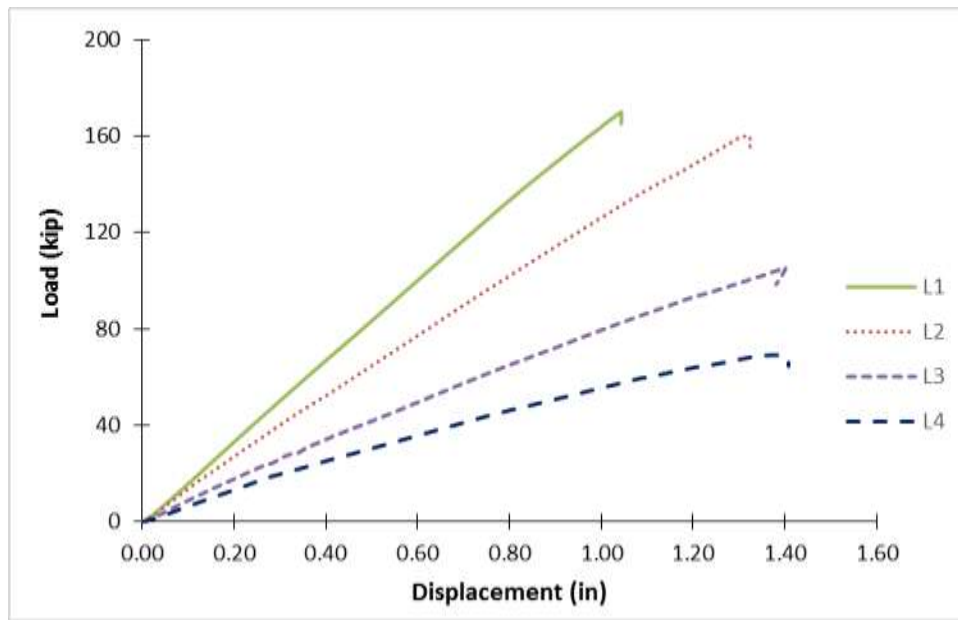


**Figure 9-24 Comparison of the bridge specimen's load-carrying capacities with concentrated loads applied at different locations.**

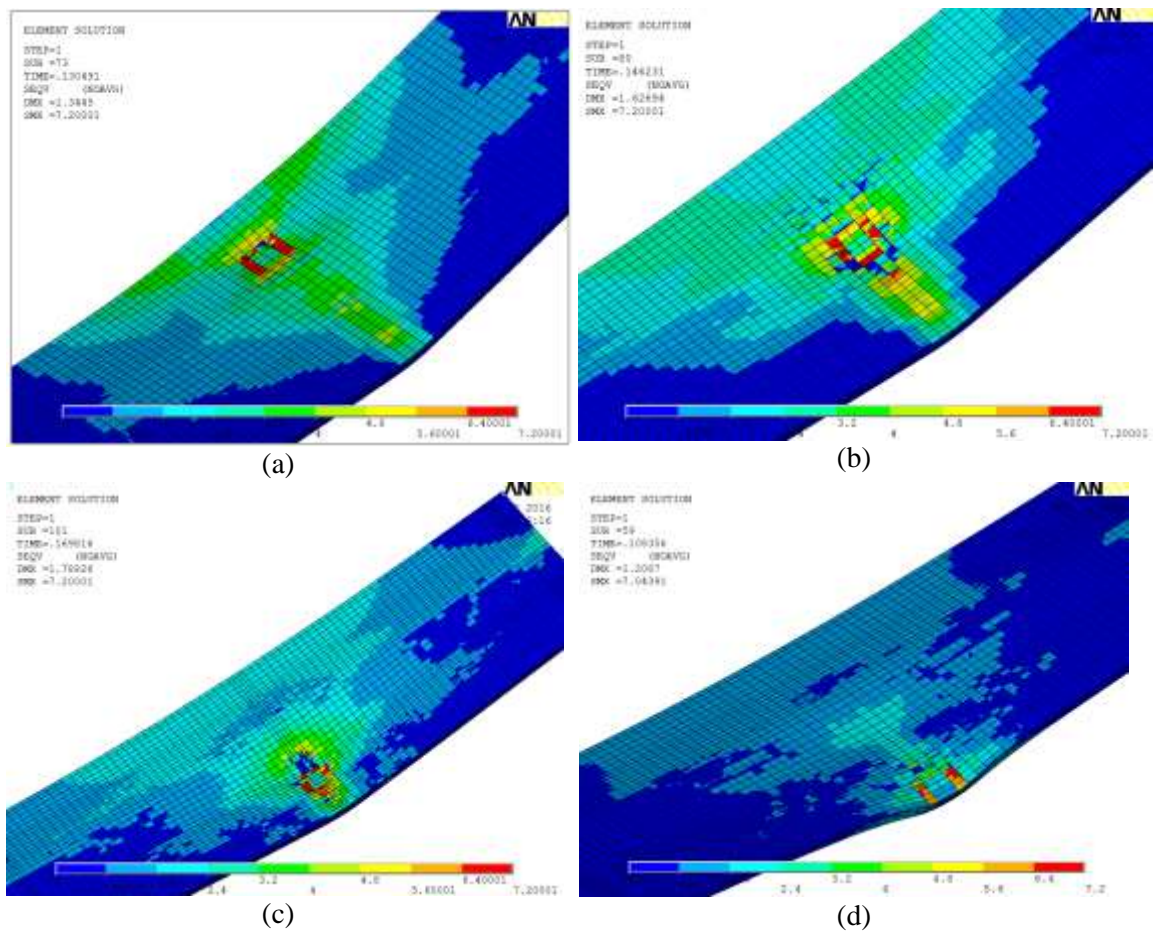
The stress distributions for each analysis is illustrated in Figure 9-25. In the first three load cases L1, L2 and L3, the punching shear was the dominant mode of failure. For the load case L4 with the load applied over the overhang, the mode of failure was combination of both punching shear and on-way shear.

The load distributed around the critical perimeter for each load case is shown in Table 9-7. For the load applied at L1 location, the load distribution at the critical perimeter



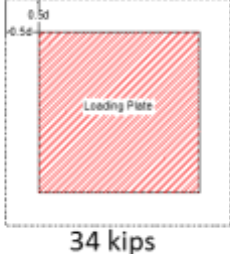
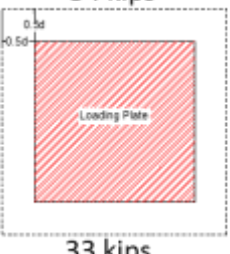
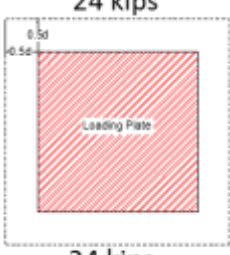
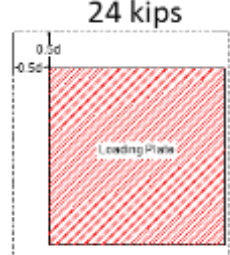
was found to be affected by the compressive membrane action and direct load transfer effects and has been discussed previously. When the load was applied at the center of the deck which is the location L2, the load distribution at the critical perimeter was similar to that occurred at location L1, except the portion that was parallel and close to the top flange of the damaged girder. This portion was found to carry less load than the other portion that was parallel and close to the top flange of the intact girder (42 kips vs 53 kips). This could be explained by considering the middle portion of the deck (between two girders) is supported by two fictitious beams. One beam has a flexural stiffness equivalent to that of the intact composite section comprising of the intact girder and the deck portion over it while the other beam has a stiffness equivalent to that of the damaged composite section comprising of the damaged girder and the deck portion on top of it. With a clear span distance of 6.8 in. and less than  $2d$  and the flexural stiffness provided by one side is smaller than other side, the effect of direct load transfer will also be smaller in one side than the other. That is why the shear resistance of the deck along the critical perimeter that is parallel and close to the weaker supporting beam was 42 kips while it was 53 kips on the other side. With the properties of the composite section, the lateral stiffness of the slab in this case can be calculated following the procedure that has been described in the proposed method. It should be note that both intact composite section and damaged composite section have similar lateral stiffness. The predicted punching shear capacity for this particular loading by using the proposed method was 137 kips. This calculation only considers the CMA and direct load transfer effects on the portion of the critical perimeter that is parallel and close to the intact girder.

When the load is applied at the overhang of the damaged girder, the critical perimeter has only three sides because the load was applied near the edge of the slab. Since the load was applied at the edge of the slab, the CMA effect was not developed. Moreover, the flexural stiffness of the damaged girder and the deck at this fracture location was negligible, the effect of direct load transfer also can be neglected as explained previously. Similar to the case where the load is applied at the center of the damaged girder, the punching shear resistance of the slabs now could be predicted using either the proposed method or practice codes. The predicted values are in good agreement with the FE results with 52 kips for ACI code, 64 kips for BS 8110 code and 60 kips for the proposed method.



**Figure 9-25 Stress distributions under concentrated load at (a) L1, (b) L2, (c) L3 and (d) L4.**

**Table 9-7 Comparison of Punching Shear Resistance of Slabs at Locations L1, L2, L3 and L4 and the predicted values.**

| Loading Location | Loading Distribution at Critical Perimeter  | $P_{FEA}$ (kips) | $P_{proposed}$ (kips) | $P_{ACI 318}$ (kips) | $P_{BS 8110}$ (kips) |
|------------------|---|------------------|-----------------------|----------------------|----------------------|
| L1               | <p>52 kips</p>  <p>51 kips</p>   | 172              | 155                   | 77                   | 88                   |
| L2               | <p>53 kips</p>  <p>41 kips</p>   | 160              | 137                   | 77                   | 75                   |
| L3               | <p>28 kips</p>  <p>28 kips</p> | 104              | 89                    | 77                   | 75                   |
| L4               | <p>20 kips</p>  <p>24 kips</p> | 69               | 60                    | 52                   | 64                   |

## 9.9 Summary

The proposed shear span factor is able to capture the influence of  $\frac{a_v}{d}$  (or direct load transfer effect) on the shear resistance of two-way slabs under concentrated loads close to the top flanges of the supporting girders. Both effects of CMA and direct load transfer are predicted adequately by the proposed method. The results predicted from the proposed method are in good agreement with both experimental and FEA results. Practice codes such as BS 8110 and ACI 318-08 are very conservative in predicting the punching shear capacities of slabs when the CMA and direct load transfer effects involve. However, when the slab-supporting girder is completely fractured, the ACI 318-08 or BS 8110 codes are shown to be adequate to predict the punching shear capacity of bridge slab over the damage location as the influence of these effects on shear resistance of slabs are negligible.

When the bridge slab fails in one-way shear manner, using the effective width determined by 45° horizontal load spreading from the far side of the load with the proposed shear span factor results in the best predictions. The current beam shear provisions without shear span factors are likely to result in very conservative values when the load is applied closed to the supports or to the top flanges of the supporting girder. The shear span factor proposed in this study can be used to predict the shear capacity of the bridge slabs failing in either one-way or two-way shear failure modes. The proposed shear span factor shows a better correlation with the test and finite element analysis results than the shear span factor proposed by Regan (1982). All of the comparisons indicated the proposed shear span factor can be used in compliance with either ACI-318 08 or BS 8110 shear provisions.

In addition to verified and calibrated nonlinear finite element models, the simplified method presented in this study can serve a tool to predict the capacity of a

damaged twin steel box-girder bridge subjected to concentrated loads. With this simplified method, the process to develop the probability density function for the load-carrying capacity of the twin steel box-girder bridges which requires carrying out a large number of simulations, as discussed in Chapter 2, can be simplified significantly. The simplified methods could serve as a first check in the redundancy evaluation assessment procedure that this research is aiming to develop eventually.

## **Chapter 10 Proposed Notional Approach for Evaluating Redundancy of Twin Steel Box-Girder Bridges**

Although simplified methods proposed in Chapter 9 can serve a first-level check in the redundancy assessment procedure which this research is aiming to develop ultimately, detailed nonlinear finite element analysis still serves as the final-check and the most reliable method. However, addressing the redundancy of all two steel box-girder bridges within inventory of a given state requires significant amounts of financial, labor and computer resources. The notional approach proposed in this chapter is to reduce the level of effort involved by grouping the two steel box-girder bridges within a state inventory into several groups and developing a notional simple-span two steel box-girder bridge that would represent each group and then carries out the detailed nonlinear finite element analysis on the notional bridge. By proving the notional bridge redundant, all bridges within the group under consideration, are also redundant.

### **10.1 Key Components of the Notional Approach**

The notional approach will include the following major components:

1. Development of a calibrated nonlinear finite element model:

As provided in Chapter 5 & 6, this research has developed a nonlinear finite element model that is able to capture the failure modes of damaged twin steel box-girder bridges under concentrated loads. The comparisons between the test results and the FEA results also indicate that the model is well calibrated and verified.

2. Development of a notional simple span bridge model that represents multi-span bridge within in the inventory requires carrying the following tasks:
  - a. Develop grouping criteria: The grouping criteria is determined based on the geometrical characteristics of in the inventory such as type of bridges, designed lane-load number, the length of each span, number of spans, radius curvature and cross-section. Based on these criteria, bridges of interest can be categorized into several groups.
  - b. Develop the notional simple span bridge: Once select bridges are categorized into groups, a notional simple span bridge model that can represent all the bridges within each group needs to be developed. The notional simple span bridge model is suggested to have the following characteristics:
    - i. Has the shortest radius of curvature
    - ii. Has the longest span length
    - iii. Has the smallest cross-section

By defining the notional simple-span bridge model this way, it can serve as a conservative model for the entire group. As a result, if the notional simple-span bridge model satisfies all the redundancy criteria and is classified as redundant, all the bridges within the group will also do.

An example of using the notional approach is shown in Table 10-1. The notional simple span bridge model is actually the small-scale bridge specimen that was tested in this study. Two-span and three-span bridge models considered here are modified from this notional simple span model with different spans and span lengths; however, the bridge cross-section and material properties are kept the same. All the models are analyzed with

a full-depth fracture in one of the girder at the middle of one span. The load is applied right over the fracture location to simulate the worst-case scenario. The (\*) indicates in which span the fracture occurs and the load is applied. In this table, the ultimate load-carrying capacity of different multi-span twin steel box-girder bridges and its notional simple span bridge model are compared. The results indicate that the notional simple span is able to represent conservatively two-span and three-span twin steel box-girder bridges in the inventory.

**Table 10-1 Validation of the Notional Approach.**

| <b>9x36 Over Damaged Girder</b> | <b>Span Length (ft)</b> | <b>Capacity (kip)</b> | <b>Capacity Ratio</b> | <b>Avg. Ratio</b> |
|---------------------------------|-------------------------|-----------------------|-----------------------|-------------------|
| Notional Model                  | 30*                     | 164                   | 1.00                  | 1.00              |
| Two-Span Bridges                | 30*-10                  | 195                   | 1.19                  | 1.31              |
|                                 | 30*-20                  | 226                   | 1.38                  |                   |
|                                 | 30*-30                  | 224                   | 1.37                  |                   |
| Three-Span Bridges              | 30*-20-20               | 199                   | 1.21                  | 1.38              |
|                                 | 30*-20-30               | 221                   | 1.35                  |                   |
|                                 | 20-30*-20               | 246                   | 1.50                  |                   |
|                                 | 30-30*-30               | 244                   | 1.49                  |                   |

\*: the span where the fracture takes place and the load is applied.

- Once the notional simple-span bridge model is developed, it will be analyzed and assessed by using the calibrated finite element models that was developed in this study. The analysis results such as the ultimate load-carrying capacity and maximum deflection will be reported to check against redundancy criteria which will be fully developed in future research. The approach to develop these redundancy criteria has been discussed in Chapter 2 and will be elaborated more in next section (Section 10.2).



4. The last step in the notional approach will be the decision-making process. If the notional simple span model satisfies all of the redundancy criteria, the entire group, which the notional model represents for, will automatically satisfy as well and will be considered as redundant, and therefore can be removed from the “fracture critical” list. If the criteria are not satisfied, divide bridges again into smaller groups and repeat the process from Steps 1 to 4. In case that only one bridge is left within the group, that bridge will be modeled and analyzed as a full model. If that particular bridge still doesn’t meet the criteria, it will remain in the “fracture-critical” list.

The overall procedure for this notional approach is summarized in the following flow-chart:

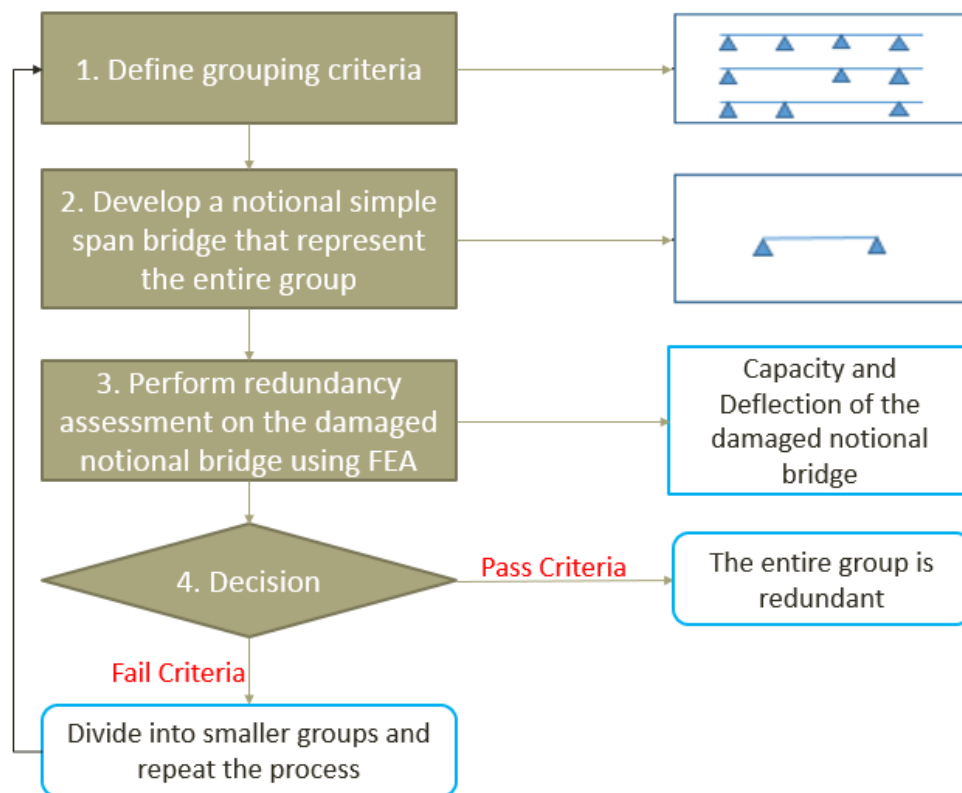


**Figure 10-1 Summary of notional approach.**

## 10.2 Suggestions for Developing Redundancy Criteria

As briefly discussed in Chapter 2, the development of redundancy criteria such as the load and deflection limits that damaged two steel box-girder bridges must resist will demand carrying out reliability-based analysis with a safety level agreed upon by bridge owners.

This effort to develop such criteria could consist of the following steps:

1. Establish a probability density function (PDF) of load-carrying capacity of the damaged bridges: This requires a large amount of data of the ultimate capacity of the damaged two steel box girder bridges. As indicated in this research, the shear failures are likely the governing failure modes for a damaged twin steel box-girder bridges as subjected to concentrated load. Therefore, the process to develop such PDF curve could be facilitated by using the simplified method that has been proposed in this dissertation assuming a fictitious full-depth fracture in one girder. Yield-line analysis, proposed in TxDOT Research Project 9-5498, might be used as an alternative solution for checking and comparison purposes. Once the enough data is collected, the PDF of resistance of the damaged bridges can be developed using any available distribution-fitting tool.
2. Establish a safety level and PDF of load level for damaged twin steel box-girder bridges that is acceptable by agencies. This safety level could be established by consensus or through reliability analysis of bridges that are agreed to be redundant and can be expressed in term of probability of failure or reliability index. According to NCHRP Report 406, a damaged bridge could be considered redundant if its reliability index is greater than 0.8. This redundancy criterion

was developed based on reliability analysis of a large number of common four-girder bridges, assuming all four-girder bridges are redundant.

Using similar approach, the probability of failure or reliability index that is specific for two steel box girder bridges can be developed by performing reliability analysis on a substantial number of three steel box-girder bridges assuming three steel box-girder bridges are redundant. This process will also establish the position of PDF for load, which in turn will provide the load level that damaged two steel box-girder bridges must resist.

3. With PDFs of load (in Step 1) and resistance of damaged bridge (in Step 2) are available, the next step is to calculate probability of failure (PF) or reliability index for damaged bridges under consideration.

Figure 10-2 illustrates an example showing the probability of failure for a full-depth fractured two steel box girder bridges computed using Monte-Carlo simulation. This example assumes the PDF of required strength (load) following lognormal distribution with median of 800 kips and coefficient of variation (COV) of 0.1 and the PDF of resistance of damaged bridges is also lognormal distribution with median 840 kips and COV of 0.1. Figure 10-3 illustrates how the probability of failure changes as the capacity of the damaged bridge varies from 700 kips to 1000 kips. Assuming the safety level required in term of reliability index is 0.8 as Ghosn and Moses (1998) suggested, this requires a damaged twin steel box-girder bridge, or a notional simple-span bridge must have a capacity greater than 810 kips.

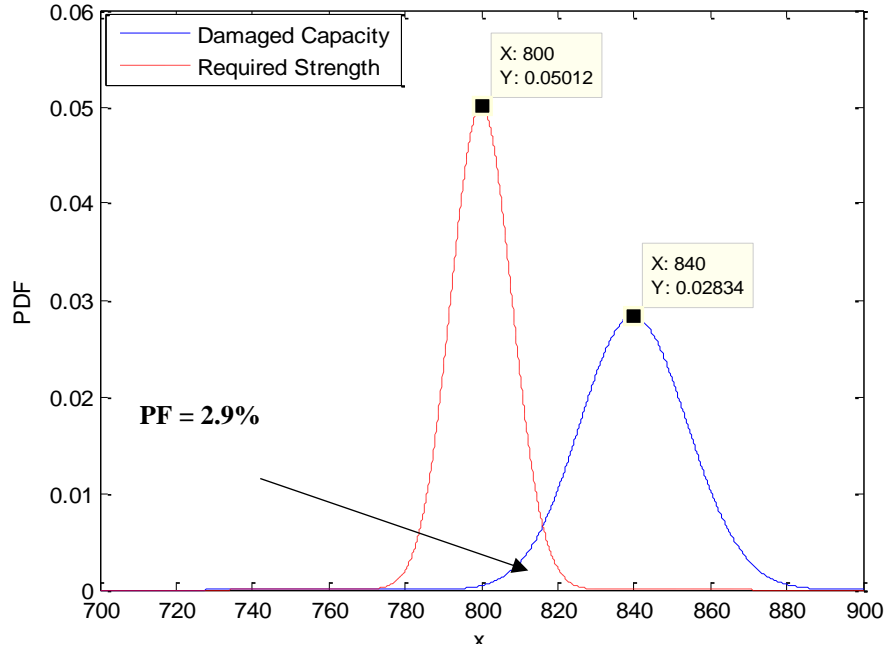


**Figure 10-2 Lognormal PDFs for Required Strength (median = 800, COV = 0.1) and resistance of Damaged Bridge (median = 840, COV = 0.1)**

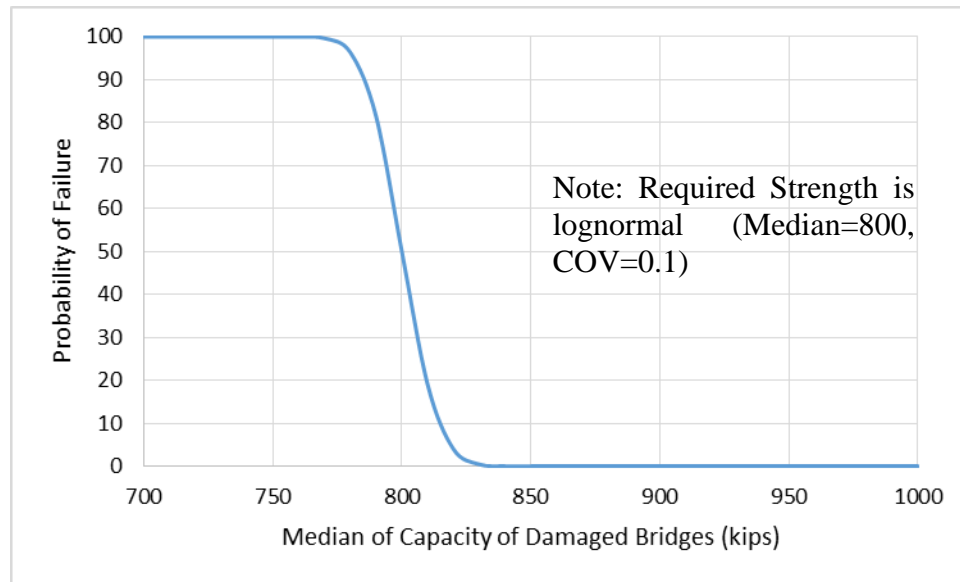


**Figure 10-3 Cumulative Density Function of Damaged Bridges.**

Another important issue, as related to load capacity of the damaged bridges, is that the damaged bridges should be able to sustain permit loads that are issued automatically,

without bridge office involvement. This permit will be determined by participating agencies and bridge officers.

Moreover, the ability of a damaged bridge to carry the traffic until the damage is detected and repaired without jeopardizing public safety also needs to be considered. This consideration requires establishment of the allowable deflection so that the bridge can maintain its functionality during the time period that damage will go on without detection. This aspect of the problem could be checked approximately while conducting finite element analysis on the notional bridges.

## Chapter 11 Parameters Affecting Load-Carrying Capacity of Bridge

In order to investigate the sensitivity of the research findings to variations in some of the key parameters, several finite element simulations and analyses were performed. Parameters investigated in this study include span length, railings, and degree of structural indeterminacy and presence of cross-frames.

The parametric study was carried out under the same loading configuration that was used in Test D, assuming this was the worst loading scenario. The purpose of this parametric study was to investigate whether variations of these parameters would affect the failure mode and capacity of the specimen under concentrated loading configuration. In this parametric study, only post-fracture behavior was considered. The load was incrementally applied until collapse was detected.

### 11.1 Cross-frames

As demonstrated in Test D, the contribution of cross-frame to the load-carrying capacity wasn't significant. It is interesting to check how much the capacity of the specimen will change if all external cross-frames connecting two girders are removed. As illustrated in Figure 11-1, removing the external cross-frames reduces the specimen's load-carrying capacity only slightly from 104 kips to 94 kips. Once the cross-frames were removed, the intact girder retained almost the same stiffness and displacement as before, while the deflection of the fractured girder increased significantly. This indicates that the external cross-frames play important roles in controlling the relative deflection between the girders in the damaged bridge. However, both models had punching shear failure in the concrete deck as the failure mode.

It is also important to note that under different loading configurations, the effect of external cross-frames will vary. For example, in Test A, the contribution of external cross-frames was observed to be larger than it was in Test D. This was because in Test A, the load was applied directly over the top flanges of the damaged girder, and hence more load was distributed to the damaged girder than it was in Test D, where the load is applied only over a small portion of the deck at the center of the damaged girder. Note that the load resisted by the damaged girder should be transferred to the intact girder by means of the external cross-frames and the deck; therefore, as more load is applied to the damaged girder, the external cross-frames is become more effective in transferring load.

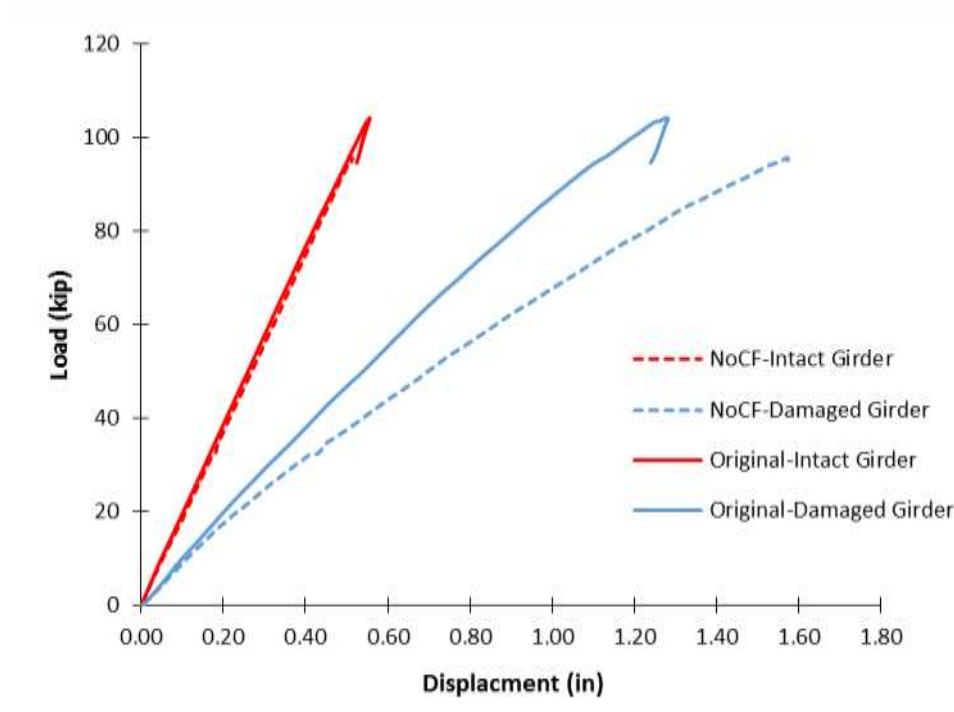


Figure 11-1 Effects of cross-frames.

## 11.2 Railing

The deflection and capacity of the specimen with and without presence of the railing system is shown in Figure 11-2. Since the railing system was poured using the same concrete mix used to cast the deck, it was modeled to have the same nonlinear properties as the deck. The reinforcement was modeled using smeared-reinforcement approach as the concrete deck and the geometry of the railing can be referred in Figure 3-3. However, the expansion joints between the railing segments were neglected in the model for simplification. Moreover, the model assumed the full connection between the rail and concrete deck.

As expected, the model with the railing system deflected less than the model without the railing in both girders. The additional railing also increased the capacity of the specimen because when engaged it acted as deep beam on the edge of the deck and increased bending stiffness of the deck. The capacity of specimen was increased from 104 kips to 134 kips with the presence of the railing. Furthermore, that fact that concrete deck under the loading pad was crushed in both cases indicates that the specimen failed in punching shear whether with or without the presence of the railing.



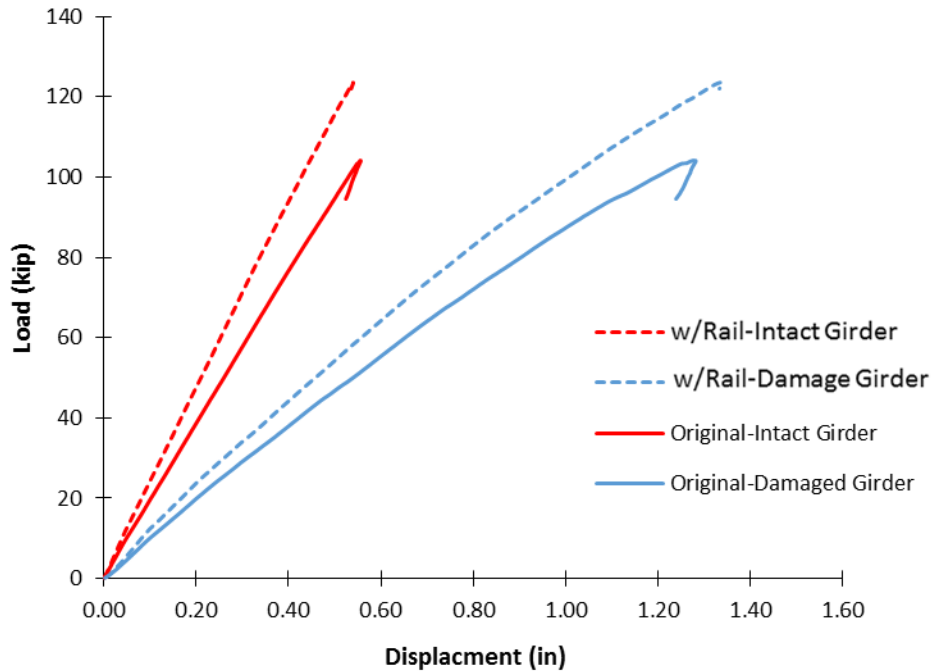


**Figure 11-2 Effects of railing system.**

### 11.3 Structural Indeterminacy and Cantilever End

Similarly to the railing system, bridges with continuous spans possess higher stiffness than the simply-supported bridge as demonstrated in elastic tests. The structural indeterminacy and continuity was found to provide additional sources of redundancy for the bridge system. In the event that one girder is fully fractured, the load applied to the fractured girder can be redistributed to the intact girder as well as neighboring spans; therefore, chance of collapse can be reduced significantly in multi-span bridges.

The continuity was modeled by simply introducing two vertical restraints at the center of each girder, additional to the original model. This approach is similar to the way it was setup in the elastic tests, which are shown in Figure 3-20. The comparison of both models is illustrated in Figure 11-3. The specimen with two spans had better performance than the

simply-supported model in both displacement and capacity aspects. Similar to other cases above, the simulation was terminated due to the excessive crushing of concrete deck near the loading area. This suggests that shear failure was still a potential mode of failure of the specimen under this concentrated loading configuration.

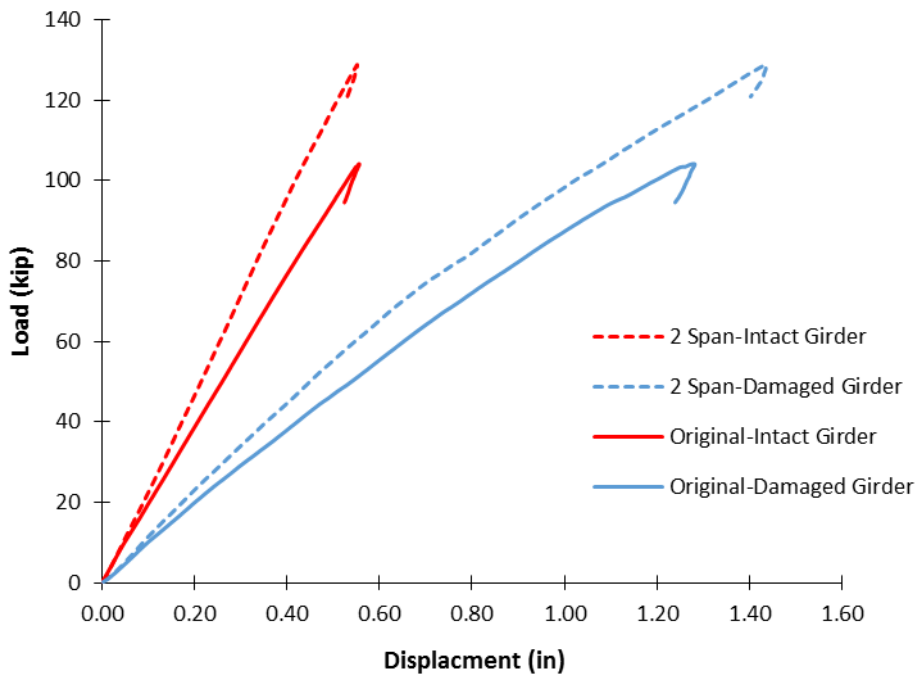


Figure 11-3 Effects of continuity.

#### 11.4 Bridge Span Length

This small-scale model with different span lengths was analyzed to investigate the potential effects of span length on the behavior of bridges. In order to isolate and study only the effect of span length, the external cross-frames and the cantilever end were removed in these analyses. Table 11-1 compares capacity and girder displacements for different specimens with different length. In this case, span lengths will be used because

all models had the same girder dimension. In case that the girder dimensions are different, the ratio of span length to girder depth will be a better criteria to use.

**Table 11-1 Effects of Span Length on the Bridge Performance.**

| Length (ft) | Capacity (kip) | Intact Girder Displacement (in) | Damaged Girder Displacement (in) |
|-------------|----------------|---------------------------------|----------------------------------|
| 30          | 80             | 0.33                            | 1.67                             |
| 22          | 70             | 0.1                             | 1.19                             |
| 18          | 75             | 0.05                            | 1.10                             |
| 12          | 74             | 0.008                           | 0.65                             |

As illustrated, the variation of span length did not significantly influence either the capacity of the specimen or the failure modes. However, as the length of span (or ratio of span length to girder depth) got smaller, the bending stiffness of the bridge increased. Therefore, it reduced the displacement of both girders significantly. The models again failed due to the crushing of concrete deck underneath of loading area.

## 11.5 Summary

The effects of the external cross-frames, railing, structural indeterminacy, and span length on the capacity of the bridge specimen were investigated, under a concentrated loading. Overall, the presence of cross-frames and railings and additional continuity were found to increase the stiffness of structure and improve the capacity of the bridge. The capacity improvement can be seen clearly when adding the railing or continuity. It is also found that varying the span length of the specimen does not affect much the capacity of the bridge. In all of the cases, the specimen was failed under the same failure mode which was punching shear.

It is also important to note that these effects may vary under different loading configurations. For instance, if the load is applied in a more distributed manner, the effects of external cross-frames, railings and structural indeterminacy might increase and varying the length of specimen might also affect the capacity of the bridge.

## Chapter 12 Summary and Future Considerations

### 12.1 Research Summary

According to AASHTO *LRFD Bridge Design Specifications*, twin steel box-girder bridges are currently classified as bridges with fracture critical members (FCMs), in which a failure of a tension member leads to a collapse of the bridge. However, there are several evidences indicating that twin steel box-girder bridges are redundant and still able to carry a significant amount of traffic load with little noticeable change to their global behavior. The main objectives of this current FDOT-sponsored research study, presented in this dissertation, are to provide an understanding of the behavior of twin steel box-girder bridges and to develop complete methodology and associated tools that can be used to evaluate performance of these bridges after damage and remove them from the fracture critical list, where possible.

The suggested methodology is a two-step process. The first step will consist of simple hand calculation that is based on the research study conducted at the University of Texas-Austin. Further investigation on this method will be needed in future research.

The second approach is referred to as the notional approach. The notional approach considers finite element analysis as the main method to assess performance of damaged twin steel box-girder bridges. However, performing a detailed nonlinear finite element analysis on every single twin steel box-girder bridge within inventory of a given state requires a significant amount of labor and financial resources. To address this challenge, the notional approach suggests grouping twin steel box-girder bridges in the inventory into groups and developing a notional simple span twin steel box-girder that represents all of

the bridges within a given group. The detailed nonlinear finite element analysis is then carried out on the notional simple-span bridge only. By doing so, a significant amount of the effort and resources required will be reduced.

The details of the notional approach are provided in Chapter 2 of this dissertation. The majority of the information needed to evaluate the redundancy of the twin steel box-girder bridges using the notional approach has been addressed within this dissertation. The remaining works are left to be completed under future research.

Following are elements of the notional approach of evaluating the redundancy of twin steel box-girder bridges.

Task 1: Access to calibrated nonlinear finite element model that accurately depicts the modes of failure under types of loading specified by *AASHTO LRFD Bridge Design Specifications*. This research study has developed a test verified nonlinear FEM model.

Task 2: Criteria to group twin steel box-girder bridges within the inventory of a given state DOT and develop notional simple-span twin steel box-girder bridge representing the group. This dissertation provides preliminary approaches for grouping the state inventory of twin steel box-girder bridges. However, additional work is recommended, to be carried out in future study.

Task 3: Establishment of the load level that damaged twin steel box-girder bridges must resist, as well as establishment of other serviceability limit states that must be checked to ensure public safety. The procedure for establishing a load level that damaged twin steel box-girder bridges must carry is outlined in this report. The use of arbitrary load level is questioned by many bridge owners and has

remained one of the obstacles for resolving the question of redundancy of twin steel box-girder bridges. As discussed in Chapter 2, development of probability density function (PDF) for load-carrying capacity of the damaged bridges, considering realistic modes of failure is a critical step in establishing the load safety level. This dissertation has provided a simplified method to predict the punching shear strength of slab under concentrated wheel load. This simplified method will facilitate the process of developing the PDF of the capacity of the damaged bridge since it requires a large number of simulations.

Task 4: Development of a Guide for application of the notional approach for assessing redundancy of damaged twin steel box-girder bridges with examples and other documentations, such as video tapes that would assist state DOTs. It is recommended that this task be completed after completing the proposed pooled fund study.

Discussions on approaches to develop the load level as well as other serviceability criteria in Task 4 for a damaged twin steel box-girder bridge have been presented in Chapter 2 of this report. The efforts to develop calibrated and verified detailed nonlinear finite element models are documented from Chapter 3 through Chapter 8. Chapter 9 provides a summary of the results of a parametric study on twin steel box-girder bridges and the start of the process for establishing the notional simple-span bridge model and grouping criteria. Chapter 10 proposes a simplified method of predicting the ultimate punching shear capacity of the damaged bridges under concentrated load, assuming the punching shear failure mode governs as observed in the experiment.

The remaining portion of this summary and conclusion provides highlights of the results obtained in this project. Complete discussions of each of the following sections can be found in the appropriate chapters within this dissertation.

Summaries of the important observations obtained from the different activities carried out within this research study are provided in the following sections. The summary is provided in the context of experimental work; however, within each section, associated numerical works that have been carried out are included.

## **12.2 Field Tests of In-Service Bridge**

Elastic field tests on a twin steel box-girder Ft. Lauderdale bridge were conducted and its performance was observed. Following are conclusions obtained from the results of the field testing and associated finite element analysis:

- In general, the test-observed deflections were in good agreement with results obtained from FEM analysis, within 5%.
- Comparison of the collected testing strains (and corresponding computed stresses) in the structure and the resulted stresses from finite element analysis of the bridge shows a partial fixity at the abutment in contrast to the ideal pin assumed in the finite element models. This observation agrees with the conclusions of previous field tests conducted by other bridge researchers.
- For the type of truck and load used, the field test result indicated a dynamic amplification factor of approximately 12%. It is important to note that this finding is based on the experimental results of two dynamic tests. One test was carried out



with the truck moving at crawling speed (~3mph) while in the other test, the truck was moving at roadway speed (~30mph)

- The strain response histories showed evidence of slight thermal drift, which is typical for load tests that occur over several hours. In an attempt to reduce the impact of the thermal drift, a thermal correction based on a linear drift was applied to all of the selected processed data in order to reduce this effect.

### **12.3 Laboratory Tests on Small-Scale Specimen**

To comprehend the behavior of twin steel box-girder bridges in nonlinear range, examine the modes of failure, and calibrate three dimensional 3-D finite element models, a small-scale test specimen was constructed and numerous tests were carried out including elastic tests, a cyclic fatigue test, and ultimate load tests. The following sections provide a brief discussion of the results obtained. For a more detailed discussion refer to various chapters within this report.

The laboratory test specimen was subjected to a number of tests before and after simulating damage in the test specimen. The first series of tests were elastic tests, in which the test specimen was subjected to a single concentrated load over the EG, or two concentrated loads with one load over each girder. The purposes of these elastic tests were to examine linear elastic responses of the laboratory bridge specimen, the effects of railing system and continuity as well as the effects of different loading configuration on the specimen before and after the damage was simulated.

The second test was a cyclic fatigue test. The purpose of this cyclic test was to see what would happen to the bridge specimen under the traffic load assuming a fracture or damage occurred in the bottom flange without being noticed.

Ultimate load tests were the last series of tests, in which the laboratory specimen was loaded to failure. All the ultimate load tests were carried out under the damage condition in which one girder was completely fractured. The purposes of the ultimate load tests were to investigate the behavior, the maximum load-carrying capacity, and failure mode of twin steel box-girder bridges when the web and bottom flange of one of the girders was completely fractured.

### **12.3.1 Conclusions from Elastic Tests Conducted on Laboratory Test Specimen**

In general, a total of 18 elastic tests were carried out. The effects of both rail and continuity on linear-elastic behavior of the bridge specimen were investigated under either unsymmetrical loading or symmetrical loading configuration. The responses of bridge corresponded to different damage levels were interpreted and are summarized as follows:

- The rail and continuity was found to increase the stiffness of the structure; therefore enhancing the load-carrying capacity of the specimen.
- In addition to the deck, the cross-frames played an important role in transferring the applied load from the damaged girder to the intact girder. It should be noted, however, that depending on the loading configuration, the contribution of cross-frames might vary.

- In general, the elastic responses of the undamaged specimen and of the specimen with bottom flange fractured in one girder were comparable. The maximum displacement increased by an average of 6.5 % as the bottom flange was fractured.
- As a result, the strain in the intact girder was found to increase significantly, as the damage intensity increased. This indicates that as the damage takes place, the load resisted by the damaged girder is transferred to the intact girder.
- When the bottom flange and webs were completely fractured, the flexural stiffness of that damaged girder was negligible.

### **12.3.2 Conclusions from Cyclic Tests Conducted on Laboratory Test Specimen**

In this cyclic load test, the laboratory bridge specimen was loaded unsymmetrically at mid-span on the damaged girder with the rail on but no continuity. Assumption was made that the governing fatigue category is type C. Further it was assumed that the details were designed for infinite life with a corresponding threshold stress value of 10 ksi. This in turn demanded that the specimen be subjected to a single concentrated load of about 60 kips, directly over the damaged girder. Before the start of the cyclic test, the bottom flange of one of the girders was completely cut to simulate complete fracture of bottom tension flange. The objective of this particular cyclic test was to observe the time that it would take for crack to propagate from the bottom flange to the bottom of deck and to observe the behavior of the small-scale test specimen in the process. After applying about 213,000 loading cycles, the crack propagated from the bottom tension flange, through the web and to bottom of concrete deck. With an assumed ADTT of 1286 trucks, this would translate to approximately 5.5 months for the crack to grow from bottom flange, all the way to

bottom of concrete deck. When the crack reached the bottom of concrete deck, the deflection increased approximately 0.3 in. for the damaged girder and 0.13 in. for the intact girder. The changes to global deflection and deck performance during entire cyclic test were relatively small.

### **12.3.3 Conclusions from Ultimate Load Tests Conducted on Laboratory Test Specimen**

A total of five ultimate load tests were carried out under the full-web fracture damage condition, in which one girder had its web and bottom flange completely fractured. The first ultimate test (ultimate Test A) was carried out after the elastic and cyclic tests. The steel box-girders after conclusions of Test A were in a good condition, except for the complete fracture of bottom tension flange and web in one of the girders. Therefore, a decision was made to reconstruct the specimen using the same girders. By doing so, only the new deck is needed and savings can be made. The other four ultimate load tests were carried out on the reconstructed test specimen. The following sections provide a brief summary of each ultimate load test carried out.

In ultimate Test A, the load was applied through the 9 in. x 36 in. loading pad covering the entire width of the damaged girder. The bridge showed a maximum capacity of 156 kips which was two times more than the weight of one HS-20 truck. After reaching the maximum capacity, the specimen capacity dropped to 133 kips at a displacement of 2.5 in. due to crushing of concrete deck, under the applied concentrated load. The bridge specimen was still able to hold this load level before the test was halted due to a significant drop in load-carrying capacity at 5.5-in. displacement. During this extended loading period,

the collected data indicated that the stiffness of the deck played a major role in redistributing the applied load to intact girder. The cross-frames also helped to transfer the load from the damaged girder to the intact girder. The cross-frame forces were found increasing after the peak capacity obtained which was associated with crushing of the deck. The intact girder did not yield during the entire test.

In ultimate Test B, the same loading configuration as in Test A was used, but with loading moved over the intact girder. The test was stopped when the loading plateau occurred at 270 kips. The testing was stopped to limit the damage to the test specimen and allow conduct of additional tests. No major damage occurred, just minor cracking on the top surface of the deck. The intact girder showed significant yielding at the bottom flange with more than 8,000  $\mu\epsilon$  while the strain in the damaged girder was negligible. Strain data in both longitudinal and transverse reinforcements, located over the damaged girder and center of the deck, were small compared to those located over the intact girder. This strain distribution pattern, in addition to the observation that both girders experienced similar displacements along the length, indicated that the applied load was mainly resisted by the intact girder. The calculated plastic moment capacity of the intact girder was 239 kips. As mentioned earlier, the test was stopped before complete failure of intact girder. Therefore, the ultimate load-carrying capacity of intact girder or its experimental plastic moment capacity was not obtained experimentally.

In ultimate Test C, the load was applied through a 10 in. square loading pad placed over the center of the intact girder. The specimen carried up to 180 kips before the loading pad suddenly punched through the deck. In general, the specimen showed similar behaviors to those observed in Test B, such that both girders experienced similar displacements and

the applied load was mainly resisted by the intact girder. The recorded strains indicated that the girders did not yield at the time of failure. The fact that neither of the girders yielded and the participation of the damaged girder was negligible indicates the capacity of the specimen, for the type of the loading used, is primarily dependent on the capacity of the deck and its interaction with the intact girder.

In ultimate Test D, the load was applied through a 10 in. square loading pad again, but over the center of the damaged girder. The specimen carried up to 83 kips of load before the loading pad suddenly punched through the deck. This failure mode was similar to that observed in Test C. No yielding was observed in the steel girders at the time of failure. The strain data at the bottom flange suggested the load was transferred to the intact girder uniformly within 5-ft distance measured from the mid-span. The load transferred through the cross-frames was found to be less than 2 kips. This suggested that most of the applied load was transferred to the intact girder through the deck. Although this test and Test C showed identical failure modes, the specimen failed much sooner than it in Test C. This suggests that the punching shear capacity of deck is influenced by the existence of damage in the girder.

In ultimate Test E with a four-point loading configuration, the specimen carried up to 230 kips. The area of each loading point was 10 in. x 10 in., the same as it was in Tests C and D. This improvement in the load-carrying capacity of the specimen was due to the spreading of the applied load into four-point loading. The deck was cracked and damaged significantly along the center line of the bridge, especially where the wheel loads were applied. The intact girder was just right at yielding point. Data from both girders and cross-frames suggested that the load was transferred to the intact girder mainly through the deck.

Overall, the concrete deck was found to fail dominantly in shear in all the tests, except Test B in which loading was stopped before the specimen reached its load carrying capacity. Under single concentrated loading configuration, the specimen deck failed predominantly in two-way shear failure modes, commonly referred to as punching shear failure. When the specimen loaded over the entire width of the girder or with more than one loading point, one-way shear failure mode prevailed. Practice codes such as BS 8110 and ACI 318-08 were found to be very conservative when predicting the punching shear capacities of slabs with short shear spans. It is because compressive membrane action and direct load transfer effects are not considered in these practice codes. However, the punching shear strength of bridge slabs can be estimated by the simplified method described in Chapter 10. This simplified method has shown to give good predictions to both numerical and experimental results. And when the supporting girder is fully damaged or fractured, the CMA and direct load transfer effects are negligible. Therefore, the punching shear capacity of slab portion over the damaged girder can be estimated by BS 8110 or ACI 318-08 practice codes.

In general, a good match between experimental data and finite element analysis results was observed. The percentage differences between FEM analysis results and elastic test data in term of maximum displacement obtained was 5.1% on average. The finite element models were also able to capture the overall behaviors, the modes of failure, and the maximum load-carrying capacity as well as damages that were observed in the ultimate load tests. This verified the accuracy of the finite element modeling techniques that have been employed to study the behavior of steel twin box-girder systems in this project.

It should be noted that no previous research studies dealing with redundancy of twin steel box-girder bridges address shear failure of deck. This is an extremely important point when developing methodology to assess the redundancy of twin steel box-girder bridges after experiencing fracture of tension elements.

#### **12.4 Summary of Proposed Approaches**

In addition to verified and calibrated nonlinear finite element models, the simplified approach including simplified methods proposed in this study was found to be a reliable tool to predict the capacity of a damaged twin steel box-girder bridge when subjected to concentrated loads. The proposed methods have shown that both effects of CMA and direct load transfer in bridge slabs can be captured adequately. With this proposed method the effort to develop the probability density function for the load-carrying capacity of the twin steel box-girder bridges which is required in the notional approach can be simplified significantly. Moreover, the simplified method could also serve as a first check in the redundancy evaluation assessment procedure that this research is aiming to develop eventually.

In addition to the simplified approach, the study also proposes a notional approach that utilizing the experimentally verified and calibrated nonlinear finite element models. The notional approach provides grouping criteria so that the two steel box-girder bridges within a state inventory can be categorized into several groups and propose a notional simple-span two steel box-girder bridge that would represent each group so that the detailed nonlinear finite element analysis will be carried out on only the notional bridge. By proving the notional bridge redundant, all bridges within the group under consideration, are also



redundant. By using this notional approach the effort required to perform redundancy assessment on every single twin steel box-girder bridge can be reduced significantly. The components of this notional approach have been discussed in detail in Chapters 10 and 2 including what have been done and what will be done in future research.

## **12.5 Suggestions for Future Study**

In general, this dissertation provides an in-depth understanding of the performance of twin steel box-girder bridges and develops calibrated three dimensional nonlinear finite element models that can be used in future research. This dissertation also provides a roadmap for development of a complete procedure for assessing redundancy of twin steel box-girder bridges and possibly removing them from fracture critical list. Discussions in Chapter 2 and in this summary chapter identify the remaining tasks that are required to completely develop the comprehensive methodology that allows DOTs to assess the performance of damaged twin steel box-girder bridges and determine whether or not these bridges are redundant. These remaining tasks and approaches to complete these tasks will be proposed for future research. In future research, other possible loading conditions will be also considered before a full recommendation that shear failure in the deck is the governing failure mode of twin steel box-girder bridges. The effects of CMA and direct load transfer effects could also be considered in future testing since the data related to these effects are very scarce for two-way bridge slabs, especially for twin steel-box-girder bridges in its intact and damage conditions. These data could be used to address the question such as what limit of the effective length should be used when incorporating the shear span factors for bridge slabs fail in one-way shear.

## References

- ACI Committee 318 (2008). *Building Code Requirements for Structural Concrete (ACI 318-08) and Commentary*. American Concrete Institute, Farmington Hills, MI.
- Altidis, P., and Adams, V. (2005). *Analyzing Hyperelastic Materials with Some Practical Considerations*. Retrieved from <http://www.ewp.rpi.edu/hartford/~ernesto/S2015/FWLM/TermProject/Misulia/Altidis2005-ANSYSUsersGroup-HyperelasticMaterials.pdf>
- American Association of State Highway Transportation Officials (2010). *AASHTO LRFD Bridge Design Specifications*. Washington, D.C.
- Aoki, Y. and Seki, H. (1971). Shear Strength and Cracking in Two-Way Slabs Subjected to Concentrated Loads. *ACI Publication SP-30*, pp 103-126.
- Azad, A.K., Baluch, M.H., Abbasi, M.S.A., and Kareem, K. (1994). Punching Capacity of Deck Slabs in Girder-Slab Bridges. *ACI Structural Journal*, Vol. 91, No. 6, pp. 656-662.
- Barnard, T. J. (2006). *Constructing a Full-Scale Horizontally-Curved Twin Steel Trapezoidal Box Girder Bridge Segment to Determine Redundancies in Fracture Critical Bridges*. M.S. Thesis, University of Texas at Austin, Austin, TX.
- Barnard, T., Hovell, C.G., Sutton, J. P., Mouras, J.M., Neuman, B.J., Samaras, V.A., Kim, J., William, E.B, and Frank, K.H. (2010). *Modeling the Response of Fracture Critical Steel Box-Girder Bridges*. Report FHWA/TX-10/9-5498-1, Center for Transportation Research, University of Texas at Austin, Austin, TX.
- Braestrup, M. W. (1980). Dome effect in reinforced concrete slabs: elastic-plastic analysis. *Journal of Structural Division, Proceedings of ASCE*, Vol. 106, No. ST6, pp. 1255-1262.
- British Standards Institution (1997). *Part 1. Code of practice for design and construction*. British Standards Institution, BS 8110, London.
- Brotchie, J.F. and Holley, M.J. (1971). Membrane action in slabs. *ACI Publication SP-30*, pp 345-377.
- Christiansen, K.P. (1963). The effect of membrane stresses on the ultimate strength of an interior panel in a reinforced concrete slabs. *Structural Engineer*, Vol. 41, No. 8, pp. 261-265.

- Connor, R.J., Dexter, R., and Mahmoud, H. (2005). *NCHRP Synthesis 354: Inspection and Management of Bridges with Fracture-Critical Details*. Transportation Research Board, National Academy Press, Washington, D.C.
- Dassault, S. (2007). *ABAQUS Analysis User's Manual*, Version 6.7, ABAQUS, Inc., Rising Sun Mills, R.I.
- Federal Highway Administration (2012). *Clarification of Requirements for Fracture Critical Members. Memorandum*. Retrieved from <https://www.fhwa.dot.gov/bridge/120620.cfm>
- Fisher, J.W., Pense, A.W., and Roberts, R. (1977). Evaluation of Fracture of Lafayette Street Bridge. *ASCE Journal of the Structural Division*, Vol. 103, No. ST7, pp.1339-1357.
- Frangopol, D.M., and Liu, M. (2007). Maintenance and management of civil infrastructure based on condition, safety, optimization and life-cycle cost. *Structure and Infrastructure Engineering*, 3 (1), 29-41.
- Frangopol, D.M., and Nakib, R. (1991). Redundancy in Highway Bridges. *Engineering Journal*, 28 (1), 45-50.
- Ghosn, M., and Moses, F. (1998). *NCHRP Report 406: Redundancy in Highway Bridge Superstructures*. Transportation Research Board, National Research Council, Washington, D.C.
- Ghosn, M., Moses, F., and Frangopol, D. M. (2010). Redundancy and robustness of highway bridge superstructures and substructures. *Structure and Infrastructure Engineering*. 6.1-2: 257-278.
- HNTB-Milwaukee Transportation Center (2005). *A Study of the Marquette Interchange HPS Twin Box Girder Structures*. Report WI-1060-05-1222, Milwaukee, WI.
- Hognestad, E. (1951). *A Study of Combined Bending and Axial Load in Reinforced Concrete Members*. University of Illinois Engineering Experimental Station, Bulletin Series, No. 399, pp. 128.
- Hognestad, E., Hanson, N.W, and McHenry, D. (1955). Concrete stress distribution in ultimate strength design. *ACI Structural Journal*, Vol. 52, No. 6, pp. 455-479.
- Hon, A., Taplin, G. and Al-Mahaidi, R.S. (2005). Strength of Reinforced Concrete Bridge Decks Under Compressive Membrane Action. *ACI Structural Journal*, Vol. 102, No. 3, pp. 393-401.

- Hovell, C. (2007). *Evaluation of Redundancy in Trapezoidal Box-Girder Bridges Using Finite Element Analysis*. M.S. Thesis, University of Texas at Austin, Austin, TX.
- Kachlakev, D., Miller, T., and Yim, S. (2001). *Finite Element Modeling of Reinforced Concrete Structures Strengthened with FRP Laminates*. Final Report SPR 316, Oregon, USA.
- Kathol, S., Azizinamini, A., and Luedke, J. (1995). *Strength Capacity of Steel Girder Bridges*. Final Report RES1(0099) P469, University of Nebraska, Omaha, NE.
- Kirkpatrick, J., Rankin, G.I.B., and Long, A.E. (1984). Strength evaluation of M-beam bridge deck slabs. *Structural Engineer*, Vol. 62B, No. 3, pp. 60-68.
- Kuang, J.S. and Morley, C.T. (1992). Punching Shear behaviour of restrained reinforced concrete slabs. *ACI Structural Journal*, Vol. 89, No. 1, pp. 13-19.
- Kuang, J.S. and Morley, C.T. (1993). A Plasticity Model for Punching Shear of Laterally Restrained Slabs with Compressive Membrane Action. *International Journal of Mechanical Sciences*, Vol. 35, No. 5, pp. 371-385.
- Lantsoght, EOL, de Boer Ane, van der Veen Cor, and Walraven J.C. (2015). Effective shear width of concrete slab bridges. *Proceedings of the Institution of Civil Engineers*, Vol. 168, No. 4, pp. 287-298.
- Lee, D.J. (1994). *Bridge Bearings and Expansion Joints*, 2<sup>nd</sup> Ed. London: E & FN Spon.
- Leibenberg, A.C. (1966). *Arching action in concrete slabs*. National Building Research Institute Bulletin, No. 40, CSIR Research Report No. 234, Pretoria, South Africa.
- Mattock, A. H., Kriz, L.B., and Hognestad, E. (1961). Rectangular concrete stress distribution in ultimate strength design. *ACI Structural Journal*, Vol. 57, No. 8, pp. 875-926.
- Mufti, A.A. and Newhook, J.P. (1998). Punching Shear Strength of Restrained Concrete Bridge Deck Slabs. *ACI Structural Journal*, Vol. 95, No. 4, pp. 375-381.
- National Transportation Safety Board (2008). *Collapse of I-35W Highway Bridge Minneapolis, Minnesota, August 1, 2007*. Highway Accident Report NTSB/HAR-08/03. Washington, DC.
- Neuman, Bryce J. (2009). *Evaluating the Redundancy of Steel Bridges: Full-Scale Destructive Testing of a Fracture Critical Twin Box-Girder Steel Bridge*. M.S. Thesis, University of Texas at Austin, Austin, TX.

- Okleston, A.J. (1958). Arching action in reinforced concrete slabs. *Structural Engineer*, Vol. 36, No. 6, pp. 197-201.
- Park, R. (1964). Ultimate strength of rectangular concrete slabs under short-term uniform loading with edges restrained against lateral movement. *Proceedings of Institution of Civil Engineers*, Vol. 28, No. 2, pp. 125-150.
- Park, R., and Gamble, W.L. (1980). *Reinforced concrete slabs*. Wiley Interscience, New York.
- Podolny, W. Jr., and Muller, J. M. (1982). *Construction of Design of Prestressed Concrete Segmental Bridges*. New York, NY: John Wiley and Sons.
- Pham, H., Doust, S., Yakel, A., and Azizinamini, A. (2014). *Comprehensive Evaluation of Fracture Critical Bridges*. Final Report SPR-P1(09) P321, Florida International University, Miami, FL.
- Pham, H., Gull, J., Mohammadi, A., and Azizinamini, A. (2016). *Managing Florida's Fracture Critical Bridges – Phases I & II*. Final Report BDV29-977-17, Florida International University, Miami, FL.
- Rankin, G.I.B and Long A.E. (1997). Arching action strength enhancement in laterally restrained slab strips. *Proceedings of the Institution of Civil Engineers, Structures and Buildings*. Vol. 122, No. 4, pp. 461-467.
- Rankin, G.I.B, Niblock R.A., Skates A.S., and Long A.E. (1991). Compressive membrane action strength enhancement in uniformly loaded, laterally restrained slabs. *Structural Engineer*, 1991, Vol. 69, No. 16, pp. 287-295.
- Salim, W. and Sebastian, W.M. (2003). Punching Shear Failure in Reinforced Concrete Slabs with Compressive Membrane Action. *ACI Structural Journal*, Vol. 100, No. 4, pp. 471-479.
- Schwendeman, L.P., and Hedgren, A.W. (1978). Bolted repair of fractured I-79 girder. *ASCE Journal of the Structural Division*, Vol. 104, No. 2, pp. 134-143.
- Taylor, R., and Hayes, B. (1965). Some Tests on the Effect of Edge Restraint on Punching Shear in Reinforced Concrete Slabs. *Magazine of Concrete Research*, Vol 17, No. 50, pp. 39-44.
- Taylor, S.E., Rankin, G.I.B. and Cleland, D.J. (2001). Arching action in high-strength concrete slabs. *Proceedings of the Institution of Civil Engineers, Structures and Buildings*. Vol. 146, No. 4, pp. 353-362.
- Tong, Y.P. and Batcherlor, B.deV. (1971). Compressive Membrane Enhancement in Two-Way Bridge Slabs. *ACI Publication SP-30*, pp 271-286.

- West Virginia DOT (2016). *Silver Bridge*. Retrieved from [http://www.transportation.wv.gov/highways/bridge\\_facts/Modern-Bridges/Pages/Silver.aspx](http://www.transportation.wv.gov/highways/bridge_facts/Modern-Bridges/Pages/Silver.aspx)
- Westergaard, H.M. and Slater W.A. (1921). Moments and stresses in slabs. *Journal of American Concrete Institute Proceedings*, Vol. 17, pp. 415-538.
- Willam, K.J., and Warnke, E.P. (1975). Constitutive model for the triaxial behavior of concrete. *Proceedings of International Association for Bridge and Structural Engineering*, Vol. 19, pp. 174.
- Wood, R. H. (1961). *Plastic and elastic design of slabs and plates*. Thames and Hudson, London.
- Zheng, Y., Taylor, S. and Cleland, D. (2010). Investigation of Ultimate Strength of Deck Sabs in Steel-Concrete Bridges. *ACI Structural Journal*, Vol. 107, No. 1, pp. 82-91.

## VITA

### HUY VAN PHAM

Born, Phu Yen, Viet Nam

|             |   |
|-------------|---|
| 2006 - 2009 | Green River Community College, Highest Honor<br>Auburn, WA                                    |
| 2010 - 2011 | B.S., Civil Engineering, Highest Honor<br>Georgia Institute of Technology<br>Atlanta, GA      |
| 2012 - 2013 | M.S., Civil Engineering, GPA 4.0/4.0<br>Georgia Institute of Technology<br>Atlanta, GA        |
| 2013 - 2016 | Ph.D., Civil Engineering<br>Florida International University<br>Miami, Florida                |
| 2012 - 2013 | Research Assistant<br>Georgia Institute of Technology<br>Atlanta, Georgia                     |
| 2013 - 2016 | Research and Teaching Assistant<br>Florida International University<br>Miami, Florida         |
| 2014 - 2015 | National Accelerated Bridge Construction Conference Organizing<br>Committee<br>Miami, Florida |

### PUBLICATIONS and PRESENTATION

- Pham, H., Doust, S., Yakel, A., Gull, J., Azizinamini, A. (2015). "Comprehensive Evaluation of Fracture Critical Bridges". 2015 Transportation Research Board Annual Meeting Proceedings, Washington, D.C.
- Pham, H., Taghinezhad, R., Azizinamini, A. (2016). "Experimental Investigation of Redundancy of Twin steel Box-Girder Bridges under Concentrated Load". 2017 Transportation Research Board Annual Meeting Proceedings, Washington, D.C.

- Pham, H., Azizinamini, A. (2016). “Ultimate Strength of Twin Steel Box-Girder Bridges under Concentrated Loads”. To be submitted to ASCE Journal of Bridge Engineering.
- Farzad, M., Mohammadi, A., Shafieifar, M., Pham, H., Azizinamini, A. (2016). “Development of Innovative Bridge Systems Utilizing Steel-Concrete-Steel Sandwich System”. 2017 Transportation Research Board Annual Meeting Proceedings, Washington, D.C.
- Taghinezhad, R., Gull, J., Pham, H., Olson L., Azizinamini, A. (2016). “Acoustic Emission Monitoring during the Construction of a Post-Tensioned Segmental Bridge”. 2017 Transportation Research Board Annual Meeting Proceedings, Washington, D.C.